Mechanistic Studies of Interface Formation Between AA3003 and AA4045 Alloys During Fusion™ Casting

by

Massimo Di Ciano

A thesis

presented to the University of Waterloo

in fulfillment of the

thesis requirement for the degree of

Doctor of Philosophy

in

Mechanical Engineering

Waterloo, Ontario, Canada, 2015

AUTHOR'S DECLARATION

I hereby declare that I am the sole author of this thesis. This is a true copy of the thesis, including any required final revisions, as accepted by my examiners.

I understand that my thesis may be made electronically available to the public.

Massimo Di Ciano

Abstract

Fusion™ casting is a unique Direct Chill (DC) continuous casting process whereby two different alloys can be cast simultaneously, producing a laminated aluminum ingot. Empirically derived operating ranges exist for Fusion™ casting of specific alloy combinations. When followed, the resulting ingots are of high quality. Despite this, oxide entrainment at the core-clad interface as well as inconsistent clad alloy thickness have reduced product yields. The objective of this thesis was to study the interface formation process in Fusion™ casting, with special emphasis on determining the mechanisms at play. A more fundamental understanding of the process can potentially lead to improvements in Fusion™ ingot yields and the ability to cast other alloy combinations which are currently not used to make Fusion™ ingots.

Both experimental and mathematical modelling methodologies were employed to examine the Fusion™ casting of AA3003-core/AA4045-clad ingots. Tests were conducted using an analog/immersion test system designed and built at the University of Waterloo. The immersion tests provided a means to examine wetting and bonding between dissimilar aluminum alloys under closely controlled conditions. Results from these analog/immersion tests showed that the AA3003 sample oxide was permeable and good wetting occurred with the AA4045 melt provided an adequately inert atmosphere is maintained in the furnace during sample immersion into the melt. Also, the addition of small amounts of Mg to the AA4045 melt was shown to further facilitate the wetting and interface formation process.

In parallel, lab-scale Fusion™ casting plant trials were conducted at the Novelis Global Research and Technology Centre in Kingston, Ontario. Simulations of these experiments were performed to determine the steady-state conditions during Fusion™ casting. Other observations and measurements made during the Fusion™ casting experiments included: oxide motion

measurements, AA3003 surface characterization, metallography of as-cast interfaces, and mechanical testing of as-cast interfaces.

It was found that during the lab-scale Fusion™ casting trials, AA4045-clad successfully wets and creates a metallurgical and mechanically sound interface with the AA3003-core shell . Wetting of the interface is facilitated by the oxide motion on the AA4045 sump and the AA3003 sump, providing clean contact between the AA4045 liquid sump and the AA3003 solid shell. Although oxides are present on the AA3003 shell surface, they do not appear to be an intrinsic barrier to wetting and bond formation. It is postulated that wetting and bond formation is a result of discrete penetration of AA4045 liquid at AA3003 oxide defect sites followed by dissolution of the underlying solid AA3003 by liquid AA4045 and subsequent bridging between discrete penetration sites. While remelting of the AA3003 surface was not necessary to obtain a sound Fusion™ cast interface spot exudation on the AA3003 chill cast surface during reheating and partial remelting of the shell did improve the wetting and bonding process as it provided macroscopic oxide defects along the chill cast surface due to local deformation and fracture of the oxide that facilitated penetration of the AA4045 liquid through the oxide and into the underlying AA3003 solid shell.

Based on the results of this study, it is recommended that further improvements in Fusion™ casting yield and interface quality can be made by 1) reducing mold heat extraction and cooling at the sides of the ingot, 2) using a wiper blade in the AA4045 melt close to the AA3003 interface to reduce AA4045 oxide incursion into the interface, 3) providing an inert gas shield at the AA3003/AA4045 melt interface and 4) adding small amounts of Mg to the AA4045 melt.

Acknowledgements

First and foremost, I would like to thank my two supervisors, Dr. Mary Wells and Dr. Dave Weckman. I have learned a great deal from both of them, and it has not gone un-appreciated. This thesis would not be complete if not for their support and work over the last four and a half years.

I had the pleasure of working with the following colleagues over the years and would like to thank them for their efforts and input on this thesis project: Dr. Etienne Caron, Dr. Amir Baserinia, Rosa Ortega Pelayo, and Harry Ng.

Additionally, I want to thank Novelis Inc. and NSERC for financial support, as well as the following people: Dr. Simon Barker, Dr. Don Doutre, Dr. Graeme Marshall, Dr. Mark Gallernault, Paul Nolan, Rick Lees, Gary Hay, and Amanda Owens.

The technical staff at the University of Waterloo, for being a great resource throughout the duration of this thesis project: Andy Barber, Jim Baleshta, the mechanical engineering machine shop staff, Neil Griffet, Mark Griffet, Yuquan Ding and Nina Heinig.

An additional thank you to my committee members for their time in reviewing this work: Michael Worswick, Adrian Gerlich, Mario Ioannidis, and Ravi Ravindran.

Finally, I would like to acknowledge the kind words of support I have received from family members and friends over the past four and half years.

Table of Contents

AUTHOR'S DECLARATION ii

Abstract iii

Acknowledgements vi

Table of Contents vii

List of Figures xi

List of Tables xxii

Chapter 1 Introduction 1

1.1 Aluminum cladding 1

1.2 DC continuous casting 2

1.3 The Fusion™ casting process 5

1.4 Bonding and the core/clad interface in Fusion™ cast ingots 8

Chapter 2 Background 13

2.1 Core/Clad interface formation: the Fusion™ casting patents 13

2.2 Fusion™ casting research in the literature 16

2.3 Joining of aluminum at high temperatures: the oxide problem 17

2.3.1 Formation of Al_2O_3 18

2.3.2 Kinetics of aluminum oxidation 20

2.3.3 Mechanisms of wetting and joining of aluminum at high temperature 28

2.4 Aluminum alloy solidification 35

2.4.1 AA3003: alloy description and solidification characteristics 36

2.4.2 AA4045: alloy description and characteristics 41

2.4.3 Fusion™ casting AA3003 and AA4045 44

2.5 Surface phenomena in DC casting 45
2.6 Summary, objective and scope 48
Chapter 3 Experimental Apparatus & Methods 49
3.1 Introduction 49
3.2 Laboratory scale Fusion™ caster 50
3.2.1 Fusion™ casting trials 54
3.2.2 Analysis of Fusion™ cast ingots 64
3.3 Interface formation laboratory analog test: apparatus 72
3.3.1 Interface formation testing 75
3.3.2 Analysis of interface formation test samples 88
Chapter 4 Observations from Fusion™ Casting Trials of AA3003 and AA4045 Ingots 95
4.1 Introduction 95
4.2 Thermofluid model predictions of Fusion™ casting trials 96
4.2.1 Temperature, fraction solid (f_s), and velocity contours 97
4.2.2 Extracted model results 103
4.3 Visualization of oxide film motion 116
4.3.1 Discussion 123
4.4 Observations of the AA3003 chill cast surface 128
4.4.1 Discussion 144
4.5 Observations of the as-cast interface 147
4.6 Mechanical testing of Fusion™ cast interfaces 158
4.7 Discussion 166
4.7.1 Metallurgical defects at the AA3003/AA4045 as-cast Fusion™ interface 168

4.8 Summary 171
Chapter 5 Analog Interface Formation Test Results: the Influence of Temperature, Sample Oxidation, and Atmospheric Condition 174
5.1 Introduction 174
5.2 Remelting tests 175
5.3 Oxidation tests 184
5.4 Macroscpoic Observations from Immersion Tests 191
5.5 Discussion: AA3003 Remelting and Other Implications for Fusion™ Casting Practices 193
5.6 Relative oxide thickness and oxide morphology with SEM 197
5.6.1 Discussion 205
5.6.2 Comparison of AA3003 surface oxides 207
5.7 Summary 209
Chapter 6 Effect of Mg Impurity on Wetting and Interface Formation 211
6.1 Introduction 211
6.2 Effects of Mg in the Al-1Mn core sample on wetting and interface formation 212
6.3 Effects of Mg in the Al-10Si clad alloy melt on wetting and interface formation 221
6.4 Microscopy of sample surface and final contact line regions 224
6.4.1 Fast immersion test 234
6.5 Surface oxide uniformity, morphology, and defect observations 240
6.5.1 Oxide Uniformity 240
6.5.2 Oxide Morphology 245
6.5.3 Oxide Defects 247
6.6 Discussion 251

6.6.1 Meniscus effect on sample and melt contact condition 251
6.6.2 A final interface formation mechanism 255
6.6.3 Al-1Mn oxide film penetration 258
6.7 Summary 265
6.8 Practical Applications 268
Chapter 7 Conclusions and Recommendations 271
7.1 Conclusions 271
7.2 Recommendations for future work 271
References 276
Appendix A Tests performed prior to use of interface formation test apparatus 286
Appendix B Sample oxidation calculations 289
Appendix C FIB section low resolution images 293
Appendix D Reduction of Al_2O_3 by Mg 296

List of Figures

Figure 1-1 – Vertical DC casting. (a) General arrangement of process, and (b) mould assembly. Images taken from reference [12]. 4

Figure 1-2 – Schematic of a Fusion™ casting machine (a) clad alloy cast prior to core alloy, (b) core alloy cast prior to clad alloy. Item 12- Conventional DC casting mould; Item 13- Direct water spray; Item 14 and 14a- Mould dividing plate (or chill bar); Item 15- Core alloy feeding nozzle; Item 16- Clad alloy feeding nozzle; Item 17- DC casting dummy block/starting block; Item 18- Core alloy liquid sump; Item 20 and 23- Solid aluminum material; Item 21- Clad alloy liquid sump. Images taken from reference [9]. 6

Figure 1-3 – (a) Schematic of the Fusion™ casting process with region of interest with respect to interface formation encircled in red. Image taken from reference [9]. (b) Schematic of the initial region of contact between the core and clad alloys in Fusion™ casting. 9

Figure 2-1 – Equilibrium phase diagram for the Al-O binary system. Image taken from Wriedt [25]. 19

Figure 2-2 – Parabolic aluminum oxidation rate data reported in the literature. 26

Figure 2-3 – Qualitative spreading types described by Wall and Milner [53]. (a) Sub-oxide spreading and dissolution of the substrate, in systems where the solubility of braze alloy in the substrate alloy is high. (b) Sub-oxide spreading via a discrete penetration point, in systems where the solubility of the braze alloy in the substrate alloy is low. 31

Figure 2-4 – Al-Mn phase diagram. Image taken from McAlister and Murray [70]. 37

Figure 2-5 – A typical/representative solidification microstructure of as-cast AA3003. Sample cooling rate 0.5 °C/s. Image taken from Bäckerud *et al*. [71]. 39

Figure 2-6 – FactSage [72] predictions of AA3003 mass fraction solid (f_s) as a function of temperature for equilibrium and Scheil cooling conditions [73]. 40

Figure 2-7 - Aluminum-silicon binary phase diagram. Original image was taken from McAlister and Murray [75]. 42

Figure 2-8 Factsage [72] predictions of AA4045 fraction solid (f_s) as a function of temperature for equilibrium and Scheil cooling conditions [73]. 43

Figure 2-9 – AA4045 as-cast microstructure. 44

Figure 2-10 – Calculated Scheil solidification curves for AA3003 and AA4045 [73], superimposed to highlight the overlap in solidification range. 45

Figure 2-11 – High tilt angle micrograph of Al -1 wt% Mg alloy which has been heated to 640˚C. A raft of the original surface has been lifted up by exudation of new material. Image taken from McGurran and Nicholas [82]. 47

Figure 3-1 – (a) Schematic of the lab scale Fusion™ caster. Image courtesy of E. Caron [22]. (b) Cross section of the lab scale Fusion™ caster. Image courtesy of H. Ng [83]. 51

Figure 3-2 – Fusion™ caster as setup in Novelis' Global Technology Centre in Kingston Ontario. Image courtesy of S. Barker [84]. 53

Figure 3-3 – Cross-sectional schematic showing position of starting block in the casting mould prior to start of a casting trial. 55

Figure 3-4 – Cross-sectional schematic showing steady state casting of Fusion™ ingot along with the parameters that are controlled during casting. Image from [85]. 57

Figure 3-5 – Pouring temperature in core and clad molten metal inlets measured during casting trial 2-1. 59

Figure 3-6 – (a) Side view of casting mold and showing camera orientation, working distance ~1.4m from ingot sump, and (b) top view of casting mould showing field of view (1 and 2) captured during casting trials. 62

Figure 3-7 – Illustration of the procedure used at the end of casting to preserve AA3003 material cast against chill bar for casting trial 2-1 in Table 3-2. 63

Figure 3-8 – Schematic (side view) of final dimensions from the top portion of the 'interrupted' Fusion™ cast ingot, for casting trial 2-1 in Table 3-2. 64

Figure 3-9 – Schematic (section of ingot looking down from the top) indicating the mechanical test sample positions from (a) as-cast interface samples, loading axis parallel to interface. (b) Base metal samples, loading axis perpendicular to the interface. 67

Figure 3-10 – (a) Solid model and (b) mesh for the thermofluid model of the laboratory scale Fusion™ caster [22] installed at Novelis' Global Technology Centre in Kingston Ontario. Image taken from Caron *et al*. [22]. 70

Figure 3-11 – Schematic of the analog test apparatus. 73

Figure 3-12 – Macro photo of a prepared AA3003 sample prior to immersion testing. 77

Figure 3-13 – Test procedure used for tests conducted on large OD sample, see Table 3-8. 79

Figure 3-14 – Typical sample heating curve for 38.5 mm OD diameter sample. 80

Figure 3-15 – Typical sample heating curve for 9.5 mm OD diameter sample compared with larger, 38.5 mm OD, sample. 85

Figure 4-1 – Contact conditions between core and clad alloys in Fusion™ casting, with questions marks indicating areas of interest. 96

Figure 4-2 – Contour plots of results from simulation # 2 (see Table 3-5), from the *x*-*z* plane of the solid model domain (see Figure 3-10), taken at the centerline of the ingot, y = 0 mm. (a) Temperature, and (b) Fraction solid (f_s). 98

Figure 4-3 – Contour plots of results from simulation # 2 (see Table 3-5), from the *z*-*y* plane of the solid model (see Figure 3-10), taken at the interface (x = 0 mm) between the AA3003 and AA4045 domains. (a) Temperature, and (b) AA3003 f_s. 100

Figure 4-4 – Velocity contour plots of results from simulation # 2 (see Table 3-5). Normalized vector vectors included in both plots to indicate direction of flow tangential to the indicated plane. (a) Section of the *z*-*x* plane of the solid model, taken at the clad metal inlet, y = 102 mm (see Figure 3-10). (b) Top surface of the core and c lad domains. 102

Figure 4-5 – Schematic of the Fusion™ model interface with axes and key dimensions labelled. (a) *x*-*z* plane, longitudinal section. Casting time is defined as the distance z along the model, starting from z = 0 mm, divided by the casting velocity, v. (b) *x*-*y* plane, transverse section of the Fusion™ model. 104

Figure 4-6 – Model calculated core alloy (a) surface temperature, as well as core/clad interfacial temperature, for model run number 3, and (b) corresponding f_s for the AA3003 core alloy at the AA3003/AA4045 interface. 106

Figure 4-7 – Model calculated (a) peak temperature of the interface for all four model runs, and (b) corresponding minimum fs of AA3003 at AA3003/AA4045 interface during Fusion™ casting. 108

Figure 4-8 – Model calculated (a) rise in core alloy temperature as a result of contact with the molten clad metal, for all four model runs, and (b) corresponding rise in core alloy fs at the interface 110

Figure 4-9 – Model calculated clad liquid contact time with core alloy shell before final solidification of the interface. 114

Figure 4-10 – Schematic of top view of casting mould showing fields of view (FOV_1 and FOV_2) captured during casting trials. 117

Figure 4-11 – Video images of clad sump surface oxide (FOV_1) for casting trial 2-1. (a) t = 0s, (b) t = 15s, and (c) t = 30s. 118

Figure 4-12 – Measured velocity of clad sump oxide for three different segments, (a)-(c), recorded during casting trial 2-1. 119

Figure 4-13 – Video images of core sump surface oxide (FOV_2) for casting trial 2-2. (a) t = 0s, (b) t = 15s, (c) t = 30s..... 121

Figure 4-14 – Measured velocity of core sump oxide for three different segments, (a)-(b) recorded during casting trial 2-2, (c) recorded during casting trial 2-3. 122

Figure 4-15 – Observed direction of oxide motion on core and clad alloy sump surfaces..... 123

Figure 4-16 – (a) Side view of Fusion™ casting process, showing core and clad shell formation on the mould and chill bar and potential anchoring point for oxide films. (b) Top view of Fusion™ casting process showing shell formation around the periphery of the mould and along the chill bar. 125

Figure 4-17 – Model calculated core alloy surface temperatures, and corresponding surface oxide growth. Casting speed of 1.12 mm/s..... 128

Figure 4-18 – Macro view of surface of AA3003 shell which was cast against the chill bar and preserved in casting trial 2-1. (a) and (b) are sections taken along the width of the ingot between y = -102 mm and y = +102 mm. (c) A section taken from the edge of the ingot..... 129

Figure 4-19 – Longitudinal sections of AA3003, (a) cast against chill bar (right side of figure was in contact with chill) and (b) centre AA3003 of the core section..... 131

Figure 4-20 – DSC results for Fusion™ cast AA3003 material. Bulk AA3003 material (dotted line) and AA3003 cast against the chill bar, taken from casting 1 (black solid line). (a) Samples heated at 0.83 K/s. (b) Samples heated to 878 K in less than 10 minutes than heated through phase transition at a rate of 0.017 K/s..... 132

Figure 4-21 – Longitudinal samples of AA3003 chill surface structure near a surface protrusion site. 135

Figure 4-22 – Backscattered electron image of surface morphology of AA3003 solidified against the chill bar. Encircled area shows intermetallic particles partially transformed from $Al_6(Fe,Mn)$ to $Al_{15}(Fe,Mn)_3Si_2$..... 137

Figure 4-23 – Surface protrusion (a) low magnification secondary electron image and (b) high magnification backscattered electron image of the boxed region indicated in (a) with a black box. 138

Figure 4-24 – (a) Secondary electron image of AA3003 surface structure. (b) Corresponding backscattered electron image of AA3003 surface structure. 139

Figure 4-25 – Secondary electron imaging of FIB cross section from chill bar cast surface. (a) low magnification image of the section, (b) high magnification image of the area above the primary aluminum, and (c) high magnification image of the area above the intermetallic particle. 141

Figure 4-26 – Schematic of the "interrupted" Fusion™ cast ingot, with region of interest indicated. This was just above the last point of contact between the AA4045 liquid and the AA3003 shell. 142

Figure 4-27 – 20 kV backscattered electron image from the surface of the area of interest depicted in Figure 4-26. Mg and O based crystals accumulated on top surface intermetallics. Mg was also present in EDS spectra from regions between intermetallic particles. 143

Figure 4-28 – Possible oxide penetration mechanism on AA3003. (a) Spot exudation of AA3003 shell, causing local break in oxide film and (b) site for AA4045 liquid penetration and subsequent dissolution of AA3003 shell..... 145

Figure 4-29 – Possible oxide penetration mechanism on AA3003. (a) AA3003 shell covered with an oxide film (b) Mg segregation to the AA3003 surface, (c) local thinning and breakdown of the AA3003 oxide film via chemical reduction by segregating Mg, and (d) penetration of AA4045 through break in surface oxide and dissolution of underlying AA3003 solid. 147

Figure 4-30 – Photo macrographs of longitudinal sections at the core/clad interface of ingot 1-1, from casting trials defined in Table 3-3. 149

Figure 4-31 – Schematic of the Fusion™ ingot cross section, highlighted areas (a), (b) and (c) correspond to the regions where the Photo-macrographs shown in Figure 4-32 are taken from. Core inlet location and clad inlet location are indicated for reference. 150

Figure 4-32 – Photo macrographs, transverse direction, ingot 1-1, from casting trials defined in Table 3-3. (a) Edge of ingot closest to the core liquid metal inlet. (b) Centre portion of ingot. (c) Edge of ingot closest to the clad liquid metal inlet. 151

Figure 4-33 – Large area optical micrographs of longitudinal sections from the top of an as cast Fusion™ ingot (ingot 1-1 from casting trials defined in Table 3-3)..... 152

Figure 4-34 – Optical micrographs of an as cast Fusion™ ingot (ingot 1-3 from casting trials defined in Table 3-3) showing semi-spherical dissolution profiles of different depths into the AA3003 portion of the ingot. (a) Transverse section, and (b) longitudinal section. 154

Figure 4-35 – Optical micrographs of an as cast Fusion™ interface. (a) Longitudinal section of ingot 1-1 (from casting trials defined in Table 3-3). (b) Transverse section of ingot 1-2. 156

Figure 4-36 – Optical micrographs of an as cast Fusion™ ingot (ingot 1-3 from casting trials defined in Table 3-3). Mn-rich intermetallic particles are present within the AA4045 portion of

the Fusion™ ingot. (a) Transverse section with polyhedral type intermetallics encircled, and (b) transverse section with script type intermetallics encircled. 157

Figure 4-37 – Schematic (section of ingot looking down from the top) indicating the mechanical test sample positions from as-cast interface samples, Note the loading axis is parallel to the interface 158

Figure 4-38 – Mechanical test results from as cast Fusion™ interfaces. (a) Tensile strength of sample divided by the tensile strength of the AA3003 base metal, (b) engineering strain at failure of sample. 159

Figure 4-39 – Fracture surface of mechanical test which had an engineering strain at failure of 27%. (a) Low magnification secondary electron image, (b) high magnification secondary electron image. 162

Figure 4-40 – Fracture surface of mechanical test which had an engineering strain at failure of 6.1%. (a) low magnification secondary electron image of the AA3003 side of the failed sample, (b) high magnification secondary electron image of the encircled area in (a). 164

Figure 4-41 – Fracture surface of mechanical test which had an engineering strain at failure of 0.8%. (a) Low magnification secondary electron image of the AA3003 side of the failed sample, (b) high magnification secondary electron image of the AA3003 side of the failed sample, and (c) low magnification secondary electron image of the AA4045 side of the failed sample. 165

Figure 4-42 – Schematic showing the effect of metal level increase, on the clad side, during Fusion™ casting. (a) Clad meniscus before metal level increase, Δz, and (b) clad meniscus after metal level increase and possible entrainment of clad oxide at the AA3003/AA4045 interface. 170

Figure 5-1 – Typical DSC result for the AA3003 material used for immersion test. Sample was heated to 828 K in less than 10 minutes than heated through phase transition at a rate of 0.017 K/s. 177

Figure 5-2 – Photo of a prepared AA3003 sample prior to immersion testing. 178

Figure 5-3 – Macro photos of AA3003 samples showing the effect of AA3003 remelting on the ability of AA4045 to wet the AA3003. Immersion of samples performed under air atmosphere. 178

Figure 5-4 – Optical metallography of AA3003 samples after tests immersion under an air atmosphere, (a) T_{peak} = 923 K; $t_{oxide,AA3003}$ = 59 nm, (b) T_{peak} = 926 K; $t_{oxide,AA3003}$ = 60 nm. 181

Figure 5-5 – Optical metallography of AA3003 sample after tests immersion under an air atmosphere; T_{peak} = 926 K, $t_{oxide.AA3003}$ = 60 nm. (a) isolated penetration of AA3003 by AA4045 near top region of AA3003 sample, (b) onset of AA4045 wetting of AA3003 sample slightly

below isolated region depicted in a, (c) near middle of sample, showing a less distinctive interface, (d) bottom of sample showing more mixing of AA3003 and AA4045 material. 184

Figure 5-6 – Calculated AA3003 sample oxidation and AA4045 melt surface oxidation for tests series conducted in this section, shown as black X's. Calculated oxide values for the remelt tests series (previous section) shown as open circles. 185

Figure 5-7 – Macro photos of AA3003 samples showing the effect of oxide thickness on the ability of the AA4045 to wet the AA3003. Immersion of samples performed under argon atmosphere. 186

Figure 5-8 – Optical metallography of AA3003 samples after tests immersion under an argon atmosphere, (a) T_{peak} = 909 K; $t_{oxide,AA3003}$ = 14 nm, (b) T_{peak} = 909 K; $t_{oxide,AA3003}$ = 54 nm. 188

Figure 5-9 – Optical metallography of AA3003 samples after tests immersion under an argon atmosphere, T_{peak} = 909 K. (a) upper edge of final contact line between AA3003 and AA4045 in sample with $t_{oxide,AA3003}$ = 14 nm, showing dissolution of AA3003 sample thin layer of AA4045 adhering to surface of AA3003 sample (etched sample), (b) final contact line region in sample with $t_{oxide,AA3003}$ = 54 nm (etched sample), and (c) bottom edge of AA3003 sample with $t_{oxide,AA3003}$ = 13 nm, showing dissolution of AA3003 sample and Mn bearing intermetallics within thin adhering AA4045 layer (etched). 190

Figure 5-10 – Effect of AA4045 melt oxidation on appearance of AA3003 exterior after immersion into an AA4045 melt. (a) Bottom surface of a typical AA3003 sample. Appearance of AA3003 exterior after immersion into (b) a heavily oxidized AA4045 melt, notice dry patch along the side (near bottom) of AA3003 sample, and (c) a lightly oxidized AA4045 melt. 192

Figure 5-11 – Effect of AA4045 melt oxidation. (a) Top view of a lightly oxidized AA4045 melt after melt re-solidification, (d) Top view of a heavily oxidized AA4045 melt after melt re-solidification 192

Figure 5-12 – Sequence of events during immersion tests in argon (shown in axisymmetric view). (a) Initial sample state showing oxidized AA3003 surface and initial AA4045 oxide film on melt. (b) Sample immersion into melt and breaking of initial AA4045 oxide film. (c) Sample immersion while exposed to inert atmosphere with only partial re-oxidation of AA4045 liquid at the meniscus. (d) Contact of AA3003 with 'clean' liquid below the contact line. 196

Figure 5-13 – Sequence of events during immersion tests in air (shown in axisymmetric view). (a) Initial sample state showing oxidized AA3003 surface and initial AA4045 oxide film on melt. (b) Sample immersion into melt and breaking of initial AA4045 oxide film. (c) Sample immersion while exposed to air with complete re-oxidation of AA4045 liquid at the meniscus. (d) Double oxide contact at the AA3003/AA4045 interface and negligible interaction between sample and melt below the contact line. 196

Figure 5-14 – Surface morphology of as-etched AA3003 sample, prior to any exposure to high temperature. (a) Backscattered SEM (4 kV) image low magnification, (b) backscattered SEM (4 kV) image high magnification. 198

Figure 5-15 – 4kV EDS spectrum of an AA3003 sample, using a 1800 μm by 1800 μm field size, prior to any exposure to high temperature. 199

Figure 5-16 – 20kV EDS spectrum of sample *air5* (see Table 3-13) oxidized at high temperature for 63.5 minutes in air, using a 1800 μm by 1800 μm field size. Note: top of Al peak is cropped in the graph. 199

Figure 5-17 – Backscattered SEM (4 kV) image showing surface morphology of AA3003 sample heated and exposed to air during the first 9 minutes of heating ($t_{oxide,\ AA3003}$ = 13 nm). Dark area identified as Mg rich region and light area identified as Mg lean area. Encirled region highlighting white and dark spot. Dark spots indentified as Mg rich and light spots likely to be dispersoids formed during sample heating, see EDS of selected areas in Figure 5-18. 200

Figure 5-18 – (a) EDS spectrum obtained from area a in Figure 5-17. (b) EDS spectrum obtained from area b in Figure 5-17. (c) EDS spectrum of a white spot from encircled area in Figure 5-17. 201

Figure 5-19 – Backscattered SEM (4 kV) image and EDS map showing surface distributions of O, Mg, Al, Mn, and Fe. White indicates high signal of species within area, black indicates less presence. Calculated oxide thickness 13 nm. 202

Figure 5-20 – Backscattered SEM (4 kV) image and EDS map showing surface distributions of O, Mg, Al, Mn, and Fe. Calculated oxide thickness 46 nm. 203

Figure 5-21 – Backscattered SEM (4 kV) image and EDS map showing surface distributions of O, Mg, Al, Si, and Fe. Calculated oxide thickness 95 nm. 203

Figure 5-22 – Normalized EDS peak intensities for oxidized AA3003 samples, as a function of calculated oxide thickness. Results are graphed against the calculated oxide thickness. All EDS spectrums obtained using 1800 μm by 1800 μm field size. 204

Figure 5-23 – Calculated oxide thickness vs. O/Al EDS peak ratios obtained from oxidized AA3003 samples. EDS spectrums obtained using 1800 μm by 1800 μm field size (black data points), data for samples heated in air and samples heated in inert environment, < 5 ppm O_2. EDS spectrums obtained on Mg rich (red data points) and Mg lean (gray data points) surface regions, using a 2 μm by μm field size. 205

Figure 6-1 – Macro photos of Al-1Mn-0.0008Mg samples for various immersion temperatures (rows) and surface oxides (columns). Melt: Al-10Si-0.0008Mg for all tests. 213

Figure 6-2 – Sample weight loss data for Al-1Mn-0.0008Mg immersed into Al-10Si-0.0008Mg for various immersion temperatures (colours) and sample oxide thicknesses (groupings). 216

Figure 6-3 – Macro photos of various Al alloys (rows) and surface oxides (columns). Melt: Al-10Si-0.0008Mg for all tests..... 218

Figure 6-4 – Macro photos of AA3003 (bottom row) compared to the baseline alloy Al-1Mn-0.0008Mg (top row), for various surface oxides (columns). Melt: Al-10Si-0.0008Mg. 220

Figure 6-5 – Sample weight loss data for various Al alloys immersed into Al-10Si-0.0008Mg, for different sample oxide thicknesses. Alloys indicated by the different colours..... 221

Figure 6-6 – Macro photos of for various Al alloy melts (rows) and surface oxides (columns). Samples: Al-1Mn-0.0008Mg for all tests. 222

Figure 6-7 – Sample weight loss data for various Al-1Mn-0.0008Mg samples immersed into various Al-10Si alloy melts, for different sample oxide thicknesses. Melt alloys indicated by the different colours. 223

Figure 6-8 – Resulting sample surface after test immersion. Al-1Mn-0.0008Mg sample immersed in Al-10Si-0.0008Mg melt at 913 K (640 °C). Calculated oxide thickness on sample prior to immersion in the melt was 28 nm. 225

Figure 6-9 – SEM image from the sample surface of test sample shown in Figure 6-8. Image from region (i) identified in Figure 6-8..... 226

Figure 6-10 – SEM images from various regions taken from the sample surface of test sample shown in Figure 6-8. (a) region ii, (b) region iii, (c) region iv, and (d) region v..... 228

Figure 6-11 – Higher resolution SEM image of the boxed-region highlighted in Figure 6-10b. 229

Figure 6-12 – Resulting sample surface after test immersion, highlighting the region at the final contact line, dark greyish in colour and discoloured from the un-immersed portion of the test sample. Al-1Mn-0.0008Mg sample immersed in Al-10Si-0.0008Mg melt at 893 K (620 °C). Calculated oxide thickness on sample prior to immersion in the melt was 11 nm. 230

Figure 6-13 – SEM images of the sample surface taken from the boxed region of the sample shown in Figure 6-12. (a) Low resolution secondary electron image, (b) corresponding backscattered electron image, (c) secondary electron image of highlighted region in (b), and (d) corresponding backscattered electron image. 231

Figure 6-14 – Secondary electron image of the sample shown in Figure 6-12. The black line shown in the image indicates the position at which EDS profiles were performed. 232

Figure 6-15 – Al, Si, and O profiles along line shown in Figure 6-14. 234

Figure 6-16 – Resulting sample surface from immersion tests performed at 9 mm/s (left) and 1.4 mm/s (right). 235

Figure 6-17 – Secondary electron image of the region below the final contact line, for the test performed at 9 mm/s. 237

Figure 6-18 – Higher magnification of the boxed area in Figure 6-17, after FIB sectioning. 237

Figure 6-19 – High magnification secondary electron image of the (a) right side of the field showed in Figure 6-18, corresponding to the region with a smooth surface morphology, and (b) left side of the field showed in Figure 6-18, corresponding to the region where the surface morphology looks similar to that of the um-immersed surface. 239

Figure 6-20 – Secondary electron image of FIB sectioned oxidized Al-1Mn samples. (a) Al-0.0008Mg sample oxidized at 913 K (640 °C) to a calculated oxide thickness of 250-275 nm and (b) higher magnification view of (a). 241

Figure 6-21 – Measured average and minimum observed oxide film thicknesses for samples examined with FIB sectioning and SEM imaging. Estimated oxide film thickness highlighted in red for comparison. 242

Figure 6-22 – Secondary electron image of FIB sectioned oxidized aluminum sample. AA3003 sample oxidized at 913 K (640 °C) to a calculated oxide thickness of 250-275 nm. (a) Oxide above an intermetallic particle at the surface of the sample. (b) Oxide above a primary α-Al region. 244

Figure 6-23 – Surface morphology of samples oxidized to an estimated oxide film thickness of 250-275 nm. (a) Alloy Id # 1, Al-1.2Mn-0.7Fe-0.2Si-0.005Mg, (b) alloy Id # 1b, Al-1Mn-0.01Mg, (c) alloy Id # 1c, Al-1Mn-0.1Mg. 246

Figure 6-24 – Higher magnification SEM image of surface morphology shown in Figure 6-23c. 247

Figure 6-25 – Examples of oxide film defects observed in FIB sectioned samples. (a) Al-1Mn-0.0008Mg sample, and (b) Al-1Mn-0.1Mg sample. 248

Figure 6-26 – Optical micrograph showing copper rich deposits on Al-0.0008Mg surface. Sample was prepared as per Section 3.3.4, allowed to oxidize at room temperature, then cathodically polarized using 0.5 V for a duration of 3 min. 249

Figure 6-27 – Oxide film defect density for oxide films grown on Al-0.0008Mg samples. Three different oxidation conditions. Defects measured by counting copper deposit sites from optical metallographs. 251

Figure 6-28 – Detailed schematic of the interface formation test, conducted in argon. (a) Sample and melt surface just prior to immersion into the melt. (b) Initial break of the Al-10Si_{liquid} oxide film, exposing clean liquid Al-10Si_{liquid} at the meniscus. (b) Re-oxidation of the meniscus. (c) Break-off of oxidized meniscus, exposing clean Al-10Si_{liquid} at the meniscus again (d) Oxidized

portion of the meniscus which has previously broken off gets entrapped at the AA3003/AA4045 interface. (e) Re-oxidation of the clean meniscus. 253

Figure 6-29 – Oxygen exposure, in Langmuir (L), for the two oxygen partial pressures used during testing. p_{O2} = 158 Torr corresponds to tests conducted in air, and p_{O2} = 1.52 x 10^{-3} Torr corresponds to tests conducted in argon. The time required to reach 3000 L, the exposure quoted by Stucki *et al.* [33] to form a closed surface oxide, is indicated in the figure. 255

Figure 6-30 – Schematic of proposed interface formation process. (a) Penetration of oxide in discrete locations, and dissolution of underlying Al. (b) Bridging of oxide film (over spacing d_2). Oxide film breakup, and continued dissolution and undercutting of region above double oxide layer. (c) Bridging below double oxide film (over spacing d_1). (d) Break away of oxide film, and continued dissolution of Al, final interface is metallurgically sound. 256

Figure 6-31 – Proposed model, by Vermilyea [59], of defect reformation on growing oxide films. Arrows indicate ionic diffusion pathways and subsequent oxide growth over top of the defect. 260

Figure 6-32 – Final proposed oxide penetration mechanism. (a) locally thin oxide, t_{oxide}, over top of a flaw, and in intimate contact with a melt layer of thickness t_{melt}. (b) Dissolution of the Al_2O_3 oxide in the Al-10Si melt (reaction written above figure). (c) Dissolution of the Al_2O_3 oxide in addition to reduction of the oxide by dissolved Mg in the Al-10Si melt (reactions written above figure). (d) Continued dissolution of the Al_2O_3 oxide results in exposure of the underlying Al-1Mn metal to the Al-10Si melt. 262

Figure 6-33 – Calculated thickness of Al_2O_3 (t_{oxide}) which can be dissolved by an unsaturated Al-10Si melt above it (t_{melt}) at 933 K (660°C). Oxygen solubility values in liquid Al from Taylor *et al.* [29] (dashed line) and Otsuka and Kozuka [28] (dotted line). 264

Figure 6-34 – Schematic depicting the implementation of Argon gas injection in conjunction with an oxide restraint [18], to improve the bonding of core and clad alloys during Fusion™ casting. 269

List of Tables

Table 1-1 – A summary of the Fusion™ cast ingots successfully cast, as identified in the literature [9], [14-16]. 8

Table 2-1 – Nominal compositional specifications for AA3003, in wt% [69]. 36

Table 2-2 – List of reactions occurring during solidification of aluminum alloy AA3003 [71]. 38

Table 2-3 – Effect of cooling rate on reaction temperature during solidification of AA3003 [71]. 38

Table 2-4 – Nominal compositional specifications for AA4045, in wt% [69]. 41

Table 2-5 – Sequence of Phase Precipitation in Hypoeutectic Al-Si Alloys [76]. 42

Table 3-1 – Measured AA3003 core and AA4045 clad alloy compositions used for the Fusion™ casting trials. 58

Table 3-2 – Process conditions used during the Fusion™ casting trials of 3003/AA4045 ingots. 58

Table 3-3 – Process conditions used during the Fusion™ casting trials of 3003/AA4045 ingots, in Reference [85]..... 60

Table 3-4 – AA3003 DSC sample and test information. *n* indicates the number of tests performed 65

Table 3-5 – List of conditions used for thermofluid simulations using the CFD model of Fusion™ casting described in [21-22]. 72

Table 3-6 – Measured AA3003 sample and AA4045 melt alloy compositions used for interface formation testing (wt% unless specified)..... 76

Table 3-7 – Interface formation tests performed with large OD samples, varying the amount of oxidation on the AA3003 sample surface prior to immersion in the melt. *n* indicates the number of test repeats. 81

Table 3-8 – Interface formation tests performed with large OD samples, varying the melt temperature. *n* indicates the number of test repeats. 82

Table 3-9 – Measured alloy compositions used for interface formation tests (wt% unless specified). 83

Table 3-10 – Outline of analog tests performed with small OD samples. *n* indicates the number of test repeats. 86

Table 3-11 – Outline of analog tests performed with small OD samples. *n* indicates the number of test repeats. 87

Table 3-12 – Outline of analog tests performed with small OD samples. *n* indicates the number of test repeats. 87

Table 3-13 – List of samples prepared for SEM/EDS oxide characterization. 91

Table 3-14 – FIB-SEM samples prepared for oxide uniformity studies. 92

Table 3-15 – Samples examined using copper decoration technique. 94

Table 4-1 – Calculated time of contact between AA3003 solid and AA4045 liquid during Fusion™ casting and average interface temperature during contact, for three positions along the width of the ingot. 115

Table 4-2 – AA3003 onset of remelting measurements from Fusion™ AA3003 samples measured with DSC. *n* indicates the number of times each test was repeated, and σ represents the calculated standard deviation in the measured results. 133

Table 4-3 – EDS and FIB-SEM results from surface of ingot cast against the chill bar, taken from the interrupted Fusion™ casting trial. *n* indicates the number of times each measurement was repeated, and σ represents the standard deviation in the measured results. 139

Table 4-4 – Comparison of various calculated values from the thermofluid model in [22] (for casting trial # 2-1, see Table 3-2) with failure strains (average values) of the Fusion™ cast interface from the same location. 167

Table 5-1 – Onset of remelting measurements from AA3003 samples measured with DSC. *n* indicates the number of times each test was repeated, and σ represents the calculated standard deviation in the results. 176

Table 5-2 – Comparison of AA3003 surface oxides: Fusion™ cast surfaces and test sample surfaces. 208

Chapter 1

Introduction

1.1 Aluminum cladding

The invention of a laminated aluminum sheet metal has its roots in the US Air Force. The idea to develop a laminate aluminum sheet occurred in the 1920's, as use of high strength aluminum (2xxx series) gained traction in the manufacture of wing skins, there were concerns regarding their susceptibility to inter-granular corrosion in sea-water environments. Research at the Aluminum Corporation of America [1-2] to alleviate this problem resulted in the invention of the famous Alclad sheet metal. Alclad sheet metal has a core (or interior) which consists of high strength aluminum, which is metallurgically bonded to an alloy with high corrosion resistance at the surface. In the early patent literature [2], the Alclad material was said to be made by casting the core aluminum alloy against solid clad material and then using a combination of heat treatment and rolling to further improve the bond between the two alloys. Modern production of Alclad is done predominately by roll bonding [3-5]. The process steps include: (i) casting separate rolling ingots for the core and clad alloys, (ii) scalping the faces of each ingot to create a smooth rolling surface, (iii) homogenizing each ingot, (iv) hot rolling each ingot, (v) cleaning and surface preparation of each ingot, (vi) co-rolling of the core and clad sheets to at least a 70% reduction to get a metallurgically sound bond between the two alloys. Successful roll bonding requires meticulous preparation of the mating surfaces prior to rolling, which further adds to process costs [6]. Since the 1920's, many other markets for aluminum clad products have emerged.

An equally important class of aluminum clad products are the brazing sheet metals [7]. A brazing sheet consists of a low melting point aluminum alloy clad onto a formable and moderate

strength aluminum core. These sheet metals are used in the fabrication of aluminum parts that require brazing processes, such as an automobile radiator. The low melting point alloy on the surface is an Al-Si near eutectic brazing alloy, whereas the core alloy is typically a 3xxx series alloy; however, various 5xxx, 6xxx, and 7xxx series alloys can also be successfully brazed together [8]. Again, roll bonding is the predominate route for fabricating brazing sheet stock.

Novelis Inc. recently developed and patented a unique variant of the Direct Chill (DC) casting process whereby two different alloys can be cast simultaneously, producing a laminate (or composite) aluminum ingot. This process, known as Fusion™ casting[1], offers some distinct advantages over current aluminum clad sheet processing routes [9]:

- The composite ingots produced via Fusion™ casting can be rolled down to thin-gauge aluminum 'clad' sheet without the meticulous cleaning procedures or high rolling reductions required in traditional roll-bonding production of clad sheet.
- The process can potentially be used to cast composite billets (ingots with round or square cross section), a product that cannot be made using standard roll bonding techniques.
- Since the core/clad metallurgical, oxide-free bond is formed during the ingot casting step, a scalping step is saved on one side of each ingot, thus reducing scrap volume and increasing overall process efficiency and yield.

1.2 DC continuous casting

Direct Chill casting (henceforth referred to as DC casting) is a casting process that is commonly used to produce rolling or extrusion ingots of various dimensions from refined aluminum alloys. DC casting can be regarded as a mature technology, as its original invention and implementation

[1] Fusion™ casting is a trademark of Novelis - Hindalco Industries Limited.

in industry can be traced back to the 1930's [10-11]. A schematic of vertically oriented DC casting is shown in Figure 1-1 [12]. In the DC casting process, liquid metal is poured into an open-ended and water-chilled mould at a steady rate. During process start up, a dummy block is positioned inside the bottom end of the mould to prevent molten metal from escaping. The water-cooled mould extracts heat from the molten aluminum and a solid shell forms around the periphery of the mould, its thickness and strength growing with the progression of time. At a predefined time after initial mould filling, the dummy block is withdrawn from the mould at a steady rate. As the solidifying ingot exits the bottom of the open ended mould, water is sprayed directly onto its exterior surfaces. This direct water spray cooling results in large surface heat fluxes, providing the majority of the cooling required to completely solidify and cool the emerging metal ingot; hence the namesake Direct Chill or DC casting. A lubricant is also added to the inside surfaces of the mould to reduce mould wear; improve the surface finish of the ingot, and to prevent the solidifying ingot from sticking to the mould [10].

Primary cooling is defined as the region where the metal is in close contact with the casting mould, whereas secondary cooling begins at the point where water sprays first impinge onto the ingot. It is understood in DC casting that the secondary cooling removes the majority of the heat from the solidifying and cooling ingot during casting. In DC casting of Mg billets, for example, the split between primary and secondary cooling has been reported as 4-11% to 96-89% [13].

In a vertical configuration, the length of the DC cast ingot is limited to the depth of the casting pit into which the ingot is lowered upon withdrawn from the mould. Vertical DC cast ingots can reach nine metres in length. Ingot cross sections can be square, rectangular, circular, and T-shaped, with sizes ranging from 0.0075 to 1 m^2 [10], depending on their final product use.

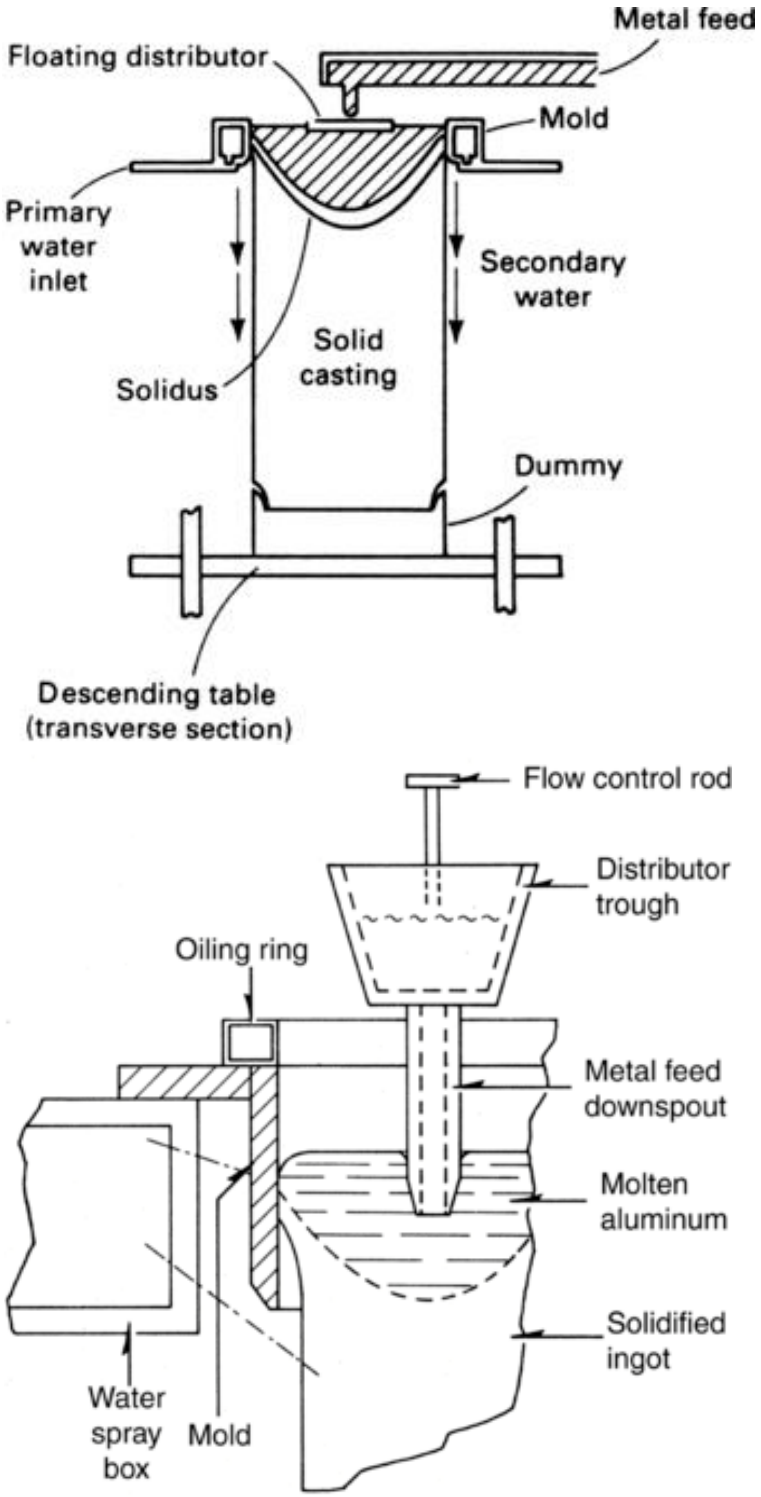

Figure 1-1 – Vertical DC casting. (a) General arrangement of process, and (b) mould assembly. Images taken from reference [12].

1.3 The Fusion™ casting process

The Fusion™ casting process is described in detail in the initial patent literature [9]. The basic principles of the process are described below. Starting with a generic DC casting mould (see numbered item 12 in Figure 1-2), a mould dividing plate is inserted into the mould (see items 14 and 14a). The mould dividing plate is typically a water-cooled metal chill bar (henceforth the dividing plate will be referred to as chill bar). The role of this device is to separate the liquid metal input (feed) streams, shown as items 15 and 16 in Figure 1-2. A design-specific starting block, item 17 (details not shown), effectively separates the two alloys at the start of the casting process. To start the casting, the higher melting point alloy (based on liquidus temperature) is poured into the side of the casting mould which is exposed to the metal chill bar, and begins to solidify around its periphery. It should be noted that the chill bar remains un-lubricated during casting. At a predefined time, the lower melting alloy is poured into the other side of the mould, and begins to solidify independently from the first alloy.

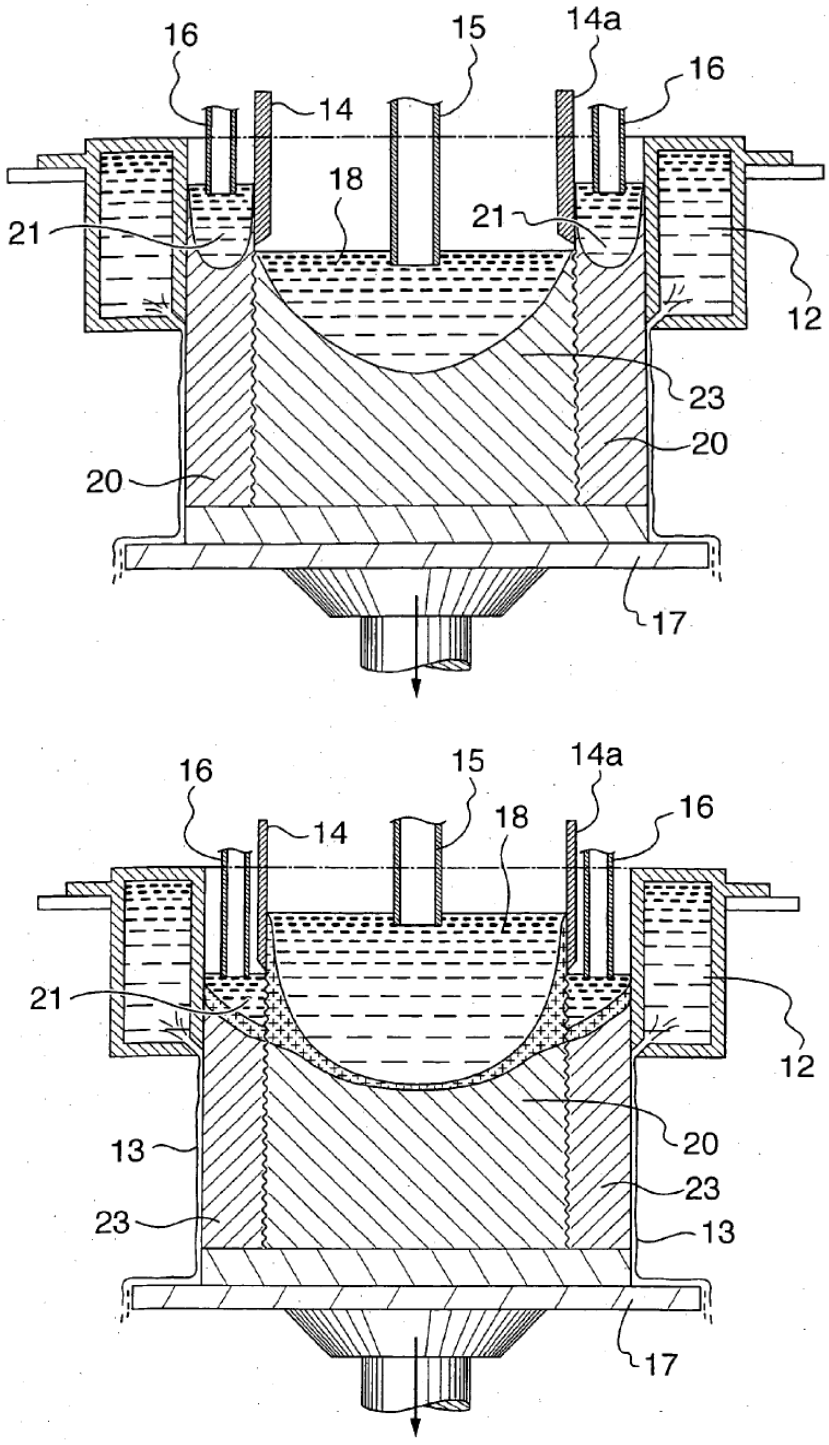

Figure 1-2 – Schematic of a Fusion™ casting machine (a) clad alloy cast prior to core alloy, (b) core alloy cast prior to clad alloy. Item 12- Conventional DC casting mould; Item 13- Direct water spray; Item 14 and 14a- Mould dividing plate (or chill bar); Item 15- Core alloy feeding nozzle; Item 16- Clad alloy feeding nozzle; Item 17- DC casting dummy block/starting block; Item 18- Core alloy liquid sump; Item 20 and 23- Solid aluminum material; Item 21- Clad alloy liquid sump. Images taken from reference [9].

In Fusion™ casting, the alloy with the higher liquidus temperature comes into direct contact with the metal chill bar, whereas the other alloy does not. As an example, in Figure 1-2a, the clad alloy has a higher liquidus temperature than the core alloy and hence the clad alloy contacts the chill bar while the core alloy does not. The converse is true for the system shown in Figure 1-2b. Once the dummy block is withdrawn from the mould, the two streams gradually come into contact with each other at a position just below the bottom of the chill bar. This is the point where initial bonding of the two alloys begins. With the proper selection of process conditions, a sound oxide-free metallurgical bond is formed between the two alloys. The final ingot is deemed a laminate, or composite, ingot.

Based on information provided in the patent [9], and in subsequent studies related to the process [14-16], it is evident that there are many core/clad combinations which can be successfully fabricated utilizing this process. Table 1-1 summarizes the various combinations which have been presented in the literature. Of particular interest for this project are the 3xxx-core/4xxx-clad ingots. Ingots of this type are used as starting stock for the rolling of clad-brazing sheet. Commercially, Novelis produces clad material for brazing applications using the Fusion™ casting process. In this combination, the 3xxx series alloys have moderate strength and formability, and make up the structural part of the clad-sheet. The 4xxx series alloys, being high in Si content, are low melting point alloys and are used as the clad brazing alloy. During furnace brazing, the 4xxx clad alloy will melt and subsequently form the brazed joints between the 3xxx core sheets.

Table 1-1 – A summary of the Fusion™ cast ingots successfully cast, as identified in the literature [9], [14-16].

Core	*Clad*	*Year*	*Ingot Size*	*Notes*
AA3003	AA4147	2005[9]	690 mm x 1590 mm x 3m ingot. Sandwich structure.	
X904	AA4147	2005[9]		X904 composition (wt%): 0.74 Mn, 0.55 Mg, 0.3 Cu, 0.17 Fe*, 0.07 Si, and Al the balance
AA3104	0303	2005[9]		0303 Liquid –Solid range: 660-659˚C
AA2124	AA1200	2005[9]		
AA6082	0505	2005[9]		0505 Liquid –Solid range: 660-659˚C:
AA6111	AA1050	2005[9]		
AA6111	AA3003	2010[14]	Sandwich structure, each clad layer was 10% of total ingot thickness.	
AA3003	X609	2010[14]	Single sided clad sheet.	X609 composition (wt%): 1.2 Si, 0.5 Cu, 0.4 Mg, 0.2 Mn, .02 Fe, and Al the balance
X900	AA4045	2007[15]	Not listed	X900 composition (wt%): 1.5 Mn, 0.6 Cu, 0.2 Mg, 0.2 Mn, and Al the balance
AA3003	AA4147	2007[15]	Not listed	
AA2124	AA1200	2006[16]	Not listed	
AA5754	AA4045	2006[16]		
Al-6Mg	AA1200	2006[16]		

*The element for this value of 0.17% was not indicated in the documentation, Fe was the assumed element.

1.4 Bonding and the core/clad interface in Fusion™ cast ingots

To produce a quality Fusion™ cast ingot, the interface between the two alloys must be free of metallurgical defects such as porosity or oxide films. Furthermore, mixing of the two alloys during solidification must be minimized since the goal is to achieve an ingot having two distinct regions (inner and outer region) that vary in alloy composition. The structure of the resulting metallurgical interface between the core/clad can also play an important role in the final properties of the clad alloy. For example, precipitate formation within the interlayer region of a

3xxx/4xxx brazing sheet (finished product not ingot) has been shown to improve the overall corrosion resistance of brazed products such as automotive heat exchangers [17].

A schematic of the region of interest, i.e., the core/clad interface, is shown in Figure 1-3. In Figure 1-3a, the Fusion™ casting apparatus is shown, in this configuration the core alloy is cast first and the clad alloy is cast second. The region circled in Figure 1-3a has been expanded in Figure 1-3b. This is the region of interest with respect to core/clad interface formation.

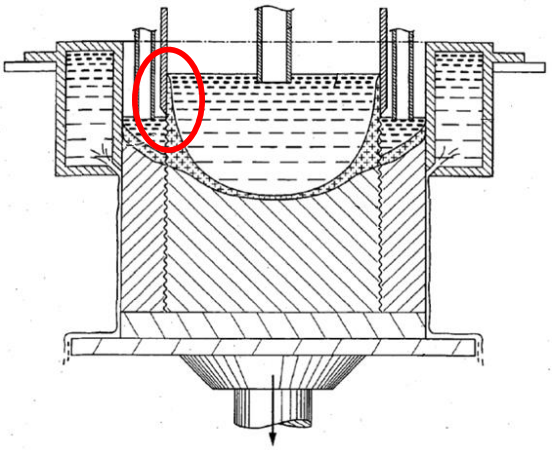

(a)

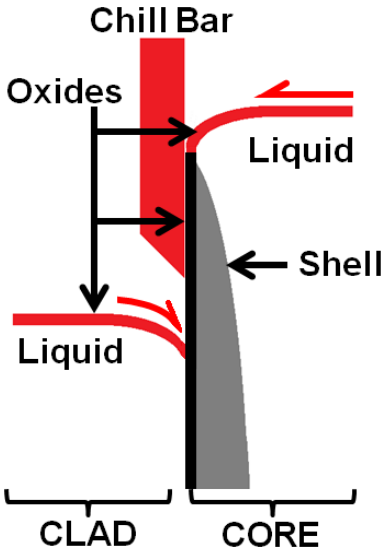

(b)

Figure 1-3 – (a) Schematic of the Fusion™ casting process with region of interest with respect to interface formation encircled in red. Image taken from reference [9]. (b) Schematic of the initial region of contact between the core and clad alloys in Fusion™ casting.

According to the original patent [9], the oxide film present on top of the core-liquid metal reservoir (or core sump) is *coherent* at this stage. Presumably, it is pulled along the top surface and down the outer edge of the solidifying shell of the core alloy. What happens to this oxide layer after it is exposed to the molten clad metal is unknown. The process is further complicated by the reheating and possible remelting of the core alloy as it comes into contact with the molten clad alloy. Similarly, there is an oxide film grown along the top exposed surface of the molten clad metal. It is not stated in the original patent whether this oxide film moves towards the exterior surface of the clad ingot or toward the core/clad bond interface during the Fusion™ casting process. The motion of the oxide film is expected to play an important role in the bonding process. After initial contact between the two alloys is made, there is a finite period of time which elapses before the two sides of the interface solidify.

To re-iterate, what is known about the Fusion™ casting process can be summarized below:

i. The core sump will have an oxide film that will be present on the solidifying shell below the chill bar.
ii. The clad sump will likewise have an oxide film present on its surface.
iii. Final Fusion™ cast sheets have high quality/oxide free interfaces, with a strong metallurgical bond between core and clad alloys [9], [14].

The major unknowns with regards to the mechanism of interface formation in Fusion™ casting are:

i. Where do the two oxide films go during Fusion™ casting.
ii. What phenomena/mechanisms are at play to remove the oxides from the core and clad at the first point of contact.

iii. What are the process parameters that affect this mechanism, as well as what range of parameters will facilitate the creation of the required oxide-free metallurgical bond at the core/clad interface during Fusion™ casting.

From a commercial standpoint, the use of Fusion™ casting has seen limited use in recent years. Of the numerous alloy combinations cast in the open literature (see Table 1-1), only 3xxx/4xxx Fusion™ ingots have managed to be produced for use in the marketplace, as feedstock to the manufacture of brazing sheet. Technical problems associated with the widespread use of Fusion™ casting for clad aluminum applications include:

i. Slower casting speeds.

ii. Higher labour requirements during Fusion™ casting.

iii. Lower yield due to product quality inconsistencies.

iv. Heat treatment and rolling of composite ingots.

Of the technical problems listed above, the problem of low yield is of relevance to this project. Specifically, oxide entrainment near the core/clad interface [18], as well as inconsistent clad thickness [19] in as-cast ingots were mentioned during conversations with senior technical staff at Novelis. Although these quality problems have been solved by developing empirical operating ranges for the Fusion™ casting of specific alloy combinations, it points to a general lack of knowledge and understanding about the interface formation process in Fusion™ casting. Thus, gaining knowledge about the interface formation process can lead to a general benefit as it could help explain why empirically derived operating envelopes function satisfactorily. Additionally, knowledge about the interface formation process can be used to help define operating envelopes for new Fusion™ casting alloy combinations.

From an academic standpoint, the topic of interface formation in Fusion™ casting of 3xxx/4xxx composite ingots has received little study. It should be noted again that the Fusion™ casting process takes place in a standard environment, i.e., in air, and the process is said to produce a high quality metallurgical bond. In aluminum brazing for instance, joining of aluminum alloys cannot typically be done in an air environment [8],[20]. Hence, understanding the interface formation process in Fusion™ casting could potentially lead to novel technological breakthroughs in other aluminum joining processes.

Therefore, the objective of this thesis was to study the interface formation process in Fusion™ casting, with special emphasis on determining the mechanistic processes at play. The thesis is intended to deliver a more thorough understanding of the interface formation process for Fusion™ casting of 3xxx/4xxx composite ingots, which has not been clearly defined in the patent [9]. The knowledge gained through this thesis study could potentially lead to process improvements in the Fusion™ casting of 3xxx/4xxx composite ingots.

The following chapter will review the Fusion™ casting literature as well as literature relevant to interface formation. Chapter 3 will outline the various experimental methods utilized in this thesis. The main results of the thesis will be presented and discussed throughout Chapters 4 through 6. A short summary of the results and conclusions from the thesis are presented in Chapter 7, along with suggestions for future work.

Chapter 2

Background

2.1 Core/Clad interface formation: the Fusion™ casting patents

The premise of bond formation in Fusion™ casting is deceptively straightforward. Divide a standard DC casting mould into two (or more) distinct sections using a chill bar, and simply pour different alloys into each section during casting. With proper control of the processing conditions; such as metal pouring temperature, metal level in the mould, casting speed, and water flow in the mould and chill bar, a high quality ingot can be fabricated. Ideally, the bond should be defect free, oxide free and with minimal inter-alloy mixing, so as not to degrade the alloy core and clad alloy compositions.

The requirements for obtaining quality bonds between the core and clad alloys during Fusion™ casting were initially identified in the original patent [9]. The key requirements are:

i. The first alloy should form a self-supporting surface before it comes into contact with the second alloy.

ii. The temperature of the first alloy, at some point during contact with the second alloy (the second alloy being either in a liquid or mushy state), should be at a temperature above its solidus temperature.

iii. The temperature of the second alloy should be above its liquidus temperature when it initially contacts the first alloy (but may also be in a mushy state).

iv. The liquid level of the second alloy should be kept 4 to 6 mm below the bottom edge of the chill bar.

Based on the information in the patent, this implies that the ‘first’ alloy has the higher liquidus temperature and should be cast first, while the ‘second’ alloy has the lower liquidus temperature and is cast second. The patent authors also state that a sound metallurgical bond between the core and clad requires that the core alloy should contact the clad alloy while it is in a semi-solid state, or that it should be reheated to a semi-solid state upon contact with the clad alloy. Furthermore, the clad alloy need not be completely liquid during initial contact with the core alloy. In short, the patent suggests that there is a finite period of time and space in which the two alloys are in intimate contact with each other with the condition that will result in a “perfect” metallurgical bond between the two alloys. However, the patent never specifically addresses how these requirements lead to a sound oxide-free metallurgical bond between the core and clad alloys, nor how these requirements manage to eliminate all evidence of preexisting oxides at the core/clad interface.

From our knowledge of the aluminum brazing process [8], one expects that the requirement for both alloys to be in a semi-solid state is not a hard requirement for metallurgical bonding to take place. Typical brazing of a clad sheet, e.g., AA3003 alloy clad with AA4045, to an unclad sheet, e.g., AA3003 alloy, is done at a temperature below the solidus temperature of AA3003. The low melting point alloy bonds with the unclad alloy; but special care must be taken to insure conditions are amenable to penetration or removal of the preexisting oxide film on the core surface in order to facilitate wetting and bond formation. A metallurgical bond is achieved between the two parts given adequate time at high temperature.

The role of surface oxides in the Fusion™ casting literature is given only minor mention in the original patent [9]. In it, the authors acknowledge that an oxide film may be present on the surface of the ‘first’ alloy; however, they go on to hypothesize that its presence may help contain

core metal from flowing/mixing with the clad metal during casting. In another section in the patent, they suggest that if the metal level of the 'second' alloy is kept a few millimetres above the bottom of the metal chill bar (i.e., dividing wall), that this may prevent oxides formed on the surface of the 'second' alloy from being entrained at the bond interface. Likewise, in a follow up patent to the original Fusion™ patent [18], it is suggested that surface oxides may be deleterious to obtaining a good interface during casting. As such, this patent describes a system where an 'oxide-skimmer' or 'wiper' is placed on the top surface of the liquid metal sumps, in close proximity to the chill bar. The role of this oxide-skimmer is to prevent entrainment of relatively thick oxides at the core/clad interface. The entrainment of thick oxides at the interface are said to cause problems with adhesion between the core and clay alloys, which can lead to the formation of blisters at the interface during subsequent heat treatment of the Fusion™ ingot as well as core/clad separation during rolling operations. It should also be noted that this patent only claims to reduce the amount of oxide being entrained at the interface; it does not claim to eliminate oxides totally from the system.

Examples of the metallurgical bonds obtained during Fusion™ casting have been described in the patent [9]. In a Fusion™ ingot composed of an Al-Mn core and an Al-Si clad, plumes/exudations of intermetallic composition of the Al-Mn alloy were found to extend up to a distance of 100 μm into the neighbouring Al-Si clad metal. Intermetallic particles with a size less than 20 μm were also found near the interface. In this specific case, the Al-Mn alloy was in a semi-solid state when it first contacted the Al-Si clad alloy. The patent authors suggest this was a requirement for good bond formation. The figure cited in the patent as evidence for this specific claim is however unclear, and does not justify the claim in the opinion of the present author. When this same alloy combination was Fusion™ cast such that the Al-Mn alloy was

5 ˚C below its solidus prior to contacting the Al-Si clad metal, a poor bond was said to be observed. The figure cited to support this claim shows a clear delineation between the two alloys at the interface. This suggests, based solely on visual observation, that the resulting bond quality was poor. Again, the evidence presented in the patent does not convincingly show that the requirements, stated in the patent (and listed as points (i) through (iv) above), are actually necessary for obtaining metallurgically sound bonds between the core and clad alloys during Fusion™ casting.

2.2 Fusion™ casting research in the literature

To date, there has been little research presented in the literature regarding the Fusion™ process. Baserinia *et al.* [21] developed a thermal-fluid model of a lab scale Fusion™ casting machine, and validation of the model was provided in [22]. Furthermore, analysis of the AA3003/AA4045 (core/clad) Fusion™ cast interfaces in [22] suggest that core reheating may not be required for obtaining a visually acceptable bond between the core and clad alloys during casting. Metallurgically sound interfaces between AA3003/AA4045 were observed in regions where thermofluid model predictions suggested no AA3003 shell reheating as a result of contact with AA4045 liquid. The as-cast interfaces appeared similar to dissolution interfaces seen by Craighead *et al.* [23]; however, no detailed process regarding interface formation between the AA3003 core alloy and the AA4045 clad alloy was given as it was outside of the scope of the paper. Additionally, interface quality was judged by visual interpretation alone, and on samples which had been prepared for optical microscopy, i.e., a relatively small fraction of the total area of interface between the AA3003 core and AA4045 clad alloy.

Lloyd *et al.* [14] studied the deformation of clad aluminum sheet, produced via Fusion™ casting. Compound tensile test coupons were fabricated such that the tensile axis was

perpendicular to the interface of an AA3003/X609 Fusion™ ingot. Tensile samples failed in the softer AA3003 alloy, indicating metallurgically sound and defect-free interfaces; however, as-cast samples were not included in the test. The three conditions that were tested in the study by Lloyd *et al.* [14] were: (i) as-rolled, (ii) rolled and tempered (to a T4 condition), and (ii) rolled and artificially aged at 453 K (180 °C). Thus, all ingots had undergone some form of rolling reduction prior to mechanical testing. As such, minimal inference as to the original as-cast interface quality can be made from the study of Lloyd *et al.* [14].

With respect to the mechanisms at play in interface formation during Fusion™ casting, no such studies exist in the literature. However, as the process involves the interaction and subsequent bonding of two aluminum alloys at high temperatures, the subject of fluxless aluminum joining is closely related and relevant to interface formation during Fusion™ casting. This will be discussed in the proceeding section.

2.3 Joining of aluminum at high temperatures: the oxide problem

In the Fusion™ casting process, the top surface of the liquid sump (see Figure 1-3) is at a high temperature and is exposed to the atmosphere. Typical metal pouring temperatures are 50 ˚C higher than the melting point of the respective alloy being cast. At these temperatures (650 - 700 ˚C), aluminum readily oxidizes to form a thin Al_2O_3 oxide film. The growth of such oxide films can impede the formation of a metallurgically sound interface in Fusion™ casting. In general, surface oxide growth in any aluminum-to-aluminum system to be joined at high temperature, can degrade final bond quality. This is due to the general understanding that Al_2O_3:

i. Has a very high melting temperature of about 2000 ˚C [24] and is essentially insoluble in aluminum [25] at processing temperatures (~500-700 ˚C).

ii. Forms on clean aluminum surfaces extremely rapidly.

iii. Is not wetted by aluminum and is a barrier to aluminum bond formation at processing temperatures and pressures associated with aluminum casting.

Unless the Al_2O_3 surface film is removed, e.g., through the use of a reducing agent such as KF-AlF_3 flux [8], bonding will likely not occur in the presence of such oxides. The physical properties of Al_2O_3, as well as its rate of formation, and its chemical stability are all relevant to the topic of interface formation in Fusion™ casting. These topics are discussed in the next three sections.

2.3.1 Formation of Al_2O_3

A review of aluminum oxidation in the solid state is given by Wefers [26]. In the presence of oxygen or dry air, aluminum will oxidize according to the following reaction:

$$2\ Al + 1.5\ O_2 \rightarrow Al_2O_3 \qquad (2\text{-}1)$$

This reaction is very exothermic with a release of -1675.7 kJ/mol of Al_2O_3 [27]. At room temperature, the reaction of a clean aluminum surface will reach a limiting thickness of about 2-4 nm within hours [24]. This initial oxide forms as an amorphous, continuous, and adherent film.

The equilibrium phase diagram for the binary Al-O system is shown in Figure 2-1 [25]. As shown in the figure, the only stable oxide in the Al-O system is α-Al_2O_3, commonly referred to as corundum. It should be noted that during high temperature oxidation of aluminum, metastable forms of Al_2O_3 grow, and not α-Al_2O_3. The melting point of Al_2O_3 is listed as 2054 °C by Wriedt [25]. Thus, the oxides which form on the top surface of the liquid sump during Fusion™ are indeed solid films. Examination of the phase diagram given by Wriedt [25] suggests that Al and O, for temperatures close to 660 °C, over the full compositional range of O, form a two-phase mixture of Al and Al_2O_3. Furthermore, the solubility of O in Al is extremely low, listed as

2.9 x 10^{-8} at% O in liquid aluminum at 660.5 °C. As such, any appreciable amount of O introduced into Al should principally result in the formation of Al_2O_3, and vice versa that Al_2O_3 should be thermodynamically stable when brought into contact with liquid Al. These solid films, if entrained at the interface during the Fusion™ casting process would therefore be expected to seriously impede interface formation.

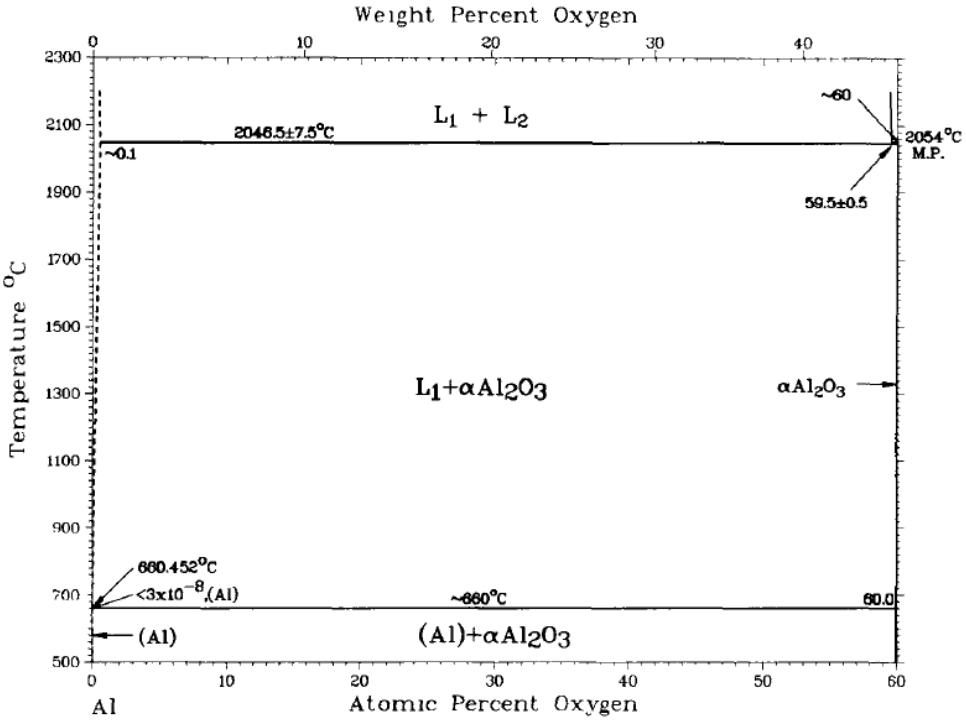

Figure 2-1 – Equilibrium phase diagram for the Al-O binary system. Image taken from Wriedt [25].

It is worth noting that the assessment of the Al-O binary system by Wriedt [25], specifically the solubility of O in liquid Al, may not be valid and may indeed be an under-estimate. Wriedt [25] concluded that oxygen solubility measurements in liquid aluminum from the literature at the time were invalid due to: experimental difficulties (hence errors) associated with these measurements and inadequate documentation within the original sources. The author adopted the following solubility for oxygen in liquid aluminum at 660.5 °C, 2.9 x 10^{-8} at% O. This is a calculated value given in Otsuka and Kozuka [28]. The value was derived using an

empirical model to extrapolate measured solubility data from other metal-O systems. As this value is extremely low, it is commonly assumed that Al_2O_3 is virtually insoluble in liquid aluminum. The value for oxygen solubility in liquid Al has, however, been challenged in a subsequent paper [29]. A critical assessment of the Al-O system, by Taylor *et al.* [29], suggests that the solubility value adopted by Wriedt [25] may be unreasonably low. In their assessment, the solubility of oxygen in aluminum at 660.5 °C is given as 7.0515×10^{-5} at% O. This value, also a calculated value, is based on a set of empirical correlations developed by Fitzner [30]. For comparison, the solubility of hydrogen in liquid aluminum at 660.5 °C is 1.16×10^{-4} at% H [31]. Hence, the often assumed notion that the solubility of O in liquid Al is zero may not be correct. The converse of this is: when Al_2O_3 is brought in contact with liquid Al that is unsaturated with respect to O, some Al_2O_3 dissociation may be thermodynamically plausible. There is an important point worth making, that the commonly held notion that Al_2O_3 is stable with respect to molten Al is not entirely true. If Al_2O_3 is brought into contact with liquid aluminum that is un-saturated with respect to O, then thermodynamically speaking, Al_2O_3 may not be stable and some dissociation may be expected. With respect to interface formation in Fusion™ casting, this is worth noting as a possible mechanism that aids this formation.

2.3.2 Kinetics of aluminum oxidation

From a thermodynamic and physical standpoint, there is a basis (explained above) for which Al_2O_3 can be thought of as an impediment to interface formation. The next logical question is in regards to the kinetics of Al_2O_3 formation. If Al_2O_3 formation on Al surfaces is sufficiently rapid, then the likelihood of having oxide-free Al surfaces prior to bonding is low. As such, interface formation in Fusion™ casting will be impeded unless special care is taken to remove the surface oxides.

Oxidation kinetic studies have been performed over a wide range of conditions. With respect to temperature, studies have been performed at ambient temperatures [32]; at elevated temperatures and with specific focus on initial oxidation of clean aluminum surfaces [33-35]; at elevated temperatures, but below melting [36-40]; and above the melting point of aluminum [41-46].

Initial oxidation of clean aluminum surfaces

Stucki *et al.* [33] used Auger Electron Spectroscopy (AES) and Electron Energy Loss Spectroscopy (EELS) to study the initial stages of oxidation of aluminum, in both the solid and liquid state. In their room temperature tests, the first detectable traces of chemisorbed oxygen on the aluminum solid surface were found after 20 Langmuir exposure[2] and Al_2O_3 formation began after 100 Langmuir oxygen exposure. At 700 °C, i.e., in the liquid state, these values increase to 1000 and 3000 Langmuir oxygen exposure, respectively. The authors suggest that at 700 °C, oxygen incorporates itself directly into the liquid and, therefore, longer exposure times are required to form a closed surface oxide.

Jeurgens *et al.* [34] used x-ray photoelectron spectroscopy to study initial oxidation of single crystalline aluminum, over the temperature range of 100-500 °C. Using an oxygen partial pressure of 1.33×10^{-4} Pa, they found that 200, 500, and 750 Langmuir oxygen exposure is required to form a closed oxide at 300, 400, and 500 °C. Here, the authors define a closed oxide surface to be the point at which the Al^0 surface plasmon signal disappears from the Al 2p XPS spectra, meaning that all Al atoms at the surface are in a Al^{3+} state, and therefore oxidized. The increase in exposure with temperature is attributed to the oxide growth characteristics which they also examined using high resolution electron microscopy. They claimed the aluminum oxide

[2] The Langmuir (L) is a unit of exposure (to a gas). $1L = (1 \times 10^{-6}\ \text{Torr}) \times (1\ \text{second})$

initially grows via an *island-by-layer* growth mechanism, and that any increase in oxide growth temperature also increases the oxygen mobility on the aluminum surface. *Island-by-layer* growth is a surface growth mechanism where chemisorbed oxygen laterally diffuses over the surface towards oxide nuclei on the surface of the aluminum. These *islands* or oxide nuclei grow in size until they coalesce and form a continuous oxide layer on the original metal surface. The lateral mobility of oxygen on the aluminum surface is a strong function of temperature, with higher temperatures allowing oxygen to migrate to islands with greater ease. Indeed, they observed both a decrease in the island density as well as an increase in overall island size with temperature.

Aluminum oxidation rates between 100-400˚C

Jeurgens *et al.* [35] continued to study the kinetics of initial oxidation within a similar temperature range as their previous study [34]. Below 300 °C, they found oxide film growth to be self-limiting. Furthermore, they found this limiting thickness to increase with oxidation temperature, with the limiting oxide thicknesses measured to be 0.5-0.9 nm for oxidation temperatures 100-300 °C. At oxidation temperatures ≥ 400 °C, the oxide growth was not self-limiting. The growth kinetics at these elevated temperatures included an initial fast regime, which was more prolonged in comparison to the low temperature kinetics, in addition to a second stage of slower but continuing oxide growth. The observed growth kinetics in this second growth regime was very nearly parabolic, indicating that oxidation is likely rate-limited by solid-state diffusion of ions through the oxide film, as per Wagner's oxidation theory [47].

It is worth noting that the studies mentioned above [33-35] were all done with a reduced oxygen partial pressure atmosphere. This is to be expected, as the main focus of study in those

papers was initial oxidation, and using a reduced partial pressure should decrease overall rates of oxidation, thereby facilitating observations and measurements of changes in oxidation rates.

Aluminum oxidation rates between 400-660˚C

Beyond 400-450 ˚C, the oxidation kinetics becomes more complex. A general understanding of what occurs is given as follows [24]. Between 400 and 450 ˚C, oxidation is parabolic. Beyond a certain point in time; however, the oxidation kinetics changes to a linear rate law. The change to linear kinetics suggests an open pathway exists between the oxidizing species and the aluminum metal. These 'open pathways' are likely a result of the onset of crystallization of the initially amorphous alumina [26]. As crystallites of γ-Al_2O_3 begin to form and grow at the metal/oxide interface, the strain generated by these newly formed crystallites and the changes in specific volume of the oxide generate high diffusion rate pathways in the underlying amorphous film. Thus, diffusion through the oxide film no longer becomes the rate defining step in the oxidation kinetics.

After another period of exposure, the linear kinetics changes again to a non-linear rate law. As the lateral growth of the crystallites creates a quasi-continuous layer of crystalline Al_2O_3 along the aluminum surface, the species transport to the metal/oxide interface becomes retarded once again by the need for solid-state diffusion through the crystalline oxide layer. Above 450 ˚C, the kinetics is less consistently reported in the oxidation literature; however, the basic phenomenon, as described above, provides a good first example of the solid-state oxidation process.

One of the first attempts to measure aluminum solid-state oxidation kinetics with oxygen partial pressures close to ambient conditions was in 1947 by Gulbransen and Wysong [36]. Using a vacuum microbalance coupled with a tube furnace, they measured isothermal weight

gain of 99.085 wt% aluminum samples over the temperature range 350-550 °C, in 10,132 Pa of dry oxygen. Using these measured weight gains, they could then calculate the isothermal oxidation rate of aluminum at the experimental temperature of interest. They fitted these measured oxidation rates to parabolic kinetics, and tabulated parabolic rate constants for two samples, from 350-450 °C, noting a deviation from parabolic kinetics at about 450 °C and above. Of the four samples they tested, there appeared to be significant sample-to-sample variability. In tests performed at 500 °C for instance, there was a factor of 6 difference in weight gain between the samples with lowest and highest weight gains. The authors noted that the manner of ingot preparation and chemical treatments used during rolling of the ingots to final gauge was the most likely reason for sample-to-sample variation in the measured solid-state oxidation rate.

In a subsequent study, Smeltzer [37] measured and tabulated oxidation kinetics of super-pure aluminum in the temperature range 400-600 ˚C, while using a vacuum microbalance to measure the weight gains of his samples. Samples were oxidized in an atmosphere of 10,132 Pa of dry oxygen. Smeltzer found that the high temperature oxidation rate could be split into three distinct parabolic type phases. The first phase, which extends over the first 20 minutes of oxidation, was best fit to parabolic oxidation kinetics. The second phase, from 20 to 80 minutes, was fit to a different set of parabolic rate constants. The phase, occurring after about 80 minutes, deviated negatively from parabolic kinetics. Although the author fit the experimentally obtained oxidation weight gain data to parabolic kinetics, Smeltzer [37] stated the shortfalls of such measurements and fitting procedures: (i) they do not aid in elucidating the mechanism of the high temperature oxidation of aluminum, (ii) the concept of diffusion-controlled parabolic oxidation does not account for variations in crystalline structure of the oxide film, (iii) the assumption that oxidation rate constants can be determined from finite linear sections of the

parabolic law plots may not be adequate, and (iv) the assumption that the numerically fitted parabolic rate constants obey the Arrhenius relation may not be adequate in light of the fact that crystallization of oxide is occurring during high temperature oxidation.

In a series of related studies, Beck *et al.* [38] and Brock and Pryor [39] used a combination of weight gain studies, electron microscopy, and electron opacity measurements to study the oxidation kinetics with more precision. Again, samples were oxidized in an atmosphere of 10,132 Pa of dry oxygen. The culmination of their work is a kinetic equation for weight gain, which includes: initial amorphous Al_2O_3 growth, nucleation and growth of crystalline γ-Al_2O_3, and continued growth of amorphous Al_2O_3 in between and above the crystalline regions. The final equation is a summation of the three growth processes [39]. As it is complex, many authors continue to use the assumption of parabolic oxidation growth kinetics when performing oxidation calculations.

In 2000, Tenório and Espinosa [40] obtained weight gain data for the first hour of oxidation of AA3004 and AA5182, two alloys used in beverage-can fabrication. They concluded that oxidation of AA3004 (which includes ~ 1 wt% Mg) is parabolic in the temperature range 450-750 ˚C. Tests on AA3004 were conducted in the presence of: air (21,275 Pa oxygen), Ar +5% O_2 (5,066 Pa oxygen), Ar +1% O_2 (1,013 Pa oxygen), and CO_2. A 7-fold decrease in weight gain (with respect to tests performed in air) was observed when oxidation was conducted in CO_2, while the Ar +1% O_2 mixture provided a 4-fold decrease in weight gain. The parabolic oxidation constants tabulated by Tenório and Espinosa [40] were given for the tests performed in air (21,275 Pa oxygen) only.

A compilation of tabulated parabolic oxidation kinetics data available in the literature, [36-40], as a function of oxidation temperature is given in Figure 2-2. The y-axis in the figure,

k_p, is the parabolic weight gain constant. The units of k_p are $(g \cdot cm^{-2})^2 \cdot s^{-1}$. Expressed in these units, k_p can be used to calculate the weight gain per unit area, *w*, of a sample as a function of time, *t*, using Equation 2-2. Assuming an adequate value for the oxide density, the weight gain can be converted to approximate oxide thickness.

$$w = \sqrt{k_p t} + const \tag{2-2}$$

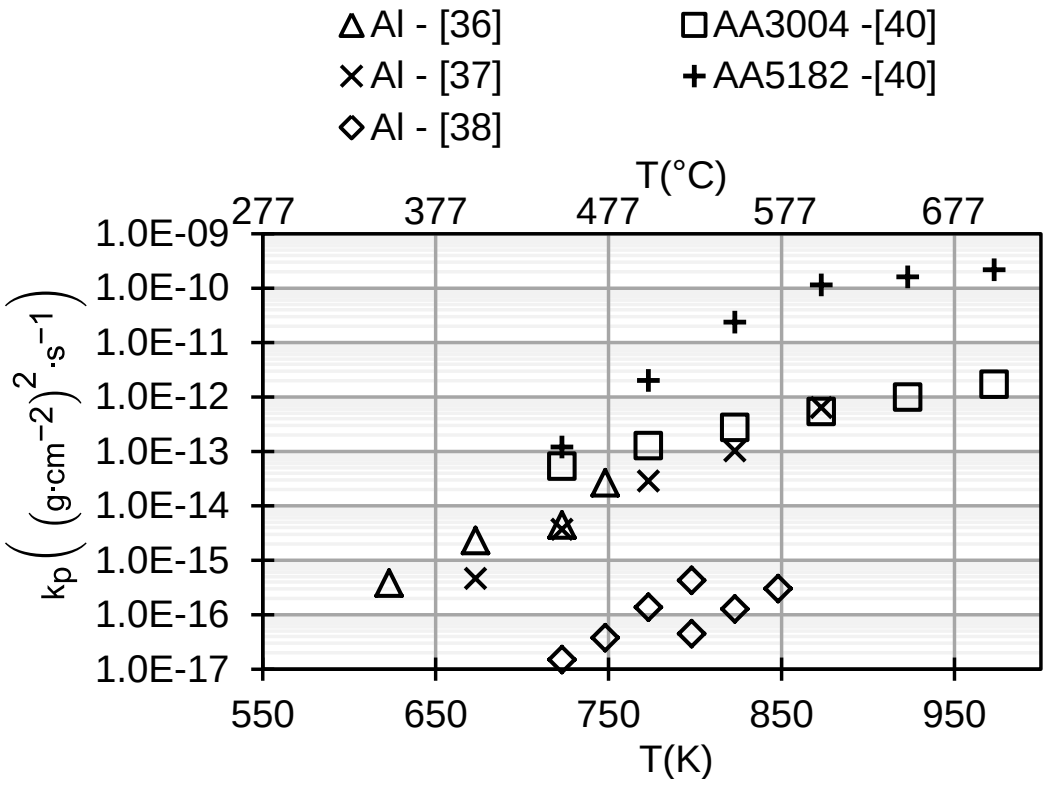

Figure 2-2 – Parabolic aluminum oxidation rate data reported in the literature.

From Figure 2-2, there appears to be general agreement in the trend of data with respect to temperature. The values of k_p from Gulbransen and Wysong [36], Smeltzer [37], and Tenório and Espinosa [40], for AA3004, are somewhat close in magnitude; despite the fact that the data from Tenório and Espinosa [40] is from an alloy containing 1 wt% Mg and was performed using a higher oxygen partial pressure. There a noticeable increase in oxidation rate for AA5182, an alloy which contains considerable Mg. Finally, the parabolic growth rate data from

Beck *et al.* [38], is considerably lower. It should be noted here that the parabolic growth rates from all other authors were derived without any attempt to isolate the simultaneous growth of amorphous and crystalline Al_2O_3 at high temperatures. The parabolic growth rate tabulated by Beck *et al.* [38] is specific to amorphous oxide growth only, hence it makes sense that it is considerably lower, since oxide crystalline oxide growth is not accounted for in this value of k_p.

Liquid aluminum oxidation rates

Initial aluminum oxide formation and growth in the Fusion™ casting process occurs on the surface of the liquid metal sumps of both the core and clad alloys (see Figure 1-3). Hence, oxidation kinetics of aluminum in the liquid state, about 660 °C, is relevant to interface formation in the Fusion™ casting process.

Drouzy and Mascré [41] have reviewed the available literature on oxidation of liquid non-ferrous alloys. Within the section regarding liquid aluminum alloys, the work of Thiele [42] is summarized from the original German text. Thiele [42] measured the effect of alloying elements on the oxidation of aluminum at 700 ˚C and 800 ˚C. Surface oxides were of the order of 900 nm thick after a 1 hour exposure time at 700 ˚C, and upwards of 2000 nm thick for exposure at 800 ˚C. At 700 ˚C the alloying elements Fe, Zn, Cu, Be, Si, and Mn had little effect on the oxidation rates, while Mg, Na, Ca, and Se noticeably increased the extent of oxidation. At 800 ˚C, the alloying elements Zn, Mn, Si, and Fe slightly increased the weight gain after exposure times of more than 20 hrs. For times less than 1 hour, he found that the extent to which these alloying elements affect oxidation cannot be clearly deciphered from the published results.

No tabulated oxidation growth rate data could be found for liquid aluminum, with the exception of the data given in by Tenório and Espinosa in [40] for AA3004 and AA5182.

2.3.3 Mechanisms of wetting and joining of aluminum at high temperature

In the Fusion™ casting process, if the surface of the core alloy shell which comes into contact with the liquid clad alloy is oxidized (see Figure 1-3), conventional knowledge suggests that the oxide is not wetted by the liquid aluminum and is chemically stable for practical oxygen partial pressures and at processing temperatures associated with aluminum casting. In the next section, the common misconception that wetting does not occur between aluminum oxide and liquid aluminum will be discussed.

Wetting of aluminum oxide by liquid aluminum

Macroscopically, the oxidation of liquid aluminum has caused many problems over the years for researchers wishing to measure the contact angle or surface tension of pure liquid aluminum [48-52]. The growth of aluminum oxide on the liquid surface of aluminum changes the surface conditions of the liquid aluminum, thereby affecting the liquid surface tension [48] and the contact angle the liquid aluminum makes with solid surfaces [49].

Gourmiri and Joud [48] conducted sessile drop measurements on liquid aluminum drops while simultaneously making surface composition measurements using Auger Electron Spectroscopy. They found droplets of liquid aluminum that were clean of oxygen had surface tensions which were 15-20% higher than surfaces with oxygen coverage (i.e., oxide films).

Molina *et al*. [49] measured the contact angle between molten aluminum and an alumina substrate during continuous heating tests in a vacuum of 10^{-4} to 5 x 10^{-5} Pa, using the sessile drop method. Below 850 ˚C, the contact angle between liquid aluminum and alumina was greater than 90°, with a peak value of 140° at close to 750°C. Above this temperature, continuous de-oxidation of the oxidized surfaces was said to occur, resulting in a continuous decline in contact angle with increasing temperature. At 1000 ˚C, contact angles less than 90° were

achieved. Also using the sessile drop technique, Laurent *et al.* [50] measured the steady-state contact angles formed between single crystal alumina and liquid aluminum as a function of temperature. Under a vacuum of 4 x 10^{-5} Pa (measured oxygen partial pressure of 10^{-15} Pa) the steady-state contact angle was reported as 103° +/- 6° at 660 °C. Using a *clean drop* technique, whereby fresh liquid metal is forced out of a syringe while under high vacuum and utilizing an oxygen getter within the furnace, Wang and Wu [51] measured the contact angle between molten aluminum and single crystalline alumina. Using this technique, they measured a contact angle of 90° at 700°C, for short exposure times. For exposure times greater than 100 L, their measured contact angles match those of Laurent *et al.*, i.e., 105°.

Clearly, the measurement of surface properties of liquid aluminum is not a trivial task, and is heavily influenced by the presence of oxygen in the system. A concise review on contact angle measurements found in the literature is given in Bao *et al.* [52]. Due to the difficulties associated with these contact angle/surface tension measurements, there is a misconception in engineering practice that liquid aluminum does not *wet* its oxide. For instance, the value of 140° at 750°C given in [49] suggesting the system is non-wetting. However, as shown by Wang and Wu [51], the real contact angle between clean aluminum liquid and alumina is much lower, about 90°, suggesting a good degree of wetting.

Thus, if clean/un-oxidized aluminum liquid comes into contact with aluminum oxide, wetting is achievable. If the liquid aluminum surface which comes into contact with aluminum oxide is itself oxidized, then wetting is unlikely to occur. Again this suggests that in the Fusion™ casting process, the fate of the surface oxides which form on the liquid core and clad sumps (see Figure 1-3), are critical to the interface formation process.

Assuming that a condition can be achieved whereby clean/un-oxidized liquid aluminum can be brought into contact with an oxidized solid aluminum surface, the liquid should wet the oxidized aluminum solid surface. However; the oxide present on the solid aluminum surface still poses a barrier to joining/bonding of the liquid and solid aluminum. Practical methods to undermine this oxide and promote bonding exist in the literature. These processes can be classified into two types; those which require the use of fluxes and those which do not [8]. Two particular methods will be reviewed, as they may provide insight into determining the interface formation mechanisms in the Fusion™ casting process: (i) joining via physical penetration of surface oxides and (ii) joining by chemical reduction of surface oxides.

2.3.3.1 Aluminum joining mechanism I: penetration through the surface oxide

Early work by Wall and Milner [53] pertaining to the wetting and spreading of liquid metals on various metal substrates at elevated temperatures, suggested that bonding between a liquid metal and its substrate will not occur if both surfaces (liquid and solid) are oxidized. However, they found that significant substrate dissolution (or erosion) took place when they initiated penetration of the oxides via a mechanical pin-prick. Based on these observations, they proposed a model of penetration, spreading, and erosion of a solid substrate by liquid metal, which requires the presence of oxide defects (mechanically induced in this case). Depending on the following factors: temperature, solubility of the liquid metal with respect to the metal substrate, and interaction time, the shape of the liquid-solid interface changes. Wall and Milner [53] describe two qualitatively different liquid-solid interfaces, which are schematically depicted in Figure 2-3. When the solubility of the substrate alloy in the liquid alloy was high, a high temperature was used and the liquid was exposed to the solid substrate for a long period of time, the final interface appeared as that depicted in Figure 2-3a. Here, extensive chemical dissolution of the

substrate by the liquid alloy takes place. Since penetration of the oxide is from a discrete point, and the final interface is semi-spherical in shape, the dissolution process can be said to be diffusion limited.

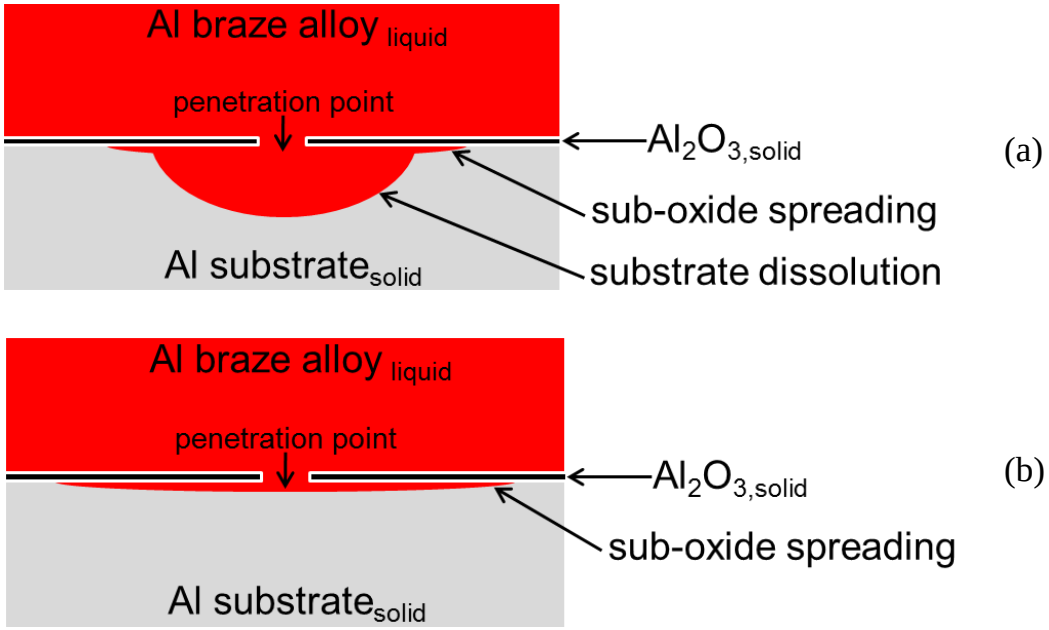

Figure 2-3 – Qualitative spreading types described by Wall and Milner [53]. (a) Sub-oxide spreading and dissolution of the substrate, in systems where the solubility of braze alloy in the substrate alloy is high. (b) Sub-oxide spreading via a discrete penetration point, in systems where the solubility of the braze alloy in the substrate alloy is low.

When the solubility of the liquid alloy in the substrate alloy was high, low temperatures were used and the liquid was exposed to the solid substrate for a short time, the final interface appeared as that depicted in Figure 2-3b. Here, minimal dissolution of the substrate was observed, and it was confined to a very thin region into the substrate. Spreading of the liquid beneath the oxide was observed, however, as a very thin band beneath the oxide. In a related study of aluminum brazing, Zähr *et al.* [54] also found that wetting and flow could be attained using nitrogen (99.999%) purge gas and using an applied force to mechanically disrupt surface oxides and provide penetration pathways for liquid braze alloy to penetrate through.

The joining/bonding process described by Wall and Milner [53] suggests that mechanical disruption can be used to generate oxide defects. These defects provide pathways for aluminum liquid to flow though and initiate chemical dissolution of the substrate. This mechanism by Wall and Milner [53] leads to the question: can naturally occurring oxide defects be potential sites for liquid alloy penetration? While this topic has not received any study in the literature, defects in aluminum oxide films have been observed in studies focusing on the resulting structure and morphology of thermal oxide films grown on aluminum.

Defects in thermal oxide films

There have been numerous studies focused on the resulting structure and morphology of thermal oxide films grown on aluminum [34], [38], [39], and [55-57]. The majority of these studies typically include transmission electron microscopy of stripped oxide films or carefully microtomed sections.

Jeurgens *et al*. [34] analyzed cross sections of oxidized aluminum samples using TEM and HRTEM. For oxide films grown at 500 °C, an oxygen partial pressure of 1.33×10^{-4} Pa, and time of 20×10^{3} seconds, they found the oxide film thickness to range from 10-80 nm thick, when measured with HRTEM. The average oxide thickness was quoted as 30 +/- 10 nm. For oxides grown at slightly lower temperatures of 300-400 °C, images showed that local necks in the oxide were present. In these 'necked' regions, the oxide was extremely thin and in some cases sub-nm, potentially constituting a defect in the oxide film. The authors attributed the non-uniform oxide thickness to the *island-by-layer* growth mechanism. In the high temperature oxide, the duplex oxide growth, i.e., amorphous oxide as well as crystalline γ-Al_2O_3 also is partially responsible for the stated non-uniformity.

TEM studies on both thermal and anodized Al_2O_3 films were conducted by Shimizu *et al.* [55-56]. Void type defects in oxide films were observed in two instances. In the first instance, the voids occurred at the oxide/aluminum interface of oxide films which were grown on pure aluminum, electropolished, then oxidized in air for 30 minutes at a temperature of 550 °C [55]. In the second instance, voids were present between adjacent layers of oxides [56]. In this study, aluminum was alloyed with 0.5 wt% magnesium. TEM sections on a sample which had been oxidized at a temperature of 450 °C, in air, for 10 minutes, displayed the presence of occasional voids between an outer crystalline (and Mg-rich) layer and an inner amorphous layer. Samples oxidized at 550 °C for a duration of 30 minutes were said to have formed extensive arrays of easy paths for diffusion of Mg.

The presence of defects in oxide films has been visualized in other metal oxide systems as well, including: room temperature air-formed and anodic Al_2O_3 films using a copper decoration technique [58], anodic Ta_2O_5 films using both optical microscopy and TEM [59], and high temperature iron oxide films using optical microscopy [60]. Shimuzu *et al.* [61], comment that that when creating anodic Al_2O_3 films on carefully electropolished aluminum substrates, defects densities are generally still up to 10^5 /cm^2.

2.3.3.2 Aluminum joining mechanism II: chemical reduction of the surface oxide

As an alternative to penetration through oxide defects (mechanically induced or other), chemical activation has proved to be a successful method to achieve satisfactory aluminum joints without the aid of fluxes. This has led to the development of fluxless brazing processes for joining of various aluminum alloys [62]. Processes utilizing chemical activation usually require a low oxygen partial pressure (not necessarily high vacuum), and addition of an active metal to the system. The role the active metal plays in the process of fluxless vacuum brazing of aluminum

alloys was described by Terrill *et al.* [62]. They suggested that in order for an active metal, M, to promote joining of aluminum parts, the following three chemical reactions must take place prior to joint formation:

$$M + \frac{1}{2}O_2(0.2\ \text{atm}) \rightarrow MO \quad (2\text{-}3)$$

$$M + H_2O(0.03\ \text{atm}) \rightarrow MO + H_2 \quad (2\text{-}4)$$

$$M + \frac{1}{3}Al_2O_3 \rightarrow MO + \frac{2}{3}Al \quad (2\text{-}5)$$

The first two reactions are essentially 'gettering' reactions, scavenging residual oxygen or water vapour in the vacuum furnace, thus preventing excess oxidation of the joining surfaces from taking place during heating. The third reaction, essential to the process, is the reduction of the existing surface oxides on the aluminum mating surfaces to be joined. This reaction is critical because by reducing the surface oxides, clean (or un-oxidized) aluminum metal becomes available at the surfaces, which is more amenable to bonding. When the low melting point alloy finally melts; the contact between the solid aluminum surface and adjoining liquid aluminum brazing alloy is clean and oxide free, thereby facilitating wetting and bonding between the solid aluminum and brazing alloy.

Terrill *et al*. [62] reported that the following active elements promote brazing:

i. Lanthanoid group elements: La, Ce, Pr, Nd, Sm.

ii. The group 1 element Li.

iii. The following group 2 elements: Be, Mg, Ca, Sr.

Additions in the 0.001 wt% range of one of these active elements to the system can be either as an alloying element in the base metal or the braze metal. Alternatively, braze promotion could also be achieved by adding active element vapours into the vacuum system (i.e.,

without alloying). They also reported on successful brazing of commercial alloys in vacuum without the intentional addition of active elements to the brazing system; however, the authors neglect to mention if any active metal impurities, such as Ca, Mg, or Sr, were present in the commercial alloys being used. It is worth noting that the alloy which was successfully brazed without active element additions (in vacuum) was indeed AA3003, the same alloy used in fabrication of Fusion™ ingots for braze clad sheet metal fabrication. There is a distinct possibility that in the studies of Terrill *et al.* [62], that Mg impurities may have been present in the AA3003. Even impurity level amounts of Mg in AA3003 (0.03 wt%) have been shown to segregate and accumulate to the surface during high temperature heat treatments, for example see Hulob and Matienzo [63] and Nylund *et al.* [64]. Once Mg segregates to the surface in sufficient concentration, it can potentially react with and reduce Al_2O_3 surface oxides, hence promoting joint formation.

Additionally, there are numerous aluminum joining technologies in the literature which operate essentially on the same principles as those discussed by Terrill *et al.* [62], and which specifically use Mg as the active element addition. These include: fluxless-vacuum brazing [65], diffusion-welding [66], powder sintering [67], and preparation of alumina/aluminum metal matrix composites [68].

2.4 Aluminum alloy solidification

As mentioned in Section 1.3, various combinations of composite alloy ingots have been produced using the Fusion™ casting process, see Table 1-1. Commercially, the Fusion™ casting process has been successfully used to produce AA3xxx-core/AA4xxx-clad ingots as feedstock for the manufacturing of brazing clad sheet. In this Fusion™ casting combination, the AA3003 alloy is solidified first as the core alloy, and the AA4045 alloy is solidified second as

the clad alloy, as shown in Figure 1-2b. As this combination is of practical significance/importance, this thesis will focus specifically on this core/clad combination.

Aluminum alloy AA3003 is introduced and discussed in Section 2.4.1, followed by a discussion of alloy AA4045 in Section 2.4.2. The focus of each section is in regards to the solidification characteristics of each alloy, as Fusion™ casting is a solidification process. A short comparison of the two alloy's solidification curves is presented in Section 2.4.3.

2.4.1 AA3003: alloy description and solidification characteristics

Aluminum alloy AA3003 is a wrought aluminum-manganese alloy which is used in a variety of applications, such as architectural panels and eaves troughs, etc., due to its good formability, corrosion resistance, and moderate strength. The compositional limits for AA3003 are listed in Table 2-1.

Table 2-1 – Nominal compositional specifications for AA3003, in wt% [69].

Al	***Mn***	***Si***	***Fe***	***Cu***	***Zn***	***Other***	
Bal.	1.0-1.5	0.6 max	0.7 max	0.05-0.2	0.1	0.05 max (individual)	0.15 max (total)

For reference, the aluminum-manganese binary phase is shown in Figure 2-4 [70]. The nominal composition of Mn in AA3003 is indicated by the vertical dashed line in the diagram. There is a eutectic reaction at 931 K (658 ˚C) and 0.01 mol fraction Mn (1.95 wt% Mn) of the form:

$$\text{Al(liq) (1.95 wt\% Mn)} \rightarrow \text{Al}_6\text{Mn(sol)} + \alpha\text{-Al(sol) (1.82 wt\% Mn)} \qquad (2\text{-}6)$$

At the eutectic temperature, the solubility limit of Mn in Al is 0.62 at% (1.82 wt%) [70]. As mentioned in Bäckerud *et al*. [71], hypoeutectic alloys with composition less than 1.5 wt% Mn exhibit a cellular structure when solidified under cooling conditions of around 1˚C/s. In commercial AA3003 alloys, the presence of Fe and Si impurities alters the solidification process. First, unlike the Al-Mn binary alloys, which solidify to form cellular dendrites, AA3003 forms

equiaxed dendrites upon solidification. Additional phases also form during solidification, as a result of the presence of Fe and Si.

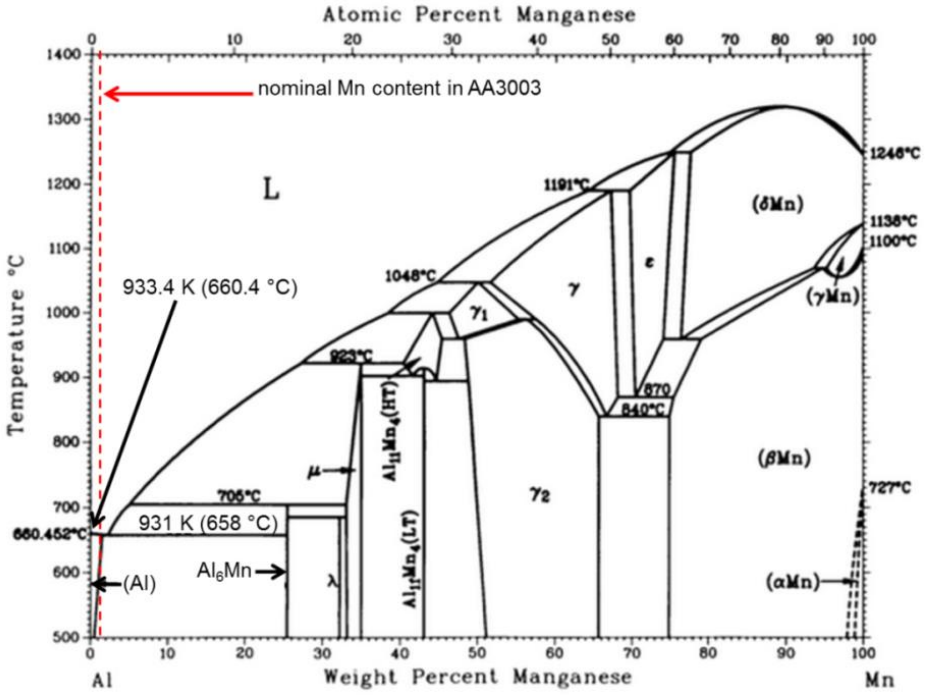

Figure 2-4 – Al-Mn phase diagram. Image taken from McAlister and Murray [70].

The solidification reactions found in commercial AA3003 alloys were identified by Bäckerud *et al*. [71] and are given in Table 2-2 and Table 2-3. AA3003 will first begin to solidify as α-Al at 655 ˚C. During non-equilibrium solidification normally observed in commercial casting processes, $Al_6(Fe,Mn)$ particles begin to precipitate from the liquid in tandem with dendritic α-Al growth. According to studies by Bäckerud *et al*. [71], the temperature at which this reaction occurs is dependent on sample cooling rate. At cooling rates less than 1.2 ˚C/s, the reaction was observed to occur at 653 ˚C, whereas under faster cooling conditions, the reaction temperature was found to range from 646-615 ˚C. In a third reaction, $Al_6(Fe,Mn)$ was found to transform via a peritectic reaction to $Al_{15}(Fe,Mn)_3Si_2$. After the transformation is complete, any remaining liquid also transforms to $Al_{15}(Fe,Mn)_3Si_2$. It is worth

noting that this final reaction is at a temperature lower than the eutectic in the Figure 2-4, as expected due to the effects of Fe and Si addition to the Al-Mn binary system.

Table 2-2 – List of reactions occurring during solidification of aluminum alloy AA3003 [71].

1st reaction	$Al_{(liq)} \rightarrow Al_{(sol)}$, dendritic network
2nd reaction	$Al_{(liq)} \rightarrow Al_{(sol)}$, dendritic network + $Al_6(Fe,Mn)_{(sol)}$
3rd reaction	$Al_{(liq)} + Al_6(Fe,Mn)_{(sol)} \rightarrow Al_{(sol)} + Al_{15}(Fe,Mn)_3Si_2$
	$Al_{(liq)} \rightarrow Al_{(sol)} + Al_{15}(Fe,Mn)_3Si_2$

Table 2-3 – Effect of cooling rate on reaction temperature during solidification of AA3003 [71].

	Cooling Rate (K/s)			
	0.5	***1.2***	***3.9***	***17***
1st reaction (K,(˚C))	928 (655)	928 (655)	928 (655)	928 (655)
2nd reaction (K,(˚C))	926 (653)	926 (653)	922-888 (649-615)	922-888 (649-615)
3rd reaction (K,(˚C))	914-907 (641-634)	914-907 (641-634)	886 (613)	862 (589)
Solidification Range (K)	21	21	42	67

An optical micrograph of AA3003 solidified with a cooling rate of 0.5 °C/s is shown in Figure 2-5. In this image, the $Al_6(Fe,Mn)$ phase is polyhedral in shape. Two of the $Al_6(Fe,Mn)$ particles in the micrograph are shown partially transformed to $Al_{15}(Fe,Mn)_3Si_2$. This corresponds to the solid state $Al_6(Fe,Mn)$ transformation, i.e., reaction 3 in Table 2-2. Additionally, in the micrograph, a noticeably finer script-type phase is observed. This phase was identified by Bäckerud *et al*. [71] to be $Al_{15}(Fe,Mn)_3Si_2$. Unlike the dark brown $Al_{15}(Fe,Mn)_3Si_2$ phase, which was a result of a solid-state $Al_6(Fe,Mn)$ transformation, this script phase is formed directly from the remaining melt upon solidification, i.e., the second form of reaction 3 in Table 2-2.

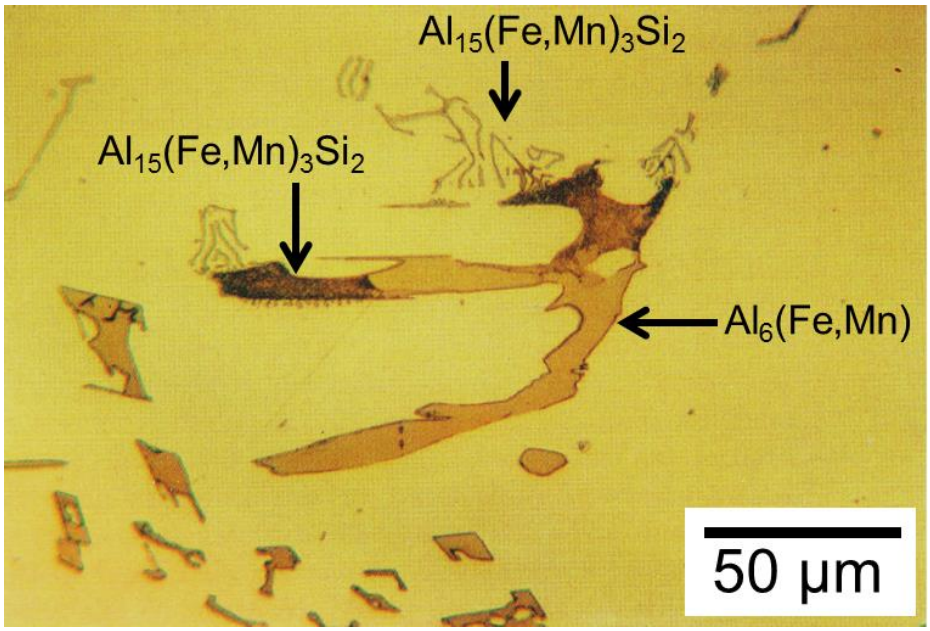

Figure 2-5 – A typical/representative solidification microstructure of as-cast AA3003. Sample cooling rate 0.5 °C/s. Image taken from Bäckerud *et al*. [71].

Aside from the solidification characteristics of AA3003, knowledge of the solidification curve, i.e., a plot of expected fraction of AA3003 solidified vs. temperature is of practical importance. First, it is essential information which is used for thermofluids modelling of the Fusion™ casting process. Second, the Fusion™ casting patent [9] suggests that the core alloy must be semi-solid or reheated to semi-solid state upon contact with the clad liquid metal in order to achieve good bonding between the alloys. The solidification curve for an alloy can be calculated using thermodynamic software, or measured experimentally. Using the thermodynamic software package FactSage [72], the solidification curve for AA3003 was calculated for the case of equilibrium solidification and Scheil solidification, see Figure 2-6. The two extreme cases, equilibrium and Scheil solidification, were calculated to have solidification ranges of 14 ˚C (642-656 ˚C) and 79 ˚C (576-655 ˚C), respectively [73]. Observations from Bäckerud *et al.* [71] regarding the change in the solidification range for AA3003 as a function of cooling rate are in general agreement with thermodynamic predictions shown in Figure 2-6.

Using a different experimental technique to that of Bäckerud *et al.* [71], Chen and Jeng [74] determined solidification curves for a number of commercially alloys. Utilizing a cooling rate of 10 ˚C/min (i.e., 0.167 ˚C/s), they measured the liquidus and solidus temperatures of AA3003 as 657 ˚C and 636 ˚C, similar to the 0.5 ˚C/s cooling rate results of Bäckerud *et al.* [71]. Although the liquidus and solidus temperatures matched well, the evolution of fraction solid (f_s), calculated using cooling curve data and a heat transfer model of the experimental setup, were slightly different for the studies of Bäckerud *et al.* [71] and Chen and Jeng [74]. In the latter study, the f_s was shown to increase linearly with temperature from ~5 to ~95%, with only a minor dip near the end point. The curve given by Bäckerud *et al.* [71] has a slight dip in between 0% and 5% f_s, then f_s increases with virtually no change in temperature, within the interval 5 ~ 65%. When f_s approaches 65%, the slope of the curve encounters a shoulder, similar in shape to the shoulder in the Scheil curve shown in Figure 2-6, with the difference being the experimental curve reaches 100% f_s at a much higher temperature then that predicted by the Scheil curve, 634 ˚C as opposed to ~576 ˚C.

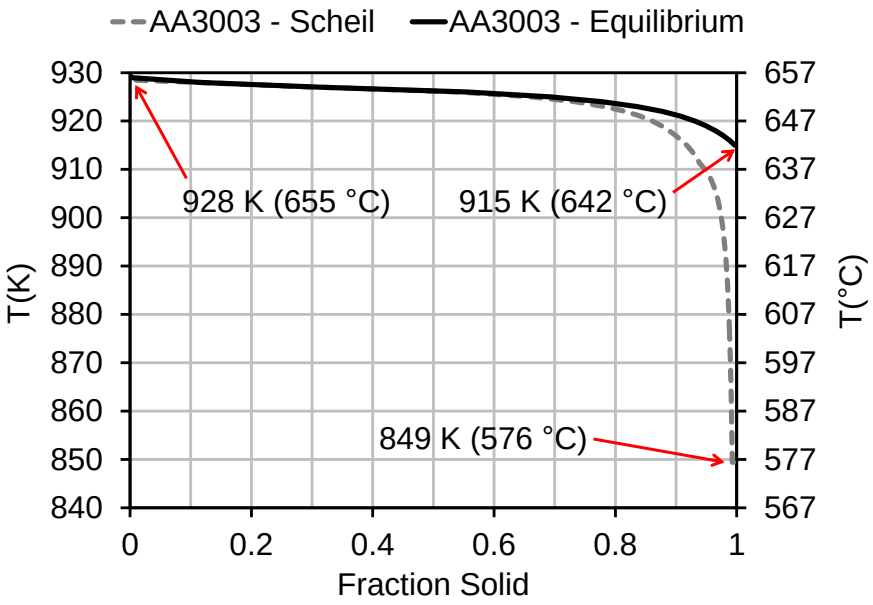

Figure 2-6 – FactSage [72] predictions of AA3003 mass fraction solid (f_s) as a function of temperature for equilibrium and Scheil cooling conditions [73].

2.4.2 AA4045: alloy description and characteristics

AA4045 is a wrought aluminum-silicon alloy. The compositional limits for AA4045 are given in Table 2-4. As a result of the silicon composition, this alloy is close to the Al-Si eutectic composition, and thus has a significantly reduced melting point and solidification range; hence its application as a brazing alloy.

Table 2-4 – Nominal compositional specifications for AA4045, in wt% [69].

Al	***Si***	***Fe***	***Cu***	***Mn***	***Mg***	***Zn***	***Ti***	***Other***
Bal.	9.0-11.0	0.8 max	0.3 max	0.05 max	0.05 max	0.1 max	0.2 max	0.15 max (total)

Al-Si alloys are typically divided into three categories: hypoeutectic, eutectic, and hypereutectic alloys, with the distinction between the three based roughly upon the eutectic composition given in the Al-Si binary phase diagram, see Figure 2-7 [75]. In general, the compositional range for hypoeutectic alloys are between 5-10 wt% Si, for eutectic alloys between 11-13 wt%, and for hypereutectic alloys between 14-20 wt% Si [76].

In a hypoeutectic Al-Si alloy, solidification begins with the formation of a network of aluminum dendrites, followed by the Al-Si eutectic reaction. At low temperature, precipitation of additional phases may occur from the remaining liquid. Table 2-5 is a summary of the phases which may form during solidification for a hypoeutectic alloy [76]. Whether or not a certain phase may form will depend on the quantity of alloying elements (Fe, Mn, Mg, and Cu) present in the specific alloy. For instance, the pre-dendritic reaction shown in Table 2-5, which forms primary $Al_{15}(Mn,Fe)_3Si_2$, will not occur in hypoeutectic alloys that do not have high amounts of Fe and Mn.

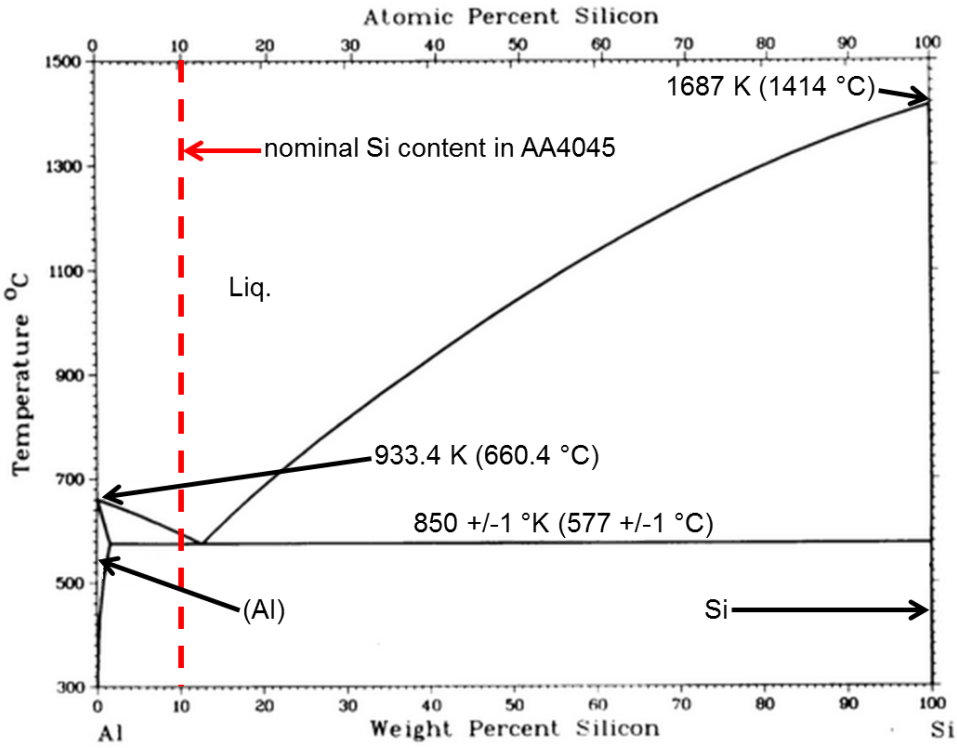

Figure 2-7 - Aluminum-silicon binary phase diagram. Original image was taken from McAlister and Murray [75].

Table 2-5 – Sequence of Phase Precipitation in Hypoeutectic Al-Si Alloys [76].

T (K,(˚C))	***Phases Precipitated***	***Suffix***
923 (650)	Primary $Al_{15}(Mn,Fe)_3Si_2$ (sludge)	Pre-dendritic
873 (600)	Aluminum Dendrites and	Dendritic
	$Al_{15}(Mn,Fe)_3Si_2$	Post-Dendritic
	and/or Al_5FeSi	Pre-eutectic
823 (550)	Eutectic Al + Si	Eutectic
	and Al_5FeSi	Co-eutectic
823 (550)	Mg_2Si	Post-eutectic
773 (500)	Al_2Cu and more complex phases	Post-eutectic

The solidification curve for AA4045, calculated using the thermodynamic software package FactSage [72], is shown in Figure 2-8. Here, there is negligible difference between equilibrium and Scheil conditions. The liquidus and solidus temperatures were calculated to be

871 K (598 ˚C) and 852 K (579 ˚C) [73]. There is a eutectic reaction at the solidus temperature of 852 K (579 ˚C), where the remaining liquid (71% mass f_s) transforms to eutectic Al + Si.

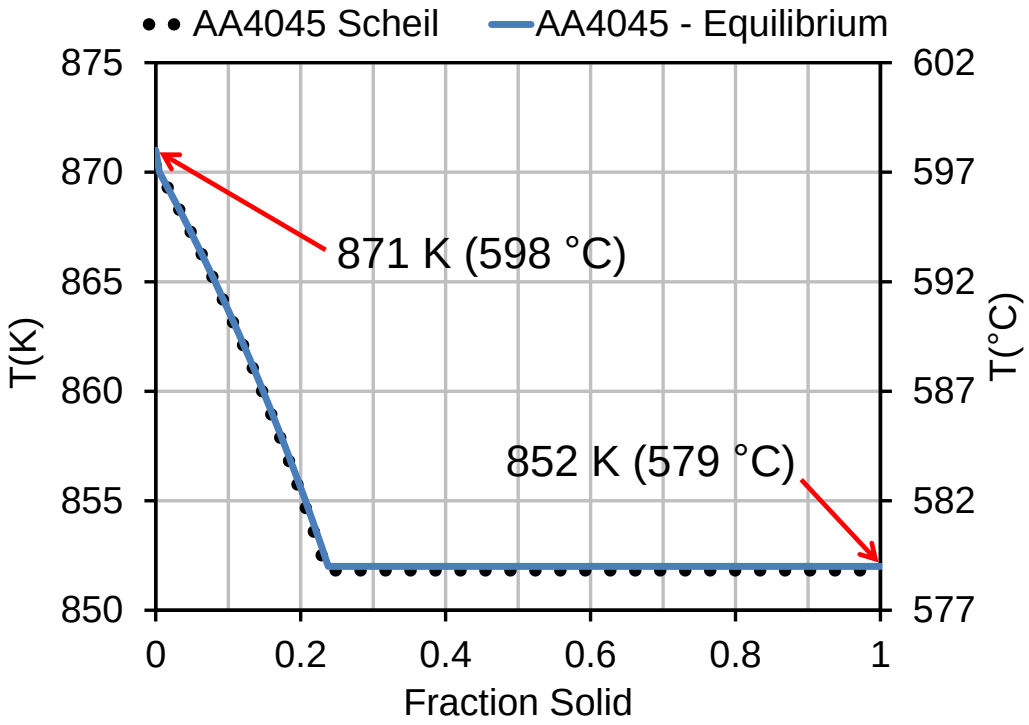

Figure 2-8 Factsage [72] predictions of AA4045 fraction solid (f_s) as a function of temperature for equilibrium and Scheil cooling conditions [73].

A typical AA4045 as-cast microstructure is shown in Figure 2-9. The primary aluminum solidifies to form a dendritic microstructure. Between these well-defined primary aluminum dendrites, a eutectic structure exits. The eutectic structure is a fine dispersion of two phases: aluminum and silicon. The eutectic morphology in an unmodified AA4045 alloy solidifies as an anomalous [77] (or sometimes referred to as irregular [78]) eutectic.

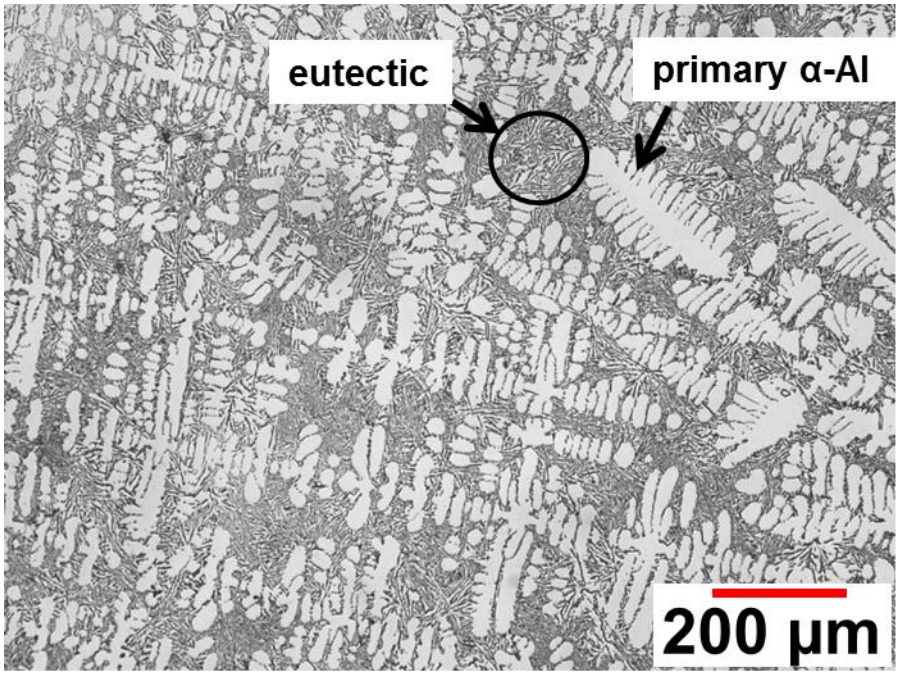

Figure 2-9 – AA4045 as-cast microstructure.

2.4.3 Fusion™ casting AA3003 and AA4045

Comparing the f_s curves for AA3003 and AA4045, shown in Figure 2-6 and Figure 2-8, respectively, there is no overlap of the curves in the case of equilibrium solidification. The solidus temperature of AA3003 is greater than the liquidus temperature of AA4045 by approximately 40 °C. A comparison of the predicted Scheil solidification curves for AA3003 and AA4045 is given in Figure 2-10. For the case of non-equilibrium Scheil solidification, there is only a very marginal overlap of the two curves. It is also worth noting that the calculated Scheil curve for AA3003 may indeed give erroneous values for the AA3003 solidus temperature. Referring to the measured solidus temperatures by Bäckerud *et al*. [71] in Table 2-3, depending on the solidification rate, the solidus temperature for AA3003 may be anywhere from 589 °C to 634 °C. As such, the real overlap in solidification curves is expected to be far less than the calculated values in Figure 2-10. As such, one would expect that there is sufficient operating

margin to produce a Fusion™ cast interface between the two alloys without having appreciable amounts of remelting of the AA3003 core.

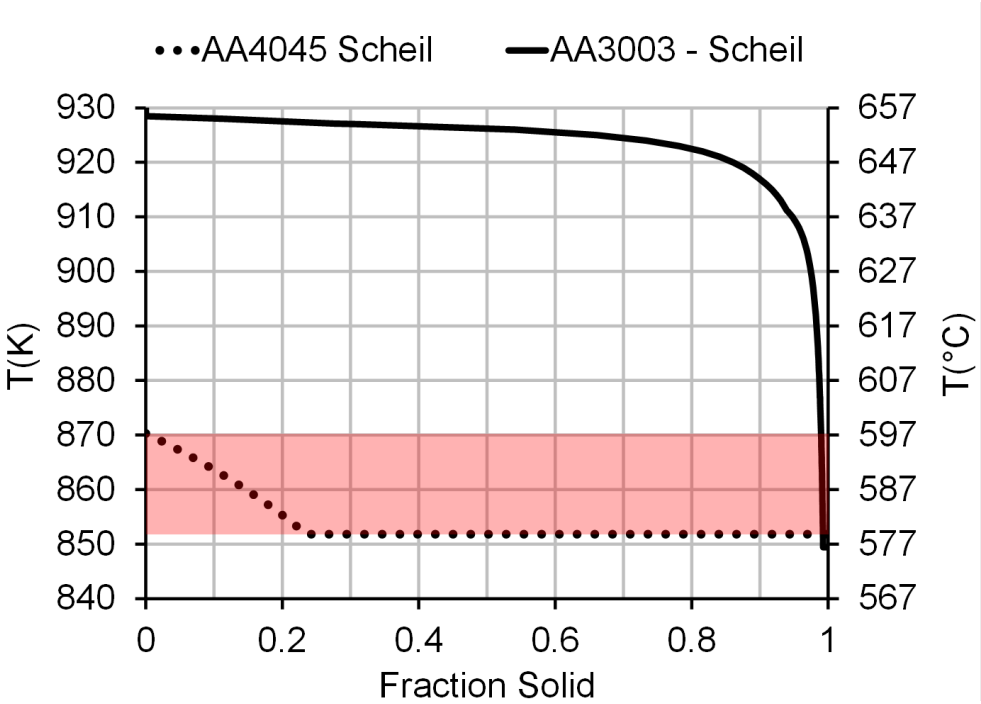

Figure 2-10 – Calculated Scheil solidification curves for AA3003 and AA4045 [73], superimposed to highlight the overlap in solidification range.

2.5 Surface phenomena in DC casting

In the Fusion™ casting process, it is also worth noting that the core alloy surface which comes into contact with the liquid clad alloy, depicted in Figure 1-3b, is continuously cast against a cooled chill bar. As such, the surface microstructure can be expected to be different than material solidified in the central portion of an ingot. This is worthy of discussion, as the surface structure may play a role in interface formation during Fusion™ casting.

While there is extensive literature regarding surface solidification phenomenon in DC casting (see examples in DC casting review by Emley [11]), an important distinction should be made here; that while the core alloy in Figure 1-3b is being continuously cast, it does not get

directly sprayed with water as does the surface of a conventional DC cast ingot. As the shell in Figure 1-3b solidifies, it also contracts due to volume change associated with liquid-to-solid phase change as well as thermal contraction of the solid. Since there is no water spray onto this shell in Figure 1-3b, the thermal contraction due to cooling of the solid shell is expected to be small. In contrast, since the surface of an ingot in DC casting is directly sprayed with water, large thermal contraction of the shell can occur resulting in a large decrease in the rate of heat extraction by the mould.

The high initial solidification rates due to contact with a cold mould in the case of DC casting (or chill bar for Fusion™ casting); along with thermal contraction and pull away of the solidifying shell from the mould, give rise to various surface phenomena such as: segregation [79] and exudation/remelting bands [80]. Of particular interest is surface exudation, as it is a plausible mechanism for mechanical breakup of surface oxides during Fusion™ casting.

To study surface exudation of non-ferrous DC cast ingots, Morishita *et al.* [81] built a macro-air-gap tester. They found that exudation occurs by flow of solute-rich liquid metal through inter-dendritic channels. As inter-dendritic material melts, they form liquid channels and provide an open pathway for liquid metal to exude to the cast surface. If the degree of reheating was slight, exudation occurred at single isolated sites, deemed spot exudation. With increased reheating, multiple channels joined together to form a network of connected pathways; with the resulting surface exudation of solute-rich interdendretic liquid covering a larger area on the surface of the ingot. Since inter-dendritic regions are typically rich in solute material, they should have a lower local melting temperature than the surrounding primary dendrites, thus they should be the first material to undergo remelting upon reheating. The flow/exudation of this liquid is then made possible by the metallostatic pressure acting upon it plus volumetric

expansion from transformation of the interdendritic solid to the liquid state. Applied to the process of Fusion™ casting, it is indeed possible that exudation (spot or otherwise), may be beneficial as an aid in oxide film breakup on the AA3003 shell external surface (see Figure 1-3).

Surface exudation with respect to brazing, not DC casting, was studied by McGurran and Nicholas [82]. Specifically, they used hot stage microscopy to study the remelting of aluminum brazing sheet and Al-Mg alloys. They observed raft-like areas on partially remelted Al-1% Mg surfaces, see Figure 2-11. The authors suggest that the lifted material in Figure 2-11 is a consequence of exuded liquid. In their procedure, the materials were heated in-situ in the SEM (under a high vacuum and low oxygen partial pressure). This suggests that the oxidation kinetics would have been reduced, and the subsequent oxide film thickness should have been thinner than if grown in air. None the less, SEM images suggest that the exuded liquid generated enough pressure to break through the oxide film and form regions of clean/fresh liquid metal.

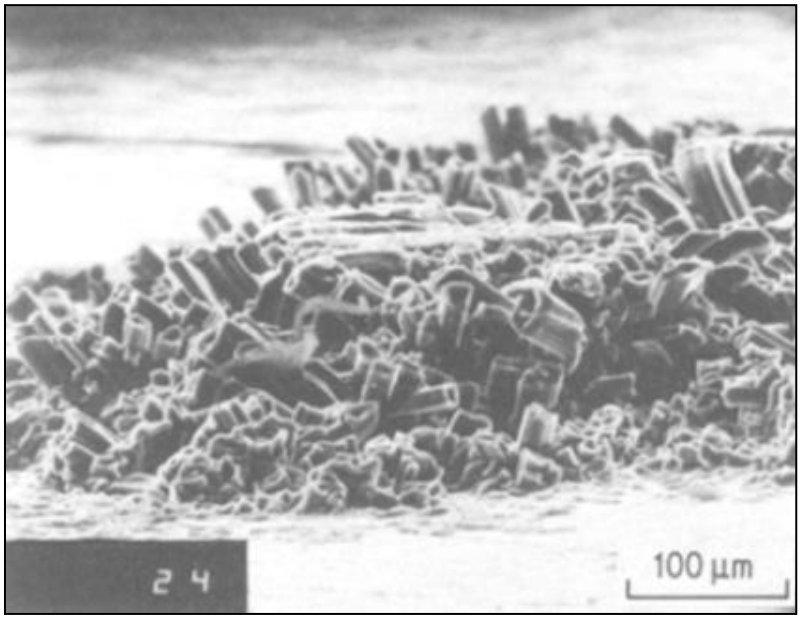

Figure 2-11 – High tilt angle micrograph of Al -1 wt% Mg alloy which has been heated to 640˚C. A raft of the original surface has been lifted up by exudation of new material. Image taken from McGurran and Nicholas [82].

2.6 Summary, objective and scope

As stated in Chapter 1, Fusion™ casting is relatively new, as the US patent for it was filed in 2005 [9]. To date, there has been little research presented in the open literature regarding the process. Although the patent suggests that the interface formed between the core/clad is oxide free, there is no physical model that adequately explains how an oxide-free interface is formed.

From our knowledge of the oxidation and joining of aluminum at high temperature, we suspect that if there is a continuous and adherent oxide film present along the surface of the core alloy as it comes into contact with the liquid alloy, then wetting should be impeded. If the oxide film is defective, or if cracks are formed in the oxide film by the action of exudation, there is the potential for penetration of the oxide. Additionally, if penetration of the oxide were to occur, dissolution of the core shell by the clad liquid should happen. The length of time for dissolution will depend on the local solidification time of the interface. The final interface may be affected by some or all of these aforementioned processes.

The goal of this thesis was to further the understanding of the interface formation process occurring during Fusion™ casting. In doing so, an experimental approach was used, which will be outlined and discussed in detail in the following chapter.

Chapter 3

Experimental Apparatus & Methods

3.1 Introduction

As stated in Chapter 1, the objective of this thesis was to study the interface formation process in Fusion™ casting, with special emphasis on determining the mechanistic processes at play. To study this process, an objective decision was made to focus on experimental methodologies.

A series of casting trials were performed using a lab-scale Fusion™ DC casting system, designed jointly by the University of Waterloo and Novelis [83]. The Fusion™ caster was installed at Novelis' Global Technology Centre in Kingston Ontario. The Fusion™ casting apparatus, methods and analysis of ingots are outlined in Section 3.2. AA3003-core/AA4045-clad ingots were cast in all cases. Effort was taken during these trials to track the motion of the oxides on the external surfaces of the core and clad sump. Additionally, the interfaces were examined using optical microscopy and mechanical testing. Furthermore, using an interrupted casting trial, an effort was made to preserve a portion of the core alloy surface which had been solidified against the chill bar, but not exposed to the clad liquid; as this is the closest one can get in obtaining a measure of the surface conditions that might exist at the core surface prior to contact with the clad liquid.

Additionally, a laboratory apparatus and test was developed to mimic the interface formation process occurring during Fusion™ casting. A series of these analog laboratory tests, in which AA3003 solid is dipped into molten AA4045 in a controlled manner, were conducted and the results were examined using optical and electron microscopy techniques. The apparatus is described in detail in Section 3.3. Tests focused on the effects of: reheating and remelting of

the AA3003 surface, the degree of surface oxidation present during initial contact of the two alloys, alloy composition, and atmospheric condition during test immersion. Additionally, various attempts were made to characterize surface oxides grown on AA3003, primarily using electron microscopy.

3.2 Laboratory scale Fusion™ caster

A lab-scale Fusion™ caster, whose detailed design is described by Ng [83], was used to conduct a series of test castings. The lab caster was installed at Novelis' Global Technology Centre in Kingston Ontario. A schematic of the caster is shown in Figure 3-1. The external casting mould is made of aluminum and is cooled by water running from the water manifold and into the mould. Mould cooling water exits the mould through small slits located at the bottom edge of the mould. These slits are evenly spaced along the entire circumference of the mould. During steady-state casting, water exiting the mould sprays onto the external surfaces of the ingot and drains into a casting pit (not shown in Figure 3-1). Water inlet temperature to the water manifold is not controlled, as water is supplied directly from unheated municipal water feeds. The mould is rectangular with dimensions 385 mm by 152 mm and with the corners of the mould rounded to a radius of 12.5 mm.

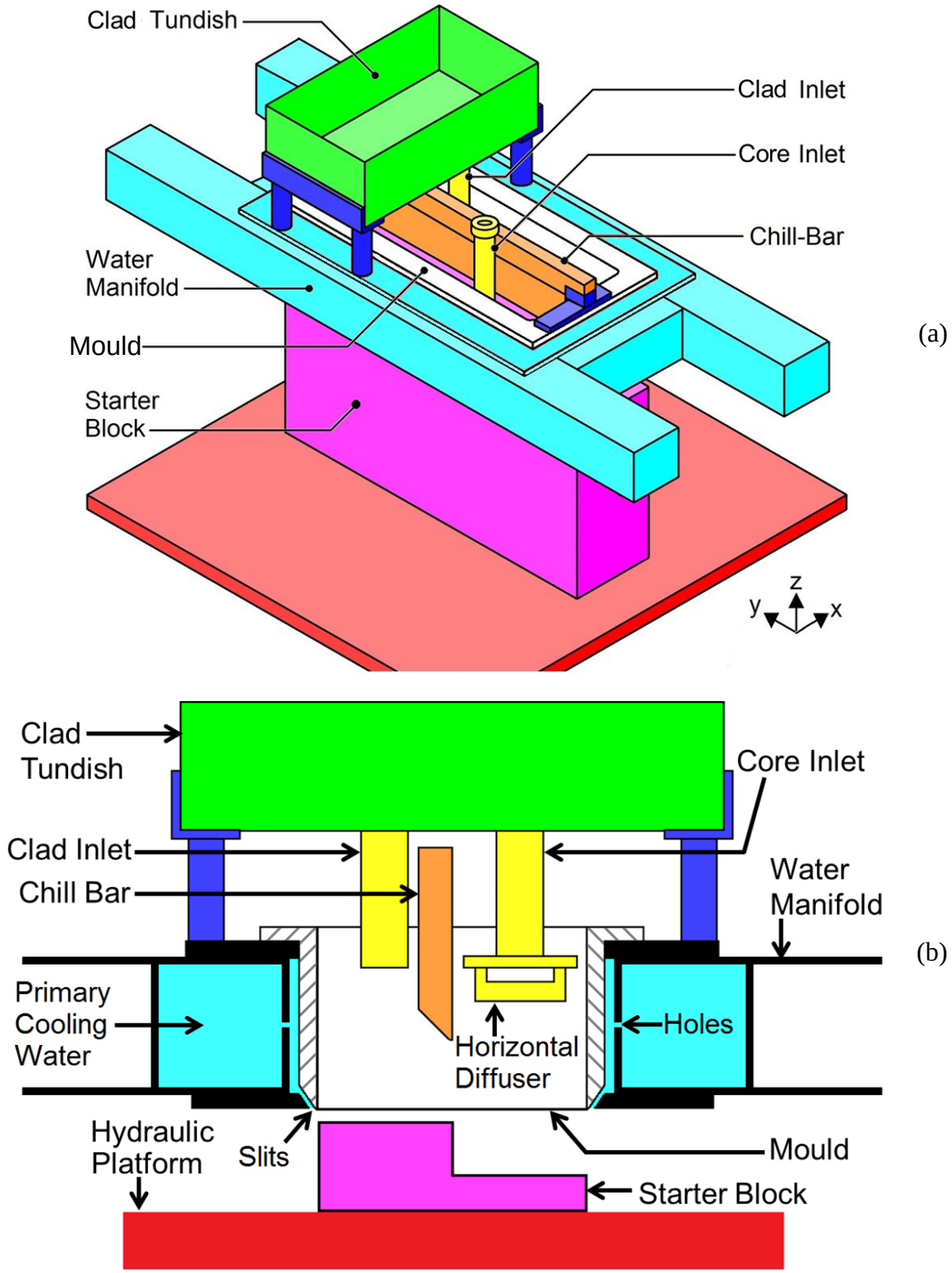

Figure 3-1 – (a) Schematic of the lab scale Fusion™ caster. Image courtesy of E. Caron [22]. (b) Cross section of the lab scale Fusion™ caster. Image courtesy of H. Ng [83].

The chill bar is the key to the Fusion™ casting process. It divides the external mould into two separate cavities, thereby allowing different alloys to be poured or cast into each cavity or section of the mould. The chill bar is fabricated from copper and is also water cooled. Two cooling circuits, drilled into the copper chill bar, are pumped with water. This water supply is independent of the supply used to feed the external casting mould. Additionally, the chill bar cooling water inlet temperature was controlled to be about 25 °C. Water loops into the chill bar and out of the chill bar with process piping and the exit stream is directed away from the casting ingot. Thus, with respect to the Fusion™ process, the chill bar water cooling is a closed loop. The chill bar is positioned in the external mould such that it divides the mould into two equal thicknesses. Hence, Fusion™ ingots cast with this laboratory caster are 50% core alloy and 50% clad alloy.

During a Fusion™ cast, core and clad liquid metals enter the mould via separate inlet tubes, shown in Figure 3-1. These tubes are made from a ceramic refractory material. An actual image of the Fusion™ casting system is shown in Figure 3-2. Liquid metal on the core side of the caster was fed directly from the holding furnace to the inlet tube via the AA3003 liquid metal transfer system (or launder) shown in Figure 3-2. The furnace in Figure 3-2 was tilted in a controlled manner during casting, thereby supplying hot metal to the transfer system and into the mould. As the furnace used to melt the clad alloy is not within close proximity to the Fusion™ casting system, the clad liquid metal was fed directly into the inlet tube via a liquid metal reservoir, called a tundish. The AA4045 clad tundish, shown in Figure 3-2, was kept full during Fusion™ by manually pouring liquid metal into the tundish from 20 kg large holding crucibles.

A refractory float and diffuser mechanism (see Figure 3-1b) was attached to the end of the core metal inlet tube to both: (i) re-direct the liquid metal flow into two horizontal streams that

run parallel to the chill-bar and (ii) as a means to control the AA3003 liquid metal level and flow rate into the core side of the casting. Due to space limitations in the clad side of the mould, no float mechanism was used at the end of the refractory AA4045 inlet tube. Instead, flow of molten AA4045 into the clad metal portion of the casting mould was performed manually, using a stopper to choke flow as necessary.

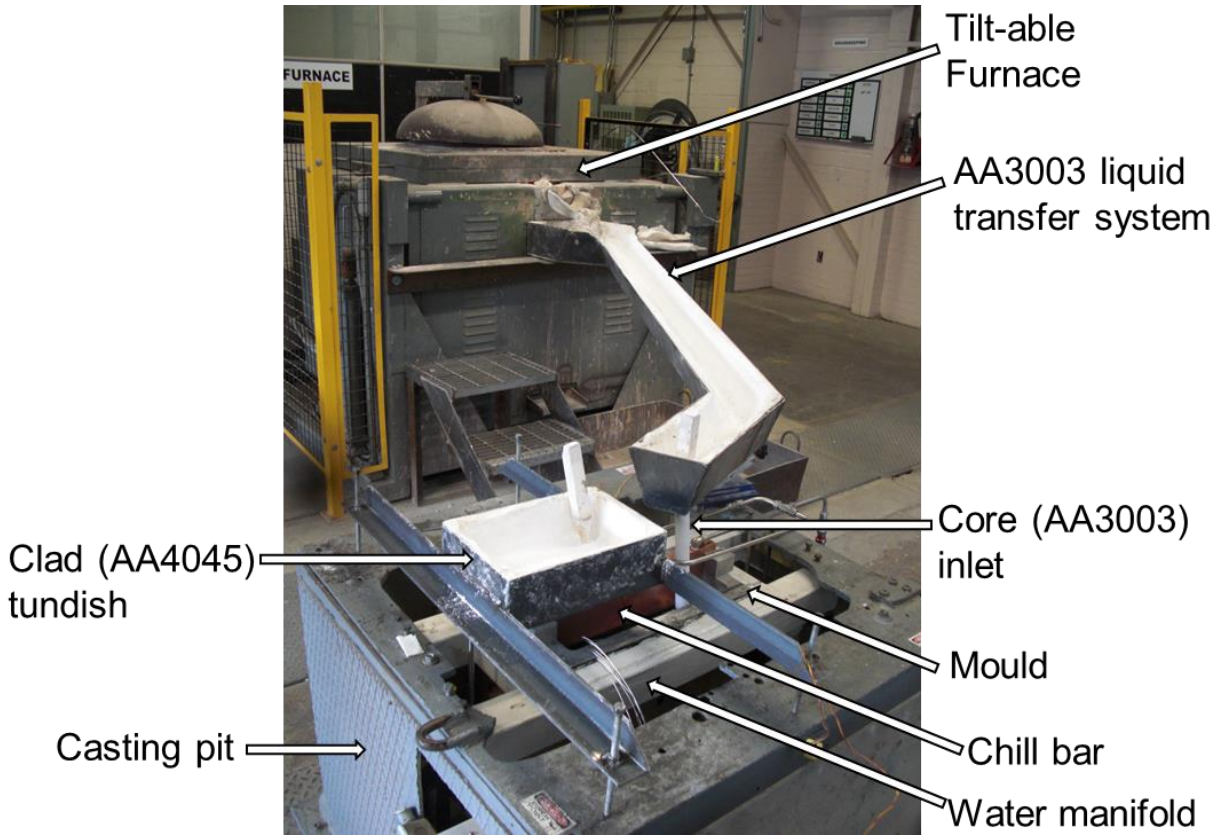

Figure 3-2 – Fusion™ caster as setup in Novelis' Global Technology Centre in Kingston Ontario. Image courtesy of S. Barker [84].

The starter block, shown in Figure 3-1, is a steel block mounted to a hydraulically controlled platform. The dimensions of the starter block are equal to the dimensions of the opening in the bottom of the external mould. Prior to the start of a casting the starting block is positioned inside the mould. During continuous casting, the hydraulic platform is lowered into the casting pit at the desired casting speed. The lowering rate of the hydraulic platform, or the

casting speed, is controllable. Typically, casting speeds are set in increments of 0.5 inch/min (0.21 mm/s) via a digital display and analog control system; however, the measured deviation in casting speed was 0.017 mm/s (5 second averaging) during actual casting trials.

3.2.1 Fusion™ casting trials

Using the casting machine described above, Fusion™ casting trials were conducted using AA3003 as the core alloy and AA4045 as the clad alloy. Initial trials, detailed in [85], focused on obtaining process data required for validation of a numerical CFD thermofluid model [22] of this lab-scale Fusion™ caster.

A general procedure that was used to cast Fusion™ ingots with this lab-scale casting machine is described as follows. Prior to casting, alloys to be cast were melted and held in separate holding furnaces. The AA3003 core alloy was melted in a large crucible inside the tiltable furnace shown in Figure 3-2, the AA4045 clad alloy was melted in a smaller holding furnace some distance away from the Fusion™ caster. Alloy compositions where measured from test coupons prior to casting using Glow Discharge Optical Emission Spectroscopy. The compositions were adjusted by adding alloying elements or pure Al until measured compositions were within acceptable specifications for the alloys to be cast. With respect to AA3003, Mn, Fe, and Si were the alloying elements which were actively controlled prior to casting. With respect to AA4045, Fe and Si were actively controlled. When both alloy melts were found to have acceptable melt compositions, the core alloy holding furnace was set to a value slightly higher than the specified pouring temperature for that particular casting trial. The clad alloy furnace was set to a temperature 50-100 °C in excess of the specified pouring temperature, to account for: (i) heat losses during manual transfer of the 20 kg pouring crucibles to the Fusion™ casting area and (ii) heat losses to ambient atmosphere (since the crucibles were un-insulated).

Before each casting trial, the starter block was positioned inside the mould, as shown in Figure 3-3. As the starter block dimensions match the dimensions of the opening of the casting mould, a small reservoir is formed on the core side of the casting mould that was essentially leak proof from the standpoint of the liquid metal. Additionally, prior to casting, both the water inlets to the mould (via the water manifold) and the chill bar were opened and the temperature and flow checked for adequacy. Typical water flow rates were 143.5 L/min per meter of wetted ingot perimeter in the mould and 100 L/min per meter of core metal in contact with the chill bar. Typical water temperatures were 15 °C for the mould and 27 °C for the chill bar.

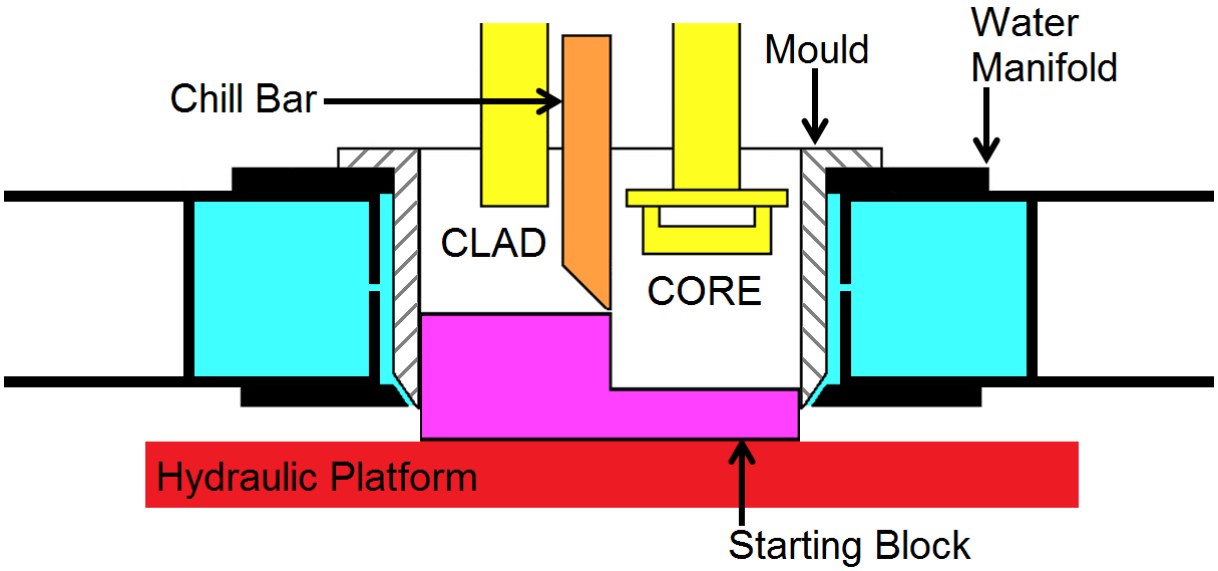

Figure 3-3 – Cross-sectional schematic showing position of starting block in the casting mould prior to start of a casting trial.

At the start of casting, with the platform in a stationary raised position, metal was poured into the core side of the mould by a technician through operation of the tilt furnace. Once the metal level in the core side of the mould reached a distance of 30 mm from the bottom of the chill bar, the flow was stopped momentarily. Over a duration of about 20 seconds, the liquid metal on the core side of the mould was allowed to partially solidify, creating a strong starting shell such that the hydraulic platform could be lowered safely without tearing of the shell and

potential liquid metal spillage into the casting pit. As lowering of the platform began, a second technician installed the float mechanism onto the end of the core liquid metal inlet tube and insured its proper functioning, while the technician operating the tilt-able furnace resumed pouring of the core alloy. In concert with this, a second set of technicians began manual pouring of the clad liquid alloy into the tundish, while one technician metered the flow manually using a stopper mechanism. The metal level on core alloy side was metered with the float to be 30 mm above the height of the bottom point of the chill bar. The metal level of the clad alloy was kept in-line with the bottom of the chill bar, using manual line-of-sight metering.

A schematic of the process during steady state is shown in Figure 3-4. Here, the various casting parameters which are controlled during steady-state Fusion™ casting have been listed: (i) metal level height on the core alloy side, 30 mm, (ii) metal level height on the clad alloy side, 60 mm from bottom of external casting mould, (iii) chill bar water flow rate, $Q_{\text{chill bar}}$, and inlet temperature, $T_{\text{chill bar}}$, (iv) mould water flow rate, Q_{mould}, and temperature, T_{mould}, (v) core alloy pouring temperature, T_{core}, (vi) clad alloy pouring temperature, T_{clad}, and (vii) casting speed, v. With the exception of the two metal levels within the mould, the casting parameters are all measured during each casting trial. The instrumentation and methods used to measure these parameters during casting have been documented in detail by Ortega Pelayo [85].

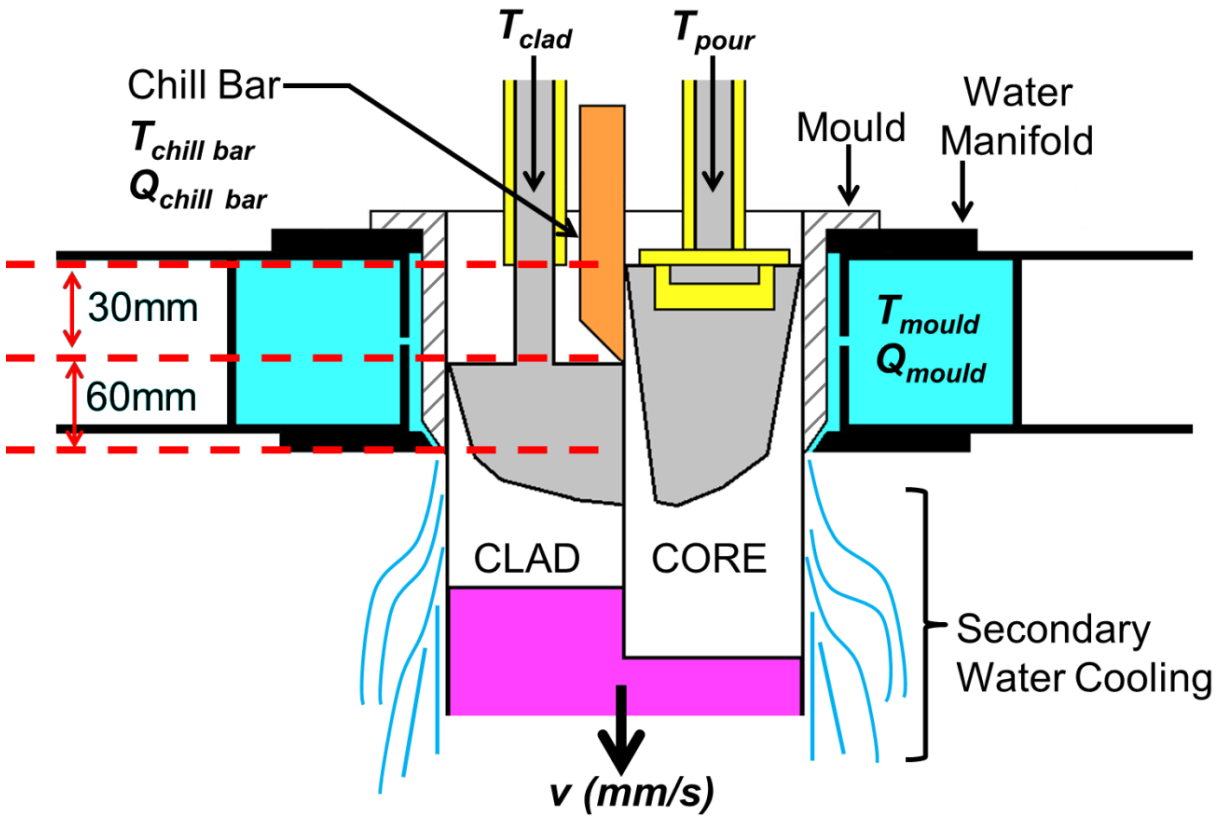

Figure 3-4 – Cross-sectional schematic showing steady state casting of Fusion™ ingot along with the parameters that are controlled during casting. Image from [85].

Using the apparatus and methodology described about, a series of three casting trials were conducted. The composition of the AA3003 and AA4045 alloys, measured prior to casting, are given in Table 3-1. The three casting trials were performed using one large AA3003 melt and one large AA4045 melt, thus the compositions listed in Table 3-1 are applicable to each of the three trials. Si and Fe content in the AA3003 alloy were within specifications listed in Section 2.4.1, and were likely due to the impurities present in the grade of aluminum used to make up the AA3003 melt. It should be noted that although some Ti impurity was present in the AA3003 and AA4045 alloys, it was not purposely added to the melt. Similarly, the Cu impurity in the AA3003 melt was not intentionally added. The Fe content in the AA4045 was likely present due to impurities in the grade of aluminum used to make up the melt as well as in the Si fines used to prepare the AA4045 melt.

Table 3-1 – Measured AA3003 core and AA4045 clad alloy compositions used for the Fusion™ casting trials.

	Al	***Si***	***Fe***	***Mn***	***Ti***	***Cu***	***Mg***	***Ca***
AA3003	Bal.	0.203	0.581	1.036	0.0163	0.0751	0.001	-
AA4045	Bal.	9.943	0.158	0.022	0.0010	0.001	0.0003	0.0010

The casting conditions for the three casting trials are listed in Table 3-2. As shown, the process parameters for the three trials were very similar. Casting trial 2-3 had a slightly higher casting speed of 1.23 mm/s vs. 1.12 mm/s and the measured AA3003 inlet temperature was also slightly higher. As the primary purpose of the casting trials was to measure motion of surface oxides, the processing parameters were intentionally not varied from values which were shown to work in previous Fusion™ casting trials [85].

Table 3-2 – Process conditions used during the Fusion™ casting trials of 3003/AA4045 ingots.

ID #	***Pouring Temperature***		***Water Temperature***		***Casting Speed***	***Casting Trial Objective***
	AA4045	***AA3003***	***Mold***	***Chill Bar***		
	K (°C)	***K (°C)***	***K(°C)***	***K (°C)***	***mm/s***	
2-1	923-933 (650-660)	963-973 (690-700)	283-293 (10-20)	298 (25)	1.12	measure oxide motion on clad sump; "interrupted" casting trial
2-2	913-933 (640-660)	963-973 (690-700)	283-293 (10-20)	298 (25)	1.12	measure oxide motion on core sump; melt poisoning for CFD model validation [22]
2-3	923-933 (650-660)	973-983 (690-710)	283-293 (10-20)	298 (25)	1.23	

Additionally, during the final phase of casting trial 2-1, the clad metal inlet flow was intentionally stopped while continuing the casting process. Labelled an "interrupted casting", the intent was to preserve a section of AA3003 material cast against the chill bar, to study the surface structure of AA3003 material that would have come into contact with liquid AA4045 metal. More details regarding the procedure used to do this are given in Section 3.2.1.2.

It is worth noting that the metal pouring temperatures are given as a range and not a discrete value in Table 3-2. A sample of the measured core and clad pouring temperatures from casting trial 2-1 is given in Figure 3-5. As shown, the process data shows some variability. This may be attributed in part to: (i) the position of the thermocouple in the core metal launder and clad metal tundish, (ii) transients associated with pouring core alloy metal from the tilt furnace and pouring clad alloy metal manually into the clad tundish.

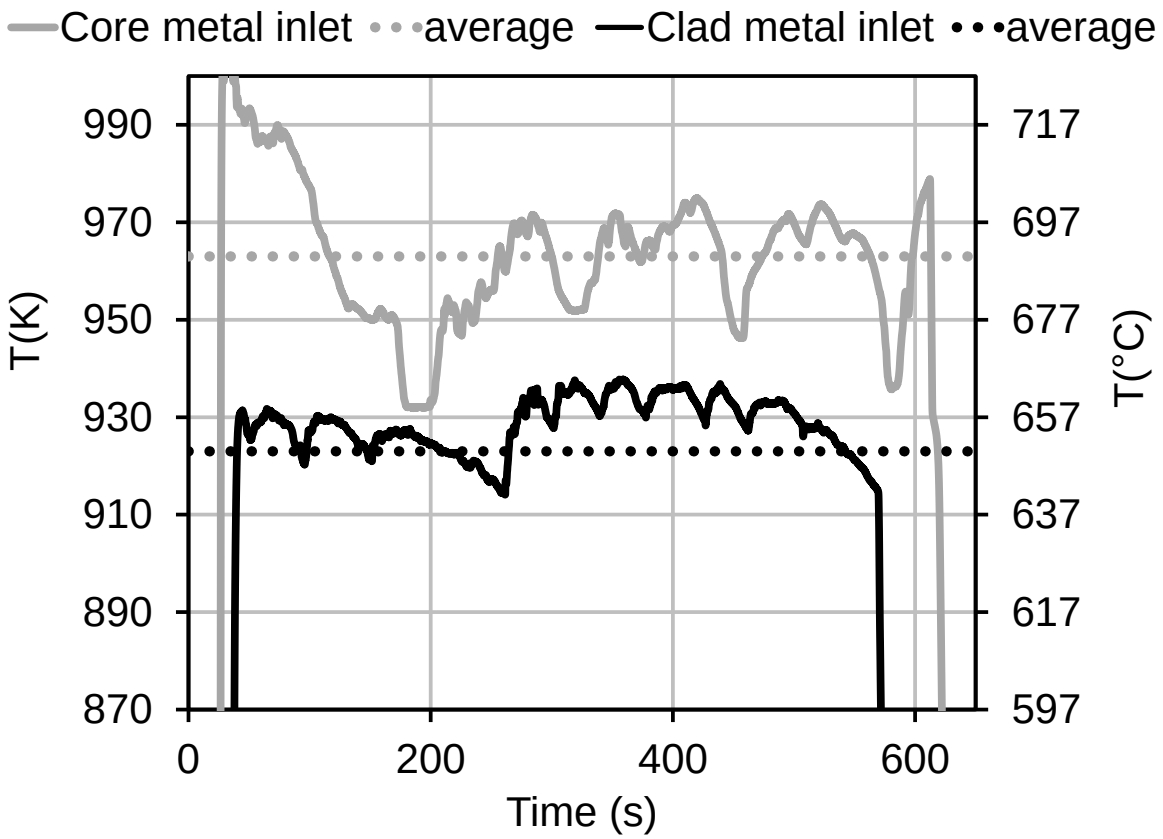

Figure 3-5 – Pouring temperature in core and clad molten metal inlets measured during casting trial 2-1.

Additionally, ingots from casting trials detailed in [85] were also examined within this thesis project. The process parameters for these casting trials are summarized in Table 3-3. The objective of these series of casting trials was to obtain data for CFD model validation. Compared to the casting process parameters in Table 3-2, the pouring temperature of the

AA4045 clad liquid metal was lower by about 20-30 °C. The water temperatures and flow rates in the mould and chill bar were consistent with the process parameters in Table 3-2. The casting speed of trials 1-1 and 1-3 were slightly higher than all the casting speeds of the trials in Table 3-2, despite using the same predefined casting speed set point on the casting machine, i.e., a casting speed of 3" per minute on the casting machine hydraulic controls. The casting speed of trial 1-2 was set as 3.5" per minute using the casting speed hydraulic controls, as such, the measured casting speed is noticeably higher for this test, 1.48 mm/s.

Table 3-3 – Process conditions used during the Fusion™ casting trials of 3003/AA4045 ingots, in Reference [85].

ID #	***Pouring Temperature***		***Water Temperature***		***Casting Speed***
	AA4045	***AA3003***	***Mold***	***Chill Bar***	
	K (°C)	***K (°C)***	***K(°C)***	***K (°C)***	***mm/s***
1-1	898 (625)	978 (705)	283-293 (10-20)	298 (25)	1.27
1-2	898 (625)	978 (705)	283-293 (10-20)	298 (25)	1.48
1-3	898 (625)	978 (705)	283-293 (10-20)	298 (25)	1.27

3.2.1.1 Oxide motion measurements

To aid in visualizing the motion of the oxide film on the top surface of the sump, exploratory tests were conducted using molten aluminum. Since the surface of the sump is extremely reflective and hard to focus on with a video camera, an inert marking dye was found which could provide a means for good focusing on the oxide surface and tracking of the motion of the oxide film. As a result of these exploratory tests, two methods were found to be satisfactory: (i) dry cobalt-silicate (Co_2O_4Si) powder (Kremer Pigments: Smalt, standard grind, No. 10000) directly placed onto the oxide surface with a shaker and (ii) a slurry-solution of ethylene glycol and cobalt-silicate powder (1:1 ratio by weight) dropped onto the surface of the oxide with an eye

dropper. While the slurry-solution worked well, it was decided to use method (i) in the end to ensure safety during casting.

To record the oxide motion, a HD video camera was set at a working distance of 1.4 m from the top of the casting sump, using an overhead camera boom. Before each test, a calibration grid was set at a working distance of 1.4 m and test video was taken of the grid, to be used for calibration afterwards. The motion of the oxide film on the clad side of the casting was imaged during casting trial number 2-1, while that of the core side was imaged during trials 2-2 and 2-3. The camera setup with respect to the Fusion™ caster and respective fields of view taken during each trial is shown in Figure 3-6.

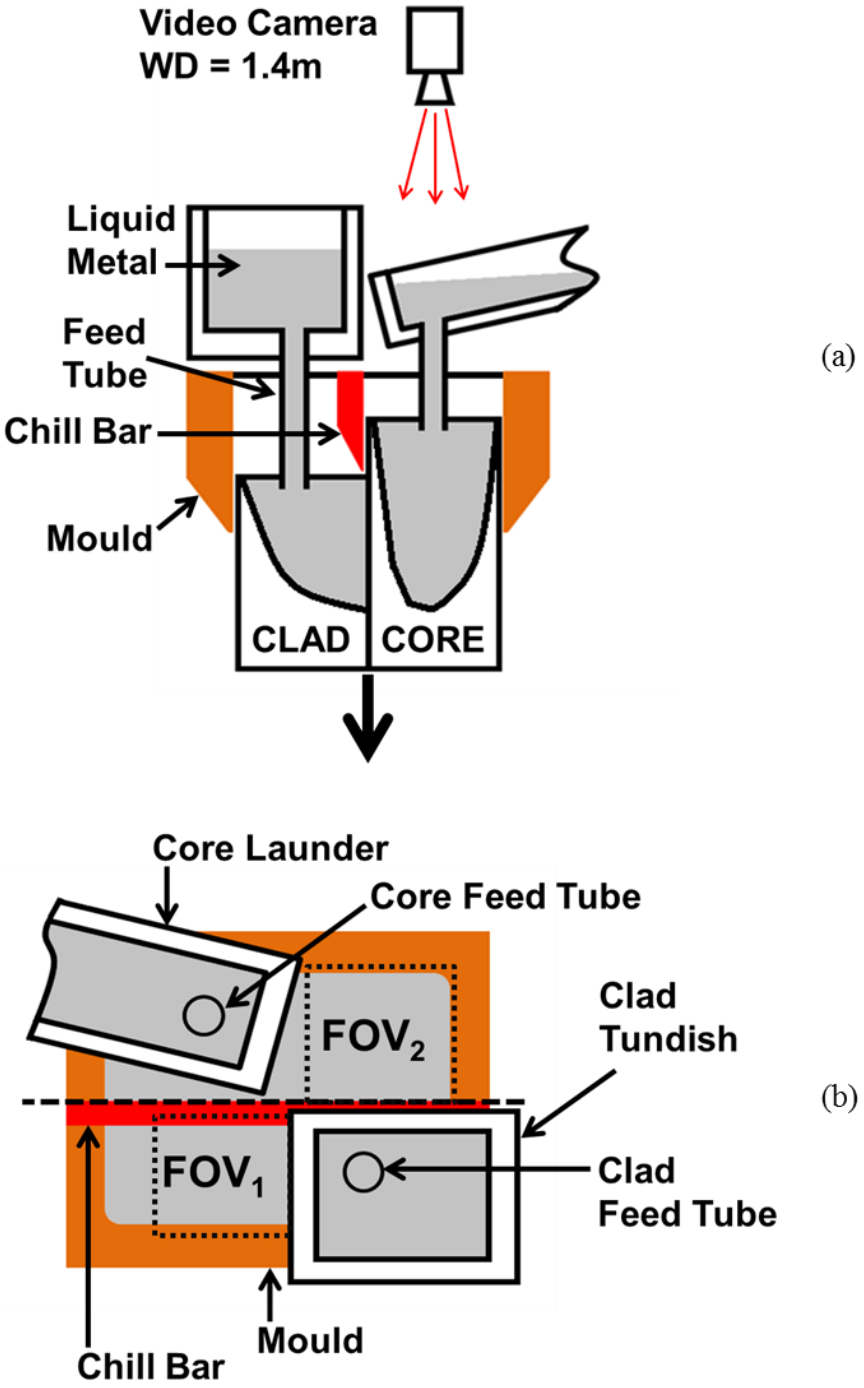

Figure 3-6 – (a) Side view of casting mold and showing camera orientation, working distance ~1.4m from ingot sump, and (b) top view of casting mould showing field of view (1 and 2) captured during casting trials.

3.2.1.2 Interrupted casting trial

In an attempt to preserve the surface of AA3003 which casts against the chill bar of the Fusion™ caster, the casting procedure during shutdown of casting number 2-1 was modified, as shown in Figure 3-7. For this cast, the liquid AA4045 stream was stopped approximately 30 seconds before the casting was stopped. This 'interrupted cast' produced an ingot in which the AA3003 at the top of the ingot was cast against the chill bar but not subsequently put into contact with molten AA4045. This provided some material that could be analyzed to give some indication of the core alloy surface microstructure just prior to immersion into the molten clad alloy.

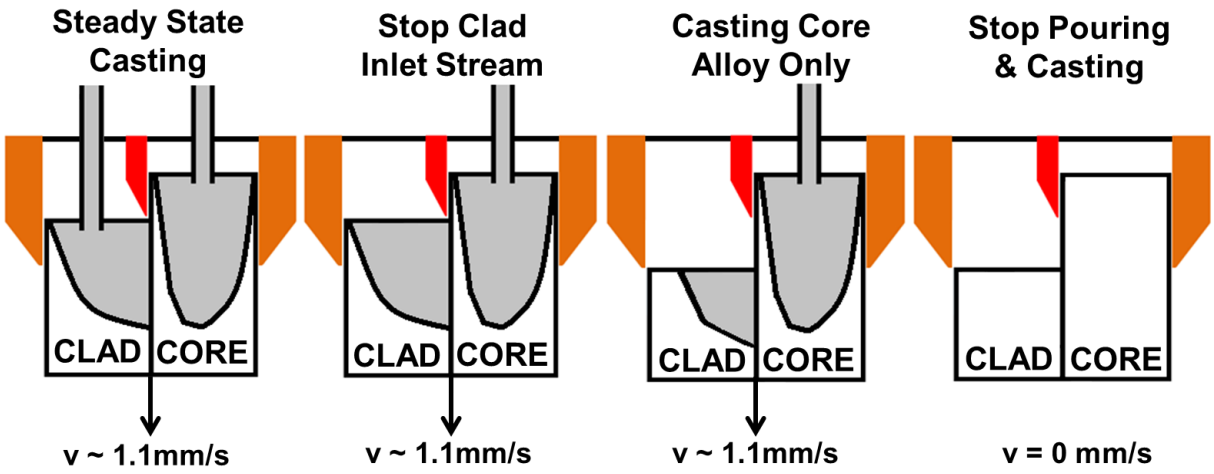

Figure 3-7 – Illustration of the procedure used at the end of casting to preserve AA3003 material cast against chill bar for casting trial 2-1 in Table 3-2.

The final dimensions of the top of the ingot are depicted schematically in Figure 3-8. The total length of the ingot above the top surface of the clad metal portion of the ingot was 68 mm in length. That 68 mm length of ingot could be visually divided into four regions. Starting with the 3 mm length of ingot closest to the clad metal surface, this region was flat in appearance. A 25 mm length above this area, which was exposed to air during casting, was noticeably blistered on its external surface. A 36 mm length above this blistered region was again noticeable flat.

The final 4 mm length of ingot was rounded, and most likely not in contact with the mould during casting.

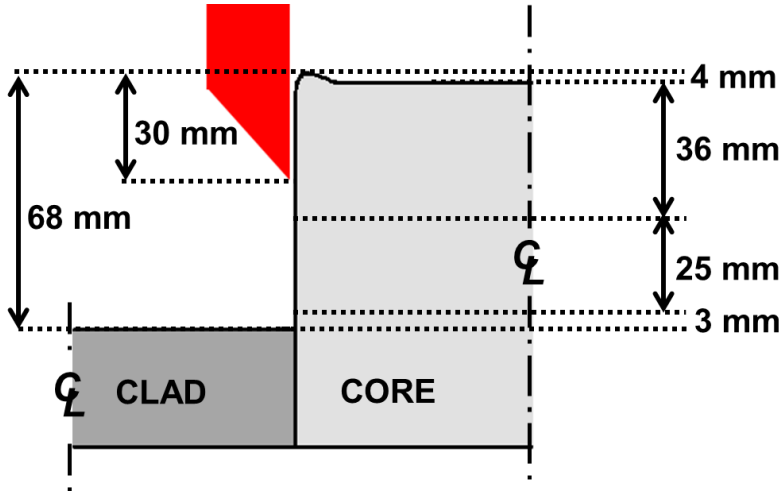

Figure 3-8 – Schematic (side view) of final dimensions from the top portion of the 'interrupted' Fusion™ cast ingot, for casting trial 2-1 in Table 3-2.

3.2.2 Analysis of Fusion™ cast ingots

3.2.2.1 Chill surface structure: differential scanning calorimetry

Differential scanning calorimetry (DSC) was performed to examine differences between the surface-cast and bulk-cast AA3003 structure obtained from samples taken from casting trial 2-1. Using a wafering saw, thin ribbons of AA3003 material were carefully cut from the chill-bar cast surface (taken from the 'interrupted cast'). The thickness of each ribbon was measured using a micrometer, and only ribbons less than 150 μm in thickness were used for DSC testing. Samples were cleaned and degreased with alcohol. The ribbons were folded over and pressed flat such that they would fit into the DSC crucible. Samples were also cut from the central portion of the AA3003 portion of the Fusion™ ingot, to represent bulk-cast material. These samples were also cleaned/degreased and pressed flat before testing to prevent poor contact between the sample and the DSC crucible. Additionally, samples taken from a DC cast AA3003 ingot were also prepared

and tested in a similar fashion. Re-heating tests were performed on a TA Instruments DSC (SDTQ600). All samples were 3 to 5 mg in weight, as per suggestions in [86] to obtain maximum signal resolution. Samples were tested at heating rates of 0.017-0.83 K/s. Samples were heated to 973 K (700 °C) to insure the entire melting curve was obtained. Test results were calibrated against pure aluminum and pure zinc samples.

The DSC tests which were conducted are outlined in Table 3-4. Here, the five samples measured came from Fusion™ cast ingot 2-1, see Table 3-2. For comparison purposes, samples from DC cast AA3003 bulk material were also tested. These correspond to the last four rows in Table 3-4. The value *n* in Table 3-4 (and subsequent tables) represents the number of times each test condition was repeated.

Table 3-4 – AA3003 DSC sample and test information. *n* indicates the number of tests performed

Ingot Casting Method	***Ingot Composition***			***DSC sample location***	***Heating Rate (°/s)***	***n***
	Mn (wt%)	***Fe (wt%)***	***Si (wt%)***			
Fusion	1.036	0.581	0.203	bulk	0.017	5
Fusion	1.036	0.581	0.203	bulk	0.33	2
Fusion	1.036	0.581	0.203	bulk	0.83	1
Fusion	1.036	0.581	0.203	chill bar surface	0.017	5
Fusion	1.036	0.581	0.203	chill bar surface	0.33	1
Fusion	1.036	0.581	0.203	chill bar surface	0.83	1
DC cast	1.1750	0.7036	0.2279	bulk	0.017	6
DC cast	1.1750	0.7036	0.2279	bulk	0.33	2
DC cast	1.1750	0.7036	0.2279	bulk	0.83	1

3.2.2.2 Mechanical testing of the as-cast core/clad interfacial strength

Tensile tests were performed to determine the quality of the as-cast AA3003/AA4045 interface. Cylindrical tensile test coupons were dimensioned and machined as per ASTM B557-10 [87-88]. The tensile axis of the samples was perpendicular to the AA3003/AA4045 interface, with the interface located near the center of the gauge length of each

sample. The tensile test samples had gauge length of 63.5 mm (2.5"), shoulder radius of 12.7 mm (0.5"), and grip length of 34.9 mm (1.375"). The sample diameter along the gauge length was 9 mm.

Using the steady-state portion of the Fusion™ ingot cast during trial 2-1, the tensile test samples were taken from 3 different section-planes within the ingot. The section planes ran parallel to the casting direction and were taken from: (i) the ingot centerline, (ii) 60 mm from the ingot centerline (consistent with the plane at which the clad inlet feed was located), and (iii) 18 mm from the edge of the ingot nearest the core inlet feed, see Figure 3-9a. To get an indication of the mechanical properties of the individual cast alloys, samples were taken from each of the respective metals, parallel to the casting direction and at the centre of each individual alloy section width, see Figure 3-9b. Two specimens were taken for each alloy, adjacent to the three sections which were tested: (i) the ingot centerline, (ii) 60 mm from the ingot centerline, and (iii) 18 mm from the edge of the ingot; for a total of six baseline specimens per alloy.

Tensile testing was done using an Instron model 4206 tensile test machine, with a crosshead speed of 4 mm/min. Sample yield stress, sample ultimate tensile stress (UTS), and sample strain at UTS were measured. Fracture surfaces were examined using a SEM (Hitachi S-3000N SEM and Zeiss Leo 1530 FESEM).

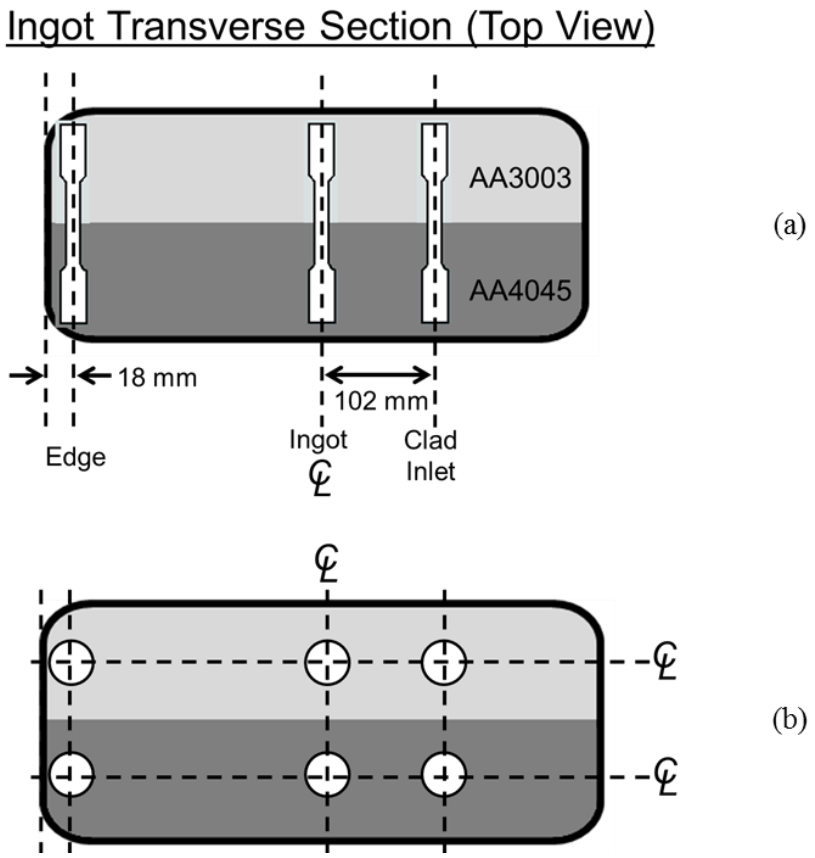

Figure 3-9 – Schematic (section of ingot looking down from the top) indicating the mechanical test sample positions from (a) as-cast interface samples, loading axis parallel to interface. (b) Base metal samples, loading axis perpendicular to the interface.

3.2.2.3 Metallographic analysis of the Fusion™ cast ingots

In addition to mechanical tests, longitudinal and transverse sections of the Fusion™ ingot from casting trial 1-3 (see Table 3-3) and 2-1 were macro-etched to ascertain the quality of the as-cast interface on a macroscopic scale. Macro-etching was performed using a 10 wt% NaOH solution, until sufficient contrast between AA4045 and AA3003 was obtained in final sections.

Optical microscopy and scanning electron miscopy were performed on samples taken from the 'interrupted casting', casting trial 2-1. AA3003 samples were imaged with a Phillips FE-SEM (XL30S FEG), equipped with an Oxford EDS detector (XMAX 80 mm^2 detector size). To determine the relative oxide thickness of the samples, the ratio of O-to-Al EDS peak intensity

were measured (to be discussed in more detail in Section 3.4.2). A field size of 1.8 mm by 1.8 mm was used to assess the trend in oxide layer thickness. AA3003 surface samples from the 'interrupted casting' trial were also examined macroscopically and with SEM. Scanning electron microscopy was also performed on selected fracture surfaces obtained from the mechanical tests performed on the as-cast interfaces (described in Section 3.1.4).

3.2.2.4 Thermofluid CFD model of the Fusion™ casting trials

Using a thermofluid CFD model developed by Baserinia *et al.* [21-22] as a separate project with Novelis, simulations were performed to determine the steady-state conditions for the Fusion™ casting trials 2-1, 2-2, and 2-3 in Table 3-2. The results of these simulations form a first approximation of the expected thermal history at the core/clad interface during Fusion™ casting; they are of importance when comparing final interface quality at different locations along the width of the ingot and were also used for the design of testing parameters for laboratory tests performed in Chapter 5 and 6.

The thermofluids CFD model is an Eulerian steady-state thermofluid model. It is based upon a model developed by Bennon and Incropera [89] which was used to calculate liquid-solid phase change for a variety of operations, including metal casting applications. The model solves the coupled mass, momentum, and energy equations for a 3-dimensional domain. The model was developed using ANSYS-CFX software, which used a hybrid finite-volume/finite-element approach to solving the conservation equations of mass, momentum and energy [21-22]. The full details regarding the material properties data, boundary conditions, and validation studies can be found in [21-22]. The basic details of the model are discussed below.

The geometry of the solid model in CFX is shown in Figure 3-10a. The solid model consists of two domains, AA3003 core and AA44045 clad. The solid model includes the inlet

streams for both the AA3003 core and AA4045 clad alloys. The inlet stream for the AA4045 domain is a cylindrical shaped inlet, which matches the dimensions of the inlet tube used in the Fusion™ casting experiments at Novelis, and is depicted schematically in Figure 3-1. To model the rectangular-shaped horizontal diffuser used on the AA3003 core inlet during the Fusion™ casting experiments (Figure 3-1), a cylindrical shaped inlet was included in the solid model and a rectangular-shaped horizontal diffuser section was omitted from the geometry of the AA3003 solid model, accounting for the geometry of the diffuser. Additionally, the AA3003 core and AA4045 clad domains were divided by an interface. Heat transport across the interface is accounted for in the thermofluid model; however, mass transport across the interface is restricted. The final mesh used for the thermofluid model calculations is shown in Figure 3-10b, with the domains (AA3003 and AA4045) and interface labelled.

A non-uniform mesh was used to discretize the solid model. It was composed of 911,000 tetrahydron elements and 223,000 prism elements. Prism elements were used near all external surfaces and in the vicinity of the AA3003/AA4045 interface. An element size of ~2.5 mm was used in these near surface and interface regions as well as the top portion of the model, for improved numerical accuracy and to be able to resolve surface-normal temperature gradients. The mesh density in the bottom portion of the ingot was larger than this. A comprehensive description of: (i) the thermofluid model, (ii) thermophysical properties of the AA3003 and AA4045 alloys, (iii) boundary conditions, and (iv) grid independence studies and model verification/validation may be found in References [21-22].

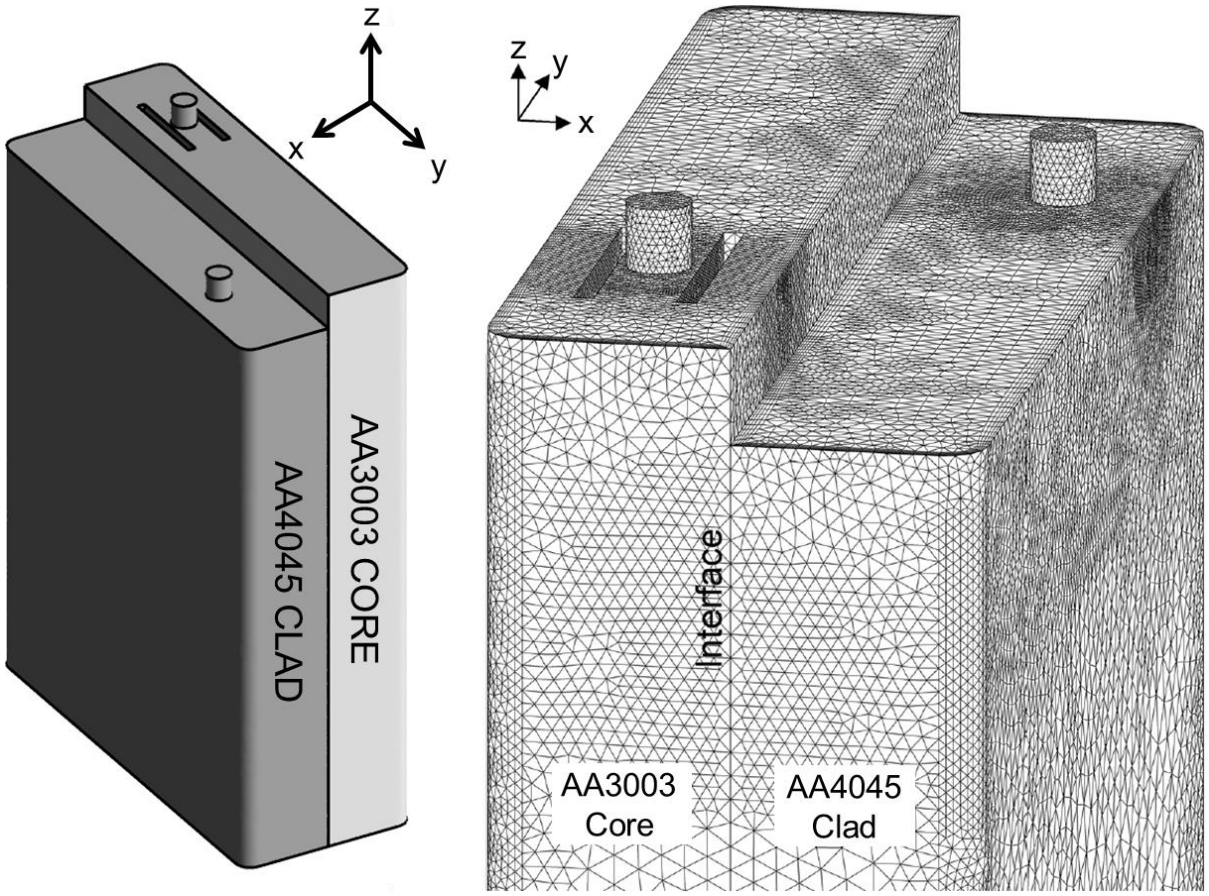

(a) (b)

Figure 3-10 – (a) Solid model and (b) mesh for the thermofluid model of the laboratory scale Fusion™ caster [22] installed at Novelis' Global Technology Centre in Kingston Ontario. Image taken from Caron *et al*. [22].

Some of the major assumptions of the model and boundary conditions with respect to fluid and material flow were: (i) the fluid-flow is considered to be in the laminar flow regime, (iii) for each material domain, a temperature (or fraction solid) dependent source term was used in the momentum equation to effectively drive the fluid to behave as a solid mass as its temperature dropped below its respective solidus temperature, (iii) free slip boundary conditions are prescribed for all external surfaces of the ingot, (iv) the boundary condition for the bottom of the ingot is model as an outflow boundary, and the velocity prescribed here is set to be equal to the measured casting speed, and (iv) the top surface of the AA3003 and AA4045 inlet tubes are

modelled as inflow boundaries, and a static pressure of zero is set as the boundary condition on this surface.

The heat transfer boundary conditions are as follows. The top surfaces of the ingot, as well as the surfaces of the inlet flow tubes are modelled as insulating boundary conditions. Prescribed heat transfer coefficients are used on the remainder of the surfaces of the model. For the secondary cooling portion of the model, boiling water heat transfer correlations, developed by Weckman and Niessen [90] were used. For the primary cooling region (the portion of the model where the mould is in contact with the ingot surfaces), calculations were performed to determine an effective heat transfer coefficient between the external surface of the ingot and the water cooled mould.

To model the solidification of each alloy respectively, the latent heat of fusion is introduced in the energy equation by implementing an effective specific heat capacity. Numerically, the effective heat capacity is described in a manner such that when the effective heat capacity is integrated over the solidification range of the respective alloy, the latent heat of fusion is recovered.

A list of the process parameters used as input to the model is given in Table 3-5. In model runs 1, 2 and 3, the clad inlet temperature was varied systematically, to cover the bounds measured during casting trial 2-1 and 2-2, see Figure 3-5. The core inlet temperature was kept constant, as it was shown to have minimal sensitivity to results. In run 4, the casting speed was increased to simulate the conditions of trial 2-3.

Table 3-5 – List of conditions used for thermofluid simulations using the CFD model of Fusion™ casting described in [21-22].

Run	***Core Inlet Temperature (K (°C))***	***Clad Inlet Temperature (K (°C))***	***Casting Speed (mm/s)***	***Mould Water Temperature (K (°C))***	***Chill Bar Water Temperature (K (°C))***	***Notes***
1	963 (690)	913 (640)	1.12	288 (15)	300 (27)	Trial 2-1, 2-2
2	963 (690)	923 (650)	1.12	288 (15)	300 (27)	Trial 2-1, 2-2
3	963 (690)	933 (660)	1.12	288 (15)	300 (27)	Trial 2-1, 2-2
4	963 (690)	923 (650)	1.23	288 (15)	300 (27)	Trial 2-3

3.3 Interface formation laboratory analog test: apparatus

Direct observation of wetting and interface formation in the Fusion™ casting process is difficult to obtain in practice, due to temperature, proximity, cost, and safety issues. As such, an analog test was designed and built which would mimic the wetting and interface formation that was expected to occur in Fusion™ casting on the laboratory scale while providing a means to control parameters relevant to interface formation: core alloy temperature, clad alloy temperature, ambient atmosphere at point of contact between core alloy shell and clad liquid, time of contact between core shell and clad liquid, casting speed, and core alloy surface oxidation prior to contact with clad alloy liquid. The interface formation test is relatively straightforward. In the test apparatus, cylindrical specimens are preheated to a desired temperature and then immersed into an aluminum melt at a predefined speed, to a desired depth, and for a pre-determined length of time. They are then withdrawn from the melt at a quick speed and cooled back to room temperature; thus, creating an interface between the specimen and the melt. The test objectives were to:

i. Determine which variables (of those listed above) have the greatest influence on the interface formation process.

ii. Determine if remelting of the core alloy surface (or test sample) is a necessary requirement for interface formation.

iii. Generate test samples which could be analyzed, microscopic or otherwise, for the purpose of determining most plausible interface formation mechanisms.

As shown in Figure 3-11, the analog apparatus consists of the following major assemblies: (i) a two-zone tube furnace, (ii) a stainless steel vessel, (iii) a sample positioning system, (iv) a sample cooling system, and (v) an ambient gas control system.

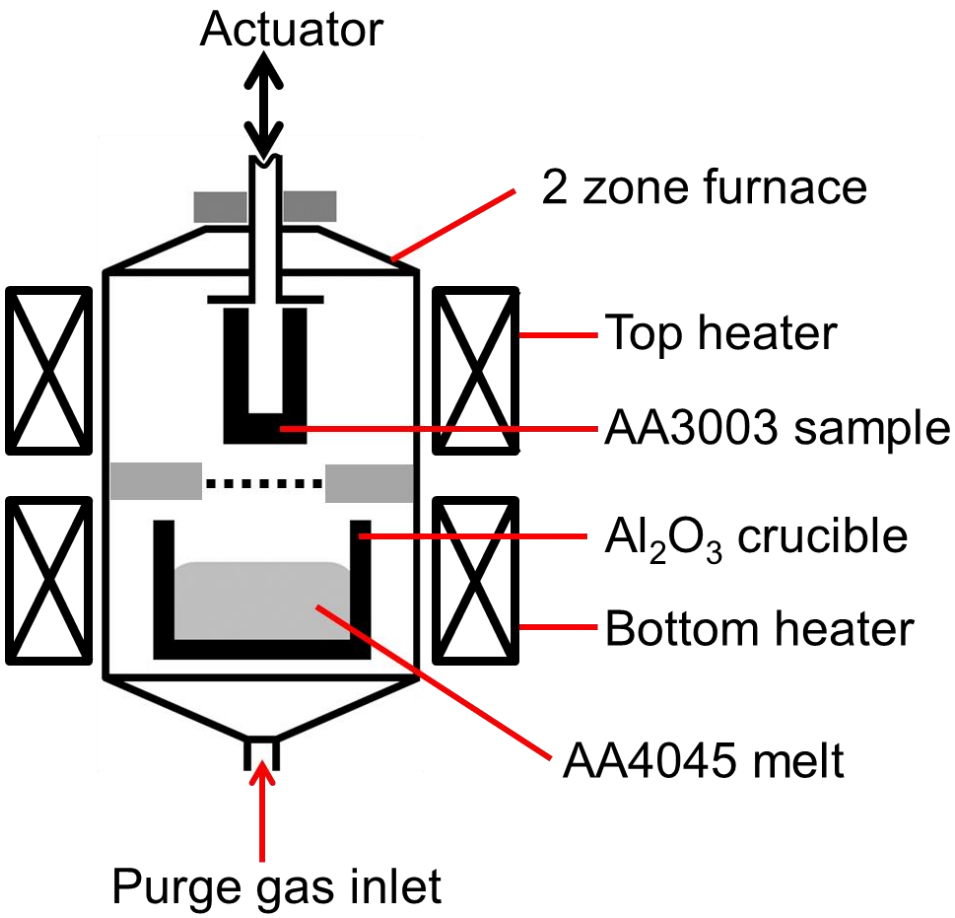

Figure 3-11 – Schematic of the analog test apparatus.

The furnace is composed of a stainless steel assembly, lined with insulating material and four semi-cylindrical heater elements (CRWS-68/240 from Omega), two heating elements for the

top zone and two for the bottom zone. The internal dimensions of the heating elements were 203.2 mm (8 in) ID and 152.4 mm (6 in) length. A stainless steel tube, sealed at the bottom end with a conical shaped flange, sits inside the furnace opening. The internal dimensions of the stainless steel vessel were 190.5 mm (7.5 in) ID and 419.1 mm (16 in) in length. Stainless steel was used as the vessel material, as opposed to glass or ceramic which is typically used in commercial tube furnaces, for durability purposes. Power output to the heating elements were controlled using two commercially available temperature/process controllers (CN7200 from OMEGA). The top heating elements were independently controllable from the bottom heating elements. Thermocouples placed in the vertical centre of each zone, 25 mm away from the internal surface of the stainless steel tube were used as control sensors to the OMEGA power controllers, with one placed in each temperature zone. Furthermore, a 32 mm thick ceramic plate was placed in between the top and bottom zones to improve the independence in temperature between the top and bottom zones of the furnace. A circular opening in the plate was necessary. As per the specification of the heating elements, the maximum achievable temperature was stated as 982 °C; however, the maximum attempted during furnace commissioning was 700-710 °C. This was much greater than the requirements for interface formation testing, 600-660 °C.

The sample positioning system was comprised of: (i) a sample holder, (ii) a DC powered linear actuator (FA-150 from Firgelli Automation), (iii) a 12 VDC power supply, and (iv) a Labview™ program [91] to control output to the DC power supply. The DC powered linear actuator had an 457.2 mm (18 in) stroke length, and a speed output of 12.7 mm/s (0.5 in/s) when 12 VDC power was applied to the actuator. Actuator speed was controlled by sending a square DC pulse wave to the DC power supply. Motion at this low speed was smooth as the frequency of the DC pulse was relatively high. To track the position of the actuator, and hence

sample position relative to the melt, a displacement transducer (LP801-450 from OMEGA) was coupled to the linear actuator.

A simple gas purge system was designed to provide covering gas inside the stainless steel vessel. Compressed argon gas (Industrial Argon, 99.995% from Praxair), was metered with a combination gas flow meter/needle valve and introduced to the bottom of the stainless steel vessel, see Figure 3-11. Typical flow rates of argon into the furnace during testing were 0.226 m^3h^{-1} (8 scfh).

Data recording during testing was done using a multifunction I/O data acquisition board (NI USB-6212 from National Instruments) and a custom Labview™ software program. Sample temperature and position were recorded during testing. All samples had holes milled into them for placement of thermocouples. Grounded, stainless steel sheathed, K-type thermocouples, with OD of 1.6 mm (from OMEGA) were used for all temperature measurements.

The following actions were performed prior to any testing with the interface formation test apparatus: (i) verification of the adequacy of the gas purging system, (ii) thermocouple calibration at high temperature, and (iii) linear transducer calibration. The details of these tests are given in Appendix A. The various tests that were performed, using the apparatus described above, will now be described in detail.

3.3.1 Interface formation testing

As the first step to fulfilling the test objectives outlined in Section 3.3, a series of interface formation tests were conducted. The initial variables which were thought to be of primary importance for evaluation were: core alloy and clad melt temperature, sample surface oxidation, and ambient atmosphere. These initial tests, described below were done using AA3003 as the sample (core) material and AA4045 as the melt (clad) material.

3.3.1.1 Effect of sample surface oxidation, ambient atmosphere, and remelting

Sample Geometry and preparation

AA3003 samples were machined from the central portion of a DC Cast 3003 ingot, to avoid inhomogeneity associated with chill zone and segregated layers found on external surfaces of DC cast ingots. AA4045 material was also taken from the central portion of a DC-cast ingot supplied by Novelis. The compositions of the AA3003 (Id # 1) and AA4045 (Id # 2) material used for analog testing are given in Table 3-6. The compositions of the two ingots provided by Novelis were measured from melt samples using Glow Discharge Optical Spectroscopy prior to casting of each individual ingot.

Table 3-6 – Measured AA3003 sample and AA4045 melt alloy compositions used for interface formation testing (wt% unless specified).

Id #	***Alloy***	***Si***	***Fe***	***Mn***	***Ti***	***Cu***	***Mg***	***Ca***
1	***AA3003***	0.2279	0.7036	1.1750	0.0160	0.0840	0.0051	-
2	***AA4045***	9.9300	0.2300	-	0.0200	-	0.0006	0.0010

The AA3003 samples were ground to a surface finish of 600 grit (on a lathe). Samples were cylindrical, 50.8 mm height and 38.5 mm OD. A macro photo of a machined AA3003 sample is shown in Figure 3-12. The central portion of the sample was hollow with a 7.4 mm ID, so that gas cooling of the sample could be done from the centre outwards. Holes for thermocouples were also placed parallel to the height of the sample, at a depth of 1.0 mm and 2.8 mm from the outer surface of the sample, and at a height of 15 mm from the bottom of the sample. Thermocouple data was used to control testing and also a priori for AA3003 oxide growth calculations.

Figure 3-12 – Macro photo of a prepared AA3003 sample prior to immersion testing.

Prior to testing, machined samples were cleaned in alcohol, etched in 5 wt% NaOH solution for 2 minutes at a temperature of 343 K, rinsed in water, rinsed in concentrated nitric acid for 1 minute (to remove smut from the surface), rinsed again in water, then dried with compressed air. Samples were stored overnight in a dry box before being used for testing, thus enabling the formation of a thin room temperature oxide layer. The surface of the as-etched samples had a characteristic scallop structure typical of long NaOH etching times [92-93], with some pitting as well. The machining marks were no longer visible when observed with a SEM.

Test Procedure

AA4045 clad alloy was first weighed with a target range of 900g and 1000g, and placed into a boron-nitride coated, cylindrical flat bottom, alumina crucible, with an ID of 92.5 mm (from MTI Corporation). The metal weight was used as input to the Labview™ software program which was used to control sample immersion depth into the melt. The AA4045 was then placed in the bottom zone of the tube furnace. The furnace was then powered on and the AA4045 was left to melt and stabilize in the bottom of the furnace. The melt was skimmed to remove dross accumulated during the melting process, using a boron nitride coated steel skimmer. The initial dross was weighed and subtracted from the initial AA4045 melt weight.

After the AA4045 melt temperature was stabilized, the melt was skimmed a second time, Figure 3-13a. After skimming the oxide on the AA4045 melt, a predetermined amount of time, t_1 (see Figure 3-13a), was allowed to elapse before inserting the AA3003 core alloy sample into the furnace to ensure a controlled oxide could grow on the surface of the AA4045 melt. Once the AA3003 sample was inserted into the furnace, as shown in Figure 3-13b, a second time, t_2, was allowed to elapse, after which the argon purge gas was opened, thereby flushing the furnace with argon. Using AA3003 sample heating curves from preliminary tests, the values t_1 and t_2 could be calculated such that the degree of surface oxidation present on the AA3003 sample and on the AA4045 melt could be systematically varied from test to test. The oxide values were then re-calculated after testing using actual heating curves from each specific test. When the sample temperature reached its predefined test temperature, the sample was then immersed into the melt, Figure 3-13c. For all tests in this series, a constant immersion speed of 1.4 mm/s was used, which is similar to the typical casting speed used in other Fusion™ casting trials. Test samples were immersed into the melt to a depth of 32 mm, then quickly withdrawn from the AA4045 melt at a speed of 9 mm/s. Thus, the time at which the sample was immersed in the AA4045 melt varied with position along the sample surface. The bottom edge of the sample was immersed for the longest time, ~ 26.5 s, while the last point of contact between the sample and the AA4045 liquid surface was in contact with the AA4045 melt for a very short period of time, ~ 0 s.

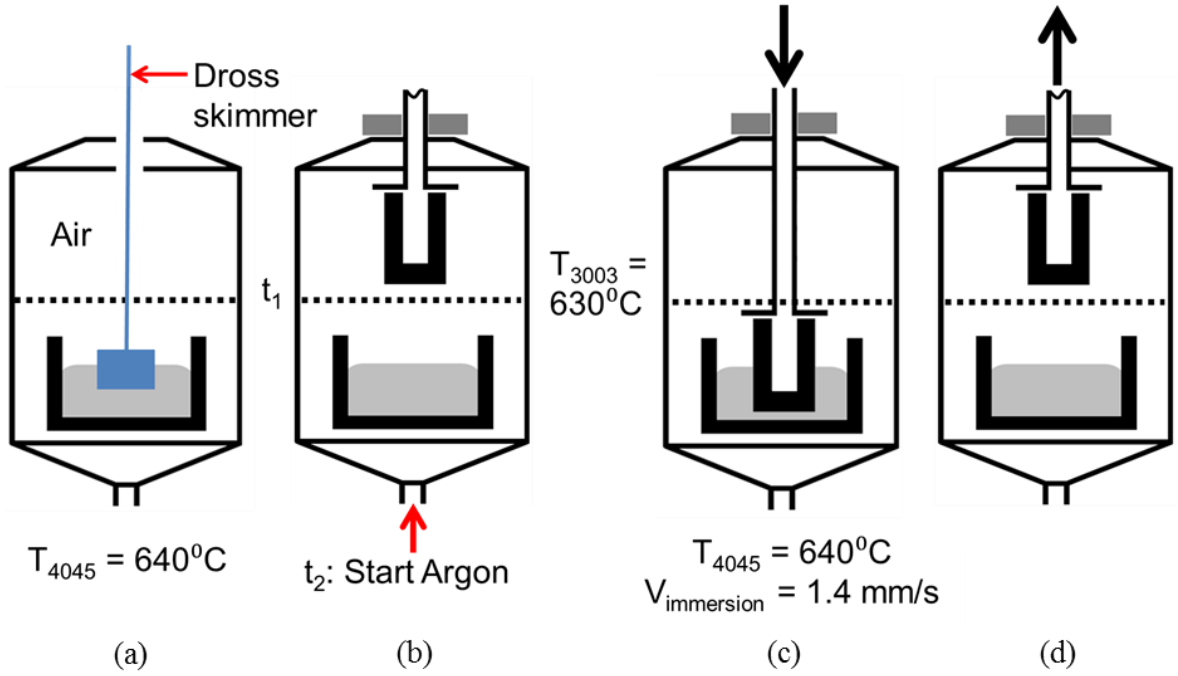

Figure 3-13 – Test procedure used for tests conducted on large OD sample, see Table 3-8.

A typical sample heating curve for the 38.5 mm OD samples used in this thesis is shown in Figure 3-14. It should be noted that the initial temperature of the sample was slightly hotter than room temperature. This is due to the fact that the sample holder, being in close proximity with the furnace assembly, was not at room temperature. Depending on the length of time, $t_{1,}$ between the initial skim and sample insertion into the furnace, the sample temperature would heat slightly prior to insertion into the furnace. The time of 0 seconds in Figure 3-14 refers to the point in time when the sample is placed into the furnace. Additionally, during contact with the AA4045 melt, the sample temperature increases to a peak temperature which was also recorded for each test.

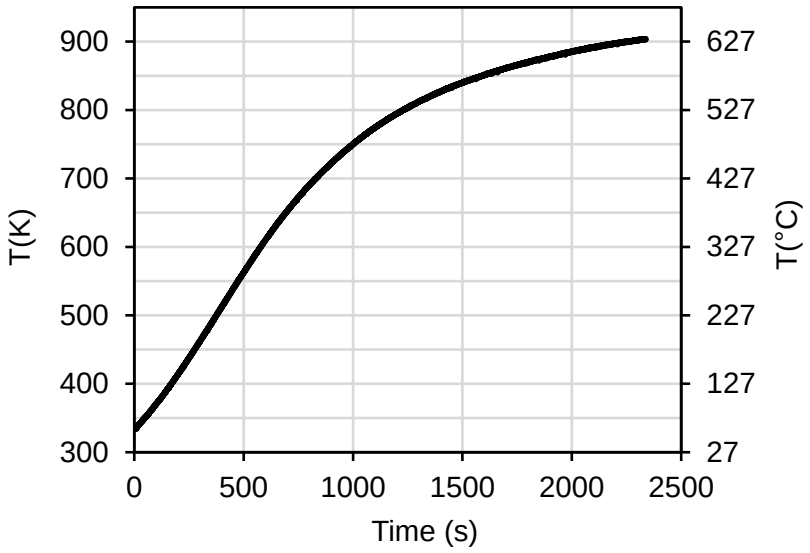

Figure 3-14 – Typical sample heating curve for 38.5 mm OD diameter sample.

Testing: sample surface oxidation

In the first series of tests, the AA3003 and AA4045 test temperatures were kept fixed as 903 K and 913 K. The test conditions are outlined in Table 3-7. By varying the time t_1, and t_2, the amount of oxidation on the sample surface prior to immersion in the melt could be altered. During final immersion of the test sample into the melt, the ambient atmosphere in the furnace was argon for all tests shown in Table 3-7. Prior to testing, a typical sample heating curve, like the one shown in Figure 3-14, was used in conjunction with oxide growth calculations, to estimate the times, t_1 and t_2, required to vary the level of sample surface oxide $\boldsymbol{t_{oxide,AA3003}}$ while keeping the melt surface oxide $\boldsymbol{t_{oxide,AA4045}}$ constant. For tests *o2-o6* in Table 3-7 this was achievable. For test *o1*, argon was purged into the furnace for 10 minutes prior to skimming the melt, thus a significantly lower melt and surface oxide was achieved. After tests, oxide growth was calculated using measured sample temperatures, melt temperatures, and testing times, t_1 and t_2. The procedure used to calculate oxide growth is detailed in Appendix B.

Table 3-7 – Interface formation tests performed with large OD samples, varying the amount of oxidation on the AA3003 sample surface prior to immersion in the melt. *n* indicates the number of test repeats.

Test	***Alloy Id #***		***Temperature, K(°C)***			***Calculated Oxide Thickness(nm)***		***Final Gas***	***n***
	Melt	***Sample***	$T_{i,\ AA4045}$	$T_{i,\ AA3003}$	$T_{Peak,\ AA3003}$	$t_{oxide,\ AA4045}$	$t_{oxide,\ AA3003}$		
o1	2	1	913 (640)	903 (630)	908-911 (635-638)	53-55	12-13	Ar	5*
o2	2	1	913 (640)	903 (630)	910 (637)	215-217	14-15	Ar	3
o3	2	1	913 (640)	903 (630)	909-910 (636-637)	217-218	38-41	Ar	3
o4	2	1	913 (640)	903 (630)	909-911 (636-638)	206-208	52-54	Ar	3
o5	2	1	913 (640)	903 (630)	908-909 (635-636)	231	71-74	Ar	3
o6	2	1	913 (640)	903 (630)	909-910 (636-637)	272-273	104-105	Ar	3

*for 2 of these 6 tests, samples were held for an additional 20 s in the melt, then raised up, for a total immersion time of ~ 20 s at the AA3003/AA4045 contact line and ~ 46.5 s at the bottom edge of the sample.

Testing: Ambient atmosphere and remelting

In this series of tests, argon was not used, i.e., the step shown in Figure 3-13b was omitted from the test procedure. Thus, the furnace ambient atmosphere was air during sample heating, and also air during sample immersion into the melt. The tests that were conducted are summarized in Table 3-8. Here, the AA3003 sample temperature was kept constant for all tests, at 903 K; however, the AA4045 melt temperature was varied from 913 K to 953 K.

Table 3-8 – Interface formation tests performed with large OD samples, varying the melt temperature. *n* indicates the number of test repeats.

Test	***Alloy Id #***		***Temperature, K(°C)***			***Calculated Oxide Thickness(nm)***		***Final Gas***	***n***
	Melt	***Sample***	$T_{i,}$ ***AA4045***	$T_{i,}$ ***AA3003***	$T_{Peak,}$ ***AA3003***	$t_{oxide,}$ ***AA4045***	$t_{oxide,}$ ***AA3003***		
r1	2	1	913 (640)	903 (630)	909-912 (636-639)	218-224	61-66	Air	6*
r2	2	1	923 (650)	903 (630)	917-919 (644-646)	225-227	59-61	Air	3
r3	2	1	933 (660)	903 (630)	923 (650)	239-241	58-59	Air	3
r4	2	1	943 (670)	903 (630)	924-926 (651-653)	253-255	57-60	Air	3
r5	2	1	953 (680)	903 (630)	925-926 (652-653)	267-270	59-60	Air	3

*for 2 of these 6 tests, samples were held for an additional 20 s in the melt, then raised up, for a total immersion time of ~ 20 s at the AA3003/AA4045 contact line and ~ 46.5 s at the bottom edge of the sample.

3.3.1.2 Effect of Mg impurities in sample and melt alloys

As mentioned in Section 2.3.3, the presence of active elements, such as Mg, can be beneficial to bond formation in fluxless brazing of aluminum [62]. The level of active metal content required to affect bond quality in fluxless brazing studies in Terril *et al.* [62] was on the order of 0.001 wt%. Furthermore, the interface formation tests that were performed in Section 3.3.3.1, used an AA3003 (alloy Id # 1 in Table 3-6) containing 0.0051 wt% Mg. As such, there was an interest in determining if the results from the AA3003/AA4045 interface formation tests outlined in Section 3.3.2.1 were being influenced by the presence of Mg. As such, a series of interface formation tests were performed, using alloys with varying levels of Mg content in both the sample alloy and the melt alloy.

Sample Geometry and preparation

To conduct a series of tests with varying Mg content in the sample and melt alloys, a series of ingots were cast at Novelis' Global Technology Centre in Kingston Ontario. The compositions of the alloys cast for these series of tests are listed in Table 3-9. Alloy compositions were determined by sampling the melt prior to casting and measuring the composition of the samples post-casting using Glow Discharge Optical Spectroscopy. Alloy *1a* and alloy *2a* in Table 3-9 represent the highest purity achievable using the raw material available at Novelis; as shown, both alloys have a residual Mg content of 0.0008 wt% Mg. This is due to impurity in the grade of Al used to make up the alloy melts, alloy Id # 3 in Table 3-9.

Table 3-9 – Measured alloy compositions used for interface formation tests (wt% unless specified).

Id #	***Alloy***	***Si***	***Fe***	***Mn***	***Ti***	***Cu***	***Mg***	***Ca***
1a	*Al-1Mn*	0.0032	0.0008	0.9612	0.0002	0.0032	0.0008	-
1b	*Al-1Mn-0.01Mg*	0.0035	0.0009	0.9808	-	0.0033	0.0114	-
1c	*Al-1Mn-0.1Mg*	0.0052	0.0011	1.0420	-	0.0034	0.1019	0.0004
2a	*Al-10Si*	9.5922	0.0005	0.0001	-	0.0028	0.0008	-
2b	*Al-10Si-0.01 Mg*	9.6026	0.0006	0.0001	-	0.0028	0.0106	-
2c	*Al-10Si-0.1 Mg*	9.6637	0.0006	0.0001	-	0.0029	0.0908	-
3	*Super pure*	0.0032	0.0008	0.0001	-	0.0028	0.0008	-

The book moulds used to cast the Al-1Mn alloys were of dimension 38.1 mm (1.5 in) by 152.4 mm (6 in) by 209.6 mm (8.25 in). These ingots were then used to fabricate test samples for interface formation testing. For these tests, a smaller sample dimension was used. Smaller samples in this case were easier to fabricate and used less material. Samples were again cylindrical in shape, 50.8 mm in length and 9.5 mm OD. A thermocouple hole was made into

the centre of the sample, from the top of the sample to a height of 15 mm from the bottom of the sample.

Prior to testing, machined samples were ground using 1200 then 2400 grit sandpaper on a lathe. The samples were then cleaned in alcohol, then etched as follows: samples were etched for 5 seconds in 5 wt% NaOH at a temperature of 343 K, then dipped into concentrated nitric acid. This process was repeated 4 times. This method of intermittent NaOH etching was suggested by Beck *et al.* [38] as a means to reduce the occurrence of surface pitting during the etch process. Samples were then rinsed in water and dried with compressed air. Samples were stored overnight in a dry box before being used for testing, thus enabling the formation of a thin room temperature oxide layer. The surface of the as-etched samples had a characteristic scallop structure [92-93].

Test procedure

The test procedure used was very similar to that given in Section 3.3.2.1. A few differences should be noted. First, due to the difference in sample size, the test samples heated differently than those in Section 3.3.2.1. In Figure 3-15, a typical heating curve for a 9.5 mm OD sample is shown in comparison with a typical heating curve from a 38.5 mm OD sample. As shown, the heating rate is higher for the smaller diameter sample, and a shorter time is required to reach the target test temperature.

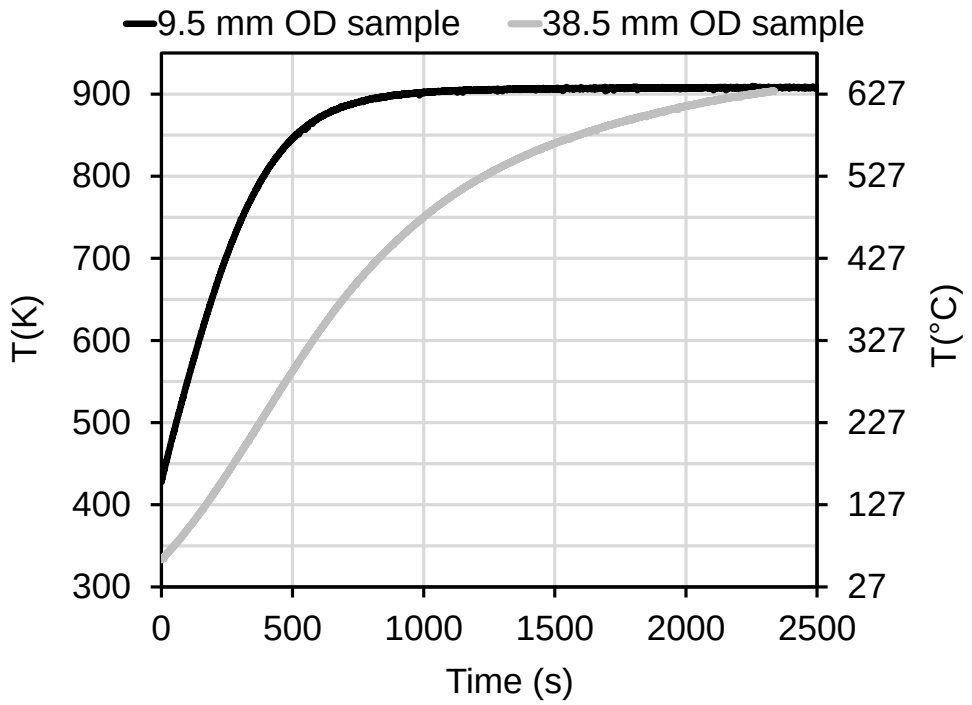

Figure 3-15 – Typical sample heating curve for 9.5 mm OD diameter sample compared with larger, 38.5 mm OD, sample.

Second, a smaller crucible was used in these tests, again to reduce material consumption and reduce the time required to melt the material before testing. For these tests a: boron nitride coated, cylindrical round bottom, alumina crucible, with ID 54.9 mm (from MTI Corporation) was used.

The final difference between these tests and those described in Section 3.3.2.1 was that no attempt was made to insure a similar oxide layer thickness on the melt prior to test immersion. The melt was still skimmed twice prior to testing: once after initial melting of the melt material, and once before the test sample was inserted into the furnace. Thus, the concept of using times t_1 and t_2, shown in Figure 3-13, to maintain a consistent melt surface was not applied. All interface formation tests were done under a final argon atmosphere. This was achieved by purging the furnace for a period of 10 minutes, with a flow rate of 0.226 m^3h^{-1} (8 scfh) prior to immersion of

the sample into the melt. Three series of tests were performed to assess the effect of Mg content on interface formation.

Testing: Baseline tests and effect of temperature and sample oxide level

The first series, the baseline tests, were conducted using only the high purity sample and melt alloys (Id# 1a and 2a in Table 3-9). The tests performed are listed in Table 3-10. These tests served to assess the effect of temperature and sample oxidation level, while providing baseline samples for comparison purposes.

Table 3-10 – Outline of analog tests performed with small OD samples. *n* indicates the number of test repeats.

Test	***Alloy Id #***		***Temperature, K(°C)***		***Calculated Oxide Thickness(nm)***	***n***
	Melt	***Sample***	***Melt***	***Sample***	***Sample***	
t1	2a	1a	878(605)	872(599)	10	3
t2	2a	1a	878(605)	872(599)	21-22	3
t3	2a	1a	878(605)	872(599)	117-126	3
t4	2a	1a	893(620)	891(618)	11-12	3
t5	2a	1a	893(620)	891(618)	25	3
t6	2a	1a	893(620)	891(618)	133-141	3
t7	2a	1a	913(640)	907(634)	13-15	3
t8	2a	1a	913(640)	907(634)	28-29	6
t9	2a	1a	913(640)	907(634)	149-159	7
t10	2a	1a	913(640)	907(634)	256-264	6

Testing: Effect of Mg impurity content in the sample alloy

In the second series of tests, the Mg content of the samples were varied, along with the sample oxidation prior to sample immersion in the melt. The tests conducted in this series are listed in Table 3-11. For these tests, the high purity melt alloy was used throughout (Id # 2a in Table 3-9). The alloys *1b* and *1c* (see Table 3-9) tests samples were fabricated using the ingots cast in book moulds, mentioned previously in this section. The alloy *1* (see Table 3-6) samples were fabricated from AA3003 DC-cast ingots.

Table 3-11 – Outline of analog tests performed with small OD samples. *n* indicates the number of test repeats.

Test	***Alloy Id #***		***Temperature, K(°C)***		***Calculated Oxide Thickness(nm)***	***n***
	Melt	***Sample***	***Melt***	***Sample***	***Sample***	
s1	2a	1b	913(640)	907(634)	14	1
s2	2a	1b	913(640)	907(634)	28-29	5
s3	2a	1b	913(640)	907(634)	155	4
s4	2a	1b	913(640)	907(634)	256	1
s5	2a	1c	913(640)	907(634)	14	1
s6	2a	1c	913(640)	907(634)	28-29	5
s7	2a	1c	913(640)	907(634)	162	1
s8	2a	1c	913(640)	907(634)	258	4
s9	2a	1	913(640)	907(634)	14	1
s10	2a	1	913(640)	907(634)	28-29	4
s11	2a	1	913(640)	907(634)	159	4
s12	2a	1	913(640)	907(634)	260	1

Testing: Effect of Mg impurity content in the melt alloy

In the third series of tests, the Mg content of the melt alloys were varied, along with the sample oxidation prior to sample immersion in the melt. The tests conducted in this series are listed in Table 3-12. For these tests, test samples were fabricated from the high purity Al-1Mn (Id # 1a in Table 3-9).

Table 3-12 – Outline of analog tests performed with small OD samples. *n* indicates the number of test repeats.

Test	***Alloy Id #***		***Temperature,K(°C)***		***Calculated Oxide Thickness(nm)***	***n***
	Melt	***Sample***	***Melt***	***Sample***	***Sample***	
m1	2b	1a	913(640)	907(634)	28-29	4
m2	2b	1a	913(640)	907(634)	157	1
m3	2c	1a	913(640)	907(634)	13	1
m4	2c	1a	913(640)	907(634)	28-29	4
m5	2c	1a	913(640)	907(634)	153	1
m6	2c	1a	913(640)	907(634)	257	1

3.3.2 Analysis of interface formation test samples

For all tests performed, macroscopic observation of the test samples after immersion were performed to qualitatively assess the interaction the sample had with the melt. Macroscopic images were taken with a digitial camera. For the tests detailed in Section 3.3.1.2, sample weight loss was recorded by measuring sample mass prior to and after testing, using a Denver Instruments SL-114 microbalance, with a precision of +/- 0.1 mg.

3.3.2.1 Metallographic analysis of interface formation test samples

Tests which were performed on large OD samples, Table 3-7 and 3-8, were cross sectioned, mounted, and polished using standard metallographic techniques. For these samples, care was taken to insure that the final polishing plane was consistent with the diametral plane. Samples were then imaged using optical microscopy.

A select number of small OD test samples, from tests in Table 3-10, 3-11, and 3-12 were examined using SEM (Hitachi S-3000N SEM and Zeiss Leo 1530 FESEM). The samples were cleaned in acetone and stored in a dry box prior to imaging. Additionally, for the tests done with small OD test samples, the sample weight was measured before and after testing, and used as a measure to gauge the extent of sample dissolution as a result of immersion into the melt.

3.3.2.2 Thermal oxide film characterization

One of the key test variables in the interface formation tests mentioned above was oxidation of the sample, whereby different heating times were used to generate a variety of oxide thicknesses on the exterior surface of the samples. The oxide films grown in this manner, by thermal

oxidation, were first evaluated using analytical calculations, as mentioned in Section 3.3.2 and Appendix B.

In addition, samples were also examined using SEM/EDS, which proved to be a useful technique to assess average oxidation and identify segregation of active metal species. The procedure to do this is described below in the heading "*Relative oxide thickness using EDS measurements*". To characterize local oxide uniformity in thermal oxide films grown on AA3003 and other alloys, FIB-SEM imaging was used; this is described in the section "*Oxide thickness and uniformity with FIB-SEM*". Finally, in an attempt to quantify surface defect populations in thermal oxide films, a copper decoration technique was employed; this is described in the section "*Oxide film defect quantification with copper decoration*".

Relative oxide thickness using EDS measurements

To assess both the relative oxide thickness and morphology of the AA3003 oxide films, AA3003 wafers were oxidized using the TA Instruments DSC then examined with a SEM. Sample preparation (polish, etch, de-smut, rinse, dry, store) were mimicked as per the procedure discussed in Section 3.2.1 above. To match the analog test heating rates (of the large diameter OD samples) with the TA Instruments DSC, experimentally measured heating curves from analog tests (specifically tests ***o1-o6*** in Table 3-8) were averaged, then segmented and fit to linear heating rates in 5 minute increments. The linear heating rates were then stitched together to form a DSC run file. The DSC purge gas could be dynamically switched during heating. Based on the DSC furnace size and argon purge rates used during testing, an estimate of 1.5 min was used as the required time to flush the furnace with inert gas. For these tests, a Parker-Bolston (UHPXN2-3200) nitrogen reformer was used as the inert gas source, with a specified purity of 5 ppm O_2. The air flow stream was taken from ambient room conditions,

whereas the inert gas stream was passed through a bed of anhydrous $CaSO_4$ (drierite) prior to purging into the DSC furnace. A summary of the tests run using this technique is shown in Table 3-13.

The resulting oxides grown on these AA3003 samples were imaged with a Phillips FESEM (XL30S FEG), equipped with an Oxford EDS detector (XMAX 80 mm^2 detector size) [3]. To determine the relative oxide thickness of the samples, the ratios of O-to-Al EDS peak intensity were measured. A field size of 1.8 mm by 1.8 mm was used to assess the trend in oxide layer thickness. A smaller field size of 2 μm by 2 μm was used to assess local inhomogeneity (unless stated otherwise). An accelerating voltage of 4 kV was used with the sample surface oriented perpendicular to the incident beam. Typical count rates with this system were 14,000 counts per second (40% dead time), and with this count rate, an acquisition time of 30 seconds was deemed adequate to get stable peak intensities in the resulting spectrums. In a comparative study of oxide measurement techniques [94], EDS methods were observed to give a similar accuracy to TEM based methods for determining oxide thicknesses, suggesting it is an adequate measurement technique. Without calibration standards, the O-to-Al EDS peak ratio could not be used to give quantitative oxide thickness values, but it was used to gauge relative oxide thickness between samples.

[3] Microscopy performed June 2013 by Paul Nolan, Senior microscopist at Novelis.

Table 3-13 – List of samples prepared for SEM/EDS oxide characterization.

Test	***Alloy Id#***	***Total Heating Time (min)***	***t1 (min)***	***t2 (min)***	***Estimated Oxide Thickness (nm)***	***Notes***
rt	AA3003	0	0	0	3	Air formed oxide, room temperature
air1	AA3003	40	9	31	13	Similar oxide thickness as o1 in Table 3-7
air2	AA3003	40	29	11	33	Similar oxide thickness as o3 in Table 3-7
air3	AA3003	40	36.5	3.5	46	Between o3 and o4 in Table 3-7
air4	AA3003	53	46.5	6.5	64	Between o4 and o5 in Table 3-7
air5	AA3003	70	63.5	6.5	95	Similar oxide thickness as o6 in Table 3-7
air6	AA3003	105	98.5	6.5	153	> oxide thickness as o6 in Table 3-7
n1	AA3003	40	-	-	13	Heating performed under N_2
n2	AA3003	70	-	-	26	
n3	AA3003	105	-	-	39	

Oxide thickness and uniformity with FIB-SEM

Using the small diameter sample size, 9.5 mm OD, oxidation tests were also performed in order to assess the oxide growth and uniformity with FIB-SEM imaging. The list of samples which were tested is given in Table 3-14. The oxidation temperature for all samples which were examined was 907 K (634 °C). On the 9.5 mm OD samples, a 4 mm wide flat was mechanically ground, then finely ground using an auto-polisher. The samples were then etched and stored using the same procedure as the samples which were used to perform immersion tests listed in Section 3.3.1.2. The oxidation time was 120 minutes, consistent with the maximum time and estimated oxide thickness for tests performed in Section 3.3.2.1. The primary purpose here was to assess the oxide thickness, uniformity, and differences in morphology between the various alloys.

Table 3-14 – FIB-SEM samples prepared for oxide uniformity studies.

Alloy	*Alloy Id # (Table 3-6 and Table 3-9)*	*Total Heating Time (min)*	*Heating Atmosphere*	*Estimated Oxide Thickness (nm)*
8Mg	3	120	Air	250-260
1Mn-8Mg	1a	120	Air	250-260
1Mn-100Mg	1b	120	Air	250-260
1Mn-1000Mg	1c	120	Air	250-260
AA3003-50Mg	1	120	Air	250-260

A combination Focused Ion Beam (FIB) milling instrument and Scanning Electron Microscope (Zeiss Model NVision 40) was used to assess the thickness and uniformity of the resulting oxides. Analysis was performed at the Canadian Centre for Electron Microscopy (CCEM), located at McMaster University[4]. Sample cross sections were prepared as follows. First, a suitable location for analysis, clean of debris, was identified in-situ using SEM imaging. To protect the surface oxide layer from damage during the ion-milling process, a sacrificial tungsten layer was deposited onto the surface in the identified region of interest. For samples where the surface oxide was expected to be > 50 nm in thickness, tungsten was deposited using an ion-beam assisted technique. A Gallium ion-beam was rastered in a grid like fashion over the region of interest. Simultaneously, tungsten hexacarbonyl gas was admitted into the SEM chamber. The interaction of the ion-beam and tungsten hexacarbonyl at the sample surface causes the gas to decompose leaving deposition of tungsten at the surface of the sample. Roughly 5 minutes was required to deposit a layer of tungsten of sufficient thickness. For instances where the oxide layer was expected to be less than 50 nm in thickness, the e-beam from the SEM was used instead of a Galium ion-beam to deposit the sacrificial tungsten layer. The e-beam assisted tungsten deposition rates were less than the ion-beam assisted deposition rates.

[4] Microscopy performed August 2014 by Travis Casagrande, microscopist at CCEM.

About 20 minutes was required in the case of e-beam assisted deposition of the sacrificial tungsten deposit. More information on FIB-SEM methods can be found in Reference [95].

After the tungsten deposit was completed, the quality of the deposit was checked to insure uniformity. If the tungsten deposit was deemed to be of good quality, ion-beam milling was used to remove material from this tungsten deposited region of interest. The process was essentially the same process used for tungsten deposition; however, for the milling process tungsten hexacarbonyl gas was not admitted into the specimen chamber. Thus, the Gallium ion-beam, when rastered over the surface of the sample, causes material to eject from the sample surface. When left for a period of time, a trench, or cross section, can be observed on the sample surface. The final trenches provided a means to view un-damaged surface oxides in cross-section. For thin surface oxides < 1 μm, this is typically not possible using traditional metallographic sectioning and polishing techniques. Roughly 5 minutes was required to mill each trench.

The trenches (or cross-sections) were imaged using the SEM on the Zeiss Model NVision 40 system, by tilting the sample to view the cross section. A tilt angle of 54° was required to adequately image the final cross sections. As image tilt in the SEM causes distortion, all images were tilt corrected using the system software prior to saving the images. All oxide thickness measurements were performed on tilt corrected images.

Oxide film defect quantification with copper decoration

Using the same sample preparation technique as that discussed in Section 3.3.3, copper decoration experiments [58] were also performed to assess the quantity of surface defects in the thermally grown oxides. The list of samples which were tested is given in Table 3-15. Again, the oxidation temperature for all samples which were examined was 907 K (634 °C). Copper decoration was performed after samples were oxidized and cooled to room temperature. The

electrolyte used was composed of distilled water with 65 g/L potassium chloride and 1 g/L copper sulfate added, giving a pH of 5 (using pH paper). Using a cell voltage of 0.5 V, an exposure time of 3 minutes was found to give adequate copper decoration, with copper sites easily observable using optical microscopy.

Table 3-15 – Samples examined using copper decoration technique.

Alloy	***Alloy Id # (Table 3-6 and Table 3-9)***	***Total Heating Time (min)***	***Heating Atmosphere***	***Estimated Oxide Thickness (nm)***
8Mg	3	-	-	3
8Mg	3	20	Argon	10-12
8Mg	3	120	Air	250-260
1Mn-1000Mg	1c	-	-	-
1Mn-1000Mg	1c	120	Air	250-260

The following three chapters will present the results obtained from the Fusion™ casting trials, Chapter 4, and laboratory scale interface formation tests, Chapters 5-6.

Chapter 4

Observations from Fusion™ Casting Trials of AA3003 and AA4045 Ingots

4.1 Introduction

In this chapter, the results and observations made during the Fusion™ casting experiments using AA3003 core and AA4045 clad alloys described in Section 3.1 are presented. Thermofluid simulations were also performed using a validated model of the Fusion™ caster and the process data collected during the casting trials to determine input parameters to the model. The results of the thermofluid CFD simulations are presented in Section 4.2. These simulations provided first approximations of the expected thermal history at the core/clad interface during Fusion™ casting.

Video recordings of the casting trials were performed to reveal the nature of motion of the oxides along the top surfaces of the molten metal pools during casting. As mentioned in Section 1.4, the motion of oxides on the cast sump is expected to be a key factor in final bond quality. The results for these recordings are presented in Section 4.3. Using predicted temperatures from Section 4.2, along with information gathered from the video recordings, an estimate for the core alloy surface oxidation could be made. To re-iterate, the motion of surface oxides on the top surface of both liquid sumps, shown in red in Figure 4-1, as well as the thickness and morphology of the surface oxide on the core surface prior to contact with the clad melt, shown as a black line in Figure 4-1, are of particular importance to the understanding the interface formation process.

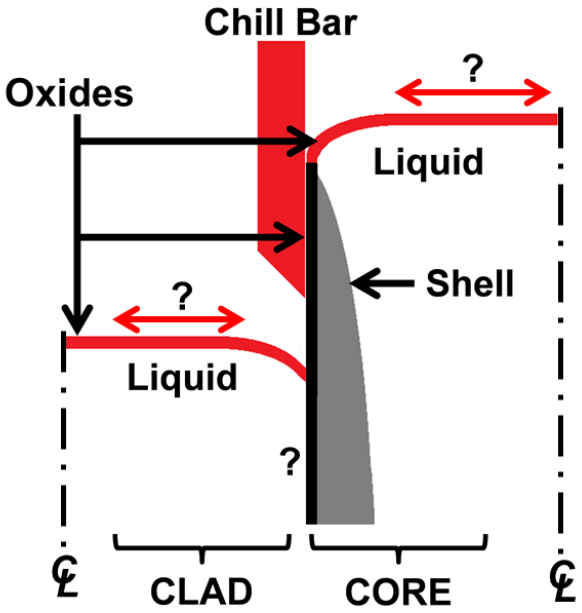

Figure 4-1 – Contact conditions between core and clad alloys in Fusion™ casting, with questions marks indicating areas of interest.

Microscopy of the core alloy surface, obtained from samples of the "interrupted" casting trial, (see Section 3.2.1.2) were examined, with results shown in Section 4.4. Sections 4.5 and 4.6 focus on the nature of the final as-cast interfaces. Macro observations and optical microscopy of the interface is presented first. These results are from previously cast ingots (see Table 3-3 for details); however, the results are qualitatively consistent with ingots cast as per Section 3.2.1. The chapter concludes with mechanical test results and fractography of the as-cast Fusion™ interfaces.

4.2 Thermofluid model predictions of Fusion™ casting trials

Using a thermofluid model developed as a separate project with Novelis [21-22], simulations were performed to determine the steady-state conditions for the casting trials 2-1, 2-2, and 2-3 in Table 3-2. The solid model and mesh are shown in Section 3.2.2.4. A comprehensive description of: (i) the thermofluid model, (ii) thermophysical properties of the AA3003 and AA4045 alloys, (iii) boundary conditions, and (iv) grid independence studies and model

verification/validation may be found in References [21-22]. The results of these simulations form a first approximation of the expected thermal history at the core/clad interface during Fusion™ casting. They are of importance when comparing final interface quality at different locations along the width of the ingot, and were also used for the design of testing parameters for laboratory tests performed in Chapter 5 and 6.

4.2.1 Temperature, fraction solid (f_s), and velocity contours

Before detailed results were extracted from the thermofluid model results files, temperature, f_s, and velocity results were plotted for various sections of the 3D model. These plots provided insight about the typical solidification patterns that evolve during Fusion™ casting.

Shown in Figure 4-2a is the predicted temperature contour results from simulation # 2 (see Table 3-5), from the *x*-*z* plane, taken at the centerline of the ingot (y = 0 mm). In Figure 4-2b, the corresponding fraction solid (f_s) is shown. Various observations can be made regarding the temperature and f_s results:

i. There is an appreciable sized AA3003 shell solidified against the copper chill, with f_s greater than 0.90.
ii. Both the AA3003 and AA4045 sump profiles appear to be asymmetric with respect to the AA3003/AA4045 interface.
iii. The AA3003 shell undergoes only slight reheating due to contact with the AA4045 sump.
iv. The AA4045 liquid sump is significantly deeper than the AA3003 sump.

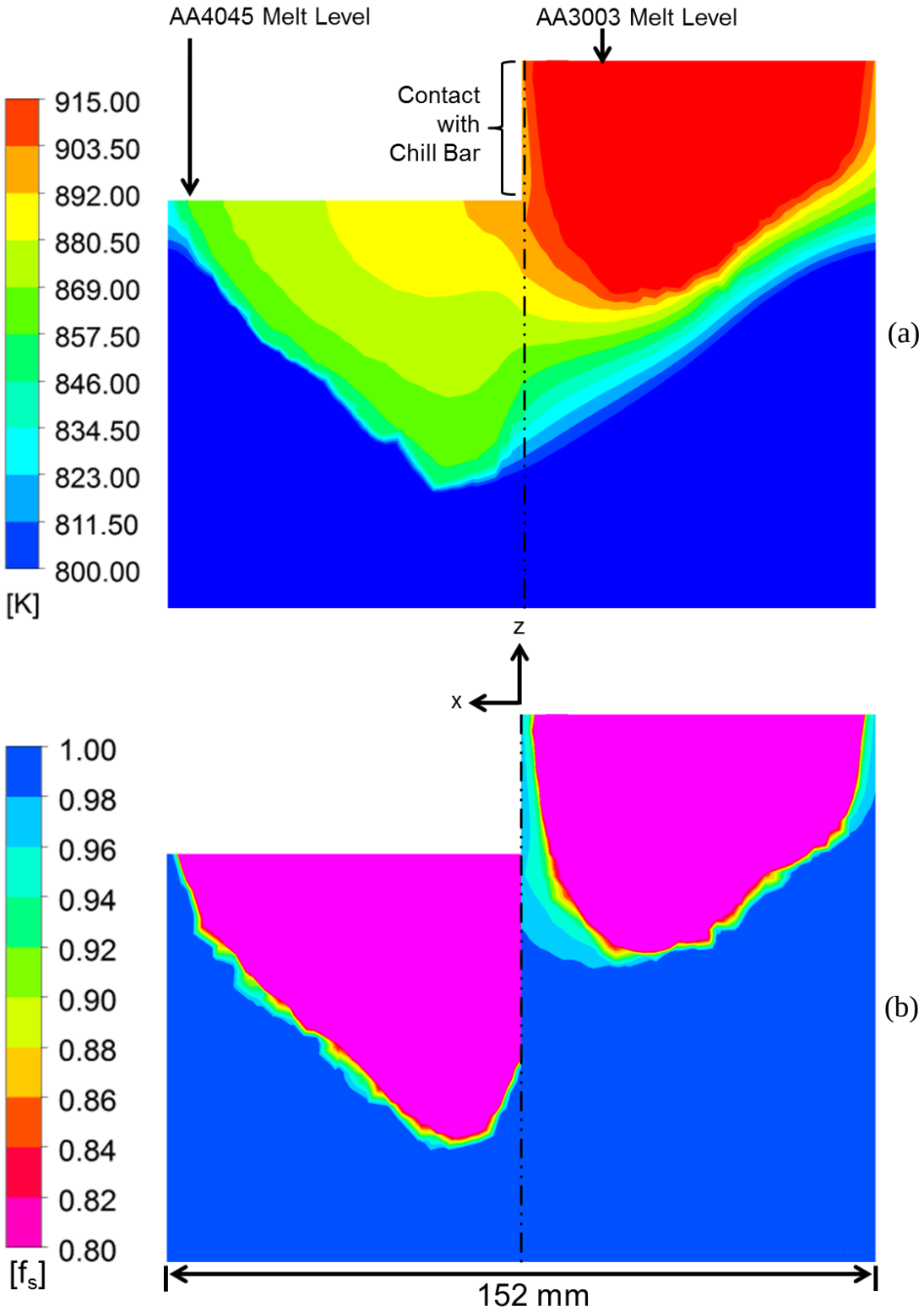

Figure 4-2 – Contour plots of results from simulation # 2 (see Table 3-5), from the *x*-*z* plane of the solid model domain (see Figure 3-10), taken at the centerline of the ingot, y = 0 mm. (a) Temperature, and (b) Fraction solid (f_s).

The thick AA3003 shell solidifying against the chill bar reduces the likelihood for break-through of the shell upon contact with the AA4045 melt, which is beneficial from a processing perspective. This has been examined in detail in previous Fusion™ casting research reported by Baserinia *et al.* [21]. The shape of the AA4045 and AA3003 sump profiles are both asymmetric. This behaviour matches previous calculation and experimental verification results in Caron *et al.* [22]. The last two observations are more relevant to the AA3003/AA4045 interface formation process. The Fusion™ casting patent suggests that reheating of the shell is a requirement for obtaining metallurgically sound bonds; however, only slight reheating of the AA3003 shell upon contact with the AA4045 sump was predicted at the center line. The predicted depth of the AA4045 sump, was significantly deeper than the AA3003 sump, resulting in a region of approximately 30-40 mm in length where fully solid AA3003 comes into contact with liquid (low f_s) AA4045. As the AA3003 shell moves down with the same rate as the ingot casting speed, in this case 1.12 mm/s, the resulting contact time between the AA3003 solid and AA4045 liquid is on the order of 1 minute at the ingot center line (y = 0 mm). This contact time is not constant across the width of the ingot, due to asymmetry in molten metal feeding (see solid model Figure 3-10), and will be elaborated upon further in Section 4.2.2.

The asymmetry in temperature and f_s is further illustrated Figure 4-3. Figure 4-3a is the predicted temperature contour results from simulation # 2 (see Table 3-5), from the *z*-*y* plane, taken at the interface (x = 0 mm) between the AA3003 and AA4045. The corresponding f_s contours for AA3003 at the interface are shown in Figure 4-3b. Along the top of the *z*-*y* plane, there are two observable hot spots (labelled **a**), these are associated with the AA3003 inlet stream. As shown in Figure 3-10, the AA3003 inlet stream is divided into two horizontal jet streams by a diffuser mechanism. These two horizontal jet streams of molten AA3003 create hot

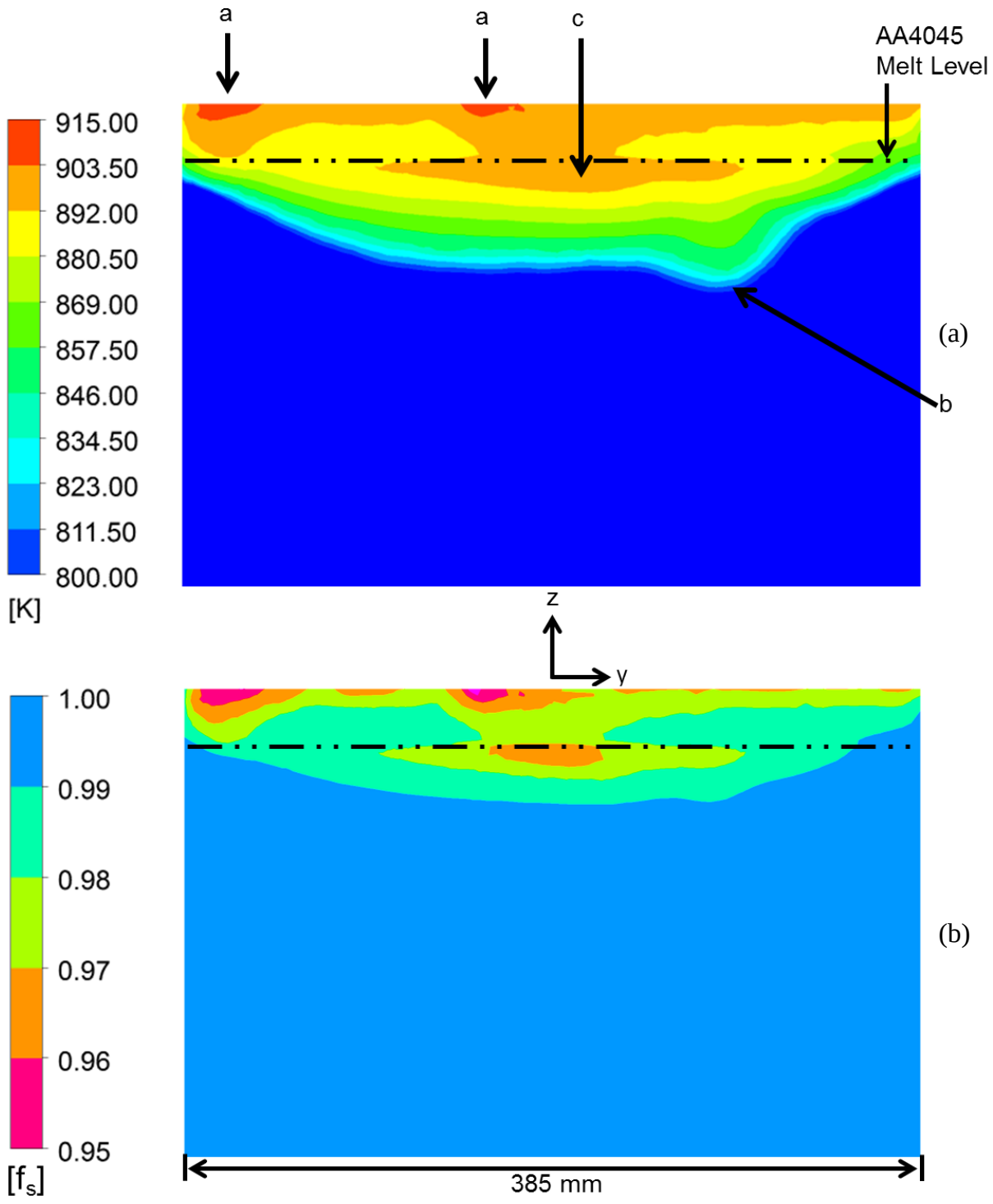

Figure 4-3 – Contour plots of results from simulation # 2 (see Table 3-5), from the *z*-*y* plane of the solid model (see Figure 3-10), taken at the interface (x = 0 mm) between the AA3003 and AA4045 domains. (a) Temperature, and (b) AA3003 f_s.

spots at the outlet of the diffuser openings. A second hot spot (labelled **b**) can be observed in Figure 4-3a, at the y position consistent with the clad inlet jet stream, y = +102 mm. Unlike the core inlet metal stream, the clad inlet stream was fed vertically into the sump, due to space constraints, see Figure 3-10. This vertical jet stream created a hot spot its liquid metal jet impinges the bottom of the AA4045 sump. In Figure 4-3a the result of this hot spot manifests itself as a hot spot along the AA3003/AA4045 interface and a local depression of the sump.

A third hot spot (labelled **c**) is shown clearly in Figure 4-3b at the centerline (y = 0 mm) of the ingot. This hot spot occurs for three reasons. First, it is the furthest point from the narrow edge of the ingot. Since the majority of the heat extraction is provided by DC cooling along the periphery of the ingot, this point only receives cooling via diffusion from the wide face of the ingot; however, near the edges of the ingot (y = +/- 192.5 mm), there is enhanced cooling provided by the narrow face of the ingot in addition to the wide face of the ingot. Second, the other two hot spots (**a** and **b**) from the AA3003 and AA4045 metal jet streams appear to be an influencing factor, as both hot spots are in close proximity to this third hot spot. Also, this hot spot occurs below the AA4045 melt level position, i.e., after the AA3003 metal comes into direct contact with the AA4045. This is expected, as the AA4045 pouring temperature was 923-933 K (650-660 °C), and thus could be expected to cause some reheating in the region furthest from the edges of the ingot.

A snapshot of the predicted velocity results from simulation # 2 (see Table 3-5) are shown in Figure 4-4, for different sections of the solid model. Figure 4-4a is a section of the x-z plane, taken at the clad inlet (y = 102 mm) position (see Figure 3-10). Figure 4-4b is a view from the top of the solid model, showing both the velocity contours on the core and clad sumps. The flow in the AA4045 sump is a strong function of the clad metal inlet jet stream, see Figure 4-4a.

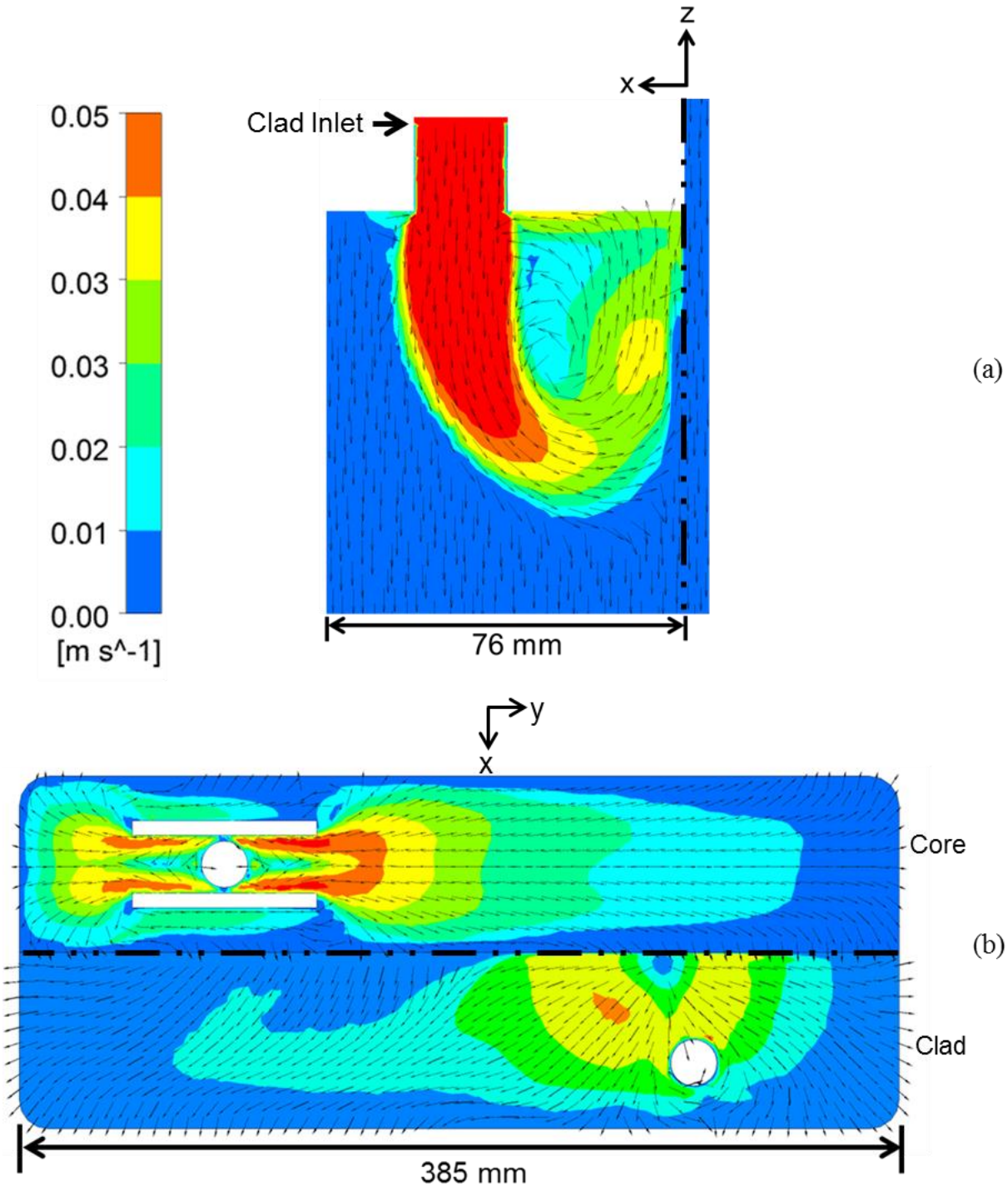

Figure 4-4 – Velocity contour plots of results from simulation # 2 (see Table 3-5). Normalized vector vectors included in both plots to indicate direction of flow tangential to the indicated plane. (a) Section of the *z*-*x* plane of the solid model, taken at the clad metal inlet, y = 102 mm (see Figure 3-10). (b) Top surface of the core and c lad domains.

Here, the flow from the inlet stream hits the bottom surface of the AA4045 sump (i.e., the liquid/solid interface), causing a recirculation of flow in the counterclockwise direction. This recirculating flow from the inlet jet stream causes the free surface flow of the AA4045 sump to be directed away from the AA3003/ AA4045 interface, as shown in Figure 4-4b.

This predicted surface flow would generate a viscous shear force on any oxide films present on the AA4045 sump surface. The direction of this shear force would tend to pull any oxide films on the AA4045 sump surface away from the AA3003/AA4045 interface, which would be beneficial for creating an oxide-free interface. The predicted AA3003 sump flow and surface flows are also strongly related to the molten inlet flow, and the jet streams resulting from the use of a diffuser. Here, the diffuser divides the flow into two jet streams, and the resulting surface flows generated by these streams are shown in Figure 4-4b. Unlike the AA4045 free surface, the surface flow is directed to the mould periphery as well as the chill bar. This flow pattern would not be as helpful in dragging any oxide film on the AA3003 surface away from the AA3003/AA4045 interface.

It should be noted that the magnitude of the surface flow shown in Figure 4-4b reach levels of 0.05 m/s (50 mm/s). These model predicted results, while valid, may not represent the physical reality of the surface flows, as the top surface is subject to oxide formation and hence the boundary conditions used to define the free surface in the thermofluid model [21-22] may not be valid; there is a need for real measurements of surface velocity, which is the subject of Section 4.3.

4.2.2 Extracted model results

For the purpose of this study, the most pertinent information extracted from the model were the: (i) surface temperature and f_s of the core alloy while in contact with the chill bar (and prior to it

contacting the liquid clad), and (ii) core/clad interfacial temperature and core f_s, from the point where the core and clad initially make contact until the point at which the interface solidifies.

In Figure 4-5a and b, the 3-d modelled domain and axis co-ordinate system are shown, along with key dimensions of the model. Additionally, using the casting speed, *v*, the distance along the *z* axis (parallel to the casting direction) can be converted to time, *t*, which is a useful variable to use when displaying surface temperature and interfacial temperature results.

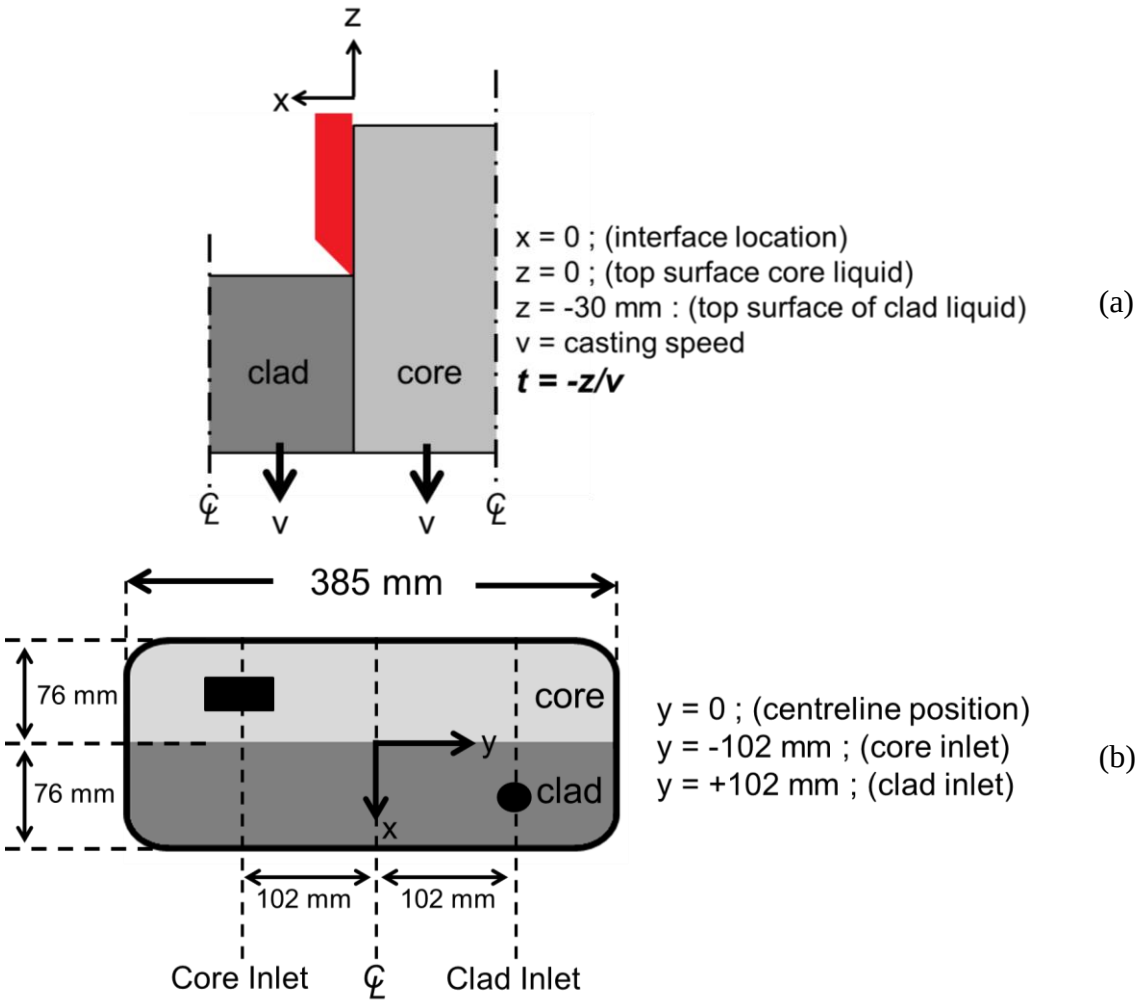

Figure 4-5 – Schematic of the Fusion™ model interface with axes and key dimensions labelled. (a) *x*-*z* plane, longitudinal section. Casting time is defined as the distance *z* along the model, starting from *z* = 0 mm, divided by the casting velocity, *v*. (b) *x*-*y* plane, transverse section of the Fusion™ model.

A typical result of the AA3003 core alloy surface temperature (prior to contact with the clad alloy liquid), and after contact with the AA4045 clad liquid is plotted in Figure 4-6. The various plots represent different positions, *y,* along the width of the Fusion™ ingot. Starting from $t = 0$ (which corresponds to the $x = 0$ mm and $z = 0$ mm position in Figure 4-5a), the surface temperature of the core alloy decreases continuously as casting proceeds. This corresponds to the region where the alloy is in intimate contact with the chill bar. There is a slight rise in core alloy surface temperature, beginning a few seconds before the core alloy comes into contact with the clad liquid. This rise in temperature is indicative of reheating of the shell due to formation of a gap between the shell and mould wall. This occurred across the majority of the width of the Fusion™ ingot; however, near the edges of the ingot (+192.5 mm and -192.5 mm) this rise in temperature does not occur. After coming into contact with the clad alloy, the interfacial temperature rises to a maximum, due to contact with the hotter clad liquid, then cools continuously until it reaches the solidus temperature of the clad alloy, 851 K (578 °C). At this point in time, the interface is considered to be solidified. The peak interface temperature occurs at the centerline of the ingot, a temperature of about 903 K (630 °C). This point is both: (i) farthest from the edge of the ingot, where additional cooling for the external mould comes into play and (ii) sufficiently close to clad inlet liquid jet stream. In Figure 4-6b, the corresponding fraction solid (f_s) is plotted. For the clad inlet and core inlet positions (+102 mm and -102 mm) there is a slight drop in f_s of the AA3003 shell as a result of contact with the AA4045 sump. At the centerline the drop in f_s is more noticeable, but still lower than a 0.01 f_s change; whereas the f_s for the other positions shown in Figure 4-6b show no decrease AA3003 f_s as a result of contact with the AA4045 sump.

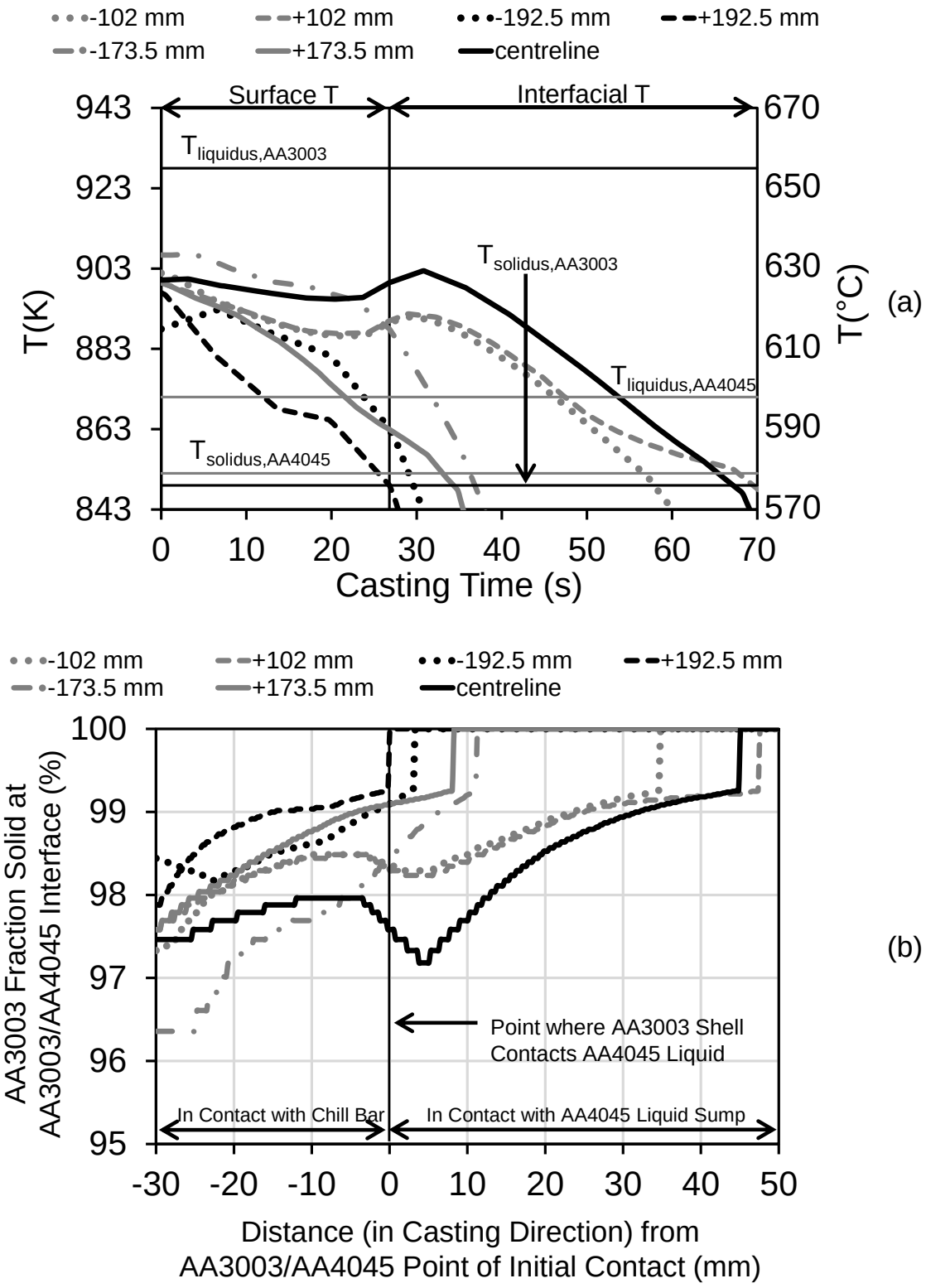

Figure 4-6 – Model calculated core alloy (a) surface temperature, as well as core/clad interfacial temperature, for model run number 3, and (b) corresponding f_s for the AA3003 core alloy at the AA3003/AA4045 interface.

The predicted maximum temperature of the interface along the width of the Fusion™ ingot from all simulations are presented in Figure 4-7a, and the corresponding minimum f_s of the AA3003 at the interface is shown in Figure 4-7b. As already shown in Figure 4-6, the maximum calculated temperature occurs at the centerline of the ingot. For the 1.12 mm/s casting speed, the maximum is around 903 K (630 °C), while the maximum for 1.23 mm/s was a few degrees higher than this. The coldest interface temperatures occur near the positive y edge: the edge nearest the clad molten metal inlet stream, but also farthest from the core metal inlet stream. This manifests itself as a cold spot along that edge, and thus decreases the interfacial temperatures in that region significantly. Along the width of the ingot, for $y < 0$, the maximum interface temperature stays relatively constant, from 885 K (612 °C) to 900 K (627 °C) until near to the external edge. The minimum estimated f_s occurs at the centerline (along the width of the ingot), and was estimated to be slightly greater than 0.96 f_s. Outside the central region of the ingot, i.e., outside the region y = -100 mm to y = +100 mm along the width of the ingot, the minimum f_s was above 0.98 f_s for all the calculated model runs, very close to being fully solid.

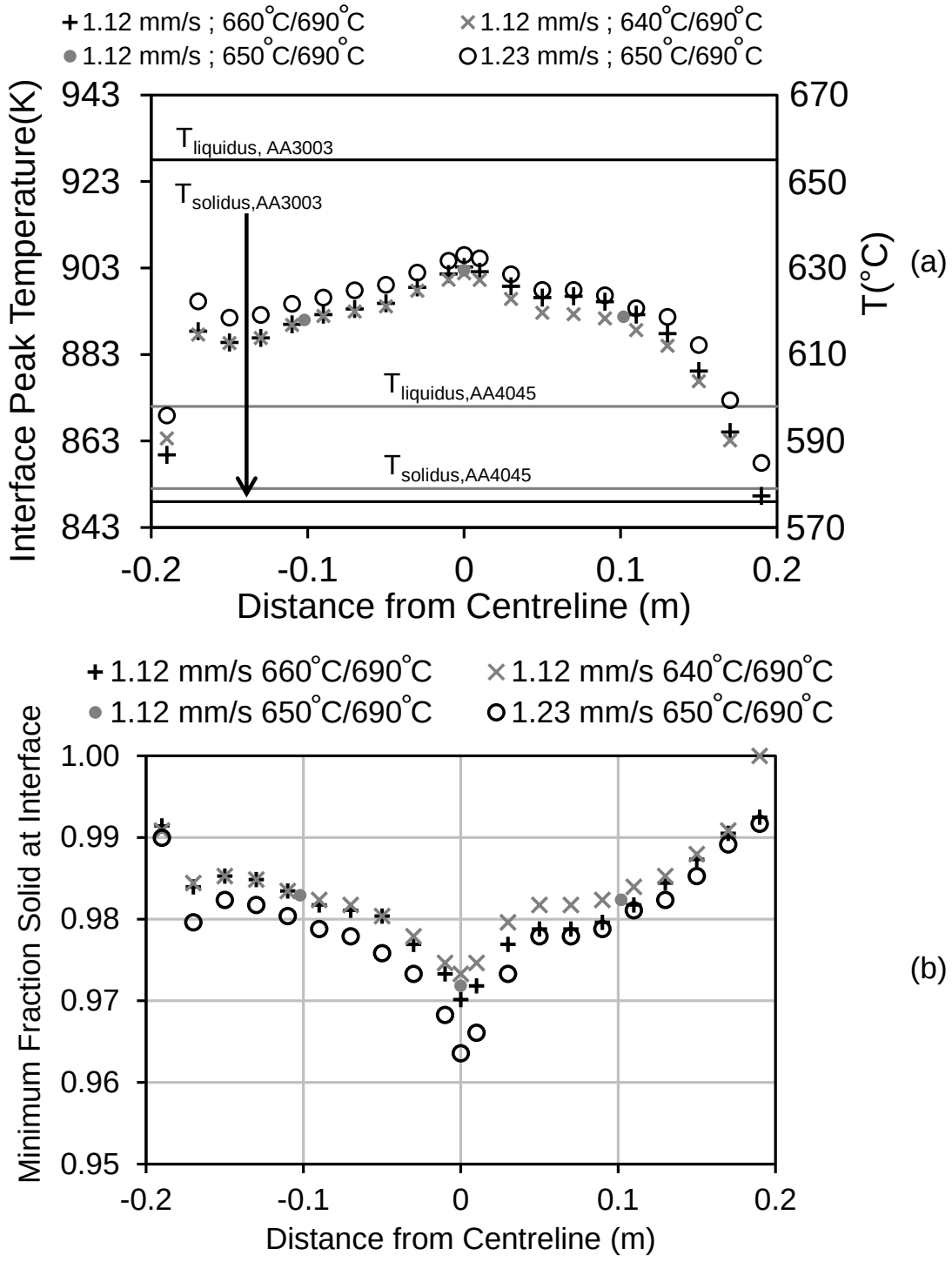

Figure 4-7 – Model calculated (a) peak temperature of the interface for all four model runs, and (b) corresponding minimum f_s of AA3003 at AA3003/AA4045 interface during Fusion™ casting.

The rise in temperature of the AA3003 core alloy surface, as a result of contact with the clad liquid, may be seen in Figure 4-8a, and the corresponding change in f_s as a result of this contact is shown in Figure 4-8b. For model runs 1-3, i.e., casting speed of 1.12 mm/s, the maximum rise in temperature is 6.5-8 K at the centerline, a value which is slightly dependent on the value of clad inlet temperature used as input into the thermofluid model. At the centerline, this corresponds to a change in f_s of just under 0.01. Aside from the centerline, the predicted change in f_s, for model runs 1-3, as a result of contact with the AA4045 sump is generally less than 0.005 f_s. For the higher casting speed of 1.23 mm/s, the maximum rise in temperature was slightly higher, about 10 K at the centerline. This corresponds to a change of about 0.015 f_s. Also, there is a clear effect of casting speed on the predicted change in AA3003 f_s at the interface as a result of contact with the AA4045 in Figure 4-8b. Increasing casting speed results in more reheating of the AA3003 shell and hence a larger predicted amount of remelting of AA3003 at the interface. At both edges of the ingot (farthest from the centerline), there is an appreciable section of the Fusion™ ingot where the AA3003 core alloy does not reheat after it comes into contact with the AA4045 clad alloy liquid. For the 1.12 mm/s casting speed this width was close to 50 mm, but for the faster casting speed, the width is slightly less than 50 mm.

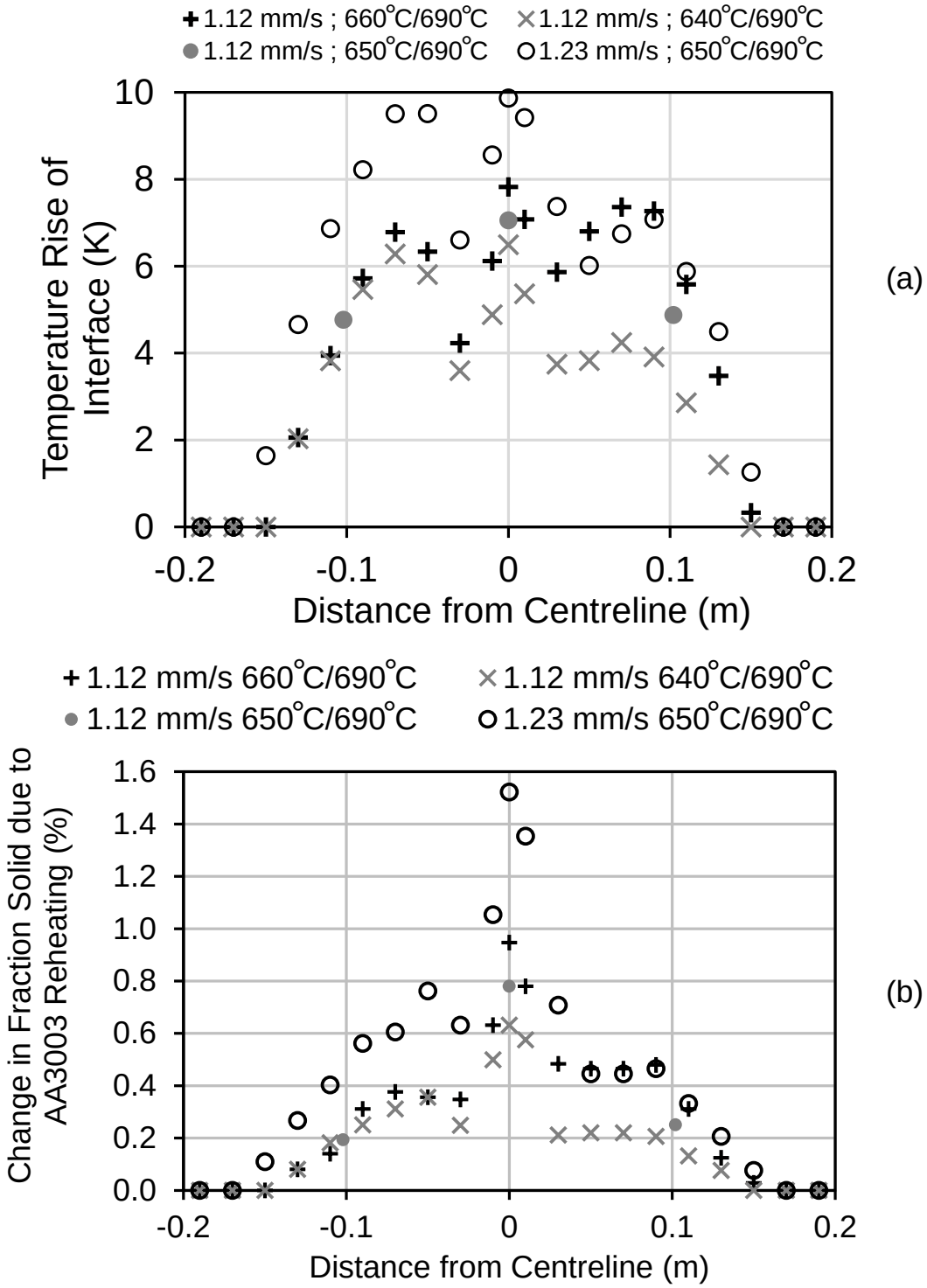

Figure 4-8 – Model calculated (a) rise in core alloy temperature as a result of contact with the molten clad metal, for all four model runs, and (b) corresponding rise in core alloy f_s at the interface.

Summary of AA3003 fraction solid (f_s) and remelting

The predicted results for minimum f_s and change in f_s, shown in Figure 4-7 and Figure 4-8, suggest that the surface of the shell is nearly 1.00 f_s, in all cases > 0.96 f_s. For the slow casting speed, 1.12 mm/s, the maximum rise in temperature, 7.8 K, corresponds to only a 0.009 f_s change in the AA3003 at the interface in contact with the AA4045 liquid. For the faster casting speed, the maximum change in f_s is only 0.016 f_s. It should be noted again that the original patent suggests that the first alloy to be cast (AA3003 in this case) should be semi-solid while in contact with the second alloy in order to achieve a sound metallurgical bond [9]. The thermofluid predictions for the set of casting trials performed in this thesis suggest that the first alloy (AA3003) was almost entirely solid (based on temperature predictions and f_s relations) while it was in contact with the second alloy (AA4045). Based on these initial thermofluid results, one might expect a poor metallurgical bond at the interface; however, given the relatively large values of f_s predicted, and the small f_s changes as a result of contact with the AA4045 sump, two questions must be posed with respect to these thermofluid results:

i. Are these small changes in f_s accurate?
ii. If so, what is the physical significance of a small change in f_s with respect to interface formation?

It is unlikely that the calculated change in f_s is accurate, for multiple reasons. First, due to the inability to measure ingot surface temperatures during casting, validation of the Fusion™ casting model [22], and the DC casting model on which it is based [96], does not include validation for surface temperature. Additionally, the density-based model for estimating heat fluxes between the solidifying AA3003 shell and the chill bar does not accurately predict shell remelting, see [96] Figure 8 and 9.

Second, the Fusion™ casting model assumes the f_s curved follows Scheil solidification during solidification and remelting [21-22]. For continuous cooling, the assumption in the Scheil solidification model may lead to inaccuracies [78,97], as it neglects the effects of back- diffusion in the solid phase and assumes a constant partition co-efficient. That there are discrepancies in calculated f_s curves (see Figure 2-6) and experimentally determined solidification temperatures of AA3003 (see Table 2-3 [71]) suggests that the f_s curve used for thermofluid calculations may have been inaccurate.

Additionally, the thermofluid model treats AA3003 as a homogenous material. The solidification and remelting is calculated solely upon the local enthalpy of the model. In actuality, the solidifying AA3003 is a multiphase material, with low melting and high melting phases. Additionally, the distribution of these phases is likely not uniform throughout the ingot. Inhomogeneity and non-uniformity of solidifying AA3003 are not captured within the model. For monotonically decreasing temperature histories, where reheating and remelting does not occur, these assumptions may be adequate to describe the f_s evolution during casting. However, when reheating or remelting occurs in regions within the solidifying ingot, the physical process becomes more complex. Using an enthalpy based model coupled with a Scheil solidification assumption, to calculate f_s, may not yield accurate calculations of f_s for instances where the temperature history does not decrease monotonically [98-99].

The sum of the above arguments suggests that while the model can be used to predict the AA3003 surface and AA3003/AA4045 interface temperature, the resulting f_s value may not be accurate. While the predicted change in f_s may not be accurate, we can for certain say that reheating of the AA3003 surface should occur due to contact with AA4045 liquid. Whether or not the reheating of the AA3003 surface causes surface remelting is questionable, given the

inaccuracies of the model mentioned above. It should be noted that the patent literature states that surface remelting (or having a semi-solid surface in contact with AA4045 liquid) is key to obtaining a metallurgically sound bond during the Fusion™ casting process [16]. However, for the reasons given above, it is unclear if surface remelting occurs, given the current thermofluid model. As such, there was a necessity for experimental work to determine if local remelting occurs on the AA3003 surface prior to contact with AA4045 liquid. This will be presented and discussed in Section 4.4.

AA3003/AA4045 contact time before interface solidification

Overlooked in both the patent [16] and in previous Fusion™ casting research [22], is the notion of contact time. Regardless of the interface formation mechanism at play, there is a finite time at which liquid AA4045 can be in contact with AA3003 before the interface solidifies. This contact time is expected to be an influencing factor on the quality of the as-cast Fusion™ interface. Here, the contact time is expressed as the time, t (as defined in Figure 4-5), which elapses before the AA3003/AA4045 interfacial temperature reaches the solidus temperature of the clad alloy, in this case 851 K (578 °C). This time was calculated from the various model runs, and is plotted in Figure 4-9, as a function of position along the width, y, of the Fusion™ ingot. As shown, casting speed (over the small increment 1.12 to 1.23 mm/s) does not significantly influence this interaction time. At the edges of the ingot the interaction time is short, about 5 seconds. This time increases approximately linearly with distance from edge of the ingot. The slope is greater at the positive y edge, i.e., the edge of the ingot which is closer to the inlet jet stream from the clad liquid metal. The maximum interaction time of 50-55 seconds occurs at the position y along the width of the ingot which is essentially coincident with inlet jet

stream from the clad liquid metal. Near the centerline of the width of the ingot, the interaction time is slightly lower than the maximum, about 40-45 seconds.

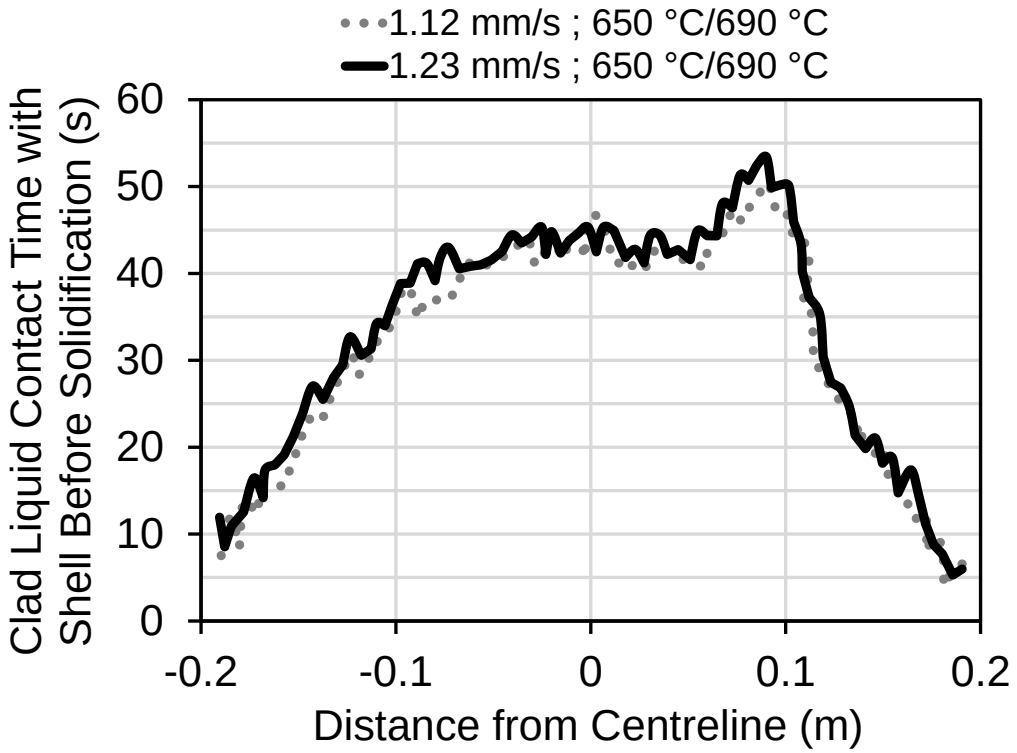

Figure 4-9 – Model calculated clad liquid contact time with core alloy shell before final solidification of the interface.

For three positions along the width of the ingot, the AA3003 solid and AA4045 liquid contact times have been listed, see Table 4-1. These positions: (i) y = -174.5 mm, (ii) y = 0 mm, and (iii) y = 102 mm, correspond to the locations where mechanical test specimens of the Fusion™ cast interfaces were fabricated, and will be presented and discussed further in Section 4.6. As shown, there is a significant difference in calculated contact times, between the near edge location and the other two locations. Depending on the interface formation mechanism, these differences in contact time could significantly contribute to the final interface quality.

Table 4-1 – Calculated time of contact between AA3003 solid and AA4045 liquid during Fusion™ casting and average interface temperature during contact, for three positions along the width of the ingot.

Location	$t_{contact}$ ***(s)***	***Average Temperature during contact,K, (°C)***	***Simulation Number***
Near edge (y = -174.5 mm)	12.3	871, (598)	Run 1
	12.3	872, (599)	Run 3
Centre Line (y = 0 mm)	41.3	881, (608)	Run 1
	41.7	882, (609)	Run 3
Clad Inlet (y = 102 mm)	47.2	871, (598)	Run 1
	47.2	875, (602)	Run 3

Summary

The information from the thermofluid predications of the Fusion™ casting trials described in Section 3.2.1 can be summarized as follows:

i. The predicted AA3003 f_s at the interface when in contact with the molten AA4045 clad alloy was very high, above 0.96 f_s in all cases.

ii. The maximum remelting of AA3003 at the interface was only predicted to be 0.016 f_s, but in general, the amount of remelting was much less than 0.006 f_s (see Figure 4-8).

iii. The maximum AA3003 temperature at the interface occurred at the centre line of the ingot and was approximately 903 K (630 °C, see Figure 4-7), a consideration used for tests in Chapter 5 and 6.

iv. The predicted surface flow on the AA4045 clad sump was away from the interface. The viscous drag imparted by the surface flow on the AA4045 sump-surface oxide could potentially help to move the oxide away from the interface. The predicted surface flow on the AA3003 core sump was not away from the interface, and hence may not help move the AA3003 sump-surface oxide away from the interface. The difference in surface flows between the AA3003 and AA4045 sumps appear to be a result of the different liquid metal feeding systems used. For the AA3003 liquid metal inlet a

horizontal diffuser was used, whereas no diffuser was used for the AA4045 liquid metal inlet.

v. The time of contact between AA3003 solid and AA4045 liquid at the interface during Fusion™ casting was between 5 and 55 seconds (see Figure 4-9). At the centre line where the temperature was hottest, the average contact time was between 40-45 seconds (see Table 4-1), which was taken into consideration for tests in Chapter 5.

4.3 Visualization of oxide film motion

While the thermofluid model is a useful tool for predicting temperature and flow distributions within the Fusion™ casting process, the model does not predict the influence of fluid flow, or any other surface phenomenon, on oxide film motion on the surface of the core and clad casting sumps. Two key physical effects: (i) oxide formation on the core and clad sumps and (ii) motion of these oxides, while of little importance from a thermofluid standpoint, are expected to play a major role in interface formation (see Section 1.4). Therefore, experiments were performed to explore the nature of the oxide film motion on the core and clad sump surfaces by direct video observation during casting trials. For casting trial 2-1 (see Table 3-2), the clad oxide surface with marker particles was recorded; the field of view which was recorded is depicted in Figure 4-10, and labelled FOV_1.

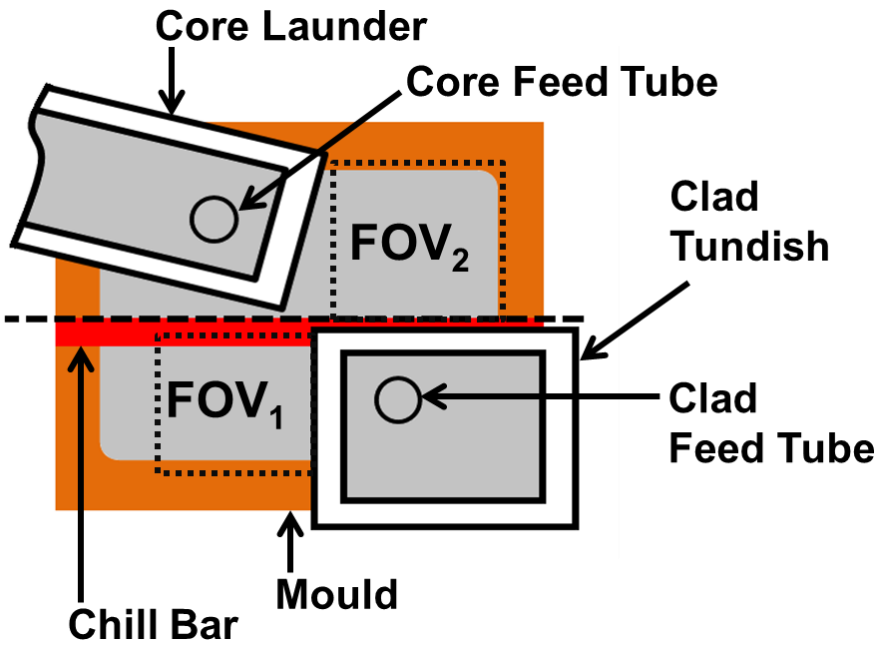

Figure 4-10 – Schematic of top view of casting mould showing fields of view (FOV_1 and FOV_2) captured during casting trials.

A sample of the motion of the surface oxide, aided with the use of cobalt-silicate (Co_2O_4Si) ceramic powders (as described in Section 3.2.1.1) is shown in Figure 4-11. The first key observation was that the motion of the surface oxide on the clad sump was away from the core/clad interface, and towards the external mould (the down direction in Figure 4-11). The velocity of the surface oxide appeared, qualitatively, to be constant. For three segments in time during the casting run, ranging 24-27 seconds in time, the motion was quantified. The results are shown in Figure 4-12. While not entirely constant, the motion of the oxide sump away from the core/clad interface was similar to the casting speed. This suggests that the oxide was pulled/dragged across the surface of the clad sump and towards the external casting mould. This was consistent with visual observations. The speed at which the oxide moves was consistent with the ingot casting speed and not with the clad liquid surface velocity predictions given by thermofluid model predictions shown in Figure 4-4. Additionally, the direction of oxide motion was consistent with the fluid flow predictions given in Figure 4-4.

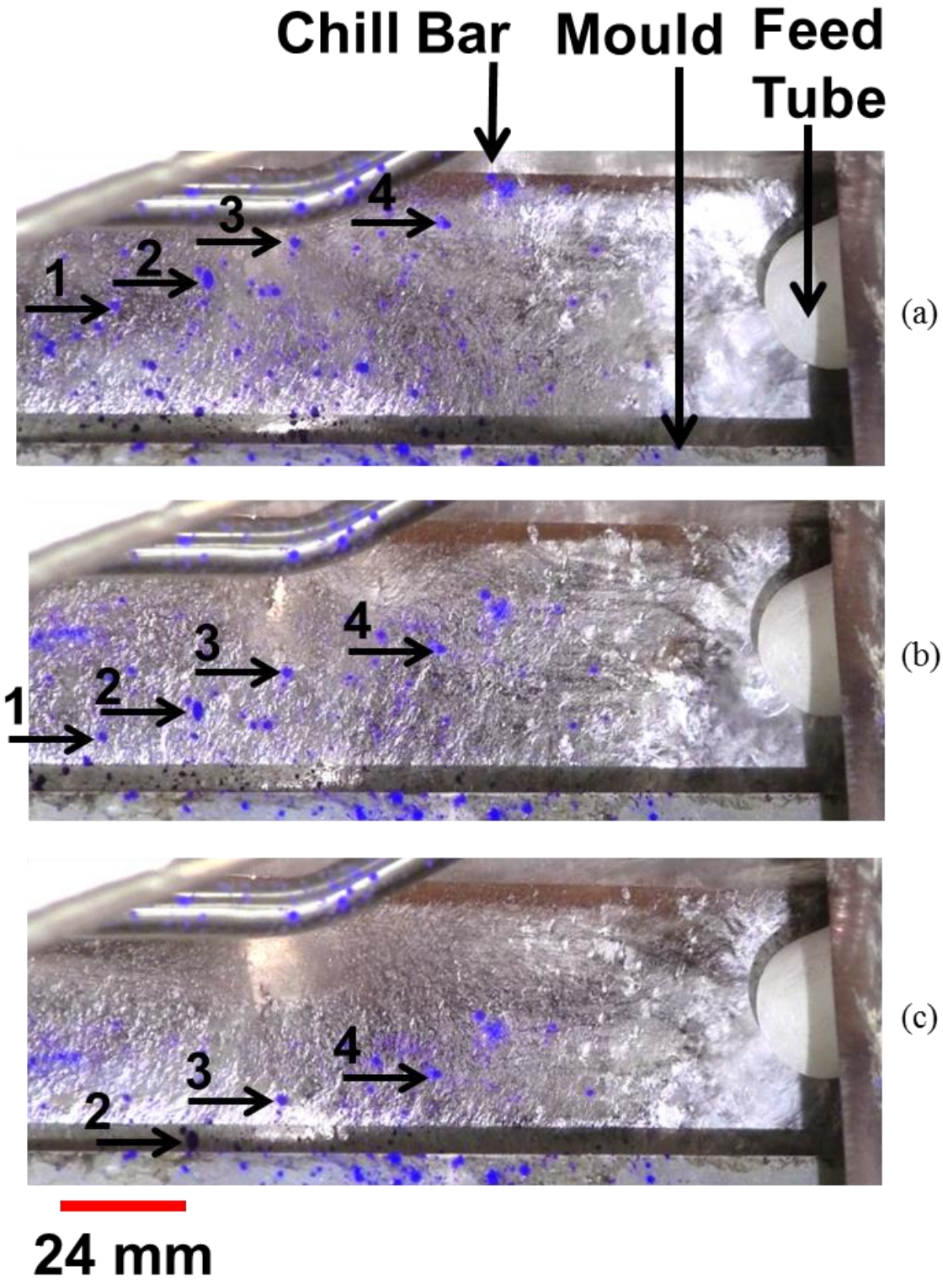

Figure 4-11 – Video images of clad sump surface oxide (FOV_1) for casting trial 2-1. (a) t = 0s, (b) t = 15s, and (c) t = 30s.

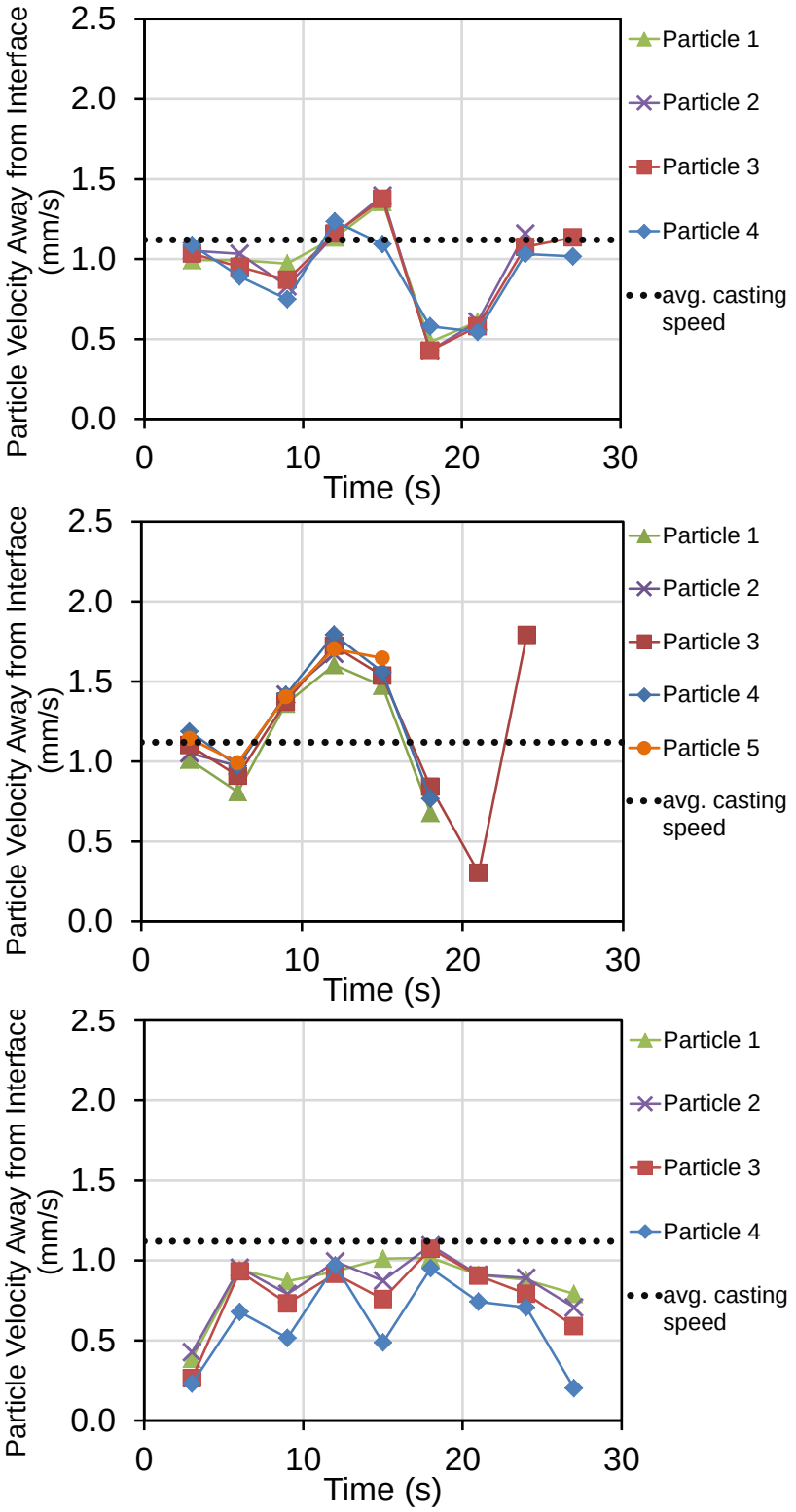

Figure 4-12 – Measured velocity of clad sump oxide for three different segments, (a)-(c), recorded during casting trial 2-1.

The surface oxide on the core alloy liquid sump was also recorded during casting trials 2-3 and 2-3. The field of view, FOV_2, for these recordings is depicted in Figure 4-10. An example of the surface oxide motion taken from still images of the recording is shown in Figure 4-13. As shown, by tracking the movement of individual particles between video images, the surface oxide on the core liquid sump also moves away from the core/clad interface and towards the closest mould and ingot surface. Qualitatively, the motion on this sump was not constant with time. Periods of time were observed where the oxide remained stagnant. The motion of the oxide appeared to be associated with visual observation of cracking of the surface oxide or fluctuation of the liquid meniscus at the chill bar or the external casting mould. When motion of the oxide surface was initiated by the aforementioned cracking, the speed of the oxide motion appeared to be greater than the casting speed.

Analyzing still images of the video recordings, the oxide motion was quantified, and the results are shown in Figure 4-14. Spikes in the oxide motion were observed in all three segments which were analyzed. These spikes were visually linked to either cracking or meniscus fluctuations. Throughout the periods in time between these spikes in oxide motion, the oxide was relatively stagnant, and much lower than the average casting speed. Again, the observed oxide motion is not consistent, in either speed or direction, with the core liquid surface velocities predicted from the thermofluid model calculations, see Figure 4-4.

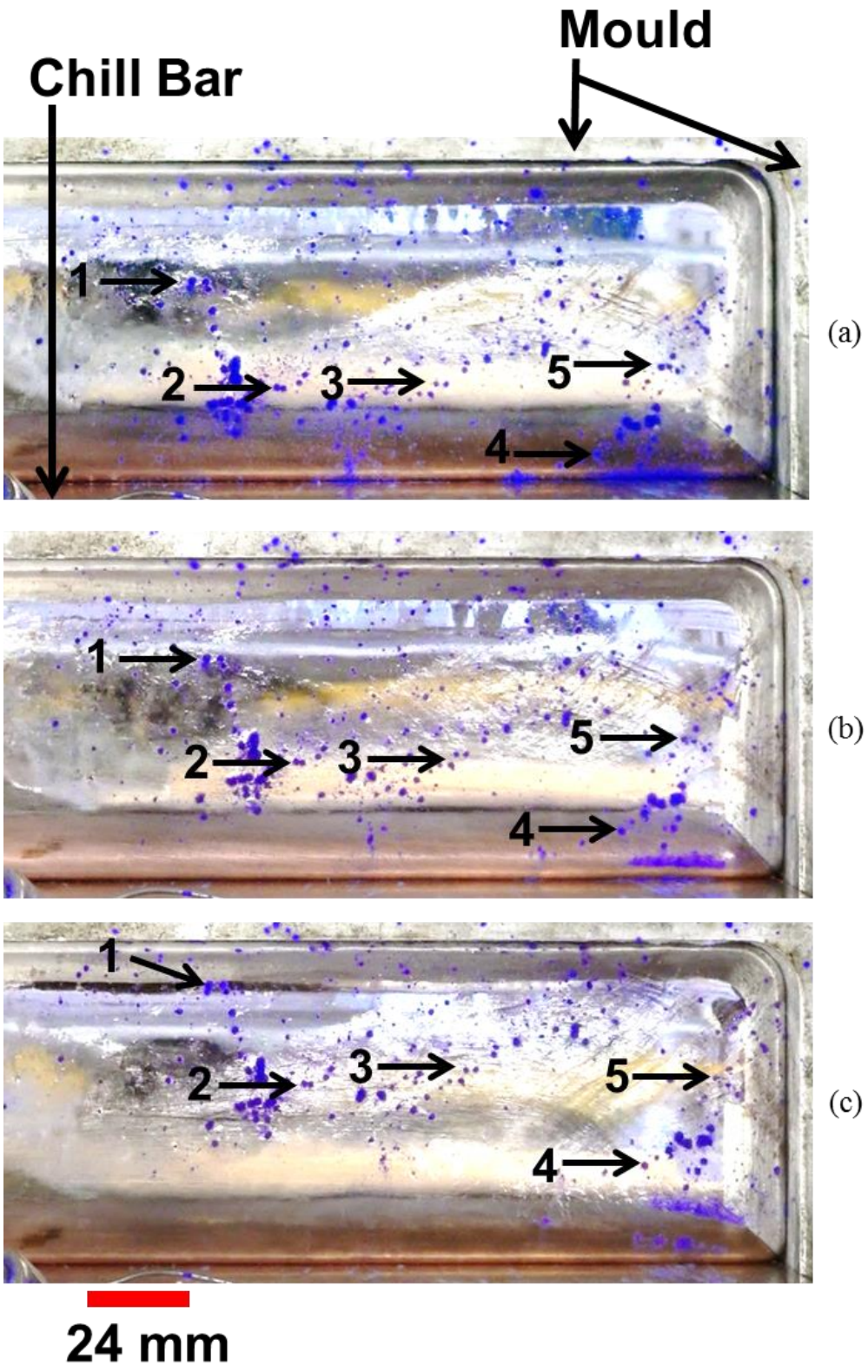

Figure 4-13 – Video images of core sump surface oxide (FOV_2) for casting trial 2-2. (a) t = 0s, (b) t = 15s, (c) t = 30s.

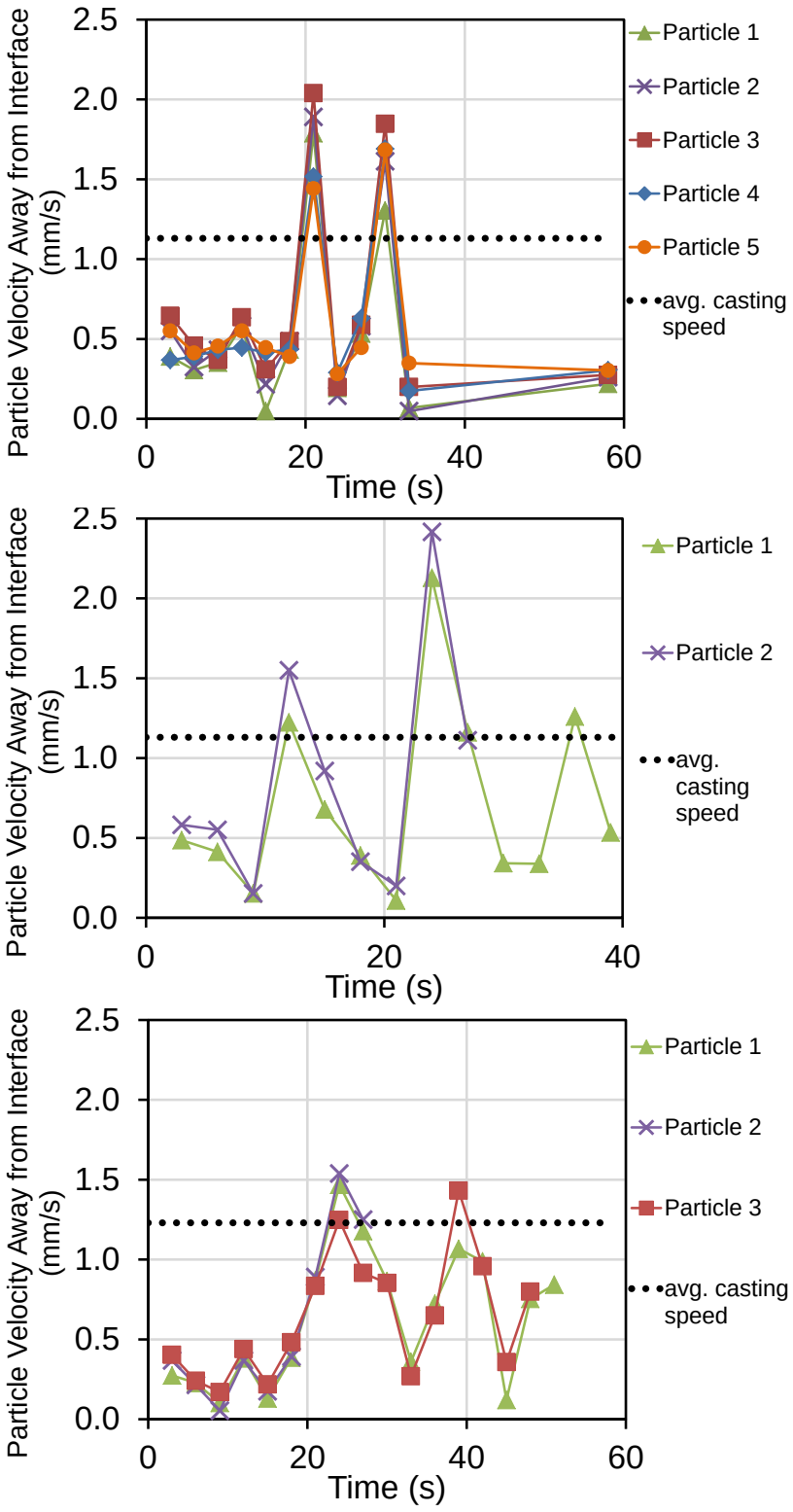

Figure 4-14 – Measured velocity of core sump oxide for three different segments, (a)-(b) recorded during casting trial 2-2, (c) recorded during casting trial 2-3.

4.3.1 Discussion

A schematic of the oxide motion observed during Fusion™ casting trials is shown in Figure 4-15. For both the core and clad, the oxides on top of their respective sumps moved away from the chill bar. As such, this would suggest that the contact condition between the AA3003 solid shell and the AA4045 clad liquid should be free of oxide entrainment from the AA4045 oxide. The AA4045 liquid will be in intimate contact with the surface of the AA3003 shell (surface of AA3003 to be examined in detail in Section 4.4).

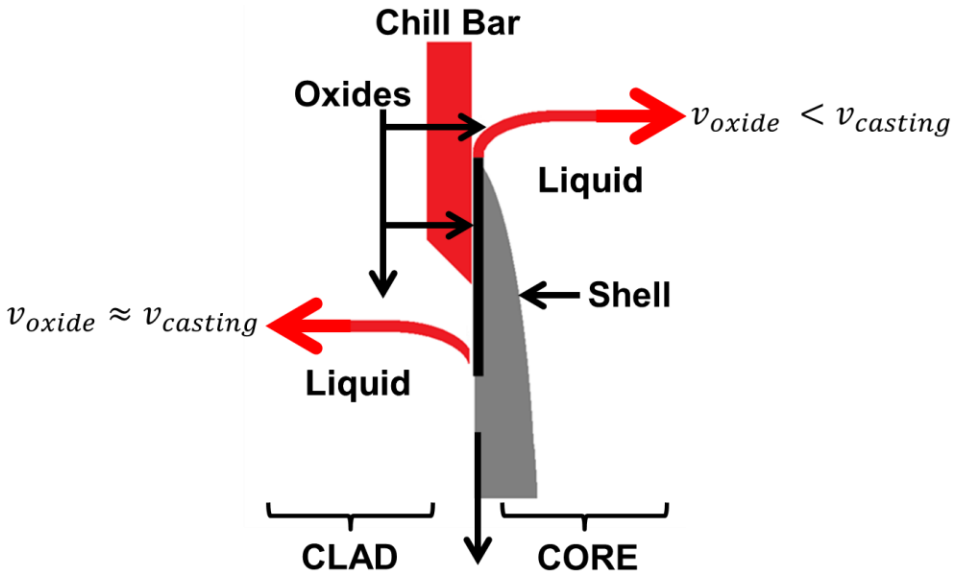

Figure 4-15 – Observed direction of oxide motion on core and clad alloy sump surfaces.

While both oxide films were observed to move away from the chill bar, the observed motion of the core and clad sumps (as in Figure 4-15) were physically different. The clad oxide was observed to move with a more or less constant speed, equivalent to that of the casting speed. The core oxide moved in a more sporadic/jerky fashion. It was stagnant at times, with no observable motion, and when it did eventually move it was coincident with points in time where fracture of the oxide film was observed.

The observed motion of the clad sump oxide film can be explained by examining the full section of a Fusion™ ingot during the casting process, shown in Figure 4-16. On the clad side of the Fusion™ ingot, a solid shell solidifies against the periphery of the external mould, whereas no shell forms at the interface. The shell provides an anchoring point for the clad sump oxide to adhere to (for 3 of the 4 sides, when viewed from above). As the ingot is cast with speed *v*, the anchored oxide moves with the clad shell as it is adhered to it. If the oxide film remains unbroken at the meniscus, and is connected simultaneously to the solidifying shell as well as the clad sump oxide film, the downward motion of the shell (from casting) will translate to motion of the oxide film away from the interface, with a speed more or less equivalent to the casting speed. Additionally, the predicted fluid flow in the clad sump could potentially aid in the observed oxide film motion, as the calculated flow patterns along the top surface of the sump runs from the interface to the external mould, see Figure 4-4. While the surface velocities may not be accurate, since the thermofluid model does not account for oxide film growth, the surface velocities would be representative of fluid flow just beneath the growing clad sump surface oxide. That the flow runs away from the interface suggests that the oxide will also have a net shear acting on its underside, in the direction away from the interface, which could aid the oxide film motion.

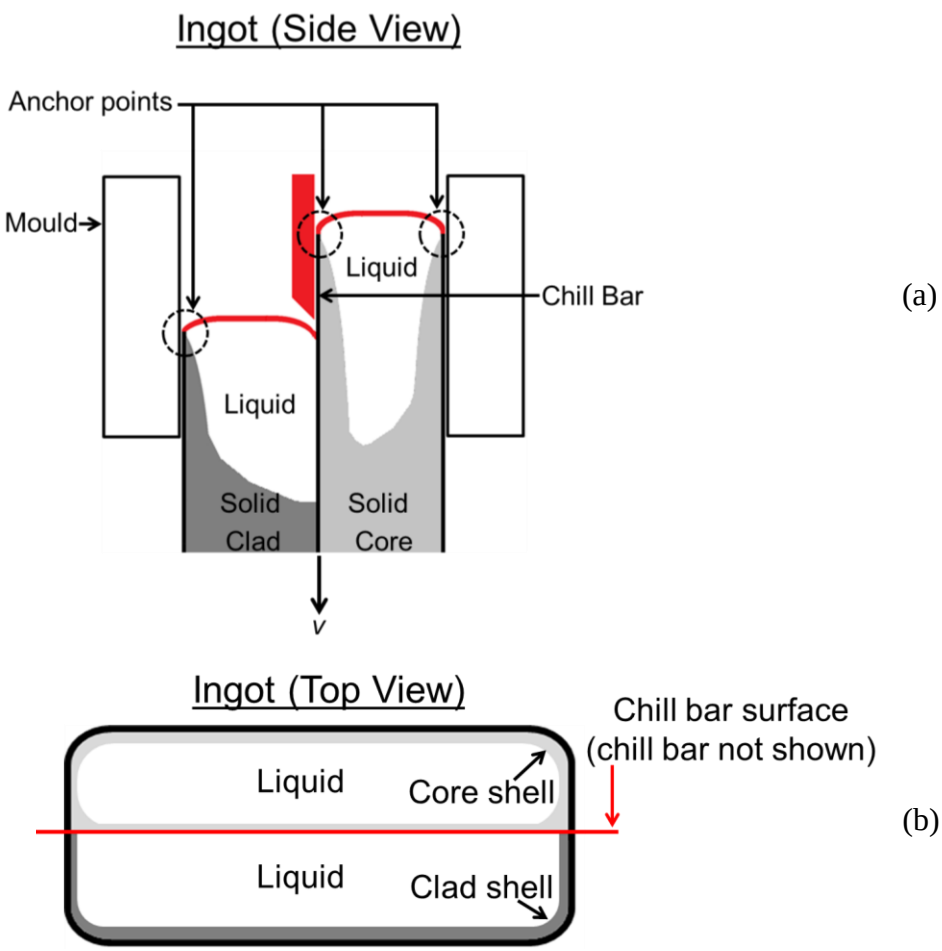

Figure 4-16 – (a) Side view of Fusion™ casting process, showing core and clad shell formation on the mould and chill bar and potential anchoring point for oxide films. (b) Top view of Fusion™ casting process showing shell formation around the periphery of the mould and along the chill bar.

On the core side, the observed oxide film on top the core sump was noticeably more stable than the clad oxide. Unlike the clad, on the core side of the Fusion™ ingot, a solid shell solidifies against both the external mould and the chill bar, thus forming a complete shell around the periphery of the core sump, as depicted in Figure 4-16b. Having a solid shell around the entire periphery of the sump may have contributed to the relative stability of the oxide film on the core sump in comparison to the clad sump. Additionally, the core liquid was fed into the mould using a submerged inlet tube, minimizing any turbulence due to the metal inlet flow. Motion of the oxide film, was predominately away from the chill bar, and seemed to only occur

when simultaneous cracking of the oxide film was observed. The motion of the surface oxide in the direction away from the chill bar is due to the asymmetry in solidification of the AA3003. As shown in the CFD model predictions in Figure 4-2 and in the study by Caron *et al.* [22], the shell which forms against the chill bar may not be at the same height as the shell which forms against the external mould, this is particularly evident when looking at the 1.0 f_s contour. Furthermore, observations by Caron *et al.* [22] from zinc-poisoned sump profiles of the Fusion™ casting process (see Figure 12 and 13 in [22]) confirm this asymmetry. Specifically, the shell which forms against the external mould was found to form at a slightly higher position in the mould relative to the shell against the chill bar. As such, this would suggest that the anchor point on the chill bar is not as strong an anchor as the remaining three sides, and when the oxide film does crack, it would likely be dragged by the stronger anchors, i.e., away from the chill bar.

Oxidation of the AA3003 chill surface

From the observations of the oxide film motion on the core sump, it was evident that the oxide is either stagnant, or moves away from the core/clad interface and towards the exterior casting mould. As the AA3003 shell solidifies against the chill bar, in Figure 4-15, thermal contraction of the AA3003 due to density differences between liquid and solid AA3003 should create a small gap between the chill bar and the AA3003 shell, allowing for air ingress and oxidation of the AA3003 surface. Assuming air ingress occurs, the thermofluid predictions from Section 4.2 can be used to calculate the approximate oxide growth on the surface of the AA3003 shell prior to it coming into contact with AA4045 liquid. Before any detailed observations of the AA3003 chill cast surface (see the proceeding section), these oxidation calculations provided a useful first estimate of the AA3003 surface oxidation that could be expected prior the point where the AA3003 core shell comes into contact with the AA4045 clad during the Fusion casting process.

The relevant time for oxidation of the surface of the core ingot shell which eventually comes into contact with liquid clad is the time it takes for the shell to traverse the vertical distance from initial solidification: i.e., z = 0 mm, x = 0 mm in Figure 4-5, to the point of contact with the liquid, z = -30 mm, x = 0 mm in Figure 4-5. Again, using the concept of casting time, t, being the distance z divided by the casting speed v, we can generate a series of temperature profiles which can be used to calculate surface oxidation. Using temperature profiles from casting trial 2-1 (casting speed of 1.12 mm/s), the resulting oxidation growth is plotted in Figure 4-17. The calculated oxide thickness is relatively insensitive to the position along the width of the Fusion™. While the oxidation kinetics are reduced slightly at the edges of the ingot, due to the corresponding decrease in surface temperatures, this is only of minor influence as the total time available for oxidation is constant and controlled by the casting speed. The predicted level of surface oxidation is somewhere between 17 and 20 nm.

The presence and amount of AA3003 surface oxidation will likely play a role in the AA3003/AA4045 bond formation process. The values predicted in Figure 4-17 are non-negligible. Furthermore, assuming that the oxide growth is uniformly grown over the AA3003 surface, one can conclude that some physical mechanism is necessary to render the AA3003 surface oxide penetrable or to chemically alter the oxide such that AA3003/AA4045 interaction can take place (see Section 2.3.3.1).

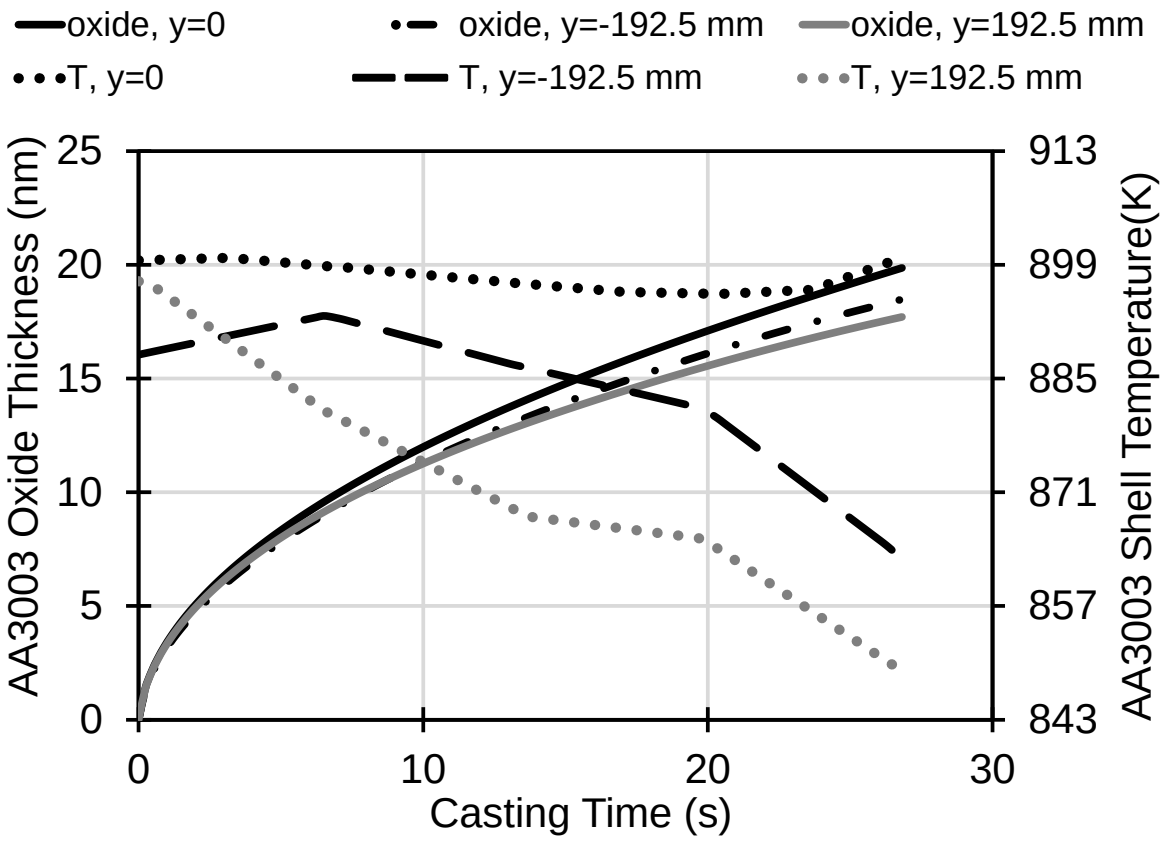

Figure 4-17 – Model calculated core alloy surface temperatures, and corresponding surface oxide growth. Casting speed of 1.12 mm/s.

4.4 Observations of the AA3003 chill cast surface

In this section, analysis of the AA3003 surface structure that was cast against the chill bar during the "interrupted" casting trial, number 2-1 (see Section 3.2.1.2), is presented. To re-iterate, in this test, the clad liquid metal flow was stopped during continuous casting of the Fusion™ ingot, in order to produce an AA3003 surface equivalent to the surface structure which would come into contact with the liquid clad during steady state Fusion™ casting. The top portion of the resulting ingot is schematically depicted in Figure 3-8, the specific region of interest is the 36 mm length of ingot, referred to as the 'chill bar' region.

Macroscopic images of the AA3003 core surface in contact with the chill bar surface are shown in Figure 4-18. Figures 4-18a and b are photographs of the AA3003 core surface taken between y = -102 mm and y = +102 mm along the width of the Fusion™ ingot. The image on the far right is from the edge of the ingot. On all samples, there are visible protrusions on the solidified surface; however, there appears to be a lower density of these protrusions near the edge of the ingot. The density of these protrusions (aside from the edges of the ingot) was variable, with no discernable trend with respect to position along the width of the ingot. The area surrounding these protrusions was relatively smooth, as indicated by the region outlined on the second image from the left. These protrusions are consistent with what might be expected to occur during local/partial remelting of the AA3003 and exudation of interdendritic liquid at the surface.

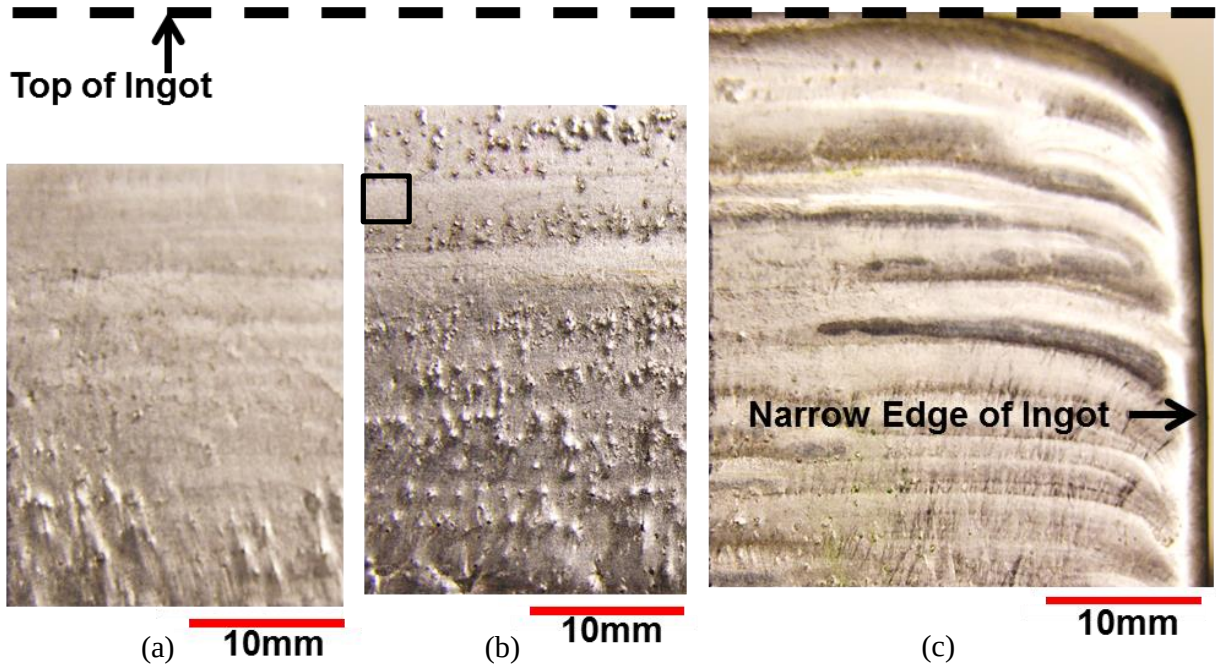

Figure 4-18 – Macro view of surface of AA3003 shell which was cast against the chill bar and preserved in casting trial 2-1. (a) and (b) are sections taken along the width of the ingot between y = -102 mm and y = +102 mm. (c) A section taken from the edge of the ingot.

As a first means to assess the structure of the surface, it was compared to that of the AA3003 centre material from the same ingot. Using optical microscopy, shown in Figure 4-19, the difference in structure is readily apparent. The surface structure appears to be much finer, and the intermetallic phases (dark gray) cover a larger area within the field of view shown.

Using carefully prepared DSC samples, described in Section 3.1.3, remelting tests were performed on bulk and surface structure samples. The DSC curves obtained from both the bulk AA3003 structure as well as the surface structure are shown in Figure 4-20. In Figure 4-20a the DSC results from the fast heating tests are shown. In both test samples, there were no observed signs of early onset of remelting, i.e., at the Scheil calculated solidus temperature of 849 K (576 °C, see Figure 2-6) there was no observed deviation of the heat flow from the baseline value, suggesting no reaction was taking place. Additionally, there was no visible difference between the two samples, in terms of the onset of remelting. However, looking at the slow heating rates tests, shown in Figure 4-20b, the differences between the bulk AA3003 and surface structure AA3003 became apparent. The first peak of the curve corresponds to melting of the $Al_6(Fe,Mn)$ intermetallics, while the second and more prominent peak is the primary aluminum melting peak. As observed, there was a noticeable difference in the ratios of intermetallic to primary Al peak heights. For the surface structure DSC samples, the intermetallic peak is much larger than the corresponding peak in the bulk AA3003 samples. This suggests that the region has a higher volume of intermetallic than the bulk does, confirming the observations from Figure 4-19.

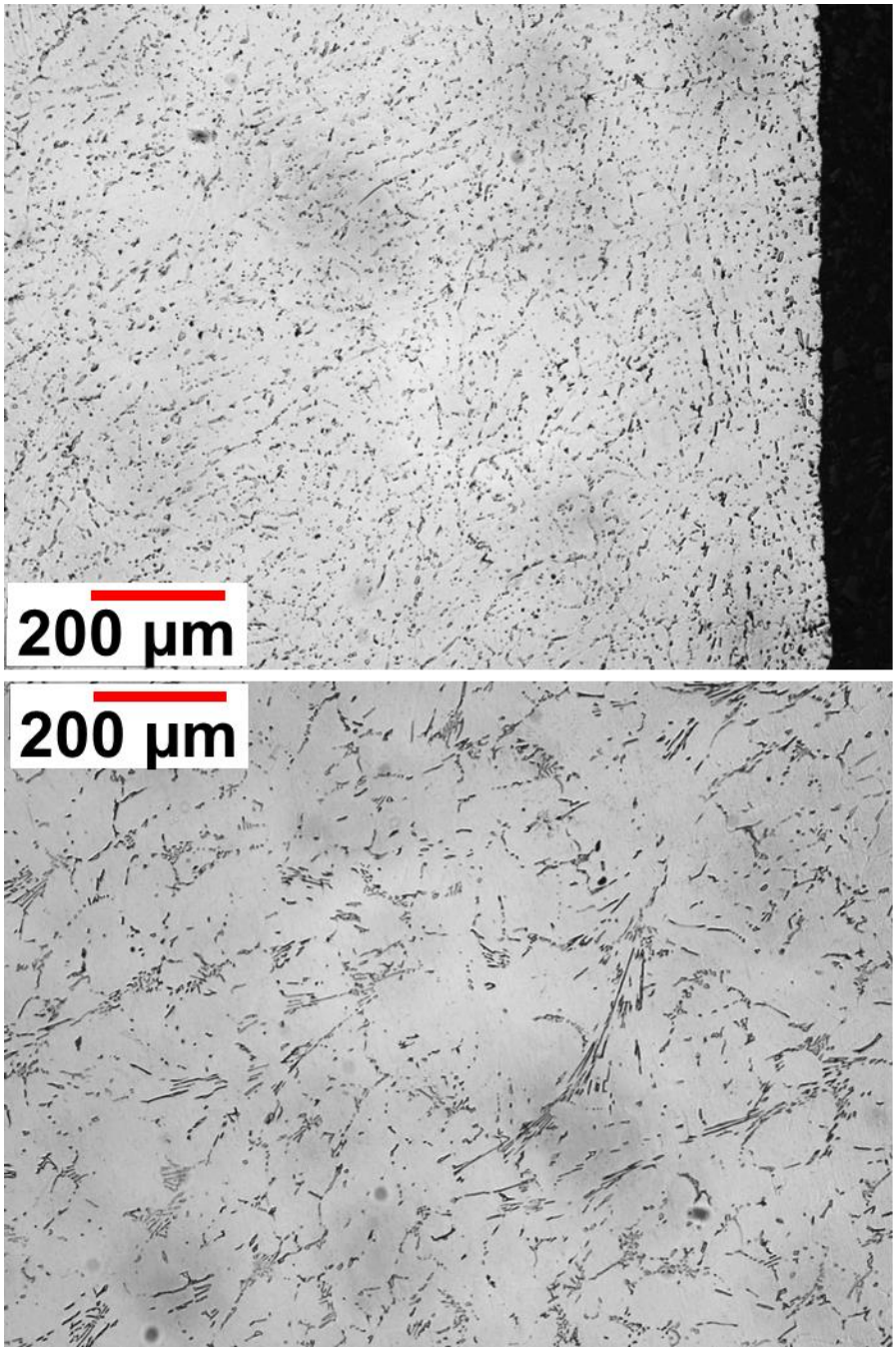

Figure 4-19 – Longitudinal sections of AA3003, (a) cast against chill bar (right side of figure was in contact with chill) and (b) centre AA3003 of the core section.

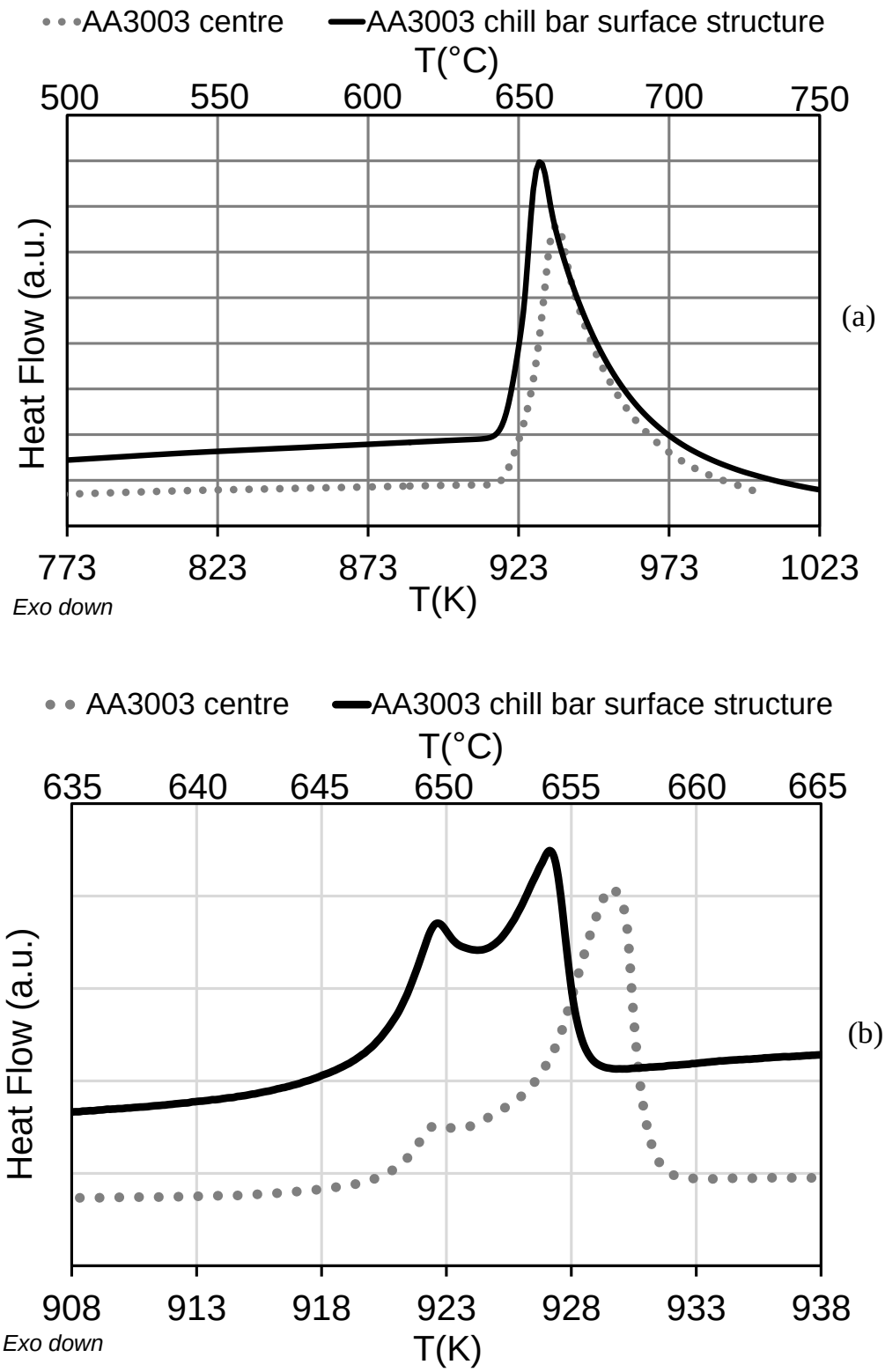

Figure 4-20 – DSC results for Fusion™ cast AA3003 material. Bulk AA3003 material (dotted line) and AA3003 cast against the chill bar, taken from casting 1 (black solid line). (a) Samples heated at 0.83 K/s. (b) Samples heated to 878 K in less than 10 minutes than heated through phase transition at a rate of 0.017 K/s.

The onset of remelting was measured, using the method of intersecting tangent lines [100-101]. The results are compiled in Table 4-2. Despite the difference in relative peak heights, the onset of remelting for both the surface structure and the bulk ingot samples are similar. There does appear to be a 2 K reduction in the onset of remelting temperature, for the chill bar surface structure, for the test conducted at the 0.83 K/s heating rate. For the low heating rate tests, this difference in onset of remelting between the surface structure and the bulk ingot is within the tests standard deviation. The onset temperatures measured using the intersecting tangent lines appear to be consistent with the equilibrium calculated solidus temperature for AA3003, 915 K (642 °C, see Figure 2-6). The deviation of 5 K (°C) may be due to the bias associated with the tangent line method when used on DSC curves that exhibit a low initial deviation/curvature from the baseline signal. A more appropriate method in these cases may be to use the 2nd derivative of the DSC signal to determine the onset of deviation from the baseline DSC signal. Regardless, the DSC results in Figure 4-20b, suggested there is a microstructural difference between the bulk AA3003 material and the chill surface structure; which is the structure which comes into contact with AA4045 liquid during Fusion™ casting. These differences in structure did not relate to measureable differences in the onset of remelting at low heating rates, as shown in Table 4-2.

Table 4-2 – AA3003 onset of remelting measurements from Fusion™ AA3003 samples measured with DSC. *n* indicates the number of times each test was repeated, and σ represents the calculated standard deviation in the measured results.

	Heating Rate (K/s)	***n***	***1st peak, Onset, K,(°C)***	***σ (K)***	***2nd peak, Onset, K,(°C)***	***σ (K)***
bulk	0.017	5	920.2 (647.2)	0.3	925.3 (652.3)	0.2
	0.33	2	920.6 (647.6)	0.05	-	-
	0.83	1	920.7 (647.7)	-	-	-
chill bar surface structure	0.017	5	919.9 (646.9)	0.3	923.3 (650.3)	0.4
	0.33	1	919.1 (646.1)	-	-	-
	0.83	1	918.8 (645.8)	-	-	-

A longitudinal section taken through a surface protrusion, shown macroscopically in Figure 4-18, was also prepared and is presented in Figure 4-21. The protrusion, clearly labelled in the figure, has caused a discontinuity on the surface. Any oxide present at the surface, prior to formation of these exuded spots, would likely be fracture/ruptured. Additionally, a large number of partially transformed intermetallics, from $Al_6(Fe,Mn)$ to $Al_{15}(Fe,Mn)_3Si_2$, were observed in the region near the protruded material, examples are encircled in black in Figure 4-21. Intermetallic material with a thin channel-like morphology was also observed in the chill surface structure and specifically near the protruded surface site in Figure 4-21, indicated with black arrows in Figure 4-21. The shape of these channels suggest that connective pathways between interdendretic fluid were present during casting. One of the channels is also shown to intersect the surface, as indicated by the black arrows on the bottom of Figure 4-21. This is qualitatively similar to the spot exudation mechanism discussed by Morishita *et al.* [81].

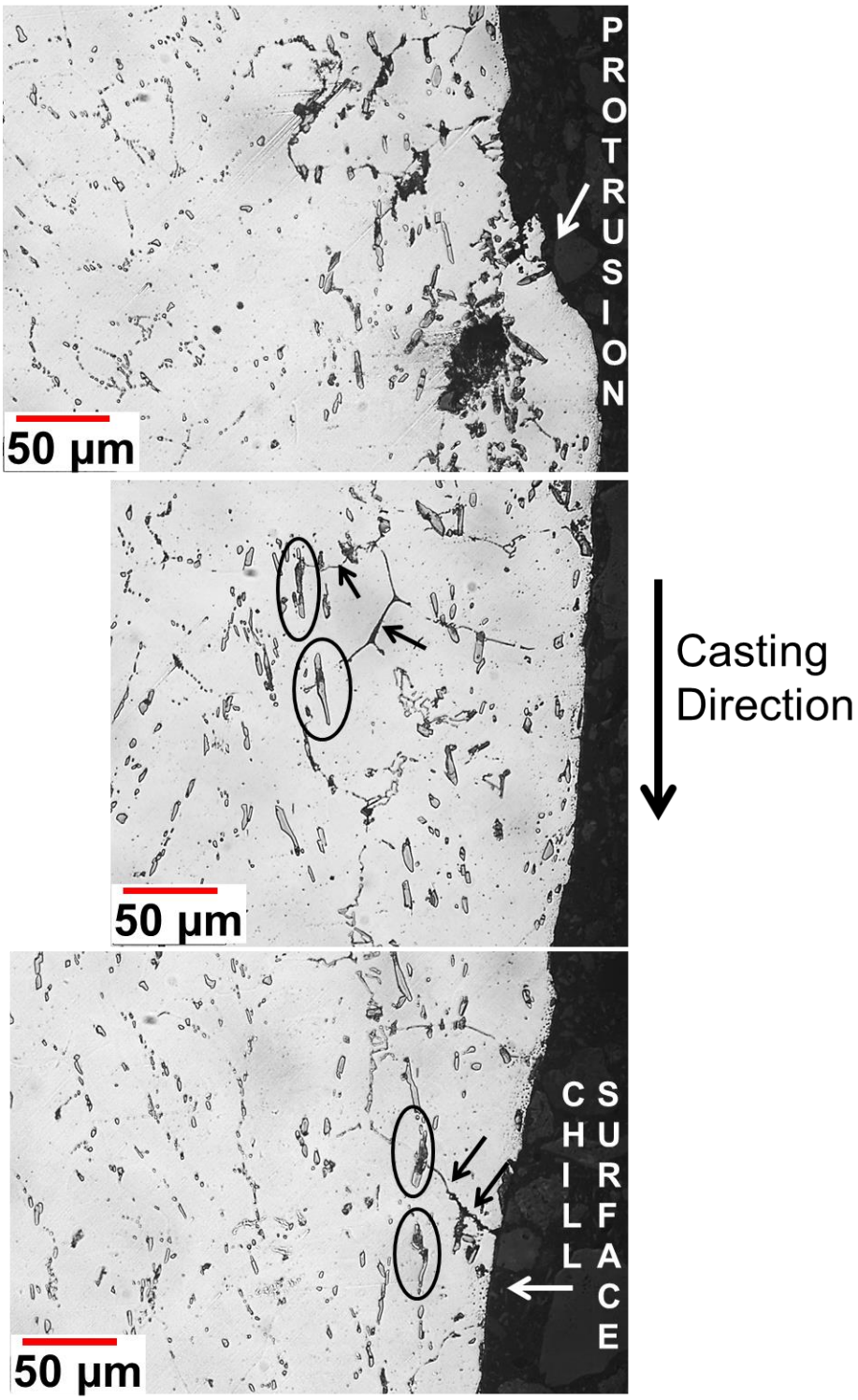

Figure 4-21 – Longitudinal samples of AA3003 chill surface structure near a surface protrusion site.

The observation of protrusions, partially transformed intermetallics, and intermetallics with channel-like morphology suggest that some local remelting of the chill surface had indeed taken place during this "interrupted" Fusion™ casting. It should be noted that the evidence of local remelting, specifically the protrusions on the chill bar surface, were seen at locations where the thermofluid calculations did not predict any reheating of AA3003 at the interface. On the rightmost image of Figure 4-18, protrusions were observed to be within ~20 mm from the edge of the ingot, where as in thermofluid calculations shown in Figure 4-8 predict no reheating within a 40 to 50 mm proximity of the edge of the ingot.

In addition to optical metallography, the sample surface was examined using a SEM. Looking at a smooth region of the surface, (i.e., the smooth region of the chill bar surface structure in Figure 4-18b) a typical surface is shown in Figure 4-22. Examining the image, the intermetallics particles which are present at the surface are predominantly long and narrow, with their long axis parallel to the casting direction. In conjunction with the optical metallographs presented in Figure 4-21, this suggests that the intermetallics at the surface have undergone some degree of transformation as well. Additionally, instances on the surface where the $Al_6(Fe,Mn)$ intermetallics have partially transformed into the $Al_{15}(Fe,Mn)_3Si_2$ phase, in both the encircled region in Figure 4-22 can be seen.

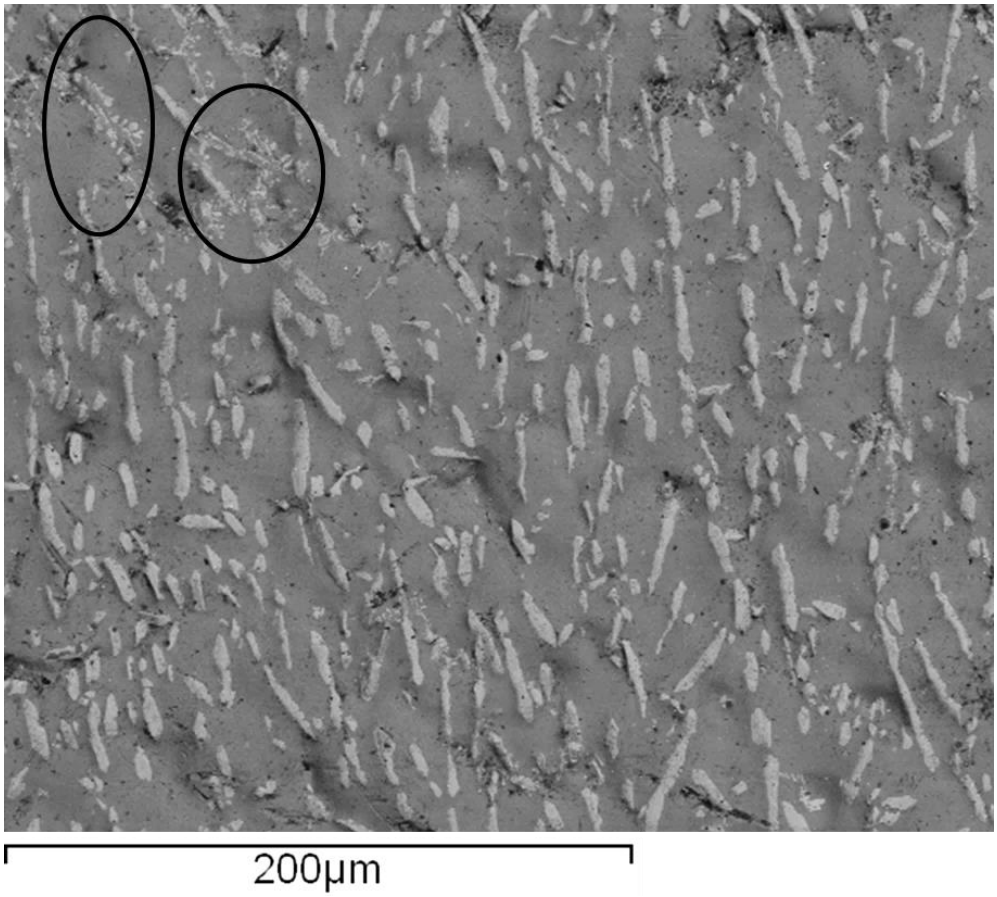

Figure 4-22 – Backscattered electron image of surface morphology of AA3003 solidified against the chill bar. Encircled area shows intermetallic particles partially transformed from $Al_6(Fe,Mn)$ to $Al_{15}(Fe,Mn)_3Si_2$.

The surface of a protruded area was also observed with SEM, see Figure 4-23a and b. In (a) the protrusion is clearly visible in the centre of the secondary electron image. It appears as a raised area on the surface. Imaging using a backscattered electron signal of the area enclosed by the black box in (a), the intermetallics at the surface can be resolved in more detail. In (b) we clearly see that the intermetallics at the surface appear to be partially transformed to the $Al_{15}(Fe,Mn)_3Si_2$ phase. This agrees with the observations from cross-sections made shown in Figure 4-21.

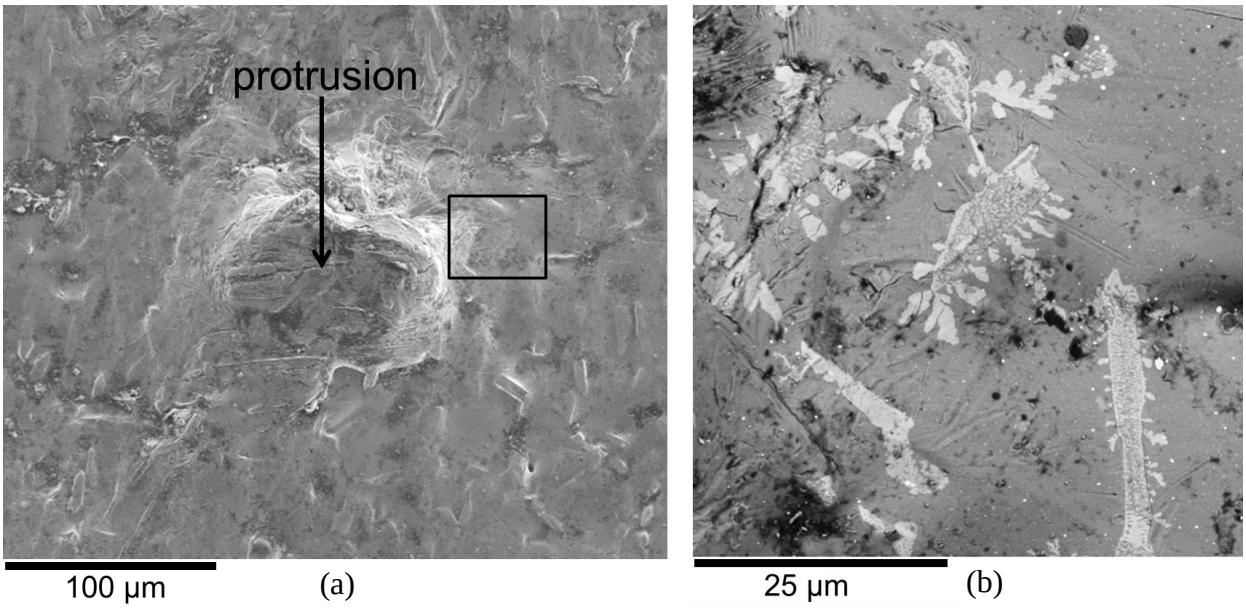

Figure 4-23 – Surface protrusion (a) low magnification secondary electron image and (b) high magnification backscattered electron image of the boxed region indicated in (a) with a black box.

The presence of surface oxides was also examined. Qualitatively, oxide films could be seen on samples when imaged with secondary electrons, see Figure 4-24a. In this image, two pieces of evidence suggested that oxides films are present on the surface. The first, circled and labelled a, appears a series of parallel streaks resembling wrinkles or fibers. Similar behaviour has been seen in other studies to be an indication of the presence of surface oxides [102-103]. The second type, circled and labelled b and c, also appear as a series of lines or wrinkles. These wrinkles are typically located surrounding the edges of intermetallic particles, as clearly evident in Figure 4-24b. The origin of these wrinkles can be associated with the volumetric contraction of the: aluminum metal and intermetallics. Upon cooling of the ingot, the aluminum metal contracts at a larger rate than the intermetallics, resulting in an undulating surface profile where the intermetallics are slightly raised on the surface. The surface oxide film deforms to follow this profile, and as a result of this deformation wrinkles are formed in the oxide. A very similar

behaviour has been observed in atomic force microscopy of hot dipped Al-Zn-Si coatings; see Figure 5 in [104].

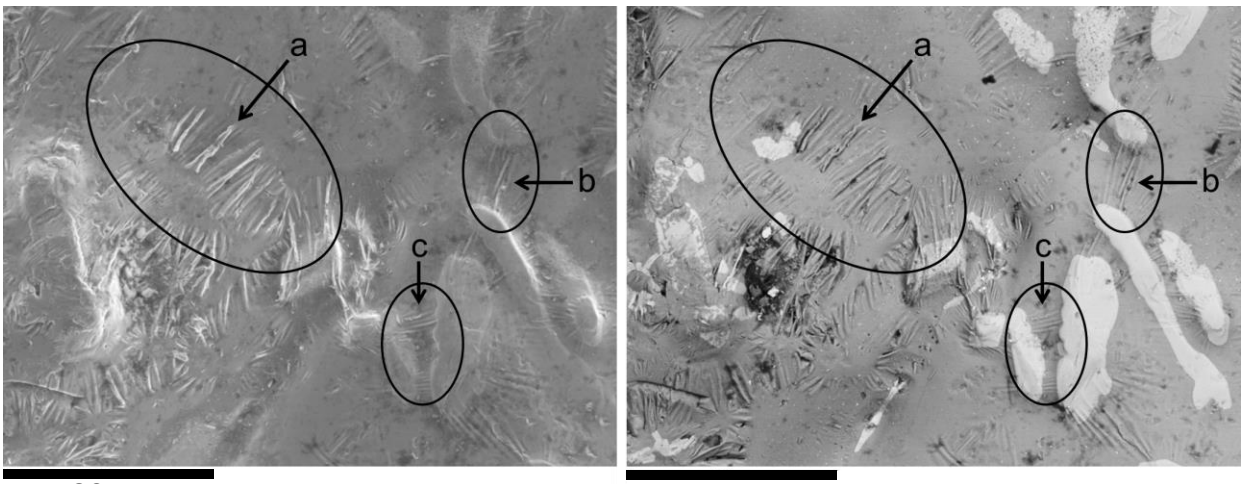

Figure 4-24 – (a) Secondary electron image of AA3003 surface structure. (b) Corresponding backscattered electron image of AA3003 surface structure.

Using the technique described in Section 3.3.2, it was apparent that an oxide film of appreciable thickness was present on the chill surface. Calculated ratios of Al and O EDS peak intensities, were appreciably greater than baseline ratios measured from air formed oxide films (2-4 nm in thickness), see Table 4-3. The spectra were obtained using a field size of 1.8 mm^2. In EDS spectra of the chill surface, only Al, O, Fe, Si, Mn, and C (contamination in the SEM chamber or during handling) no other EDS peaks were observed.

Table 4-3 – EDS and FIB-SEM results from surface of ingot cast against the chill bar, taken from the interrupted Fusion™ casting trial. *n* indicates the number of times each measurement was repeated, and σ represents the standard deviation in the measured results.

Location for EDS Data Collection	***Al/O Intensity Ratio***	***n***	**σ**	***Oxide thickness from FIB-SEM***
Chill Bar Surface	0.18	25	0.05	26 +/- 4 nm
Etched Surface	0.026	5	0.004	-

Oxide uniformity was also examined. Using a sample from the AA3003 surface in contact with the chill bar surface, FIB sectioning was performed. The surface morphology of the AA3003 surface which was sectioned was similar to that shown in Figure 4-22. Low resolution images showing the FIB sectioning process are given in Appendix C. The FIB cross-section was made to bisect both an intermetallic particle, as well as α-aluminum. A magnified view of the fabricated FIB cross-section is shown in Figure 4-25. In Figure 4-25a the W coating shows up as bright white, the α-aluminum shows up as dark grey, and the intermetallic particle was a brighter grey. The intermetallic which was sectioned, along with the aluminum, is similar to the long and thin surface intermetallics seen in Figure 4-22. In between the W coating and the aluminum, as well as between the W coating and the intermetallic, is a thin oxide layer. Under low magnification, as in Figure 4-25a it is visible but hard to measure. Under higher magnification, as in Figure 4-25b and c, although the SEM cannot pick up a high level of detail, the oxide layer thickness can be distinguished. Examination of Figure 4-22b confirms an oxide layer of about 26 nm thick over the aluminum. It is interesting to note that the oxide on top of the α-aluminum region Figure 4-25b appears to be more uniform than the oxide above the intermetallic particle shown in Figure 4-25c as well as slightly thicker. The oxide layer in Figure 4-25c is difficult to identify and measure with the resolution of the SEM used, the faint line overtop the intermetallic particle in Figure 4-25a and c as well as the observations of oxide wrinkling in Figure 4-24b suggest that some thin oxide is present over the intermetallics.

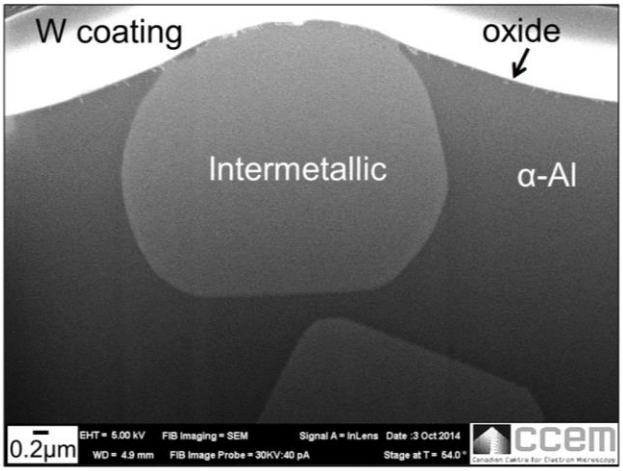

(a)

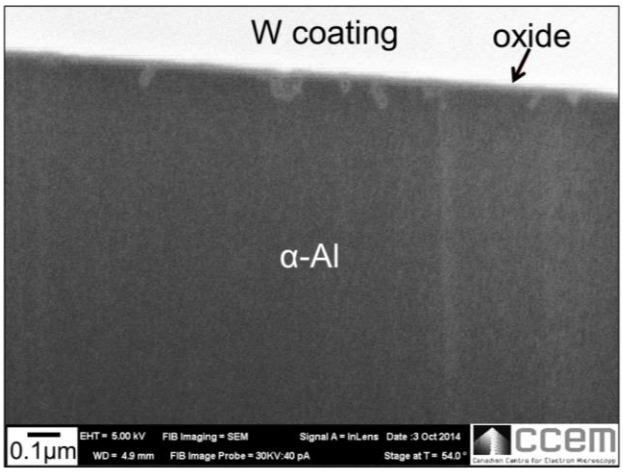

(b)

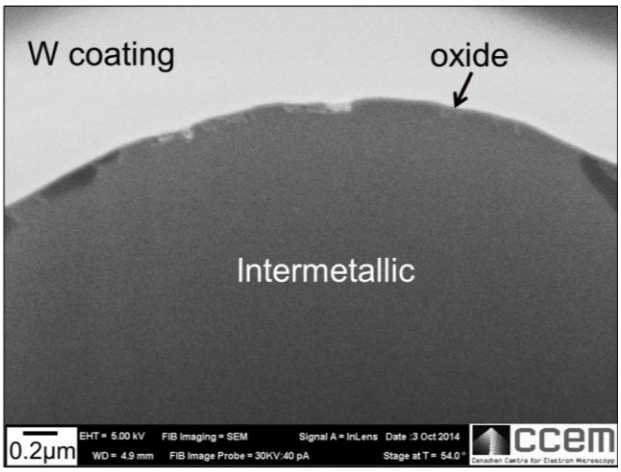

(c)

Figure 4-25 – Secondary electron imaging of FIB cross section from chill bar cast surface. (a) low magnification image of the section, (b) high magnification image of the area above the primary aluminum, and (c) high magnification image of the area above the intermetallic particle.

In addition to studying the top portion of the AA3003 surface structure that was cast against the chill bar during the "interrupted" casting trial, the AA3003 surface just above the final point of contact between the AA3003 shell and AA4045 liquid was also examined. The region of interest is depicted schematically in Figure 4-26. This region of the AA3003 shell, while never coming in contact with AA4045, coincides with the point of time during the interrupted casting, described in Section 3.2.1.2 and Figure 3-7, where pouring of the AA4045 liquid metal was stopped. Despite not knowing the thermal history of the AA3003 shell at this

location, it is still of importance to examine as it may be the closest representation of the the AA3003 chill cast surface which comes into contact with AA4045 liquid metal during Fusion™ casting. As such, two samples were examined using SEM. Two samples were examined, each one taken approximately 50 mm from each side of the centerline (y = 0 mm) of the width of the Fusion™ ingot.

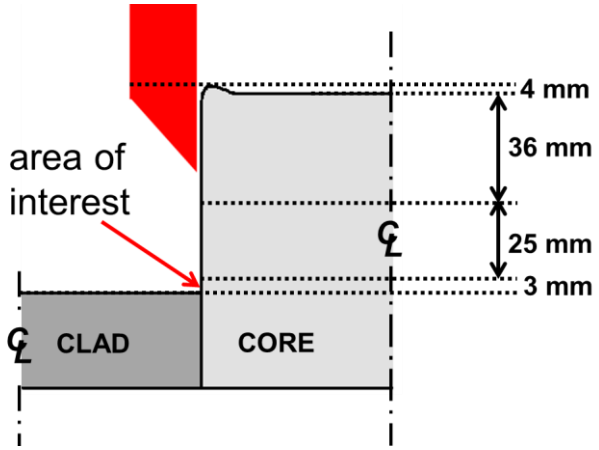

Figure 4-26 – Schematic of the "interrupted" Fusion™ cast ingot, with region of interest indicated. This was just above the last point of contact between the AA4045 liquid and the AA3003 shell.

Figure 4-27 is a SEM image typical of the surface morphology in the region defined in the preceding paragraph. The bright white particles, labelled b in the figure, were intermetallics present on the surface of the AA3003, similar in morphology to those shown in Figure 4-22. Clusters of Mg rich crystals, labelled a in the figure, were also observed on the surface in this region. As shown in Figure 4-27, the crystals appear to be predominately located above the surface intermetallics. The spaces between the intermetallics, i.e., the α-aluminum, also had Mg present at its surface. This was confirmed with EDS, using a 4 kV excitation voltage. These Mg rich crystals, as well as Mg present on top of α-aluminum, were observed on both samples. Additionally, it should be noted that Mg was not observed on AA3003 surfaces examined from the top 36 mm portion of the AA3003 chill surface samples.

Even though the temperature history of the AA3003 metal in this region was unknown, the observation of Mg at the sample surfaces (observed on both samples) suggest that there was sufficient Mg in the bulk AA3003 metal (in this case only 10 ppm, see Table 3-1) to promote Mg surface segregation. This result posed the question: could low levels of Mg help promote AA3003 oxide film breakup via surface segregation of Mg and subsequent chemical reduction of AA3003 surface oxides, similar to the mechanism suggested by Terrill *et al.* [62] in vacuum brazing of aluminum? This result proved to be one of the motivating factors for the studies performed in Chapter 6.

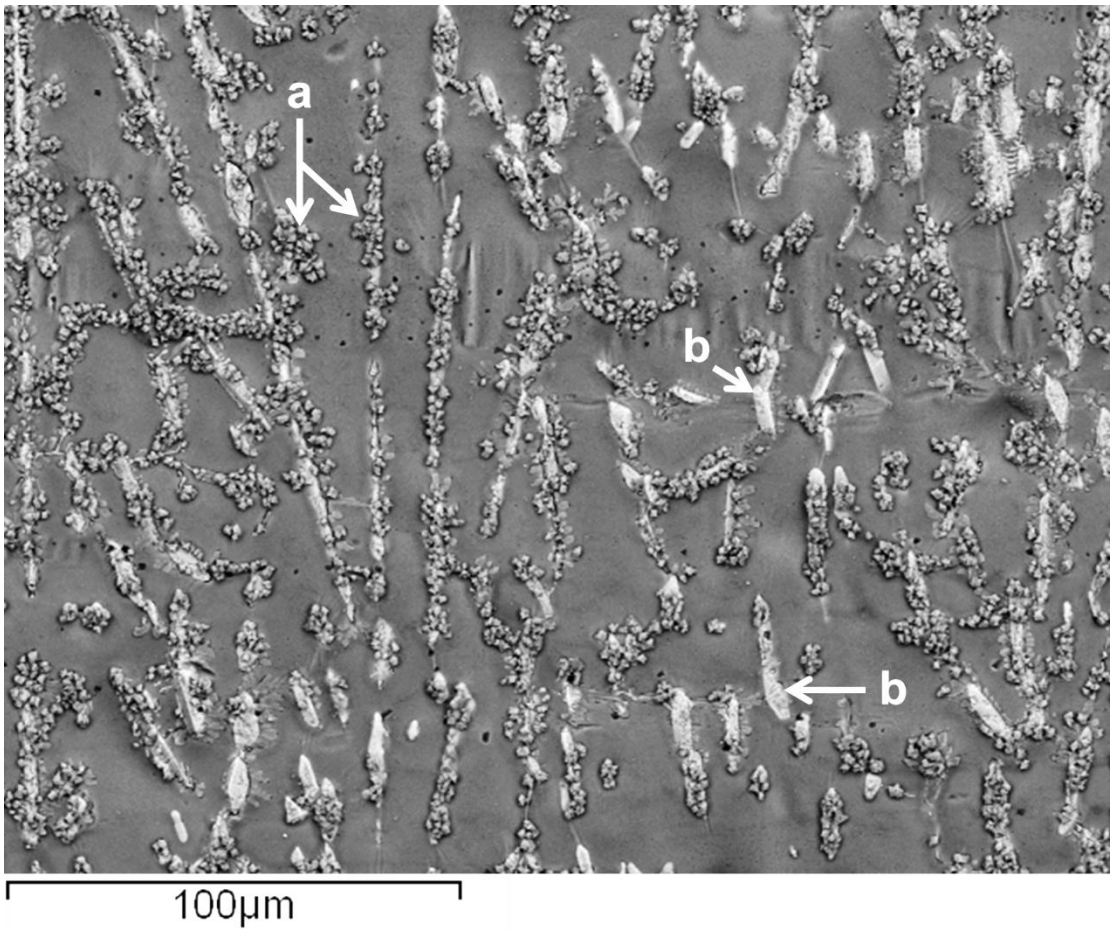

Figure 4-27 – 20 kV backscattered electron image from the surface of the area of interest depicted in Figure 4-26. Mg and O based crystals accumulated on top surface intermetallics. Mg was also present in EDS spectra from regions between intermetallic particles.

4.4.1 Discussion

Observations of the AA3003 chill surface from the interrupted cast trial, # 2-1 in Table 3-2, represent the best estimate of the surface which comes into contact with liquid AA4045 during Fusion™ casting. The key observations from analyzing this surface were:

i. An oxide film was observed on the AA3003 core surface in contact with the chill bar surface, with a thickness of ~ 25 nm.

ii. The chill surface, shows signs of "spot exudation", a local remelting phenomenon explained by Morishita *et al.* [81]. There is evidence that the density of protrusions increases from the edge of the ingot (y = +/-192.5 mm) to the centre of the ingot (y = 0 mm).

iii. A higher proportion of intermetallic phases were present in a region adjacent to the surface, which is consistent with local/partial remelting and inverse segregation.

iv. Partially transformed intermetallic particles, from the $Al_6(Fe,Mn)$ phase to the $Al_{15}(Fe,Mn)_3Si_2$ phase were observed on the chill surface.

v. The oxide film appeared thinner and non-uniform over top of the intermetallic particles on the surface.

vi. Mg segregation was not observed over the majority of the AA3003 chill surface; however, in the region just above the last point of contact between the AA3003 and AA4045 liquid (see Figure 4-26), Mg and likely Mg based oxides were found on the AA3003 surface.

Observation (i) above, that there is likely a thin oxide film covering the AA3003 chill surface prior to contact with AA4045 liquid, raises the following pertinent question: how does this oxide

film interact with liquid AA4045 once it comes into contact with it? The observations (ii) through (vi) present three possibilities.

The first possibility is illustrated in Figure 4-28. Here, the AA4045 liquid simply penetrates the oxide film through fractures/defects in the oxide film adjacent to the "spot exudations" observed on the AA3003 surface. Since the oxide film on the AA4045 sump was observed to move away from the interface (Section 4.3), the AA4405 liquid should be in intimate contact with the AA3003 shell. Therefore, any defects in the AA3003 surface oxide should be penetrable. Once penetrated by the AA4045, dissolution of the underlying AA3003 should result, along with undermining of the AA3003 surface oxide film. This is similar to the mechanistic spreading model of Wall and Milner [53], see Figure 2-3. To obtain a final bond which is metallurgically sound, sufficient contact time would be required to bridge the distance between penetration points. Upon bridging, the oxide film would then be free to break up or float away from the interface.

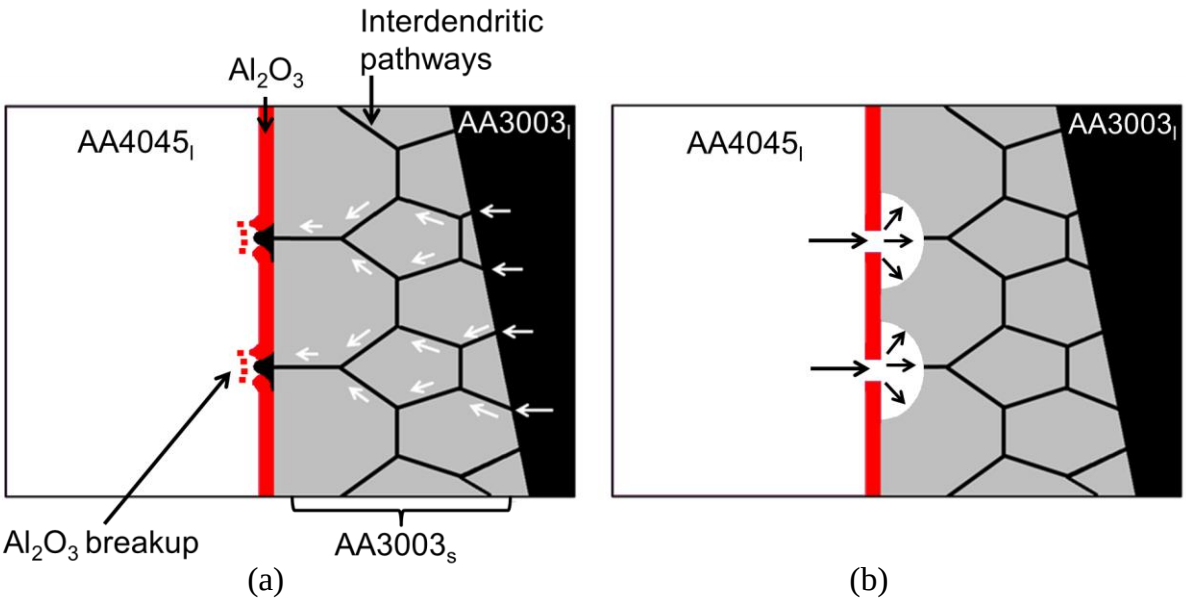

Figure 4-28 – Possible oxide penetration mechanism on AA3003. (a) Spot exudation of AA3003 shell, causing local break in oxide film and (b) site for AA4045 liquid penetration and subsequent dissolution of AA3003 shell.

The second possibility, qualitatively similar to the first, involves penetration of local defects in the AA3003 surface oxide. From observations (iii)-(iv), it can be argued that the AA3003 surface oxide is defective over the intermetallic regions.

The third possibility relies on the chemical reduction of the AA3003 surface oxide by Mg. Although, as per observation (vi), Mg was not observed on the chill surface, it was observed on the AA3003 surface just above the final point of contact with the AA4045 liquid, see Figure 4-26. While the temperature history at this exact point could not be estimated, since this was not a standard casting routine, its presence suggests the potential for Mg segregation to the AA3003 surface in this system. As such the mechanism illustrated in Figure 4-29, should not be ruled out. Here the initial Al_2O_3 surface oxide which forms is subject to Mg surface segregation when left at high temperature. The Mg then reacts with the Al_2O_3 film, creating a pathway for AA4045 liquid to penetrate the oxide layer. Thermodynamic calculations (in Appendix D) suggested that above 600 °C, only small amounts of Mg, in the range of 0.01-0.0001 wt% (depending on the thermodynamic values used for Al_2O_3) are required to chemically reduce Al_2O_3. A similar chemical reduction mechanism, for the sub-oxide spreading of gold-nickel braze alloy on stainless steel was given by Cohen *et al.* [105].

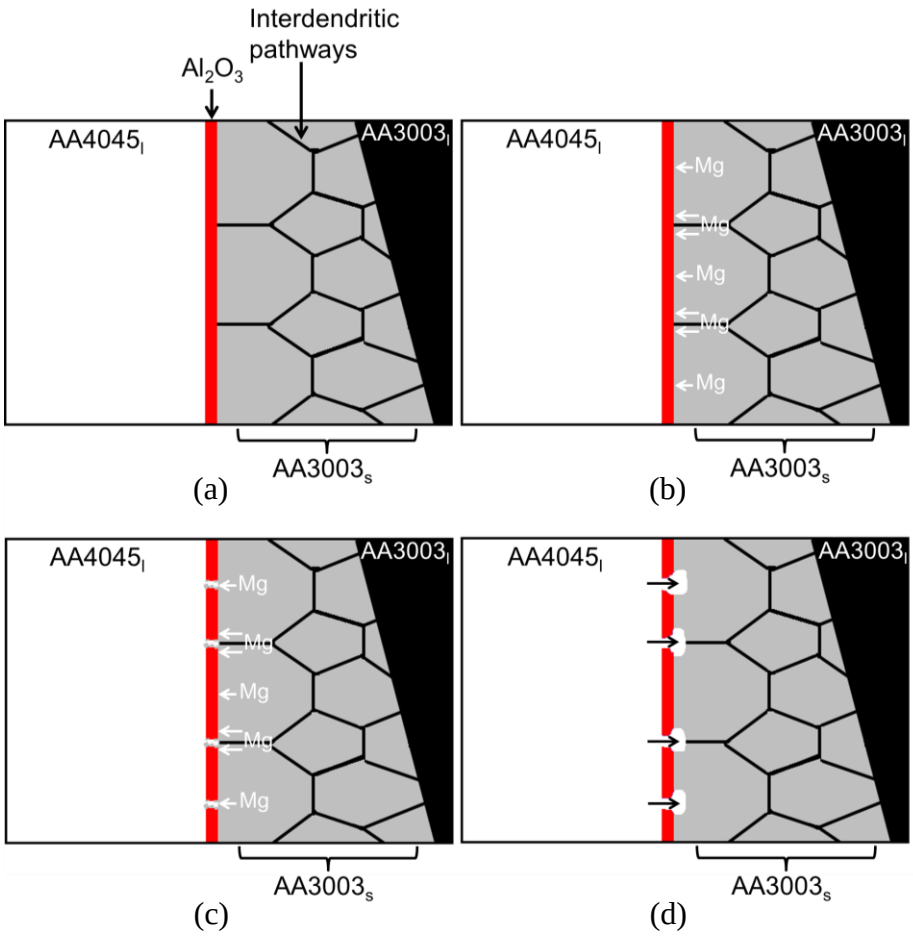

Figure 4-29 – Possible oxide penetration mechanism on AA3003. (a) AA3003 shell covered with an oxide film (b) Mg segregation to the AA3003 surface, (c) local thinning and breakdown of the AA3003 oxide film via chemical reduction by segregating Mg, and (d) penetration of AA4045 through break in surface oxide and dissolution of underlying AA3003 solid.

4.5 Observations of the as-cast interface

In this section, Fusion™ ingots were examined, with specific focus on examining the interface. Results shown from this section were taken from ingots 1-1 and 1-3, see Table 3-3. The process parameters: casting speed, and pouring temperature, for these two casting trials were identical. The casting speed was 1.27 mm/s, clad pouring temperature 898 K (625 °C), and core pouring temperature 973 K (700 °C). While the process parameters used for casting trials performed for

this thesis (and in Table 3-2) were slightly different, macroscopically the interface was qualitatively similar.

Longitudinal sections from ingot 1-1 were ground and etched, to reveal the macroscopic detail of the final Fusion™ cast interface. The two sections shown in Figure 4-30 were separated by 25 mm along the y axis of the ingot, and both are from near the centerline of the ingot. On this scale, a few observations can be made. First, the interface is not planar macroscopically. The interface undulates, as indicated by the region labelled a in Figure 4-30. On a macroscopic scale, it appeared as though these interface undulations were a consequence of changes in the local AA3003/AA4045 wetting conditions at the interface; with changes in wetting effecting local the ability for liquid AA4045 to locally dissolve AA3003 at the interface during the bond formation process. Pores were present at the interface; these are labelled b in Figure 4-30. The macroscopic observations of the interface suggested that there may not be regions of the interface which are not metallurgically sound, as both porosity and local regions of poor contact between AA3003 and AA4045 can be considered to be macroscopic defects.

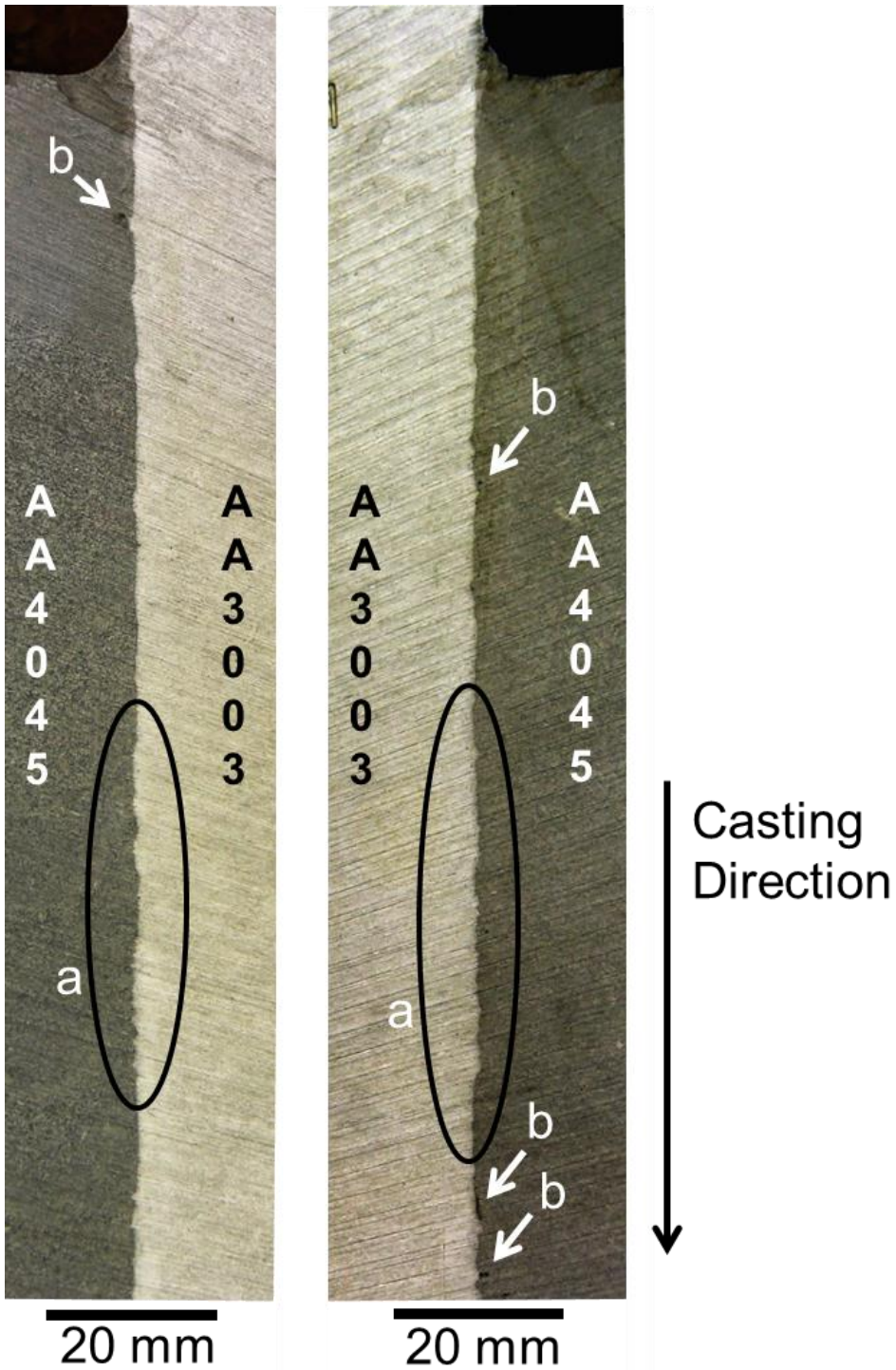

Figure 4-30 – Photo macrographs of longitudinal sections at the core/clad interface of ingot 1-1, from casting trials defined in Table 3-3.

A number of transverse sections across the AA3003/AA4045 interface of the same ingot were made. A schematic of the regions examined is shown in Figure 4-31, and the corresponding photo-macrographs are shown in Figure 4-32. The region in Figure 4-32a is the section near the left edge of the ingot, where the core metal liquid is fed into the mould. The region in Figure 4-32b corresponds to the central portion of the ingot, while the region in Figure 4-32c is the region adjacent to the clad liquid metal inlet. Observations of the transverse section revealed porosity at the interface, encircled in white in Figures 4-32a and b. Similar to the longitudinal sections, the interface between the AA3003 core and AA4045 clad was not planar. The interface was observed to undulate, which is particularly evident in Figures 4-32a and b. Although the interface does appear to be flatter in the region where the clad metal liquid is fed into the mould, i.e., Figure 4-32c, this observation was not consistent among the other transverse sections which were viewed using macroscopic etching.

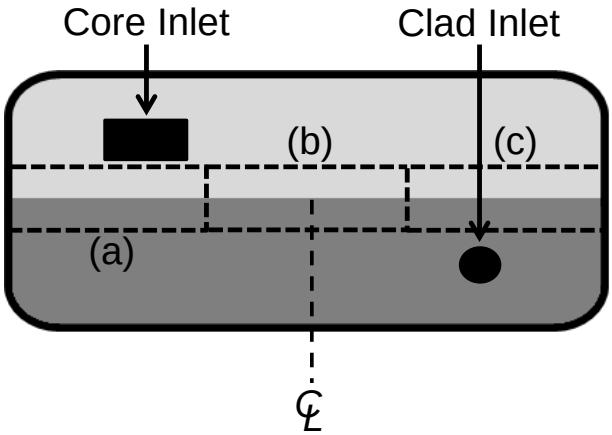

Figure 4-31 – Schematic of the Fusion™ ingot cross section, highlighted areas (a), (b) and (c) correspond to the regions where the Photo-macrographs shown in Figure 4-32 are taken from. Core inlet location and clad inlet location are indicated for reference.

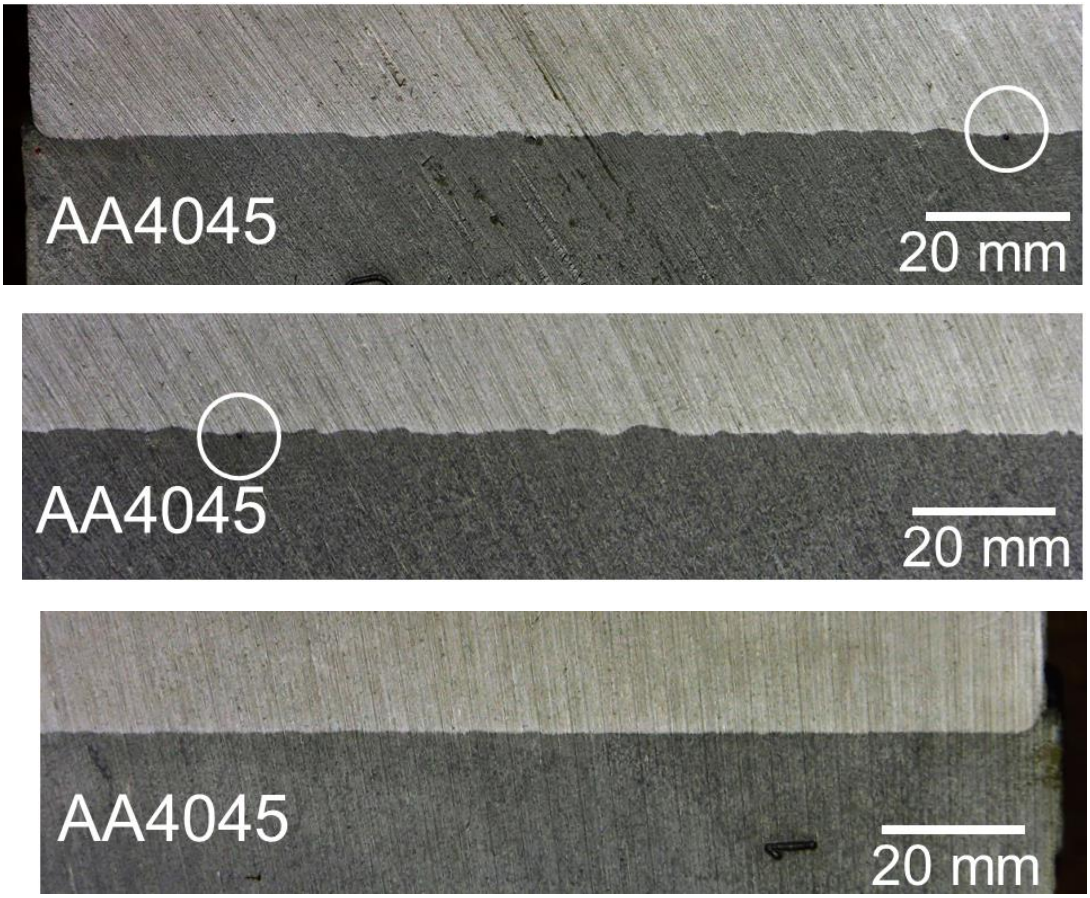

Figure 4-32 – Photo macrographs, transverse direction, ingot 1-1, from casting trials defined in Table 3-3. (a) Edge of ingot closest to the core liquid metal inlet. (b) Centre portion of ingot. (c) Edge of ingot closest to the clad liquid metal inlet.

Optical metallography of the interface, at a slightly higher resolution was conducted on the same ingot. Taking a longitudinal section from the very top of the ingot, i.e., where first contact of AA3003 and AA4045 was made during casting, shown in Figure 4-33, further highlighted the observations made on the macroscopic sections. Specifically, the interface in Figure 4-33 suggest that significant dissolution of the original AA3003 surface has taken place. The black vertical lines in Figure 4-33 represents the position of the AA3003 surface before contact with the AA40405 liquid. It is clear that the AA4045 liquid removes up to 1000 µm of the AA3003.

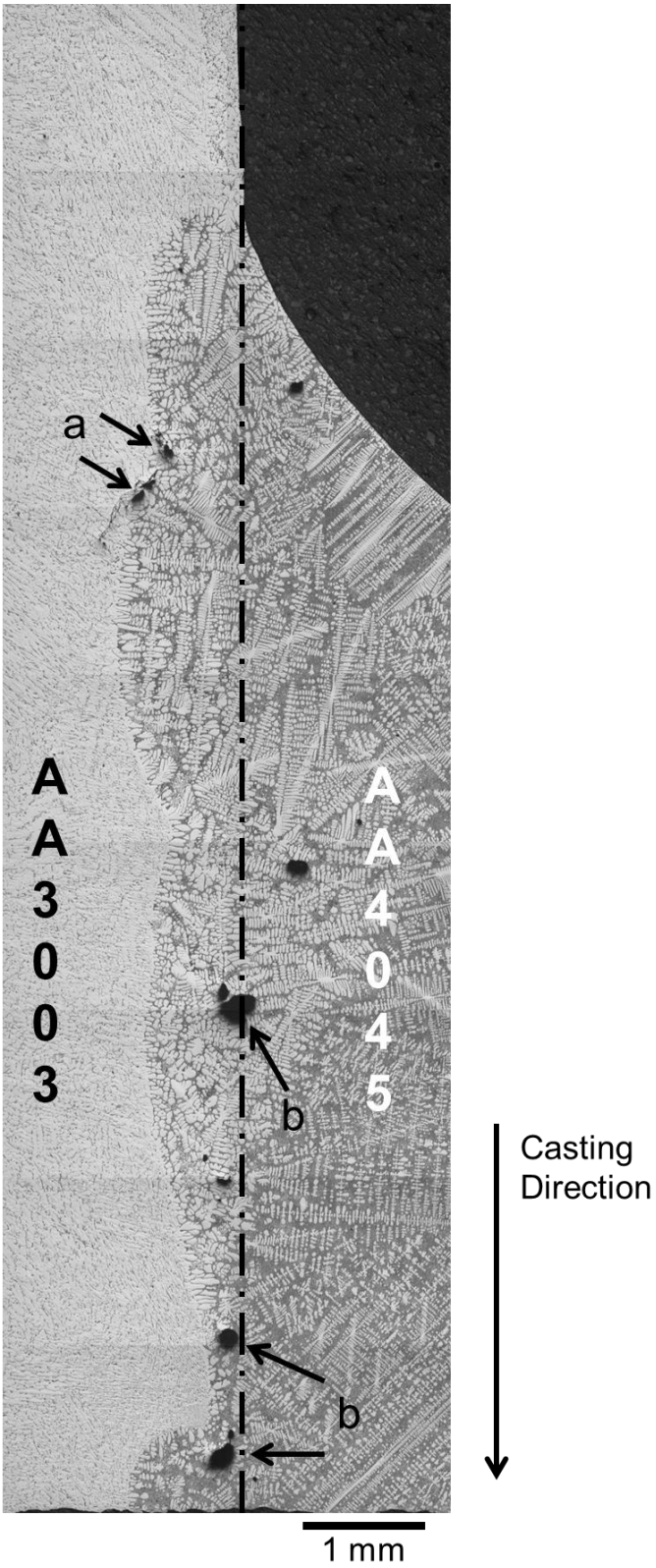

Figure 4-33 – Large area optical micrographs of longitudinal sections from the top of an as cast Fusion™ ingot (ingot 1-1 from casting trials defined in Table 3-3).

Similar to the macro-etched samples shown in Figure 4-30 and Figure 4-32, the interface is not planar. Furthermore, in this image, porosity was observed both: (i) at the final interface, as indicated by an arrow and labelled a and (ii) along the line which more or less is coincident with the vertical position of the original AA3003 surface prior to contact with the AA40445 liquid, as indicated and labelled b in the figure.

Examining numerous longitudinal and transverse specimens with optical metallography revealed that this undulating interface was common place. The interpretation is that the original oxidized AA3003 surface is undermined by the AA4045 liquid, proceeding to dissolution of the AA3003 shell. There are regions where this happens readily and regions where the process is impeded. At the locations where the oxide is undermined, the liquid AA4045 begins to dissolve away the underlying AA3003 solid. If the oxide is undermined at more or less discrete points, the dissolution below the oxide surface will extend into the solid AA3003 from this discrete point, and the interface will form semi-spherical profiles. In cross section, the resulting profile will be a series of arcs, and form an undulating interface similar to that seen in Figure 4-34.

Observations of discrete semi-spherical scallops at the core/clad were routinely observed in optical metallographic samples. Examples are shown in Figure 4-34, for both transverse sections, as in Figure 4-34a, and longitudinal sections, as in Figure 4-34b. In Figure 4-34a, the original interface is indicated with a dashed line. The depth of penetration in this case is 330 μm. Porosity is observed at the location where the original interface was located, similar to that seen in Figure 4-33. In Figure 4-34b, two semi-spherical scallops are observed to be penetrated into the AA3003 side of the interface. Here, the depth of penetration is less; however, it should be noted that in both Figure 4-34a and Figure 4-34b the maximum depth of penetration observed in each image may not have been co-planar with actual maximum depth of each semi-spherical

scallop. Without performing detailed sequential polishing and metallography, the maximum depth of the spherical cap could not be determined absolutely. However, the maximum penetration distance is likely to be on the order of 1 mm, as observed in large area optical images in Figure 4-33 and macro-etched sections Figures 4-30 and 4-32.

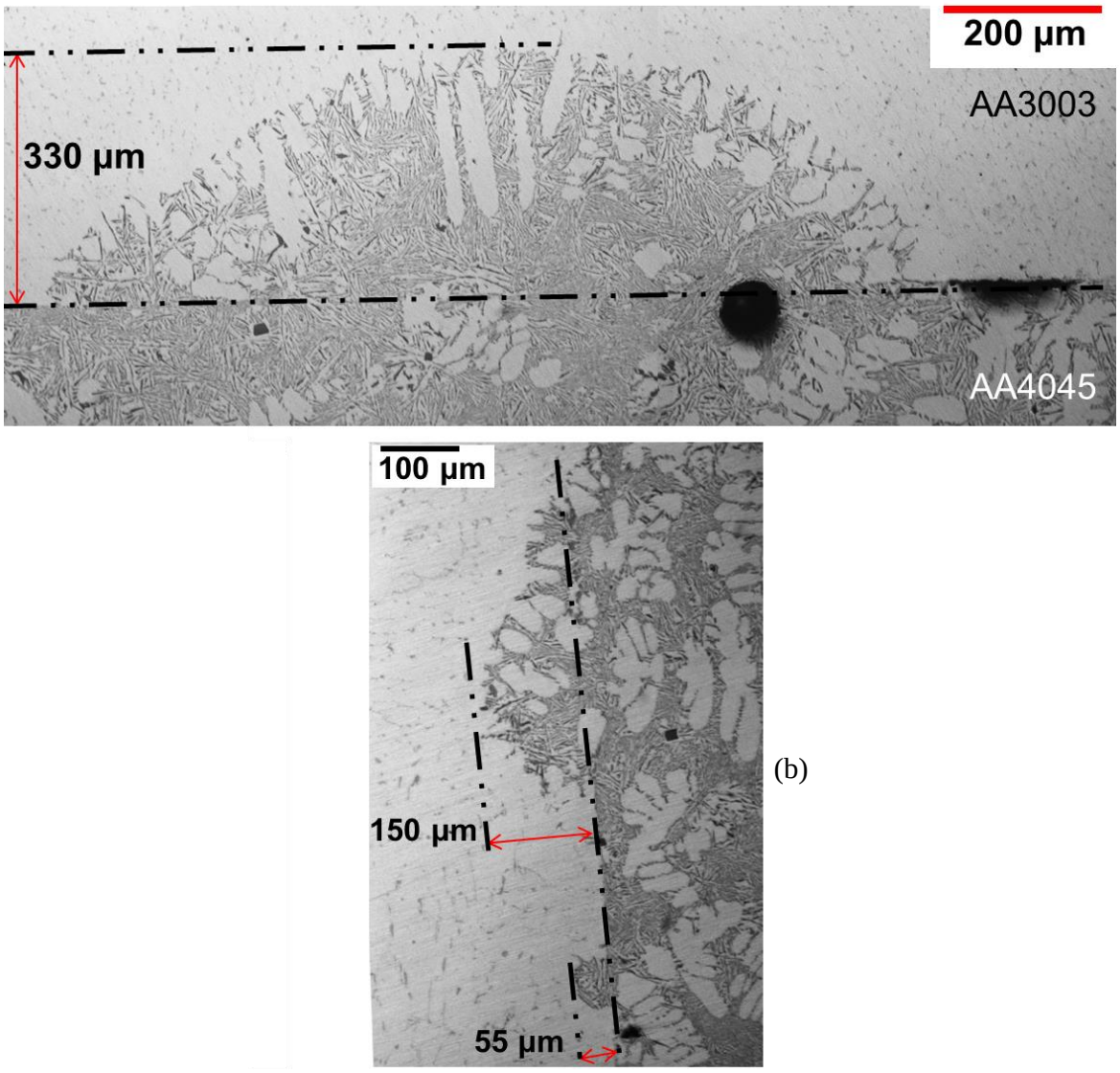

Figure 4-34 – Optical micrographs of an as cast Fusion™ ingot (ingot 1-3 from casting trials defined in Table 3-3) showing semi-spherical dissolution profiles of different depths into the AA3003 portion of the ingot. (a) Transverse section, and (b) longitudinal section.

A closer view of the final interface, for metallurgically sound regions of the Fusion™ cast ingot, are shown in Figures 4-35 and 4-36. Examining these portions of the interface, two observations can be made that further support that dissolution of the AA3003 surface does indeed take place. Firstly, epitaxial growth of α-Al; initially with a planar, but quickly transforming to a cellular and then dendritic solidification morphology from the AA3003 into the AA4045 (in Figure 4-35), is typical at the interface. This is qualitatively similar to interfaces seen in dissolution studies [106-108] as well as the aluminum brazing literature [109]. Second, Mn-rich intermetallics; both polyhedral in shape (Figure 4-36a) and script-like in shape (Figure 4-36b) were found on the AA4045 side of the final interface. Since the original composition of the AA4045 contained no Mn, it is obvious that the Mn came from the dissolution of the AA3003 and incorporation of the Mn-rich intermetallics into the molten AA4045 liquid at the interface. This results in a local enrichment of A4045 liquid near the final interface. Upon subsequent solidification of the ingot, these locally enriched Mn regions yielded a large population of intermetallics near the final interface. That the morphology of the Mn-rich intermetallics varied from script to polyhedral throughout the ingot suggest that the degree of dissolution was not uniform over the width of the Fusion™ ingot.

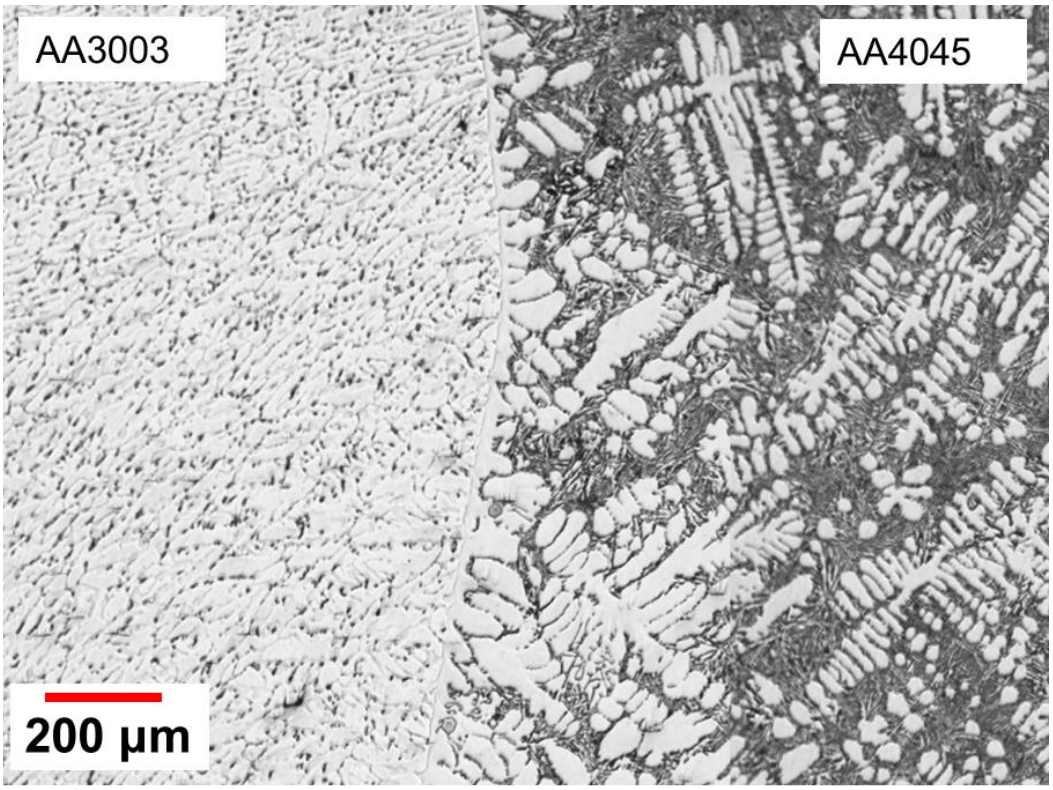

(a)

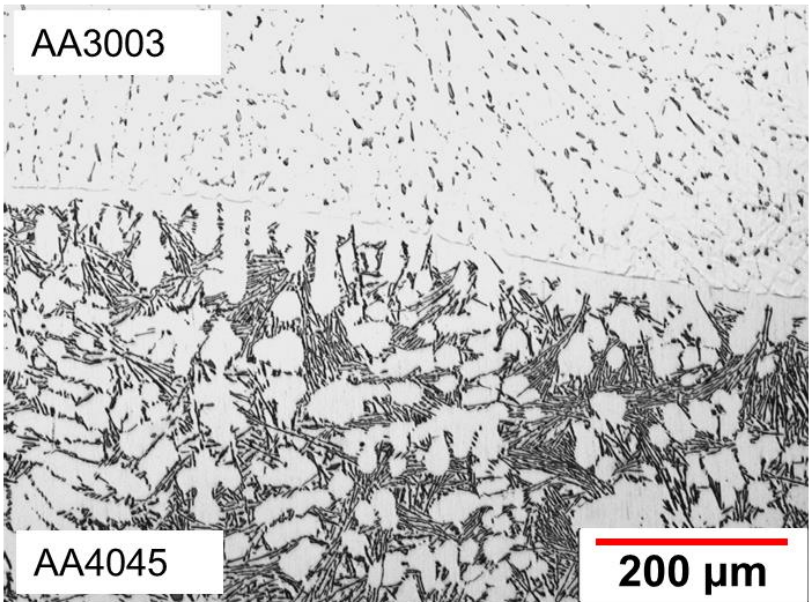

(b)

Figure 4-35 – Optical micrographs of an as cast Fusion™ interface. (a) Longitudinal section of ingot 1-1 (from casting trials defined in Table 3-3). (b) Transverse section of ingot 1-2.

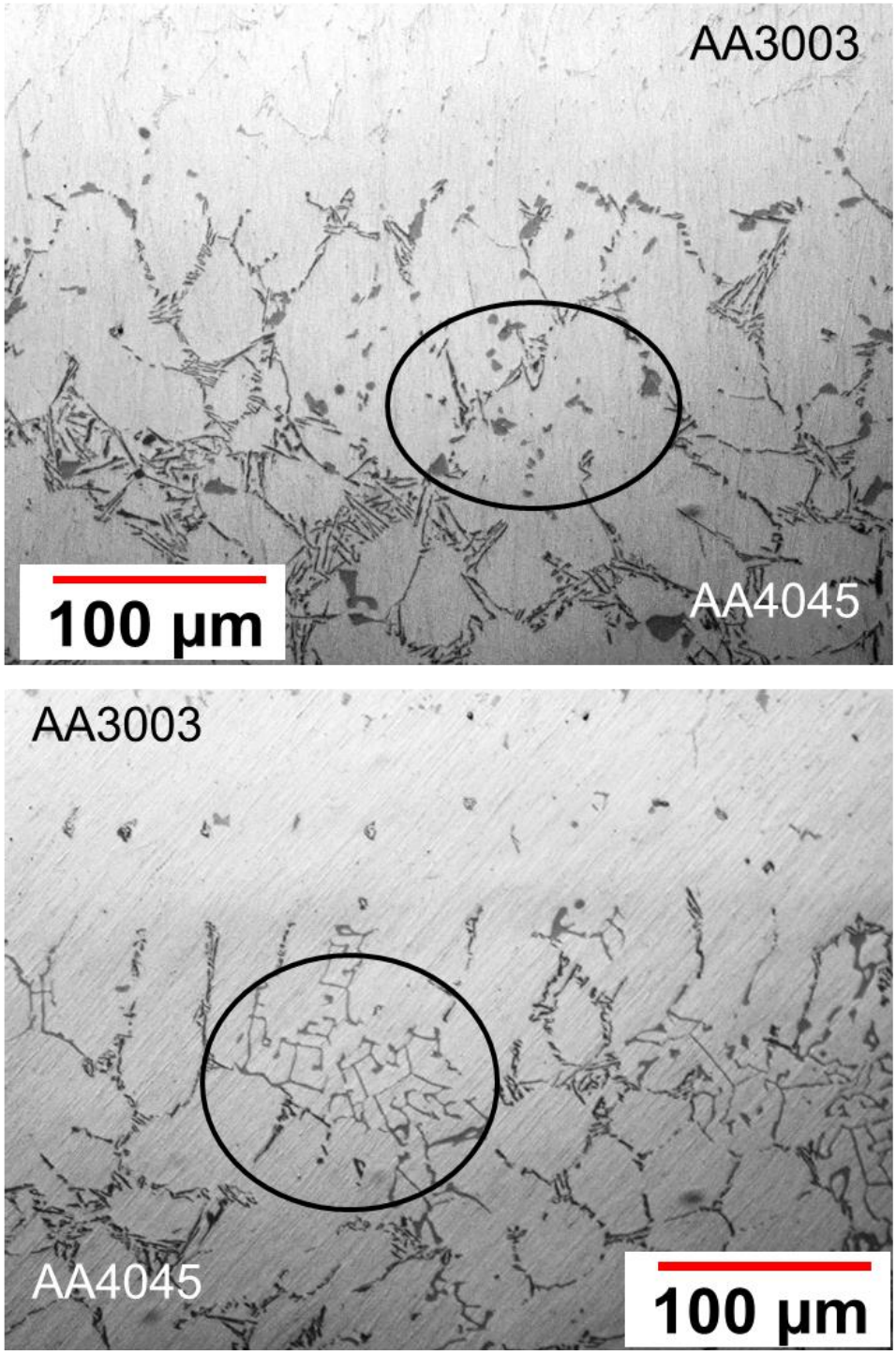

Figure 4-36 – Optical micrographs of an as cast Fusion™ ingot (ingot 1-3 from casting trials defined in Table 3-3). Mn-rich intermetallic particles are present within the AA4045 portion of the Fusion™ ingot. (a) Transverse section with polyhedral type intermetallics encircled, and (b) transverse section with script type intermetallics encircled.

4.6 Mechanical testing of Fusion™ cast interfaces

Mechanical tests were performed on tensile test samples machined from Fusion™ cast ingot 2-1. Fifteen samples, with the interface located in the middle of the gauge length, were taken from the 3 planes shown in Figure 4-37.

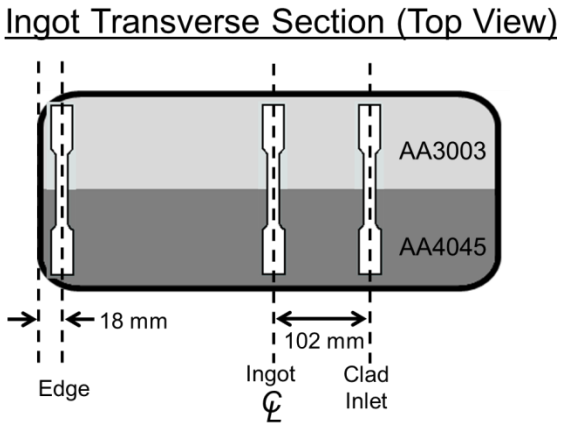

Figure 4-37 – Schematic (section of ingot looking down from the top) indicating the mechanical test sample positions from as-cast interface samples.

The results of these mechanical tests are summarized in the bar charts Figure 4-38a and b[5]. In Figure 4-38a, the values of UTS for the base metal are taken from the AA3003 metal, as fracture for all samples was either initiated at the interface or within the AA3003 side of the sample. The UTS of the as-cast AA3003 was determined through separate tests to be 133 MPa, and the % elongation was 43.5 %. From the UTS values shown in Figure 4-38a, there is a clear difference in interface quality between samples taken from the edge of the ingot and those taken from the two other locations. The UTS ratios of the samples taken from the edge of the ingot vary from 0.5 to 0.85, with an average of 0.68. For the other two locations, the UTS ratio was much greater. Aside from the one outlier from the centerline samples, the UTS ratio was above 0.9, and the fracture of the sample was in the AA3003 metal, indicating that the interfaces were most likely metallurgically sound.

[5] Tests with erroneous load cell data were omitted from the results.

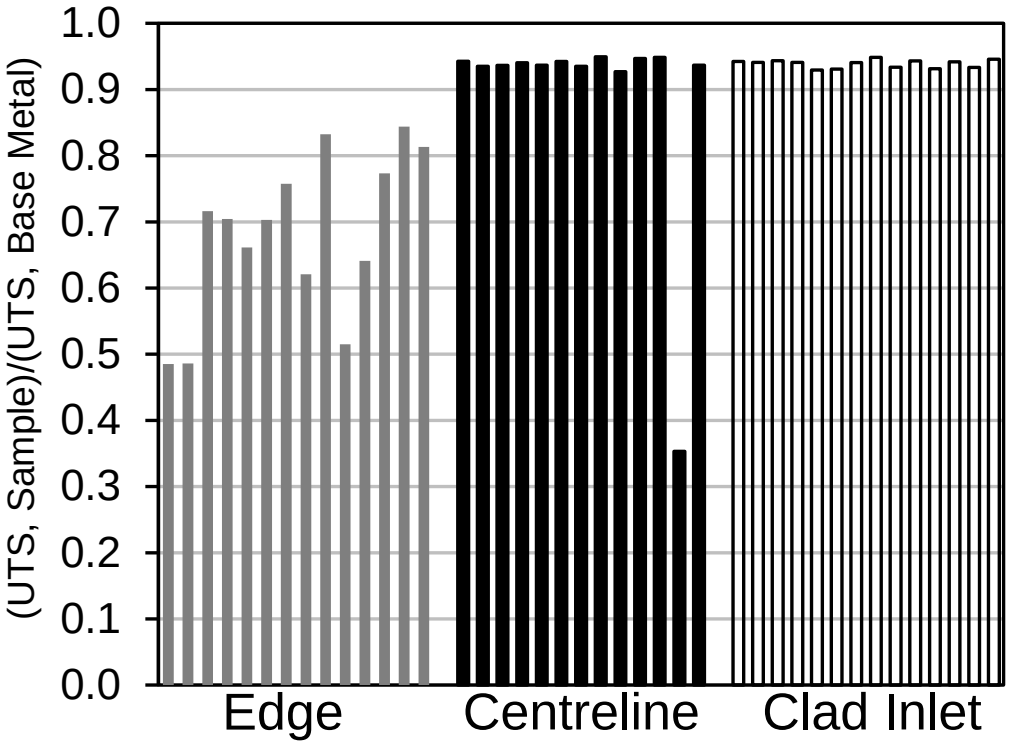

(a)

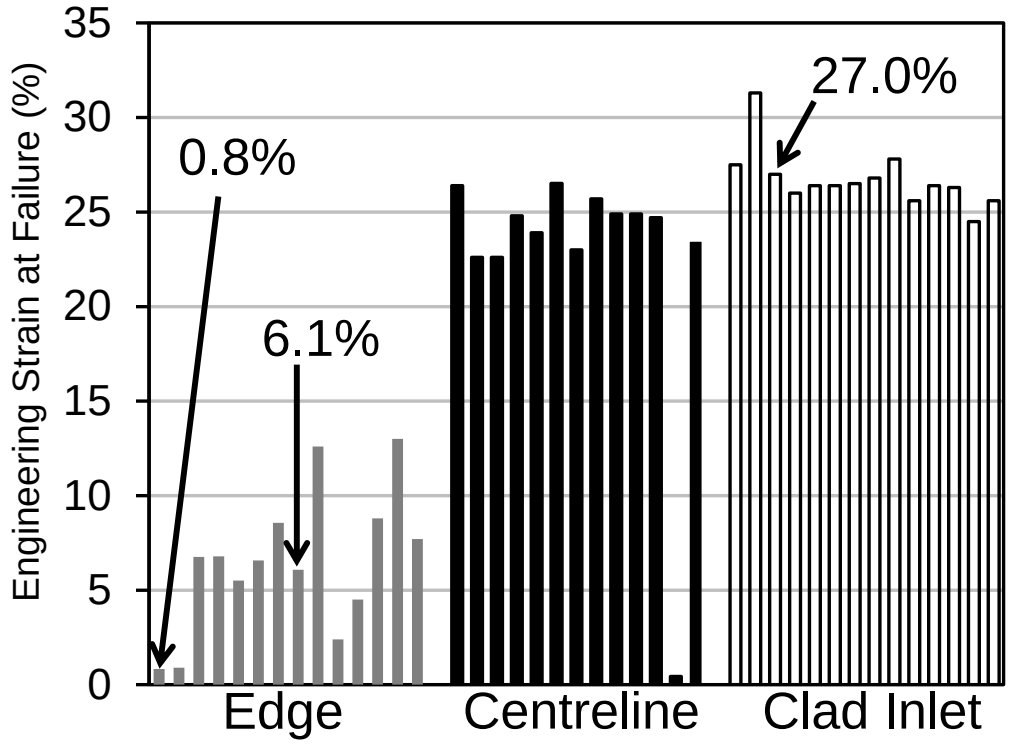

(b)

Figure 4-38 – Mechanical test results from as cast Fusion™ interfaces. (a) Tensile strength of sample divided by the tensile strength of the AA3003 base metal, (b) engineering strain at failure of sample.

Looking at the strain to failure data in Figure 4-38b, a similar trend is observed. The samples at the edge display much lower failure strains than the samples from the other two locations. There were a total of three outliers: two from the edge test samples, and one from the centerline test samples, which failed with extremely low strains. Omitting these outliers, the average strain to failure for the samples taken from the edge was 7.4 %. For the centerline and clad inlet positions, the average strain to failure values were 24.5 % and 26.7 % respectively. The strain to failure for the bulk AA3003 was observed to be 43.5 %.

A two-sided t-test [110] was performed to statistically compare the mean strain to failure results from the three locations tested. The following inferences can be made: (i) including all outliers, the edge location tensile sample mean strain to failure is less than the other two locations with a confidence level greater than 99.99%, (ii) the clad inlet location tensile sample mean strain to failure is greater than the mean from the centre line location with a confidence level between 90 and 95 % if the outliers are included in the statistical analysis, and (iii) that confidence level increases to 99.95% if the outliers are omitted from the statistical analysis.

Again it should be noted that the UTS ratios for the centerline and clad inlet positions were both above 0.9. While the average strain to failure was significantly lower than the measured strain to failure on bulk AA3003 samples (the strain to failure of the AA3003/AA4045 interface samples was almost that of the bulk AA3003), the UTS ratios were close to 1, indicating the interfacial bonds at the centerline and the clad inlet were metallurgically sound. The low observed values for the average strain to failure for the centerline and clad inlet positions may have been due to mechanical constraint effects associated with AA3003/AA4045 tensile test samples. Unlike a normal tensile test sample, where the entire gauge length is made from one (ideally homogenous) material, the gauge length of these interface tensile test samples are

comprised of 50 % AA4045 (a stronger less ductile alloy) and 50 % AA3003 (a softer more ductile alloy). The presence of the AA4045 material over half the gauge length of these interface tensile test samples may have contributed to the lower strain to failure results for the centerline and clad inlet positions.

The three outlying test samples with very low failure strains were not un-expected, since observations in Section 4.5 suggest that the Fusion™ interface does contain flaws. In fact, the motive behind performing 15 tests from each location, was to increase the likelihood of finding an outlier with such a low strain to failure and to compare fracture morphologies of low strain-to-failure samples and high strain-to-failure samples.

The fracture surface of three samples were examined using a SEM. The three samples which were examined are indicated in Figure 4-38b as samples which failed at strains of 0.8%, 6.1% and 27.0% respectively. These three samples represent: (i) the average for the samples taken from the other two locations, i.e., 27.1% strain-to-failure, (ii) the average for the edge samples, i.e., 6.1% strain-to-failure, and (iii) the low outlier(s) for strength, i.e., 0.8% strain-to-failure. Low magnification and high magnification images are presented for each of the three samples in Figure 4-39 through Figure 4-41. For the samples with a high strain to failure, Figure 4-39a and b, the fracture surface resembles that of typical ductile fracture [111]. The fracture surface for this sample is entirely within the AA3003 portion of the sample, away from the Fusion™ cast interface.

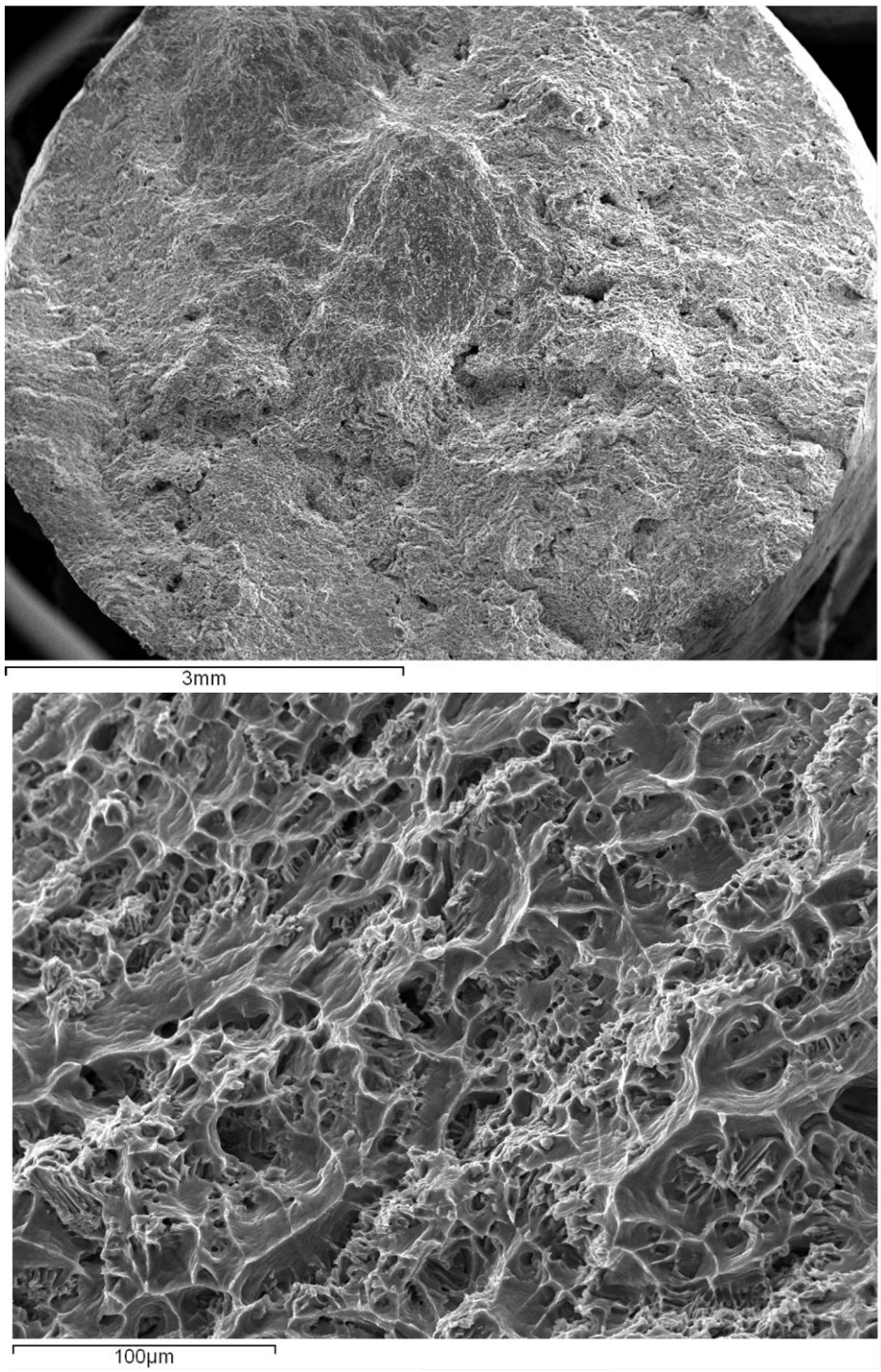

Figure 4-39 – Fracture surface of mechanical test which had an engineering strain at failure of 27%. (a) Low magnification secondary electron image, (b) high magnification secondary electron image.

For the sample which failed at a strain of 6.1%, Figure 4-40a and b, the surface is quite different. On this fracture surface, large open pores were observed, indicated with arrows in Figure 4-40a, on the AA3003 side of the interface. Aside from these pores, the remainder of the surface had regions which exhibited the typical ductile fracture surface as well as regions which showed no ductile fracture features at all, see the boxed area in Figure 4-40a. When imaged under higher resolution, the regions which did not exhibit any ductility, see Figure 4-40b, looked strikingly similar to the AA3003 core surface in contact with the chill bar surface structure shown in Figure 4-22. This would indicate that the AA3003 core surface, although in contact with the AA4045 melt, did not form a bond over these flat regions.

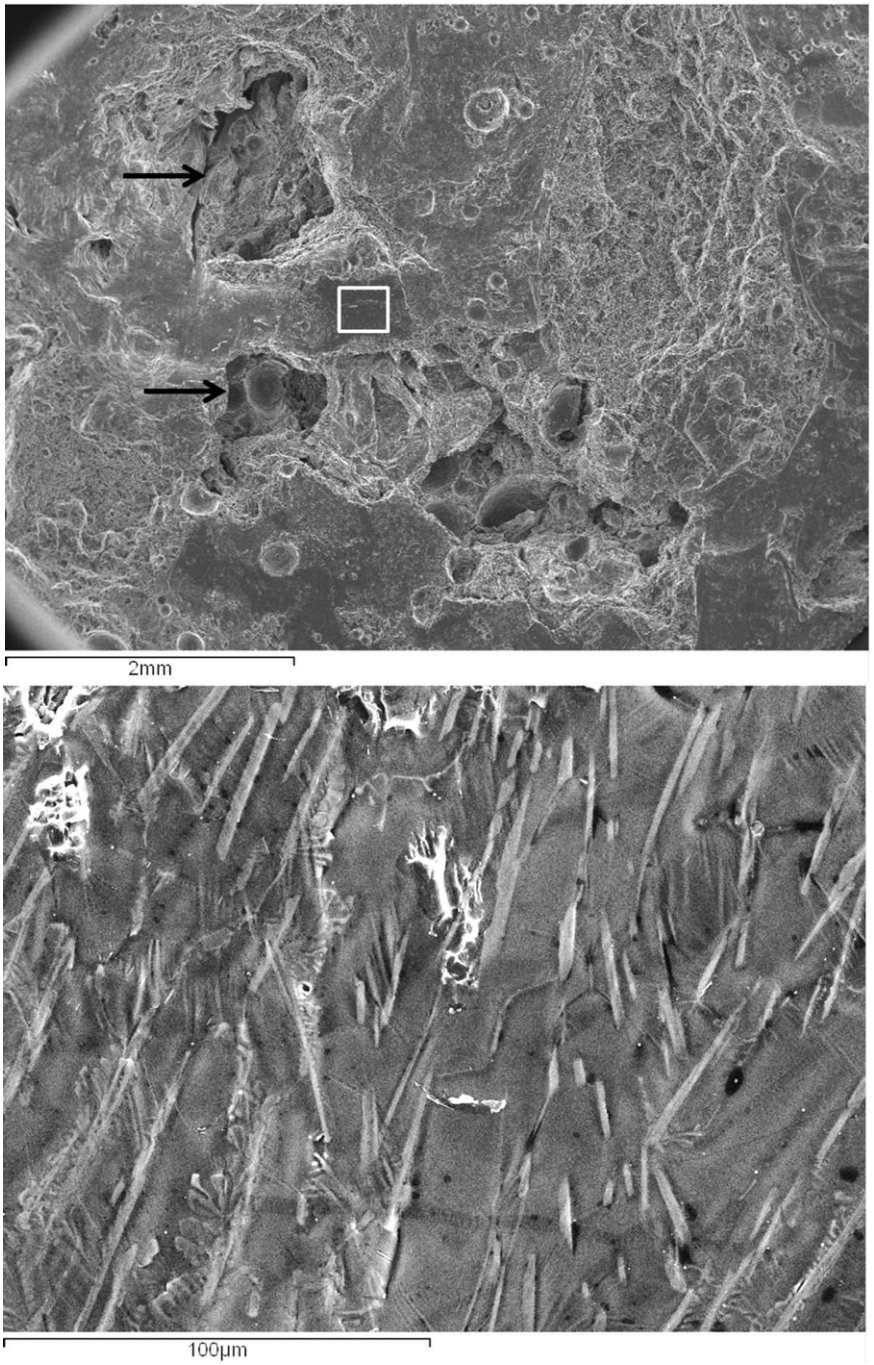

Figure 4-40 – Fracture surface of mechanical test which had an engineering strain at failure of 6.1%. (a) low magnification secondary electron image of the AA3003 side of the failed sample, (b) high magnification secondary electron image of the encircled area in (a).

The sample representing the outlier, which failed at a strain of 0.8%, is shown in Figure 4-41a-c. Here, the sample fractured at the interface. Figure 4-41a and b are images of the AA3003 side of the interface. While there were small regions of ductility present, as seen in the

upper portion of image Figure 4-41a, the majority of the surface was smooth on a macroscopic level. When this region was viewed under higher magnification, as in Figure 4-41b, surfaces features again appeared very similar to the AA3003 core surface in contact with the chill bar surface seen in Figure 4-22. Figure 4-41c is an image of the AA40045 side of the interface. In general, the surface was featureless; however, qualitative signs that oxide films were present were observed in images of this surface. Specifically, wrinkles, similar to those discussed in Section 4.4 (see Figure 4-24) were seen on the AA4045 fracture surface. This suggests that both the AA3003 fracture surface as well as the AA4045 fracture surface had oxide films present.

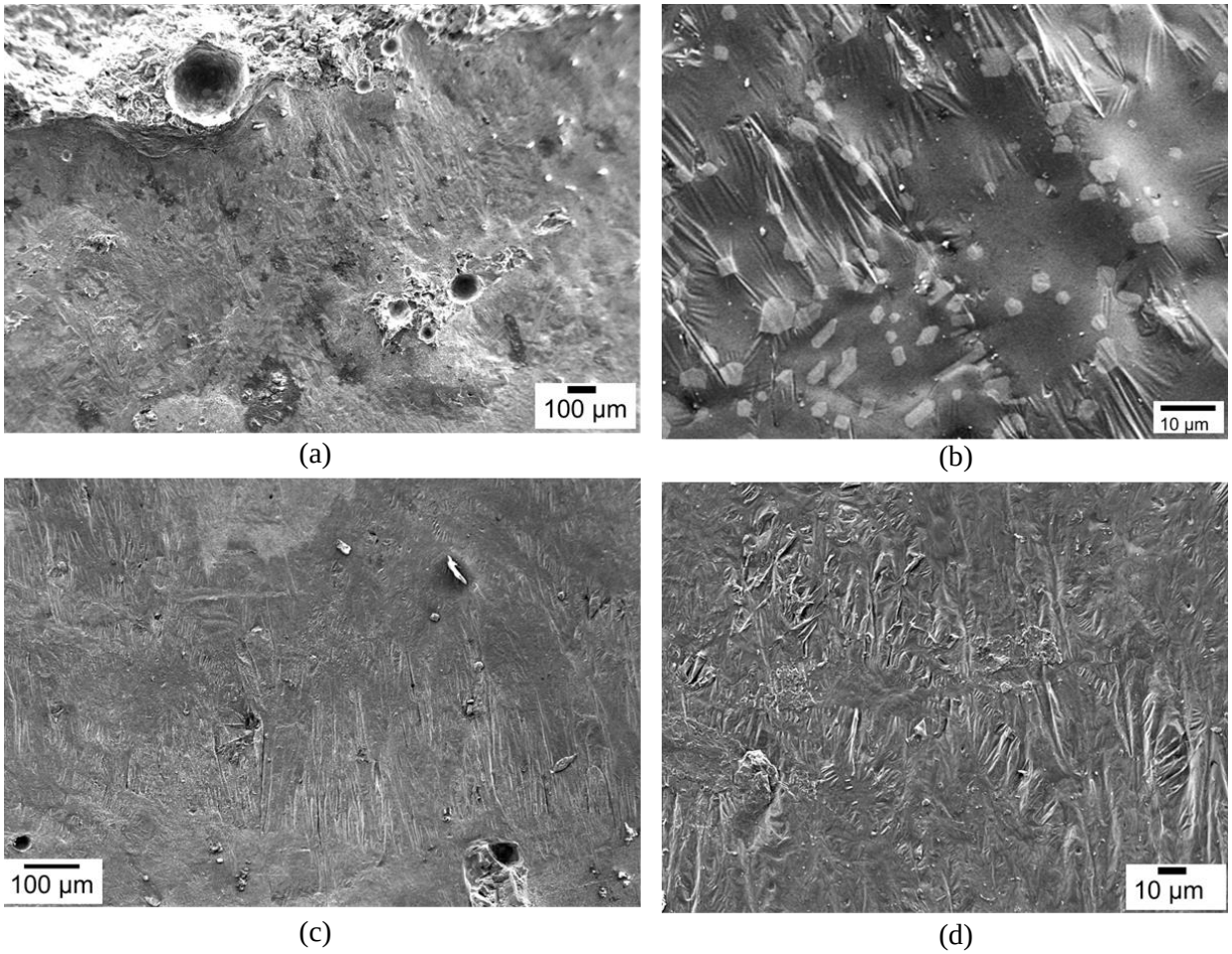

Figure 4-41 – Fracture surface of mechanical test which had an engineering strain at failure of 0.8%. (a) Low magnification secondary electron image of the AA3003 side of the failed sample, (b) high magnification secondary electron image of the AA3003 side of the failed sample, and (c) low magnification secondary electron image of the AA4045 side of the failed sample.

4.7 Discussion

From the results of Section 4.5, there is ample evidence that the AA3003 shell was subject to dissolution by AA4045 liquid during the Fusion™ casting process. First, as seen in Figure 4-33, at the final as-cast AA3003/AA4045 interface up to 1 mm of the AA3003 was removed by solutal dissolution by the molten AA4045. Additionally, the as-cast interface looked qualitatively similar to dissolution based interfaces in [106-107]. Mn bearing intermetallics were also found on the AA4045 side of the interface, suggesting that AA3003 dissolution took place and locally increased the Mn content of the liquid AA4045 in the vicinity of the interface prior to final solidification. Furthermore, semi-spherical shaped ridges at the interface were observed in both macro-etched samples, in Figures 4-30 and 4-32, as well as in optical metallographs, in Figures 4-34 and 4-36.

This, along with the observations from the AA3003 chill cast surface in 4.4, suggests that the interface formation proceeds by oxide penetration of the AA3003 shell, and solutal dissolution of underlying AA3003 by the AA4045 melt. The AA3003 dissolution undercuts the oxide, similar to the model described by Wall and Milner [53] (see Section 2.3) and proceeds until bridging of two adjacent penetration points occurs. If the interface formation mechanism is truly a penetration and dissolution mechanism, one expects the quality of the final interface to be dependent on: the dissolution rate of AA3003, the number of oxide penetration points per unit area of AA3003 surface, and the contact time between the liquid and solid shell. It should be noted that the dissolution rate of Al in liquid Al-Si was measured by Craighead *et al*. [23], and was shown to be a strong function of temperature.

Looking again at the thermofluid model predictions, in Table 4-4; this time in conjunction with the additional observations from Sections 4.4-4.6, a more complete picture is shown. The

major differences are not in minimum f_s or oxide thickness. The major differences are in contact time, and average temperature during contact. Including the observation that spot exudation on the AA3003 surface was minimal near the edge and more prolific near the centerline of the width of the ingot, the difference in mechanical test data suggests a clear link between: (i) time and temperature available for penetration, dissolution and bridging to occur between adjacent penetration sites, and (ii) quality of the final as-cast interface**.** The statistically significant (two-sided t-test) increase in strain to failure results for tensile tests taken from the clad inlet as compared to the centerline test samples indicate that the time in which liquid AA4045 remains in contact with the AA3003 shell, prior to final interface solidification, may be a more vital parameter than the reheating/remelting of the AA3003 shell in terms of interface integrity.

Table 4-4 – Comparison of various calculated values from the thermofluid model in [22] (for casting trial # 2-1, see Table 3-2) with failure strains (average values) of the Fusion™ cast interface from the same location.

Location	***min fs***	***Δfs***	***$t_{contact}$ (s)***	***Average Temperature during contact, K, (°C)***	***Calculated oxide thickness (nm)***	***Run #***	***Strain at failure (%)****	***AA3003 chill cast surface***
Edge (y = -174.5 mm)	0.98	0.0	12.3	871 (598)	20	1	7.4 +/-3.0	No spot exudation observed
	0.98	0.0	12.3	872 (599)	20	3		
Centre Line (y = 0 mm)	0.97	0.6	41.3	881 (608)	20	1	24.4 +/-1.4	Spot exudation observed on surface
	0.97	0.9	41.7	882 (609)	20	3		
Clad Inlet (y = 102 mm)	0.98	0.1	47.2	871 (598)	19	1	26.7 +/-1.6	Spot exudation observed on surface
	0.98	0.3	47.2	875 (602)	19	3		

*outliers omitted when calculated sample mean and standard deviation.

While the results clearly suggest that the presence of "spot exudates" improves the final interface quality; it is worth noting that the interface near the edge still displays partial bonding,

as evidenced by the 6.5% strain to failure and the mechanical strength values in Figure 4-38. Hence, the requirement stated in the original Fusion™ casting patent [16], that the core alloy (or 1st alloy) must be reheated/remelted while in contact with the clad alloy (2nd alloy) appears likely to result in an improved as-cast Fusion™ bond; however, it does not appear to be a necessary requirement for bond formation. Furthermore, the observations of the AA3003 chill cast surface in Section 4.4 could not adequately pin-point the mechanism of oxide penetration. The presence of "spot exudation" is likely to disrupt the AA3003 surface oxides, and improve bonding; however, there is some evidence suggesting that the AA3003 oxide film may be defective over surface intermetallics, (see Figure 4-25c). Additionally, Mg segregation was observed on the AA3003 chill cast surface (see Figure 4-27). While the temperature history at the exact locations where Mg segregation was observed was unknown, it does suggests that: given the Mg content of the AA3003 which was used during the Fusion™ casting trials, Mg may segregate to the AA3003 surface during casting. If this is the case, Mg may potentially react and reduce the AA3003 surface oxides, and provide pathways for AA4045 liquid penetrations to occur, thus facilitating interface formation.

4.7.1 Metallurgical defects at the AA3003/AA4045 as-cast Fusion™ interface

As opposed to other references in the literature [14-16], metallurgical defects were observed in the as-cast Fusion™ interfaces. Pores were observed on both longitudinal and transverse sections, see Figures 4-30 to 4-33. Pores were also observed on fracture surfaces from samples taken along the edge of the Fusion™ ingot. Furthermore, optical metallographs of the interface often displayed regions where no interaction between the AA3003 and AA4045 was observed, such as shown in Figure 4-40. The observation of pores in the as-cast interface suggests that as-cast bonds, although mechanically strong, may not be metallurgically clean bonds. This agrees

with the interface formation mechanism discussed in Section 4.4.1; i.e., that of oxide penetration, dissolution of underlying AA3003 and bridging between penetration points. If the bridging step is not completed before the AA4045 liquid solidifies at the interface, then defects, such as bare spots and pores, may persist in the final as-cast interface.

Furthermore, of the forty-five mechanical tests performed, three samples had measured failure strains of less than 1%. The fracture surfaces of these three samples displayed typical brittle behaviour, see Figure 4-41 for example. The cross sectional area of the mechanical test samples, 64 mm^2, is far greater than the spot exudation spacing on the AA3003 chill surface shown in Figure 4-18, as well as the intermetallic spacing shown in Figure 4-22. Additionally, brittle test samples were obtained from a sample taken at the centerline of the Fusion™ ingot, as well as from the edge of the Fusion™ ingot, see Figure 4-38. These two points suggest that despite beneficial conditions at the AA3003/AA4045 interface, such as: (i) liquid contact time greater than 40 seconds (for the centerline sample), (ii) peak temperature of 901-903K (628-630°C) (for the centerline sample), and (iii) sump oxide film motion away from the interface, poorly bonded areas in the as-cast Fusion™ ingot will occur from time to time on a macroscopic scale (64 mm^2). These large area defects can be explained by considering the effect of oxide motion in more detail.

To review, the oxide motion measured and presented in Section 4.3 suggested that the contact between the AA4045 liquid and the AA3003 solid shell was for the most part intimate. In spite of these observations, there is the question of stability of the AA4045 meniscus in contact with the AA3003 shell. A shortcoming of the oxide film observations was the inability to observe the AA4045 liquid meniscus in contact with the AA3003 shell. This could not be obtained because of space limitations and inadequate lighting near the meniscus.

As the metal level in the clad sump was manually controlled, fluctuations of the metal level were likely to have occurred during the Fusion™ casting process. It is hypothesized that meniscus changes due to metal level fluctuations in the sump could affect the contact condition between AA4045 and AA3003 in the manner depicted in Figure 4-42. In the scenario depicted, due to an un-steady pouring process, a sudden increase in the metal level, Δz, occurs on the clad side of the Fusion™ ingot. Subject to the rise Δz, there is a potential for the clad meniscus to come into contact with the AA3003 shell, causing entrainment of the clad surface oxide at the interface. Any entrainment would impede the contact between the AA3003 shell and the AA4045 liquid, and locally hinder bond formation between AA3003 and AA4045. Considering the clad sump metal level was manually controlled during Fusion™ casting trials, there is a distinct possibility that meniscus entrainment may have occurred. The interfaces mechanical tests which failed with less than 1% strain, see Figure 4-38, can also be qualitatively explained by this mechanism.

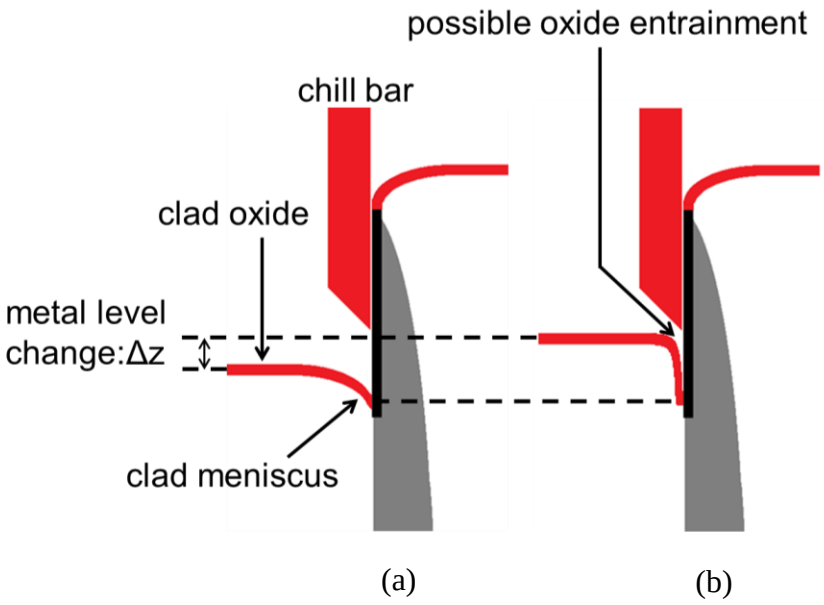

Figure 4-42 – Schematic showing the effect of metal level increase, on the clad side, during Fusion™ casting. (a) Clad meniscus before metal level increase, Δz, and (b) clad meniscus after metal level increase and possible entrainment of clad oxide at the AA3003/AA4045 interface.

While the tensile tests on as-cast Fusion™ interfaces displayed results consistent with defects being present at the interface, it should be noted that the processing route required to obtain the final product, i.e., Fusion™ clad sheet, includes reduction of the original thickness of the ingot (both hot rolling and cold rolling). As such, the final interface strength may be quite different than the as-cast interface strength; which will depend on the response of the interfacial defects to deformation. For example, porosity stemming from solidification shrinkage or H_2 gas evolution will not have Al_2O_3 on their respective surfaces, so these defects can be expected to be cold welded to 100% bond strength on rolling. When oxide films and un-wetted or un-bonded areas exist at the interface, the rolling/deformation processes will break up and disperse the oxide films at the interface. Cold welding of the core and clad will take place; however, during this process local oxide defects will be left at the interface and can limit strain to failure and strength to ≈70% at best [112].

4.8 Summary

The key observations and results from Chapter 4 were:

i. The motion of oxide films on the clad and core sumps was away from interface, facilitating intimate contact between oxide-free AA4045 liquid and the solid, oxidized AA3003 shell.

ii. Surface oxides were observed on the AA3003 chill-bar cast surface, indicating that an oxide layer was likely present prior to contact with AA4045 and AA3003/AA4045 interface formation. The surface oxide on the AA3003 chill-bar cast surface was about 25 nm in thickness, and did not appear to be uniform/continuous over surface intermetallics.

iii. "Spot exudates", i.e., local remelting, was observed on the AA3003 chill-bar cast surface, with decreasing density towards the edge of the ingot. Partially transformed intermetallics were also observed on the AA3003 chill-bar cast surface. Additionally, Mg was observed on the chill-bar cast surface near the final point of contact between the AA4045 meniscus and the AA3003 surface, indicating the potential for surface segregation of Mg to occur on the chill-bar cast surface during Fusion™ casting.

iv. The final as-cast Fusion™ interfaces displayed signs of AA3003 dissolution by the AA4045 melt prior to the solidification of the interface. Metallurgical defects, such as: porosity and incomplete bonding was observed on as-cast Fusion™ interfaces.

v. Mechanical tests performed on as-cast Fusion™ interfaces failed away from the interface, for the majority of test samples taken from the centre (y = 0 mm, see Figure 3-9) and clad inlet (y = +60 mm). Mechanical tests of samples taken 18 mm from the edge of the ingot (y = -173.5 mm) failed at the interface with very little strain.

vi. While the thermofluid results generated using the model described in [22] may not be adequate for predicting the surface remelting of the AA3003 shell, the evolution of temperature at the AA3003/AA4045 interface during casting can be accurately calculated. This information can be used to assess the time (and temperature) at which liquid AA4045 remains in contact with AA3003 prior to interface solidification, which is likely an important parameter for interface formation, as these results indicate that the interface formation is likely a dissolution and bridging process.

These results suggest that the AA3003/AA4045 interface forms by penetration of the AA3003 surface oxide by AA4045, dissolution of the underlying AA3003 material by the

AA4045, and bridging and breakup between penetration points, leading to a final clean interface between AA3003 and AA4045. However, from the Chapter 4 results, the mechanism of oxide film penetration was not determined.

Chapter 5

Analog Interface Formation Test Results: the Influence of Temperature, Sample Oxidation, and Atmospheric Condition

5.1 Introduction

In this chapter, results from immersion tests conducted with the laboratory apparatus detailed in Section 3.3 are presented. For these tests, solid samples were machined from AA3003 DC cast ingots. The compositions for the AA3003 samples and AA4045 melt material are listed in Table 3-9 (Id # 1 and Id # 2).

As the first step to fulfilling the test objectives outlined in Section 3.3, a series of analog interface formation tests were conducted. The initial variables which were thought to be of primary importance were: core alloy and clad melt temperature, sample surface oxidation, and ambient atmosphere. The initial tests, described below were done using AA3003 as the sample material and AA4045 as the melt material.

Two series of tests were conducted using large diameter samples; the details are given in Section 3.3.3.1. To re-iterate, one set of tests focused on the role of AA3003 surface remelting, and if it is a requirement for formation of a sound AA3003/AA4045 bond. Results from these tests will be presented in Section 5.2. These immersion tests were conducted under a final atmosphere of air. The other set of tests examined the effect of differing amounts of surface oxidation on the AA3003 specimens on wetting and bond formation. These test results will be presented in Section 5.3. These immersion tests were conducted in a final furnace atmosphere of argon. To characterize the thermal oxides grown on these AA3003 samples, sister samples were prepared and oxidized using similar heating rates and times. The preparation of these samples is

described in Section 3.3.2.2 and Table 3-13. Results from the characterization of these thermal oxides are presented in Section 5.5.

5.2 Remelting tests

Prior to testing, preliminary DSC tests were conducted in order to determine the onset of remelting for the AA3003 samples to be used. From these preliminary tests, the measured onset of remelting was at 920.1 K (647.1 °C). However, the alloy composition used to measure the onset of remelting was slightly different than the alloy used to fabricate the interface formation test samples. At a later date, additional tests were performed, using the DSC samples from the same ingot which was used to make test samples. The results of DSC testing are presented in Table 5-1. Here, the onset of remelting was measured to occur between 920.6-920.8 K (647.6-647.8 °C), depending on the heating rate used. The onset for the 2nd peak (see Figure 5-1 for an example of a typical DSC curve) measured by the method of intersecting tangent lines [100-101], could only be measured for the 0.02 K/s heating rate tests. With a low heating rate, the two peaks in the DSC signal are sufficiently separated such that tangent lines can be drawn for the 2nd (higher temperature) peak, and its onset can be measured. At higher heating rates, the DSC signal gets smeared, due to thermal lag in the system, resulting in significant overlap of the two peaks. Due to the overlap of peaks, a reliable tangent line could not be drawn, and the 2nd peak onset could not be measured for higher heating rates.

Table 5-1 – Onset of remelting measurements from AA3003 samples measured with DSC. *n* indicates the number of times each test was repeated, and σ represents the calculated standard deviation in the results.

Sample	***Alloy Id # (from Table 3-1)***	***Heating Rate (K/s)***	***Onset of Remelting (K,(°C))***	***2nd peak Onset (K, (°C))***	***n***	***σ***
DC Cast AA3003	1	0.017	920.7 (647.7)	925.7 (652.7)	6	0.15, 0.21
		0.33	920.6 (647.6)		2	0.47
		0.83	920.8 (647.8)		1	-

A typical DSC curve, from the 0.02 K/s heating rate tests, is shown in Figure 5-1. As noted, it is similar in characteristic to the AA3003 DSC curve from the bulk portion of the Fusion™ cast ingot presented in Figure 4-20. Comparing this DSC curve to the peak temperatures recorded during immersion testing, i.e., tests ***r1*** to ***r5*** in Table 3-8, it is clear that: (i) during tests ***r1*** and ***r2*** the measured peak sample temperature was below the measured onset of remelting, (ii) test ***r3*** was above the measured onset of remelting but below the onset for the second peak, and (iii) tests ***r4*** and ***r5*** were within the range where the second onset of remelting was measured. It should be noted that the thermocouples were at a depth of 1.0 mm below the surface of the sample, so the measured peak temperature may have been slightly lower than the peak temperature at the sample surface.

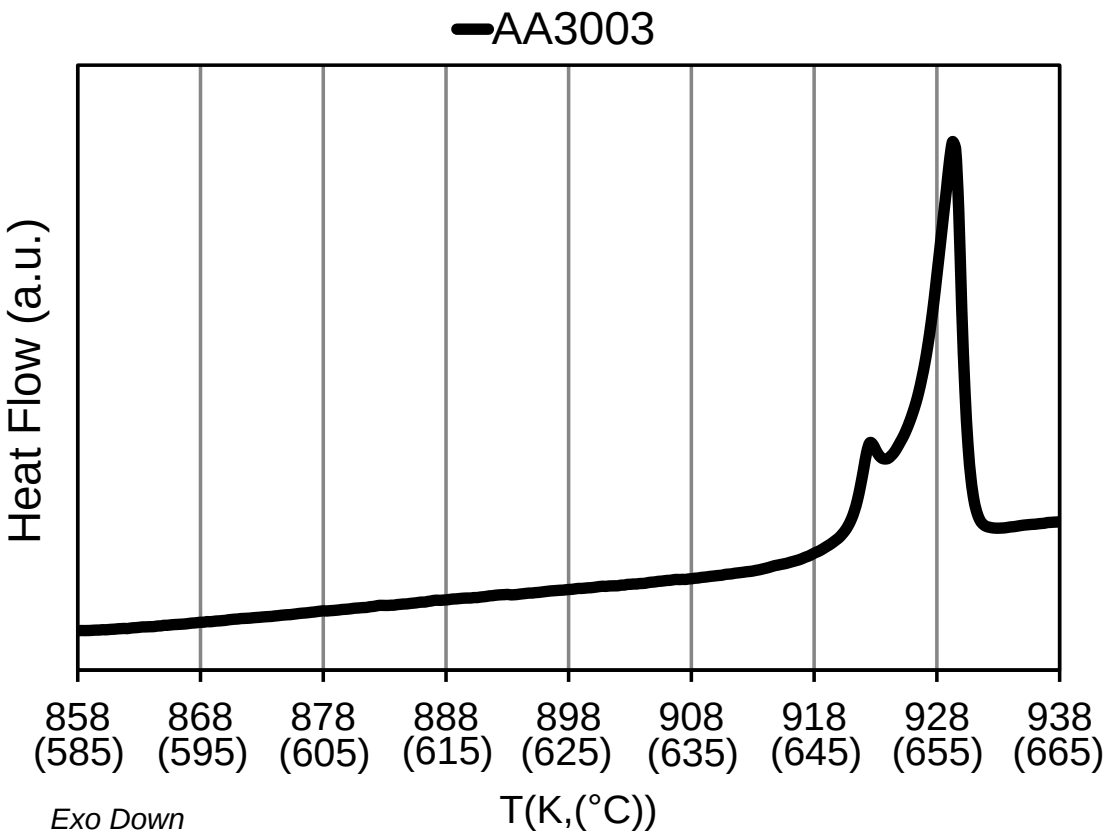

Figure 5-1 – Typical DSC result for the AA3003 material used for immersion test. Sample was heated to 828 K in less than 10 minutes than heated through phase transition at a rate of 0.017 K/s.

The exterior surface of the sample, prior to testing, is shown in Figure 5-2. To re-iterate, tests were performed by immersing the AA3003 samples into the AA4045 melt at a predefined speed of 1.4 mm/s. When the sample was immersed to a depth of 32 mm into the melt, it was withdrawn from the melt at a speed of 9 mm/s. The initial sample temperature was kept constant at 903 K (630 °C, similar to the peak temperature predicited during Fusion™ casting trials, see Figure 4-8), and the initial melt temperature was varied from 913-953 K (640-680 °C). The result after immersion in the AA4045, for the various peak temperatures shown in Figure 5-1, is shown in Figure 5-3.

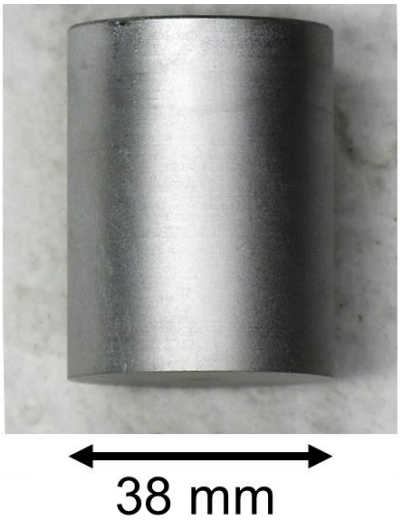

Figure 5-2 – Photo of a prepared AA3003 sample prior to immersion testing.

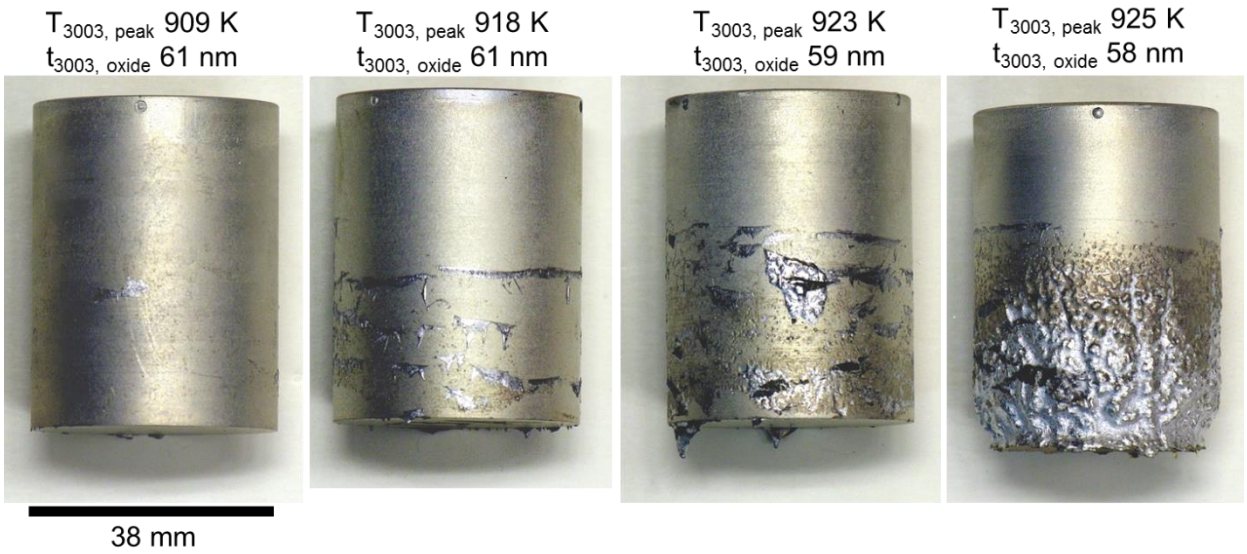

Figure 5-3 – Macro photos of AA3003 samples showing the effect of AA3003 remelting on the ability of AA4045 to wet the AA3003. Immersion of samples performed under air atmosphere.

The first two samples on the left hand side of Figure 5-3 did not reach a peak temperature higher than the measured onset of remelting, and showed no interaction between the sample and the melt at all, despite being immersed into the melt to a depth of 32 mm. Some superficial AA4045 liquid was stuck to the exterior of the samples as shown in the second sample from the left hand side; however, this material could be easily dislodged by brushing the sample surface

with a cloth. The test samples that reached a peak temperature of 923 K (650 °C), third sample from the left in Figure 5-3, also had superficial AA4045 liquid adhered to it near the top portion of the sample. However, this sample did show signs that the AA3003 surface oxide had been modified near the bottom of the sample. Here, the surface oxide was noticeably discolored (darkened). Craters in the sample surface were also observed. In addition, there were portions of the surface near the bottom of the sample which appeared shiny, an early indication that the AA3003 metal had come into contact with the AA4045 and that some interaction had occurred between the two alloys. In general, however, the overall wetting for these first three samples was not satisfactory. Additionally, two test samples (see Table 3-8) which did not reach a peak temperature where the samples would have thought to have been remelted, were left immersed in the melt for an additional 20 seconds during testing. Therefore, the total immersion time for these two test samples was ~ 20 s at the AA3003/AA4045 contact line and ~ 46.5 s at the bottom edge of the sample. The 46.5 s immersion time was similar to the predicted contact time between AA3003 solid and AA4045 liquid at the centerline during Fusion™ casting trials conducted in Chapter 4, see Table 4-1. The AA3003 samples showed little to no interaction with the AA4045 melt for a period of immersion of ~46.5 s, and were qualitatively similar to the results shown Figure 5-3.

The result from the sample which reached a peak temperature during immersion of 925 K, in Figure 5-3, was dramatically different. This result is consistent of all test samples where the sample peak temperature reached 925 K (652 °C). As shown, the sample diameter was reduced by up to 2.5 mm near the bottom edge of the sample, an indication that the sample was remelting. The exterior surface of the sample appeared shiny grey colour, similar to what was seen in only discrete locations in the 923 K (650 °C) samples. Near the top of the sample, where

the contact time with the AA4045 melt was short, a discoloration of the AA3003 oxide surface to a darkish grey colour, as well as a cratering of the AA3003 surface was observed.

Samples were also sectioned and examined with optical metallography, to assess the degree of AA3003/AA4045 interaction. On a macroscopic level, test samples which did not reach 925 K showed minimal interaction with the majority of the sample OD essentially unchanged, see Figure 5-4a. Occasionally, along the length of the sample, there were instances of sample dissolution, where the OD of the sample was reduced by a few hundred microns and silicon rich aluminum, i.e., AA4045, was clearly present at the interface.

Test samples which did reach a peak temperature of 925 K were more difficult to interpret macroscopically, as shown in Figure 5-4b. A few observations can be made of this sample cross section. First, there is a significant reduction in the diameter of the sample, which is most likely do to remelting, by contact heating from the hot AA4045 melt. The bottom of the sample, which was immersed in the melt for a longer period of time, would have been the hottest part of the sample, and likely would have begun remelting. The porosity in the AA3003 sample appears as white spots in Figure 5-4b. It should be noted that when observed under an optical microscope, these spots appeared black, suggesting they are indeed pores; however, these spots did appear white when imaged with a macro camera/lens system.

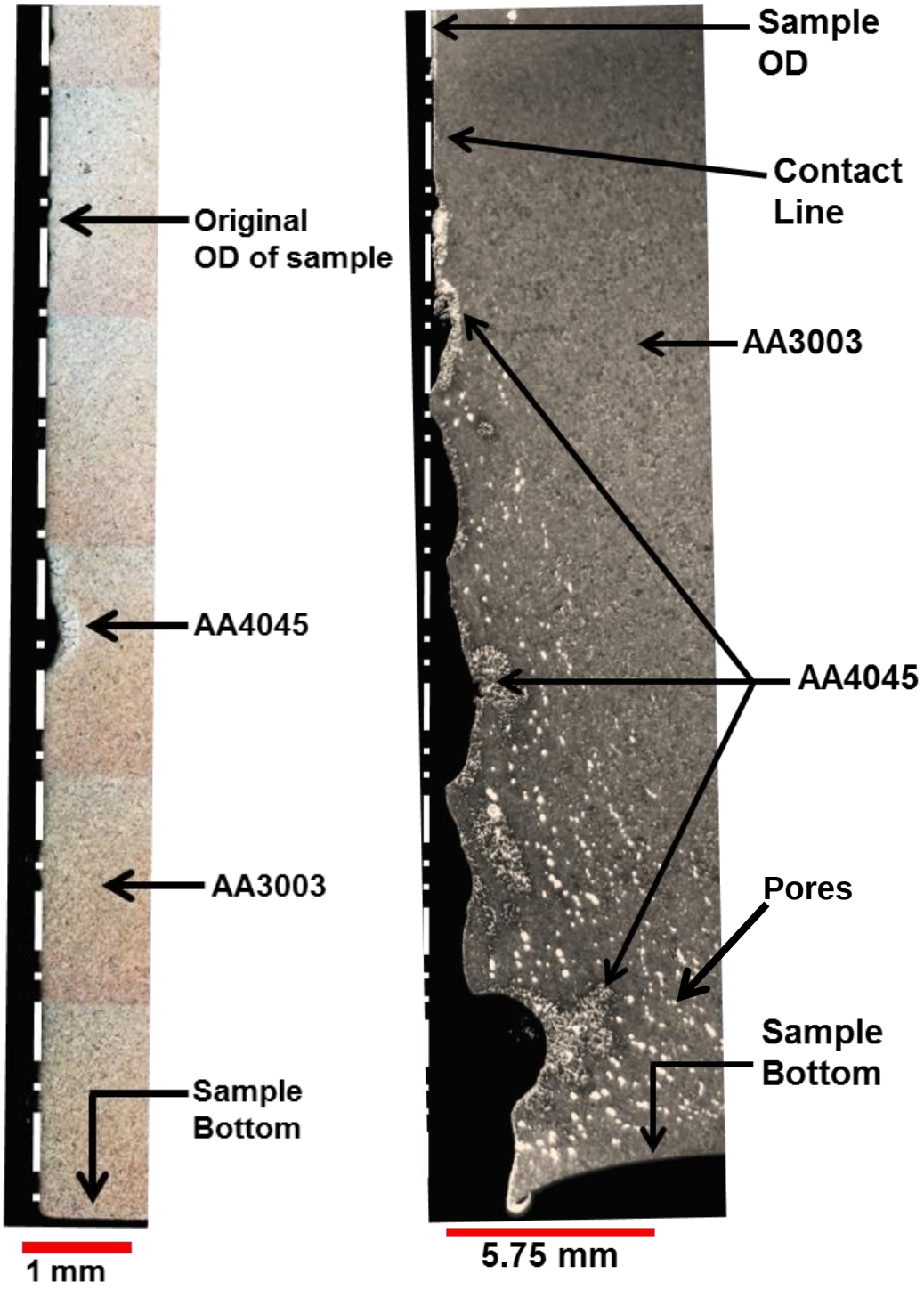

(a) (b)

Figure 5-4 – Optical metallography of AA3003 samples after tests immersion under an air atmosphere, (a) T_{peak} = 923 K; $t_{oxide,AA3003}$ = 59 nm, (b) T_{peak} = 926 K; $t_{oxide,AA3003}$ = 60 nm.

The presence of pores in the sample suggests that the AA3003 sample underwent remelting and subsequent solidification. The pores were irregularly shaped, indicating it may have been due to solidification shrinkage related. The penetration of porosity into the sample (i.e., from the OD of the sample towards the centre) goes from zero at the last point of contact between the sample surface and the melt, defined as the final contact line hereafter, to a maximum depth at the bottom of the sample. This is qualitatively consistent with how the sample would have been heated by the liquid AA4045 upon immersion, hottest at the bottom and coldest at the final contact line. Looking at the final OD of the sample, it is significantly reduced, by a few mm at the bottom of the sample. The reduction in sample diameter along the length of the sample is not continuous, although the trend is similar to the porosity previously discussed. At the outer edge of the sample, a thin layer of AA4045 can be seen, this is indicated with arrows in Figure 5-4b. The majority of the length of the sample has a thin layer of AA4045 at its outer edge, and an AA4045/AA3003 interface can be seen when viewed with higher magnification.

As mentioned previously, tests performed with sample peak temperatures in the range 908-919 K, had minimal interaction between the AA3003 solid and the AA4045 liquid, as shown in Figure 5-4a. For tests with sample peak temperature between 925 to 926 K, a thin layer of AA4045 was found adhered to the external surface of the sample which had come into contact with AA4045. The consistency of the interface varied significantly from the top to bottom edge of the sample. Again, these tests did not exhibit well defined final contact lines.

Figure 5-5 shows a series of micrographs, taken from the contact first point near the top edge, for a test with T_{peak} = 926 K, and t_{oxide} = 60 nm. In Figure 5-5a and b there is a thin AA4045/AA3003 interface along the outside surface of the sample. These two figures come from the part of the sample at the final contact line in a, and slightly below the final contact line

in b. As shown, the initial wetting and dissolution again appears discrete in nature, as evidenced by the semi-spherical interface between AA4045 and AA3003 material. Below this, the interface becomes continuous, as shown in Figure 5-5b. Here, a clear distinction between AA3003 and AA4045 material is apparent. Moving towards the middle of the sample, Figure 5-5c, the distinction between AA4045 and AA3003 material becomes less pronounced. Near the bottom of edge of the sample, Figure 5-5d, significant mixing of AA4045 and remelted AA3003 has taken place, as evidenced by the lack of obvious interface between the two materials and abundance of Mn bearing intermetallic phases (polyhedral shaped particles) on the AA4045 side of the interface.

Results from these tests suggest that when AA3003 immersion tests are conducted in air, little or no interaction between the AA3003 sample and AA4045 melt occurs when the AA3003 sample temperature remains below 925 K. Above $\gtrsim$ 925 K there is noticeable interaction between the AA3003 sample and the AA4045 liquid melt. Comparing this temperature with the DSC curve shown in Figure 5-1, suggests that some melting of the aluminum is necessary in order to break though the double oxide barrier between the AA3003 sample and the liquid AA4045. As a result of sample remelting, some AA3003/AA4045 bonding occurs; however, the final sample appearance (Figure 5-3) and the optical metallography results (Figures 5-4 and 5-5) are quite different than the Fusion™ cast interfaces presented Chapter 4.

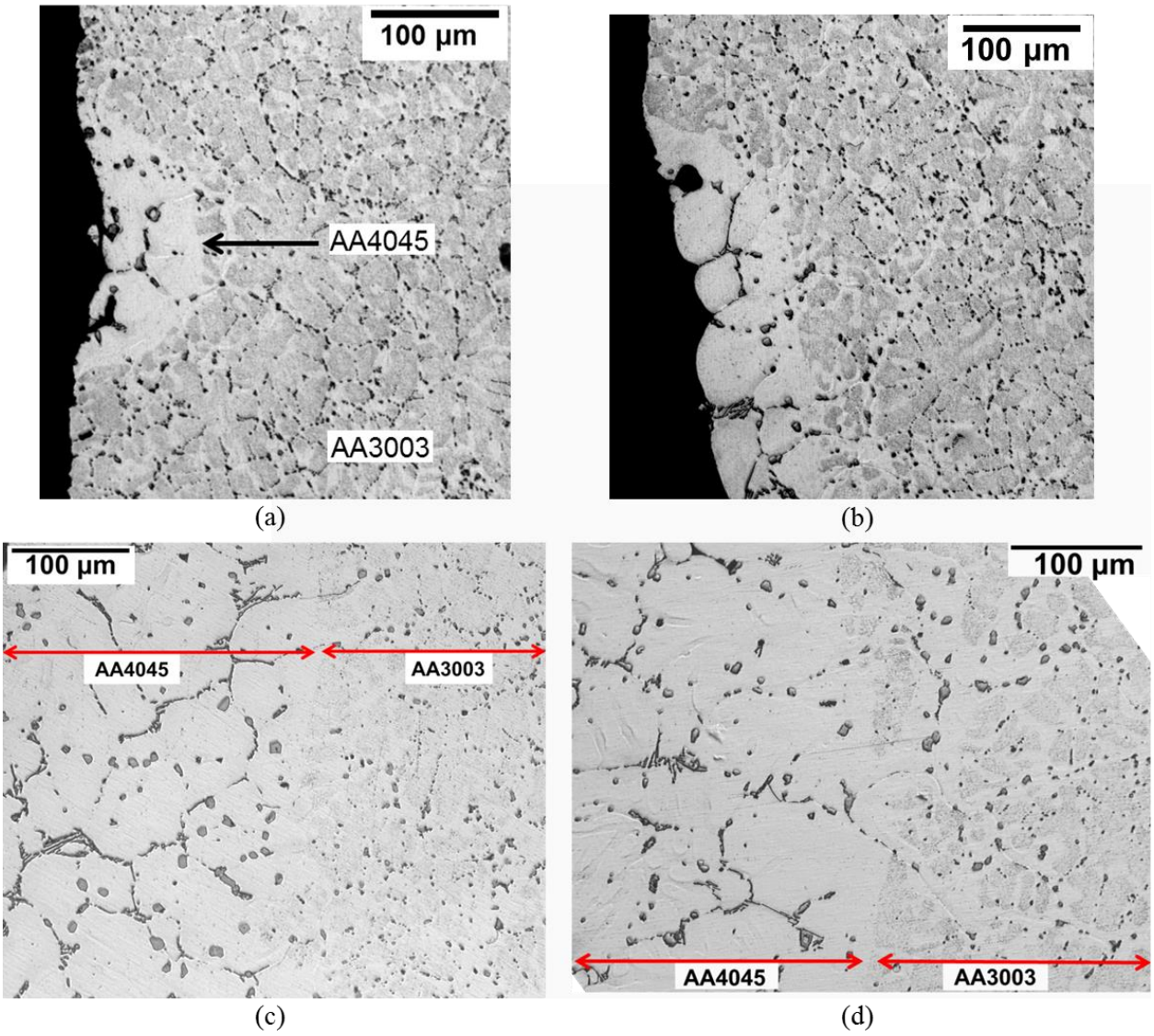

Figure 5-5 – Optical metallography of AA3003 sample after tests immersion under an air atmosphere; T_{peak} = 926 K, $t_{oxide.AA3003}$ = 60 nm. (a) isolated penetration of AA3003 by AA4045 near top region of AA3003 sample, (b) onset of AA4045 wetting of AA3003 sample slightly below isolated region depicted in a, (c) near middle of sample, showing a less distinctive interface, (d) bottom of sample showing more mixing of AA3003 and AA4045 material.

5.3 Oxidation tests

For these immersion tests, the objective was to observe what influence AA3003 surface oxidation had on interface formation. In this test series, the AA3003 and AA4045 test temperatures were kept fixed as 903 K and 913 K. The test conditions are outlined in Table 3-7.

By varying the times at which the melt and the sample were exposed to air at high temperature, see Section 3.3.1.1 and Figure 3-13, the amount of oxidation on the sample surface prior to immersion in the melt could be altered. During final immersion of the test sample into the melt, the ambient atmosphere in the furnace was argon for all tests shown in Table 3-7. After tests, oxide growth was calculated using measured sample temperatures, melt temperatures, and testing times, t_1 and t_2. The procedure used to calculate oxide growth is detailed in Appendix B.

The various estimated/calculated oxide thicknesses which were tested are shown in graphical format in Figure 5-6. Note that the *y*-axis indicates the value of oxide thickness calculated to be grown on top of the AA4045 melt prior to testing. Since there is an elapsed period of time after skimming the AA4045 liquid (cleaning the oxide off) and test immersion, there is expected to be a surface oxide on the melt. This surface oxide is broken as the sample is immersed into the melt, the role this melt oxide plays in the immersion test is otherwise not significant.

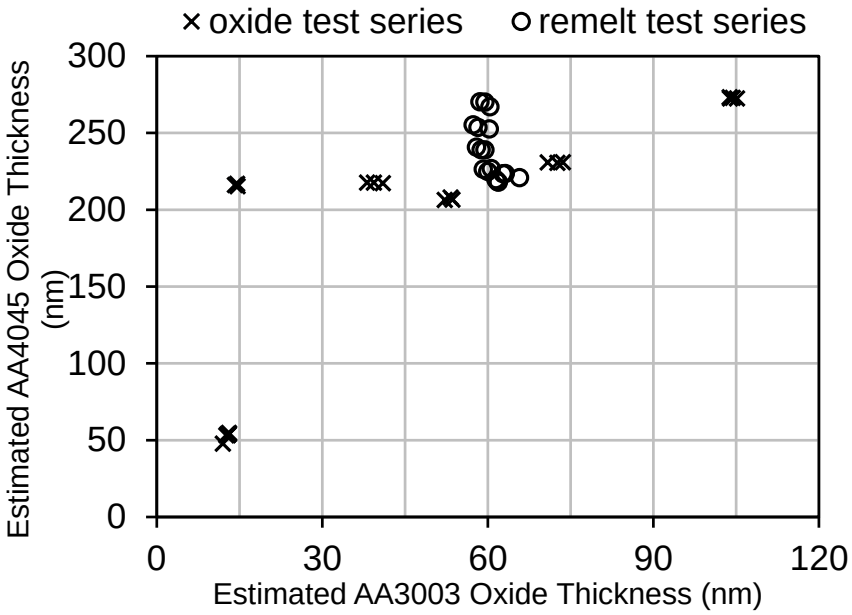

Figure 5-6 – Calculated AA3003 sample oxidation and AA4045 melt surface oxidation for tests series conducted in this section, shown as black X's. Calculated oxide values for the remelt tests series (previous section) shown as open circles.

Typical examples of the final exterior surfaces of samples from this test series are shown in Figure 5-7. For tests done with varying levels of AA3003 oxide thickness, a noticeable effect was seen on the external surface of the test samples after immersion into liquid AA4045. Samples with minimal exposure to air during heating (and lower $t_{oxide,AA3003}$) showed uniform wetting and dissolution below the final contact line between the AA4045 liquid and AA3003 solid sample. Furthermore, the final contact line appeared to be continuous around the circumference of the AA3003 sample. In samples which were exposed to air for longer periods of time during heating (thicker oxide layer), the final contact line became less continuous in nature.

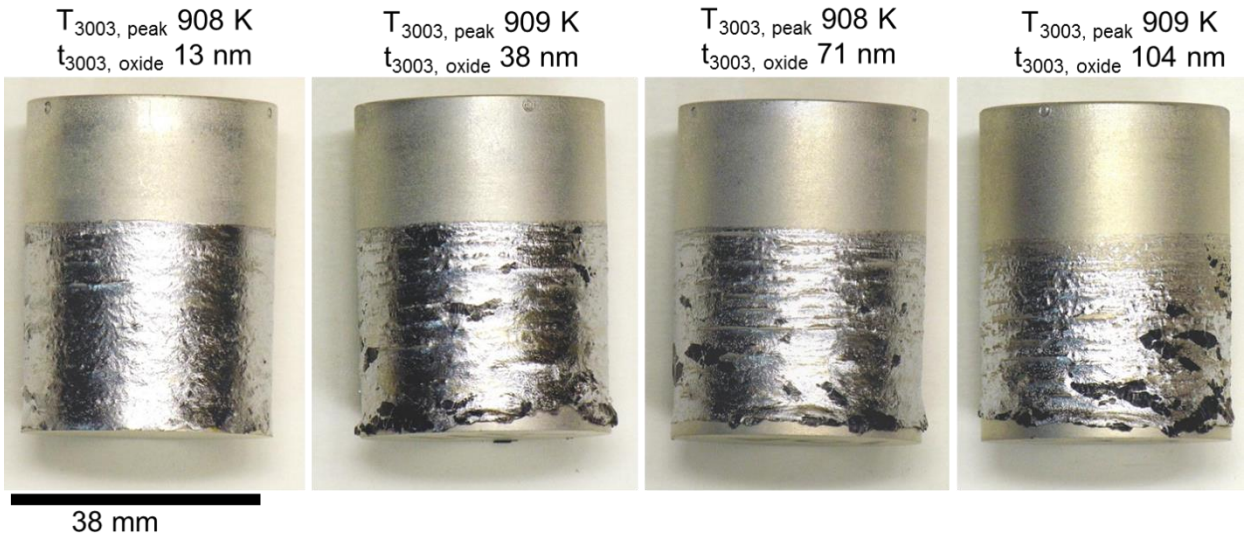

Figure 5-7 – Macro photos of AA3003 samples showing the effect of oxide thickness on the ability of the AA4045 to wet the AA3003. Immersion of samples performed under argon atmosphere.

Although wetting and dissolution was achieved on all tests conducted, several artifacts were found on the external surface of these samples. Long-and-thin (~5 mm long and < 1 mm thin) areas which were not wetting by AA4045 (hence called dry patches), were observed on all test samples. The presence/frequency of these patches increased with $t_{oxide,AA3003}$. The dry patches were always found to have their long axis perpendicular to the immersion direction.

Their presence was more evident near the final contact line (less time in contact with AA4045 liquid), rather than near the bottom portion of the sample (longer time in contact with AA4045 liquid). On tests conducted where the $t_{oxide,AA4045}$ of the AA4045 liquid was greater than 55 nm, a region near the bottom edge of the sample (in addition to the bottom surface of the sample), was not wetted by AA4045. Additionally, oxide fragments from the AA4045 liquid oxide film (black in colour) were found adhered to the AA3003 sample. The size, frequency, and location of these fragments did not follow any noticeable pattern.

Figure 5-8a and b show two longitudinal sections from tests which were conducted in argon, with a portion of the image cropped out so that they fit within a page. The sample shown in Figure 5-8a, T_{peak} = 909 and t_{oxide} = 14 nm, shows that the depth of the sample removed by the dissolution process (with respect to the original sample outer diameter) is fairly linear with AA4045 liquid contact time. This is shown as a minimum depth of dissolution at the final contact line (shortest time in contact with AA4045 melt), to a maximum depth at the bottom of the edge of the sample (longest time in contact with AA4045).

The sample shown in Figure 5-8b, T_{peak} = 909 and t_{oxide} = 54 nm, was exposed to air for a longer period of time during heating (hence thicker t_{oxide}). Similar to Figure 5-8a, it clearly shows AA3003 sample dissolution by the liquid AA4045 melt and comparable dissolution depths. Three noticeable differences were observed: 1) wetting is poor near the final contact line, and 2) the dissolution is not linear along the length of the sample, instead a ridged like pattern appears along the longitudinal direction of the sample. This is an indication of non-uniform (or discrete) penetration of the AA3003 sample by the AA4045 liquid. Near the bottom edge of the sample, where contact time between AA3003 and AA4045 liquid is longest, and the most dissolution has taken place, the ridge-like pattern is less pronounced.

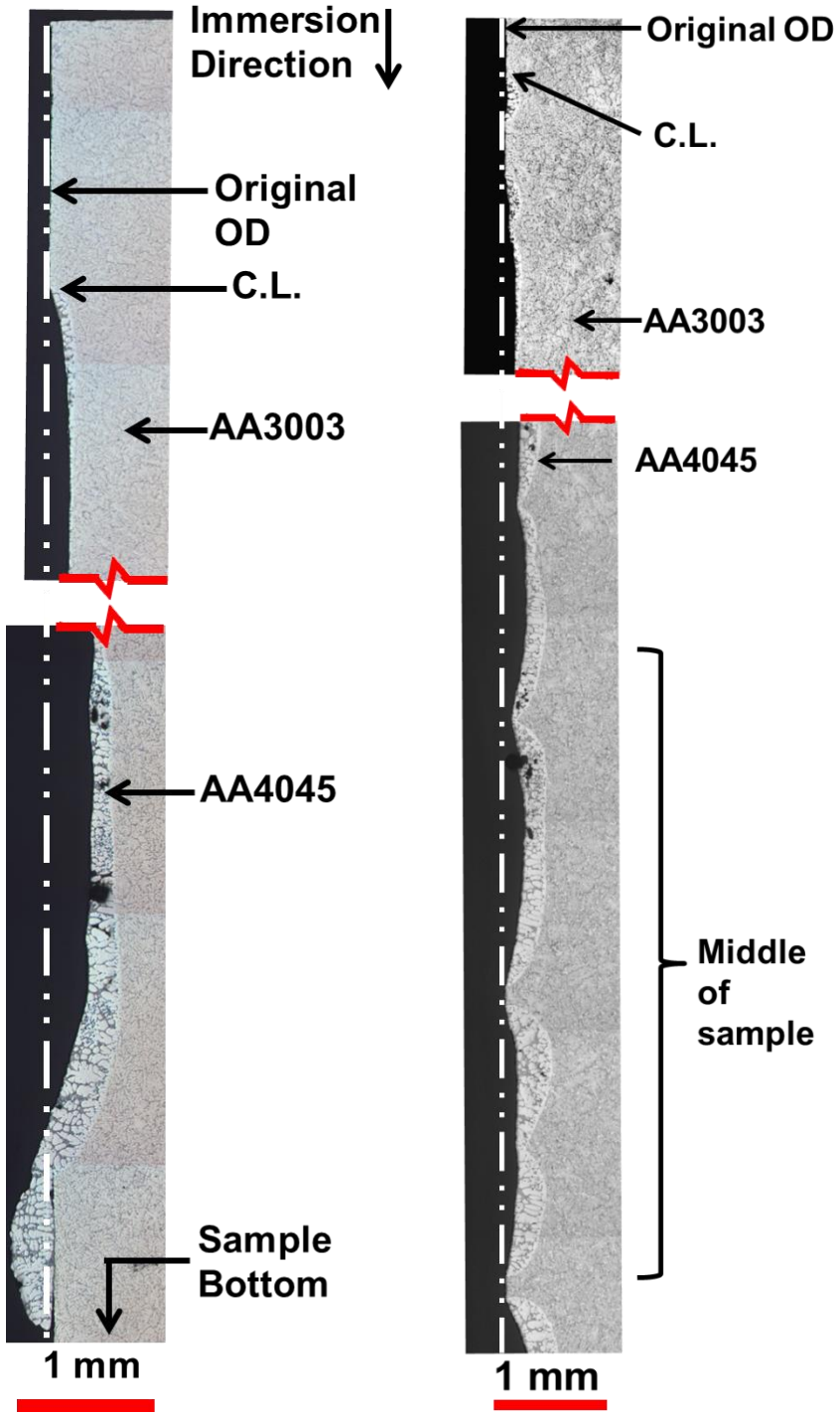

(a) (b)

Figure 5-8 – Optical metallography of AA3003 samples after tests immersion under an argon atmosphere, (a) T_{peak} = 909 K; $t_{oxide,AA3003}$ = 14 nm, (b) T_{peak} = 909 K; $t_{oxide,AA3003}$ = 54 nm.

Figure 5-9a is a magnified view of the dissolution profile taken from samples with T_{peak} = 908-911 K and $t_{oxide,AA3003}$ 12-15 nm revealed a thin layer of AA4045 material clearly bonded to the adjacent AA3003 material along the entire length of sample which was in contact with the AA4045 liquid during immersion. This is qualitatively similar to micrographs from other dissolution studies [106-107]. Tests with higher values of $t_{oxide,3003}$, did not exhibit well defined final contact lines (as mentioned previously). Typically, the first signs of wetting and dissolution of the AA3003 sample were discrete in nature, and were located near the final point of contact between AA4045 and AA3003. An example is shown in Figure 5-9b, for a test with T_{peak} = 909 K and t_{oxide} = 54 nm. The semi-spherical shape of the interface between AA4045 and AA3003 material is qualitatively similar to the 'discrete' penetration and dissolution model described by [53].

For these tests conducted in an argon atmosphere, remelting of the AA3003 sample was not a requirement for AA3003/AA4045 wetting and bond formation. The level of AA3003 surface oxidation prior to sample immersion into the AA4045 liquid melt did have a noticeable effect on the wetting and bond formation process, as evidenced by the differences in final sample appearances shown in Figure 5-10. Additionally, samples which were oxidized to an estimated AA3003 surface oxide thickness of 105 nm were wetted by the AA4045 liquid and bond formation did occur between the AA3003 solid sample and the AA4045 melt, indicating that the AA3003 surface oxide was penetrable by liquid AA4045.

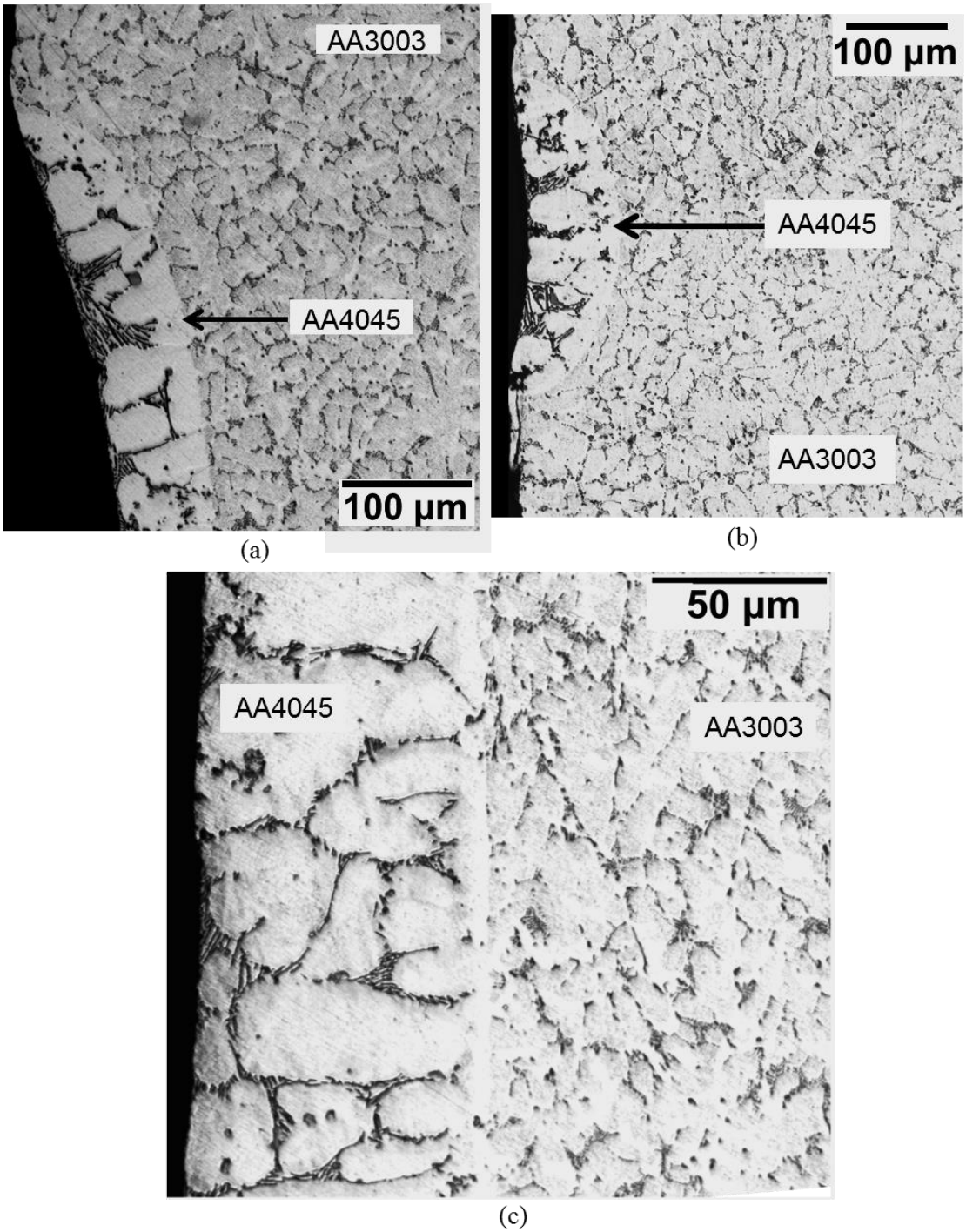

Figure 5-9 – Optical metallography of AA3003 samples after tests immersion under an argon atmosphere, T_{peak} = 909 K. (a) upper edge of final contact line between AA3003 and AA4045 in sample with $t_{oxide,AA3003}$ = 14 nm, showing dissolution of AA3003 sample thin layer of AA4045 adhering to surface of AA3003 sample (etched sample), (b) final contact line region in sample with $t_{oxide,AA3003}$ = 54 nm (etched sample), and (c) bottom edge of AA3003 sample with $t_{oxide,AA3003}$ = 13 nm, showing dissolution of AA3003 sample and Mn bearing intermetallics within thin adhering AA4045 layer (etched).

5.4 Macroscpoic Observations from Immersion Tests

For all tests which were performed in Chapter 5, the bottom surfaces of the AA3003 sample was consistently unaffected by immersion into the AA4045 melt (the horizontal portion of the sample to first come into contact with the AA4045 melt). This behaviour is shown in Figure 5-10a. Here, the bottom surface of the sample shown in Figure 5-10a does not appear to have changed as a result of being immersed into the melt. It was also observed that as AA4045 oxidation increased (either by higher AA4045 melt temperatures, or by longer exposure times to air), bare patches were found along the sides of immersed AA3003 samples. These patches were always located near the bottom of the sample (i.e., the first vertical portion of the AA3003 sample to come into contact with the AA4045 melt), see Figure 5-10b and c. Upon visual examination of the AA4045 melts after solidification and cool down, there was an obvious ring pattern found on what would have been the free surface of the AA4045 melt. This can be seen in Figure 5-11a, for AA4045 which was lightly oxidized, i.e., held in an argon atmosphere, and in Figure 5-11b, for AAA4045 melt which had been exposed to atmospheric air. This ring corresponds to the point at which the AA3003 contacted the AA4045 melt upon immersion, and subsequently broke through whatever oxide layer had been grown on the AA4045 melt during the sample heat up period.

These observations, although straightforward, serve to reinforce the importance of melt (in this case AA4045) surface condition (or cleanliness) on bond formation between AA3003 and AA4045. If the AA4045 coming into contact with AA3003 is oxidized, then the subsequent interaction between the AA3003 solid and AA4045 liquid is minimal. As the initial free surface of the AA4045 melt was always oxidized (to some extent) prior to immersion of a test sample into the melt, the result shown in Figure 5-10a was expected. This lack of interaction between

AA3003 test samples and the AA4045 melt, due to contacting oxides, was more subtly observed in tests conducted in air and below the remelting temperature of AA3003, see Figure 5-3.

(a) (b) (c)

Figure 5-10 – Effect of AA4045 melt oxidation on appearance of AA3003 exterior after immersion into an AA4045 melt. (a) Bottom surface of a typical AA3003 sample. Appearance of AA3003 exterior after immersion into (b) a heavily oxidized AA4045 melt, notice dry patch along the side (near bottom) of AA3003 sample, and (c) a lightly oxidized AA4045 melt.

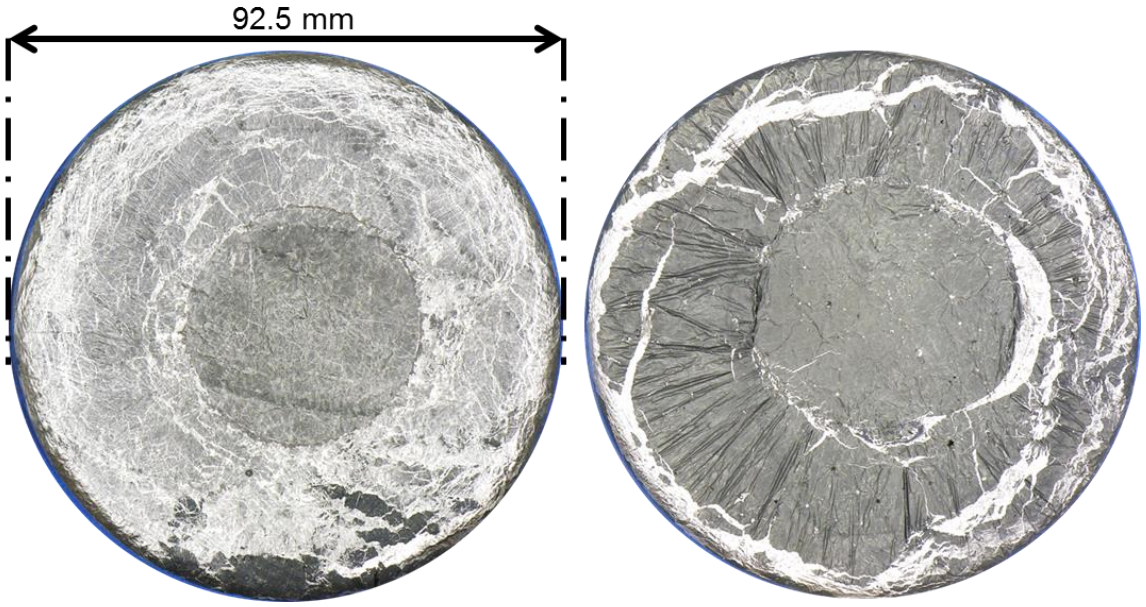

(a) (b)

Figure 5-11 – Effect of AA4045 melt oxidation. (a) Top view of a lightly oxidized AA4045 melt after melt re-solidification, (d) Top view of a heavily oxidized AA4045 melt after melt re-solidification

5.5 Discussion: AA3003 Remelting and Other Implications for Fusion™ Casting Practices

Results from the remelting tests suggest that AA3003 remelting can potentially be beneficial in achieving AA3003/AA4045 bonds. In actuality, for tests conducted in air, when T_{peak} was less than = 923 K, little or no interaction between the AA3003 sample and AA4045 melt occurred, for reasons discussed in the previous section. In these series of tests, it was apparent that in order to achieve bonding, the samples had to reach a $T_{peak} \gtrsim 925$ K. Comparing this temperature with the DSC curve shown in Figure 5-1, suggests that some melting of the aluminum is necessary in order to break though the double oxide barrier between AA3003 and liquid AA4045.

While controlled remelting of the core alloy (in this case AA3003) is a plausible mechanism for bond formation in Fusion™ casting, and is likely to occur when Fusion™ casting two alloys with significant overlap of freezing ranges, there are clear benefits and disadvantages to utilizing this technique. The benefit, as mentioned previously, is that it can easily be done in an air environment without worry of oxide film from the liquid alloy being an impediment to bonding. The disadvantages are: (i) a less defined interface, as evidenced by Figure 5-5c and d, (ii) the possibility of defects due to remelting of the core alloy (in this case AA3003), as evidenced by porosity in the AA3003 samples in Figure 5-4b, (iii) a greater potential for a remelt breakthrough of interface and casting failure, and (iv) tighter process controls. Likewise, the main disadvantage of operating in the range where AA3003 remelting does not occur is the requirement that the oxide which is being formed on the liquid alloy (AA4045 in this case) does not get entrained at the interface. Hence, the motion of the AA4045 oxide film becomes an important factor for bond formation in industrial Fusion™ casting processes. The preferred scenario is indeed that which was observed in Chapter 4, and illustrated in Figure 4-15, where both the AA4045 and AA3003 oxide films are stationary or move away from the interface, thus

AA3003/AA4045 bond formation relies solely on the oxide film characteristics of the surface of the AA3003 shell, and its time in contact with liquid AA4045.

It should be noted that the observations of the AA3003 chill surface structure made in Chapter 4 suggested that some local remelting of the AA3003 occurs at temperatures of 903 K (630 °C), and manifests itself in the form of "spot exudation". This partial remelting may breakup the AA3003 surface oxide, and hence be beneficial to AA3003/AA4045 bond formation. This behaviour, i.e., spot exudation, was not observed during heating of the AA3003 samples during immersion testing. The spot exudation mechanism, as outlined by Morishita *et al.* [81], relies on a back pressure of liquid metal (provided by the liquid sump in DC casting or Fusion™ casting) to force liquid metal out of the interdendritic channels. In the test method used for the immersion tests in Chapter 5, the AA3003 solid samples were not subject to a liquid back pressure, and hence spot exudation was not expected to occur. Thus, the observation that the samples had to reach a $T_{peak} \gtrsim 925$ K (consistent with α-aluminum melting) in order for there to be interaction between AA3003 and the AA4045 melt (for tests conducted in air) was expected. In a scenario where spot exudation could be produced during sample heating, one may expect interaction to occur between the AA3003 sample and AA4045 liquid at a lower temperature for tests conducted in air.

Based on the results from tests conducted in argon (see Section 5.3), there is ample evidence that, under certain conditions, thermal remelting of AA3003 is not a requirement for wetting and bond formation to occur between AA3003 and AA4045. This is reasonable, as studies on dissolution [23] and solutal remelting [106] show qualitatively similar metallurgical bonds to the one shown in Figure 5-9a and c, without the requirement of sample remelting. On the contrary, when tests are conducted in air, it appears that the AA3003 sample must be partially

remelted in order to obtain interaction between the AA3003 sample and the AA4045 melt. The most striking result exemplifying this difference is shown in Figure 5-3, for the samples with T_{peak} = 909 K and T_{peak} = 925 K.

The subtle role that the ambient atmosphere plays on wetting and bond formation between AA3003 and AA4045 can be explained by examining the immersion process during testing, see Figures 5-12 and 5-13. It is important to consider that during sample heating, oxidation is taking place on the AA3003 sample as well as on the AA4045 liquid free surface, Figure 5-12a and 5-13a. When the sample reached its target temperature, it was lowered into the melt. Upon immersion into the melt, the AA3003 sample must break this initial AA4045 oxide layer. At a certain depth of immersion, the oxide layer on top of the AA4045 liquid is stressed to the point at which it breaks. This action exposes fresh liquid AA4045 to the ambient atmosphere, Figures Figures 5-12b and 5-13b. It is worth noting that the bottom of the AA3003 (at a few mm along the edge of the sample) remains covered by this initial AA4045 oxide film, throughout the test. This is likely why the bottom of the sample and lower edge of the sample are not dissolved and remain relatively intact during testing, see for example Figure 5-7 test samples t_{oxide} = 71 nm and t_{oxide} = 104 nm.

The interaction of this freshly exposed AA4045 liquid surface with the ambient atmosphere, in conjunction with continual immersion of the AA3003 sample into the melt is likely to be the controlling factor in wetting and bond formation, see Figures 5-12 and 5-13c. Based on tests results, there is evidence to suggest that the argon atmosphere sufficiently slows the AA4045 oxygen adsorption and subsequent re-oxidation kinetics, such that the contact condition between AA3003 and AA4045 is oxidized AA3003 solid with clean AA4045 liquid, as shown in Figure 5-13d. Whereas when the ambient atmosphere is air, the adsorption and re-

oxidation kinetics is sufficient to change the contact condition between AA3003 and AA4045 to oxidized AA3003 solid with an oxidized AA4045 liquid, as shown in Figure 5-12d.

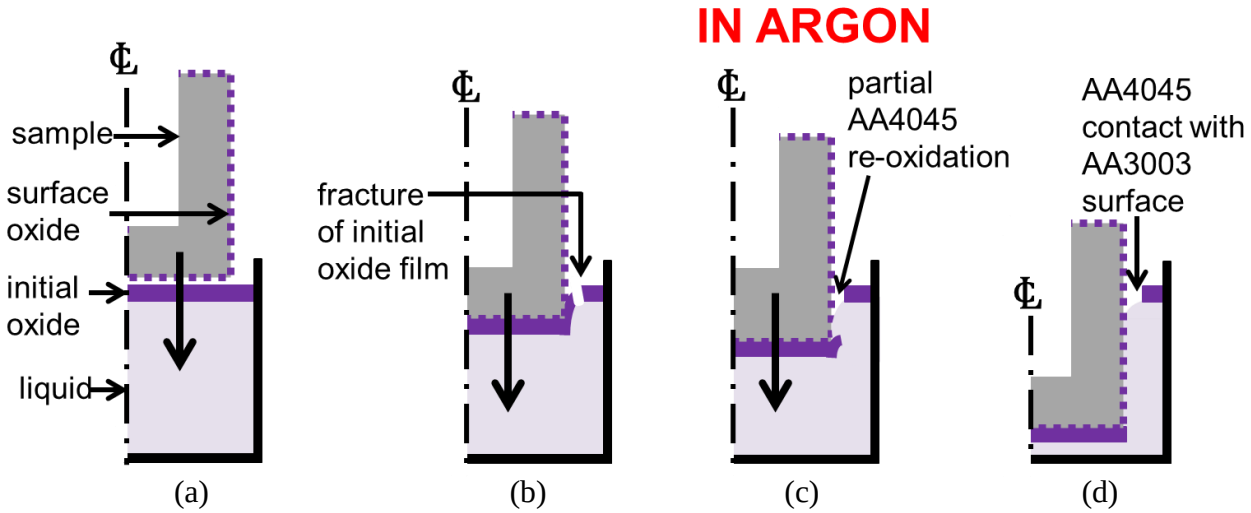

Figure 5-12 – Sequence of events during immersion tests in argon (shown in axisymmetric view). (a) Initial sample state showing oxidized AA3003 surface and initial AA4045 oxide film on melt. (b) Sample immersion into melt and breaking of initial AA4045 oxide film. (c) Sample immersion while exposed to inert atmosphere with only partial re-oxidation of AA4045 liquid at the meniscus. (d) Contact of AA3003 with 'clean' liquid below the contact line.

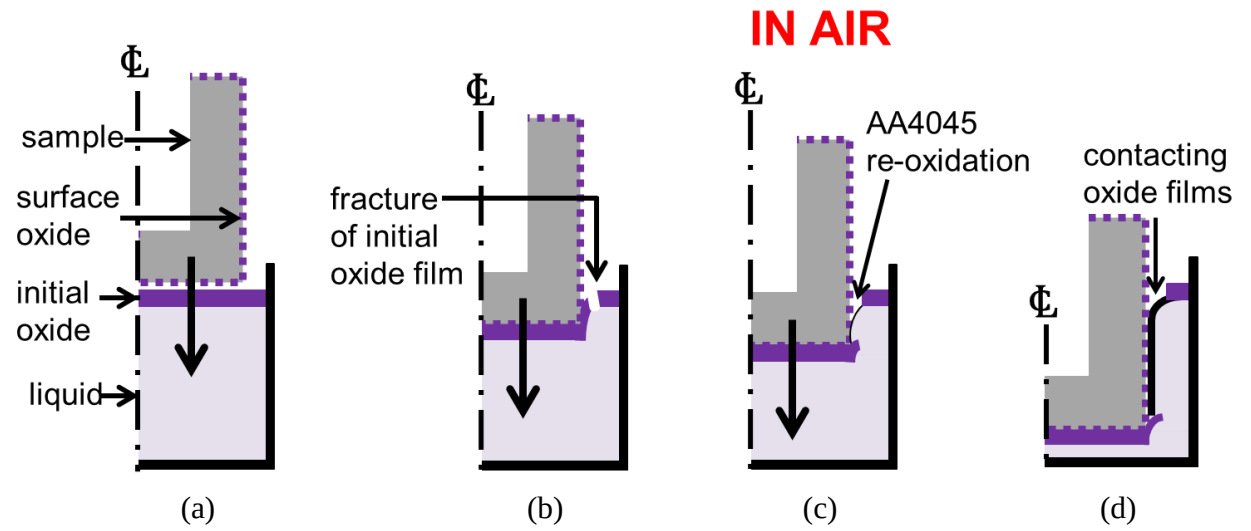

Figure 5-13 – Sequence of events during immersion tests in air (shown in axisymmetric view). (a) Initial sample state showing oxidized AA3003 surface and initial AA4045 oxide film on melt. (b) Sample immersion into melt and breaking of initial AA4045 oxide film. (c) Sample immersion and complete re-oxidation of AA4045 liquid at the meniscus. (d) Double oxide contact at the AA3003/AA4045 interface and negligible interaction between sample and melt below the contact line.

While the use of argon appeared to be beneficial in terms of promoting AA3003/AA4045 wetting and bond formation, the question still remains; what happens to the AA3003 oxide which makes it amenable to wetting and bonding? The observation from the test conducted with varying levels of AA3003 surface oxidation suggest that the oxide which grows on the AA3003 surface during heating can be sufficiently thick (~100 nm by estimate) and still be penetrated by the AA4045 liquid. Additionally, the trend was found that the bond quality, as evidenced by the: (i) lack of continuity at the contact line and (ii) increased frequency of dry areas on the sample decreased with increasing $t_{oxide,AA3003.}$ The objective in the following section was to observe what differences may exist between the samples with the lowest predicted oxide thickness and those with the highest predicted oxide thickness, and how any of the observed differences might correlate to the observed differences in wetting and dissolution of the tests samples shown in Section 5.3.

5.6 Relative oxide thickness and oxide morphology with SEM

To characterize the thermal oxides grown on the AA3003 test samples from immersion tests conducted in Section 5.3, sister samples were prepared and oxidized using similar heating rates and times. The preparation of these samples is described in Section 3.3.2.2 and Table 3-13.

The first step in assessing the morphology of the AA3003 surface oxides was to examine the as-etched sample surface. FE-SEM images of the NaOH-etched sample surface are shown in Figure 5-14a and b. As stated previously, the surface exhibited a scalloped surface, typical of NaOH etched samples. Some pitting was also present on the surface.

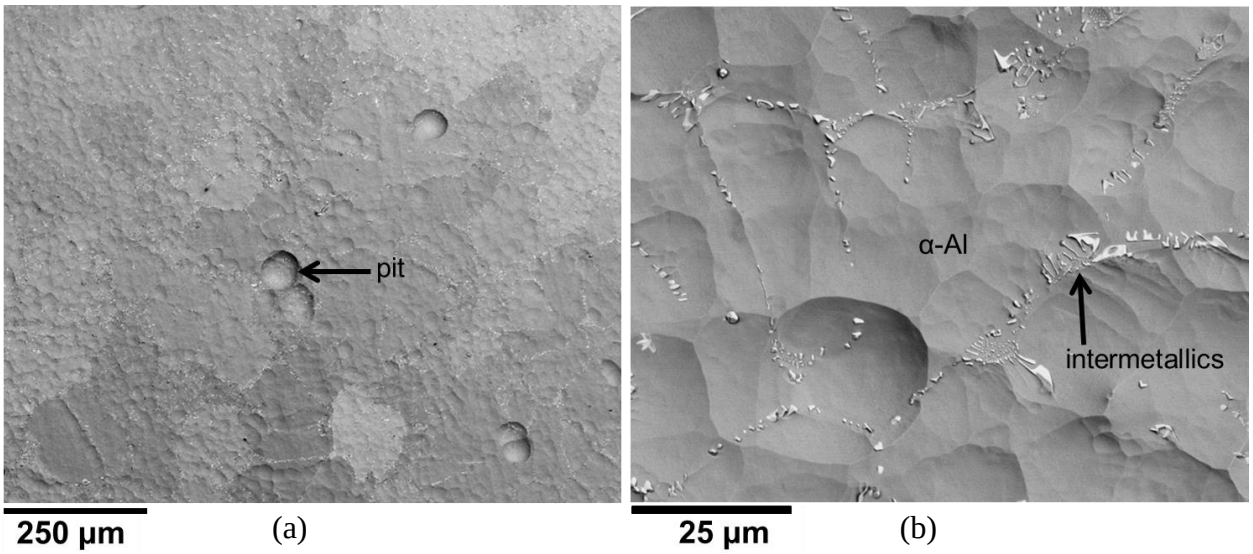

Figure 5-14 – Surface morphology of as-etched AA3003 sample, prior to any exposure to high temperature. (a) Backscattered SEM (4 kV) image low magnification, (b) backscattered SEM (4 kV) image high magnification.

A typical EDS profile, taken at an accelerating voltage of 4 kV, of the as-etched surface is shown in Figure 5-15. In the EDS spectrum, both Al and O show up in the peak analysis, as expected. C is present, likely due to contamination of the sample or EDS system. The absence of Si, Fe, and Mn from the EDS spectrum is likely due to the lower penetration depth and x-ray count rates obtained during operation; as a result of the low accelerating voltage used to image the sample surface with better resolution (4 kV). An EDS spectrum taken using an accelerating voltage of 20 kV, on an oxidized sample, is shown in Figure 5-16. The peaks have been labelled in the figure; and Si, Fe, and Mn were observed in the EDS spectrums, all of which are present in the AA3003 used to fabricate these tests samples, see Table 3-6. No other elements were found in the as-etched EDS spectrum of the as-etched samples.

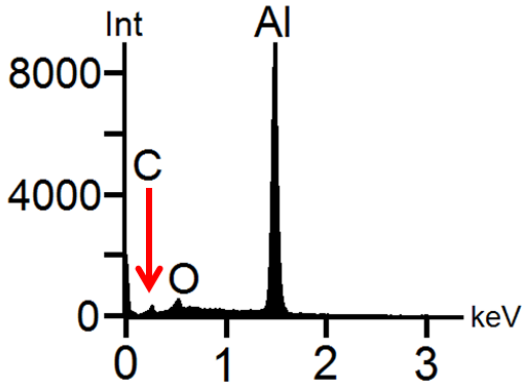

Figure 5-15 – 4kV EDS spectrum of an AA3003 sample, using a 1800 μm by 1800 μm field size, prior to any exposure to high temperature.

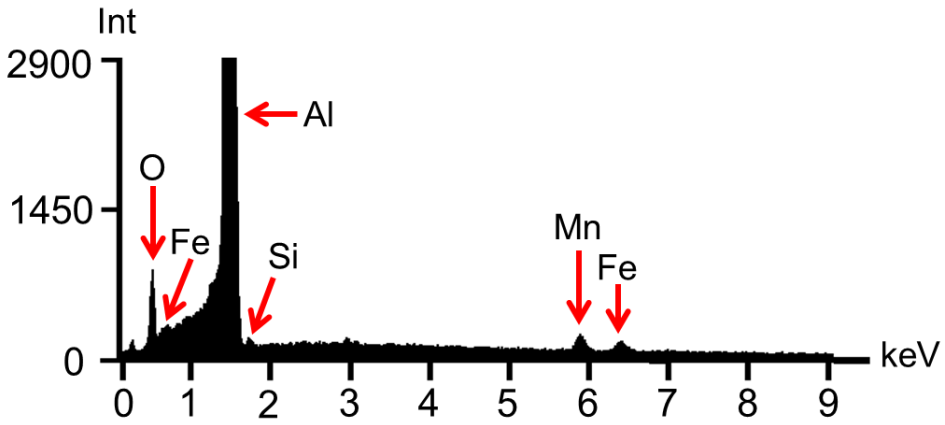

Figure 5-16 – 20kV EDS spectrum of sample ***air5*** (see Table 3-13) oxidized at high temperature for 63.5 minutes in air, using a 1800 μm by 1800 μm field size. Note: top of Al peak is cropped in the graph.

Samples oxidized at high temperatures, exhibited noticeable differences upon examination in the FE-SEM. As shown in Figure 5-17, 4 kV backscattered images revealed dark patches on the sample surface, which were not present on the as-etched samples. EDS spectrums from the dark region and light region (locations a and b on Figure 5-17) revealed the presence of Mg-rich (location a - dark area) and Mg-lean areas (location b -light area) at the surface, whereas no Mg was detectable on the as-etched sample (only 0.005 wt% Mg in AA3003), Figure 5-18a and b. Additionally, the O peak was far larger in comparison to the as-etched sample, indicating surface oxidation had taken place. Higher magnification of the seemingly Mg-lean areas revealed that

discrete populations of Mg and O rich particles, much less than 1μm in size, on the sample surface. These appeared as small dark spots on the SEM images. In addition, sub-micron sized small white spots were visible on the sample surface, which are encircled in Figure 5-17. When analyzed with EDS, see Figure 5-18c, these bright areas had elevated levels of Mn, Si, and Fe. Literature on the heat treatment of Al-Mn alloys [119-122] suggests that these are in fact dispersoids, which form during reheating of un-homogenized AA3003 material.

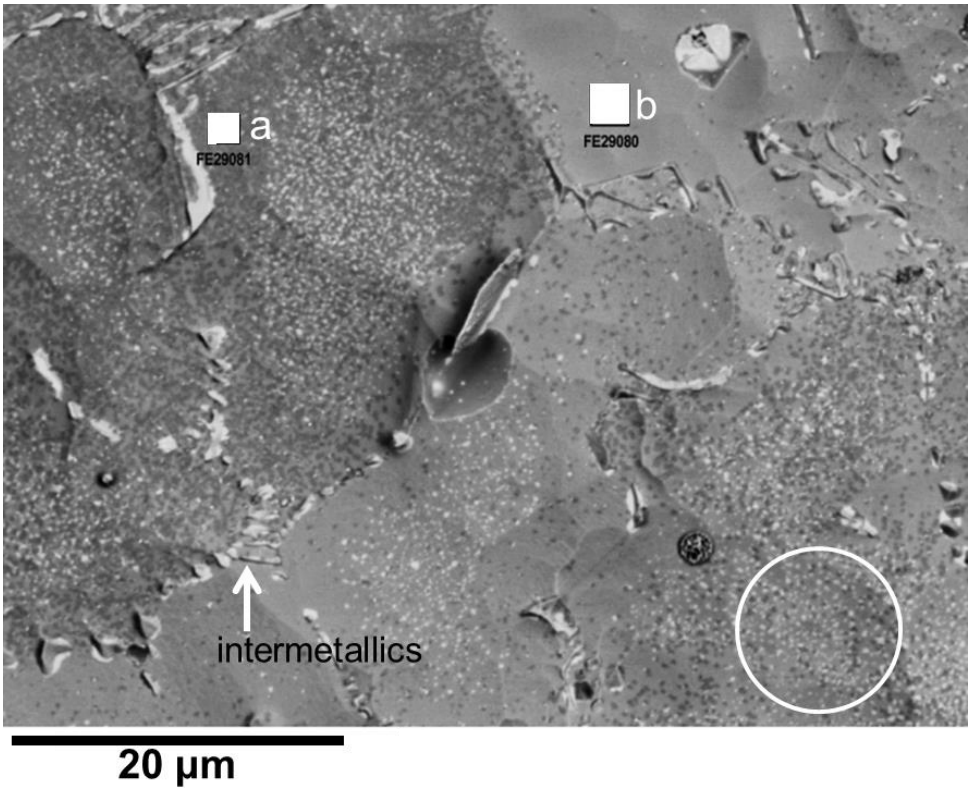

Figure 5-17 – Backscattered SEM (4 kV) image showing surface morphology of AA3003 sample heated and exposed to air during the first 9 minutes of heating ($t_{oxide,\ AA3003}$ = 13 nm). Dark area identified as Mg rich region and light area identified as Mg lean area. Encirled region highlighting white and dark spots. Dark spots indentified as Mg rich and light spots likely to be dispersoids formed during sample heating, see EDS of selected areas in Figure 5-18.

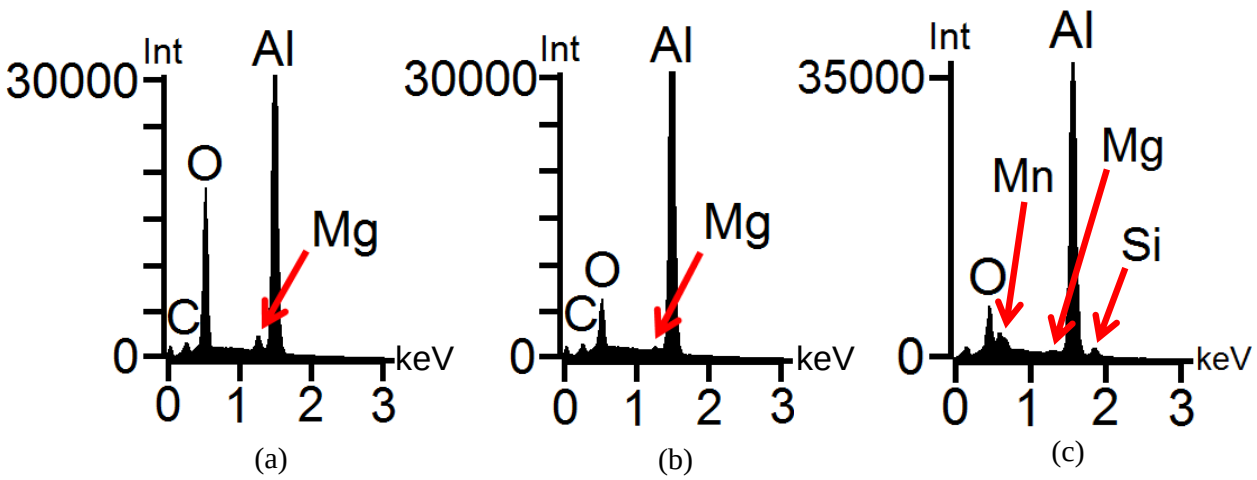

Figure 5-18 – (a) EDS spectrum obtained from area a in Figure 5-17. (b) EDS spectrum obtained from area b in Figure 5-17. (c) EDS spectrum of a white spot from encircled area in Figure 5-17.

The fractional surface coverage of the Mg rich regions was generally found to increase with air exposure time. To illustrate this, three of the samples were examined with EDS area mapping. The first sample, ***n1*** in Table 3-13, was heated in nitrogen for 40 minutes, and had a calculated oxide thickness of 13 nm. The second and third samples, ***air4*** and ***air5*** were heated in air for 46.5 and 63.5 minutes, yielding calculated oxide thicknesses of 46 nm and 95 nm respectively. The EDS maps for the three samples are shown in Figures 5-19 to 5-21. In these maps, greyscale is used to signify the intensity of the EDS spectra at each pixel in the BSE image (BSE image for each map is the upper left hand image). Bright white indicates a strong presence of the detected element, while black the opposite. For the Oxygen maps, it should be noted that small amounts of oxygen, above a zero level, where obtained in the dark regions of the map. Furthermore, the contrast on the images has been enhanced to aid the eye, thus the maps are no longer normalized as viewed in this thesis.

Mg coverage is fairly low in Figure 5-19. Mg segregation was observed to occur over top of the intermetallic particles. Additionally, discrete populations of Mg was observed to be segregated at the surface (less than 1 μm in size), within the primary aluminum grains (not quite

discernable in the maps, but readily observable on BSE images). With progressively more exposure, as in Figure 5-20 and Figure 5-21, Mg surface coverage is much more developed. In Figure 5-21 surface coverage by Mg is almost 100% complete. Additionally, in both Figure 5-20 and Figure 5-21 there appears to be little difference in Mg signal intensity between intermetallic regions and primary aluminum regions. The increasing amount of Mg surface coverage, shown in Figures 5-19 to 5-21, when compared to the sample appearances in Figure 5-7, suggest a link between sample wetting and bond formation and Mg oxide coverage at the AA3003 sample surface. Increasing Mg surface coverage appears to potentially be an impediment to AA3003/AA4045 bond formation; however, it does not explain why the AA3003 surface oxide which was lean in Mg was still penetrable by AA4045 liquid when immersion tests were conducted in argon.

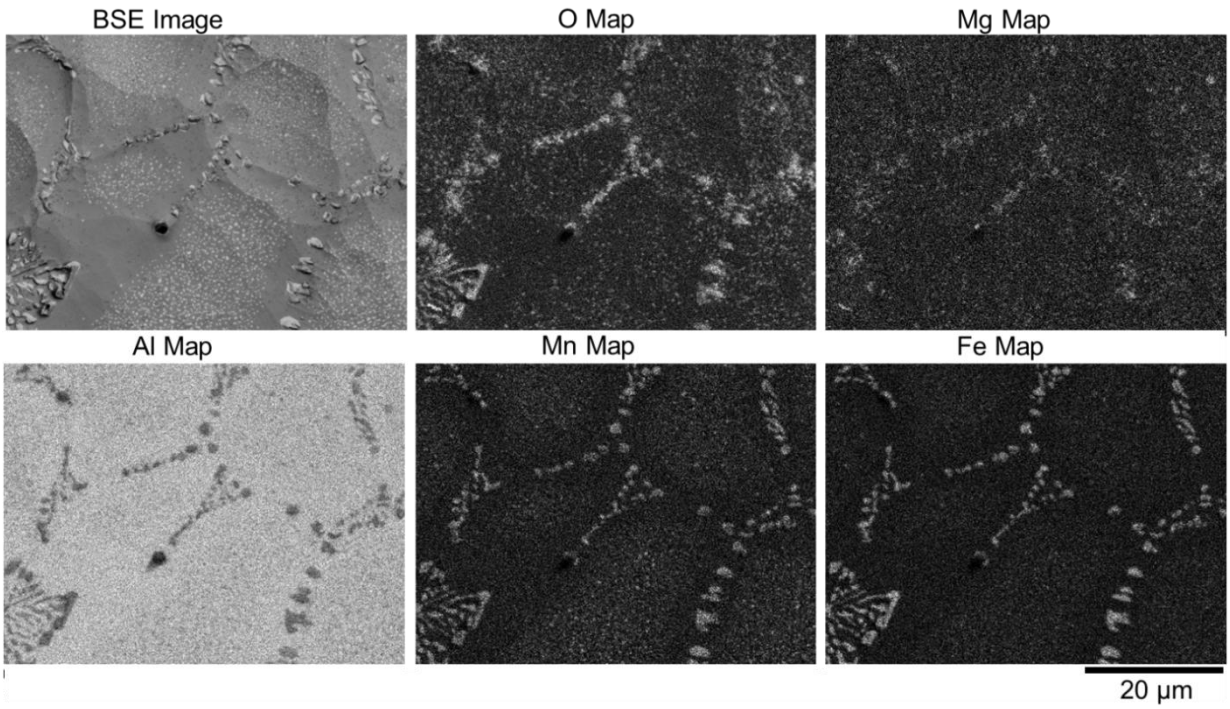

Figure 5-19 – Backscattered SEM (4 kV) image and EDS map showing surface distributions of O, Mg, Al, Mn, and Fe. White indicates high signal of species within area, black indicates less presence. Calculated oxide thickness 13 nm.

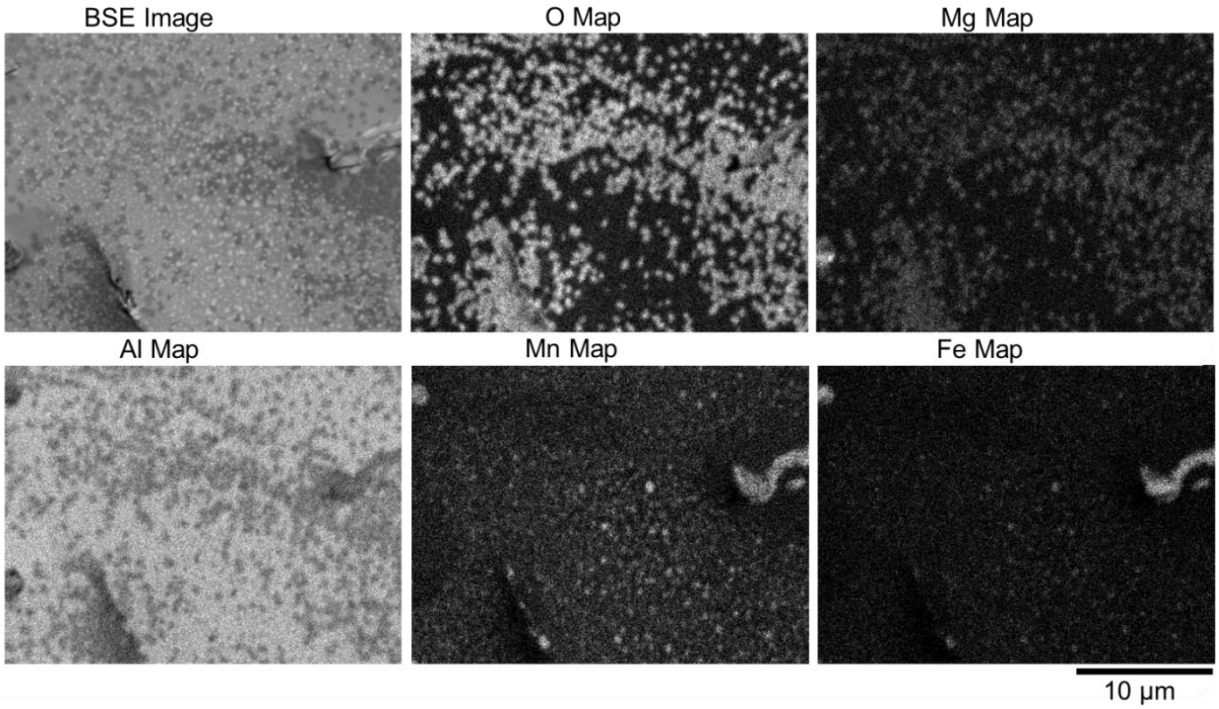

Figure 5-20 – Backscattered SEM (4 kV) image and EDS map showing surface distributions of O, Mg, Al, Mn, and Fe. Calculated oxide thickness 46 nm.

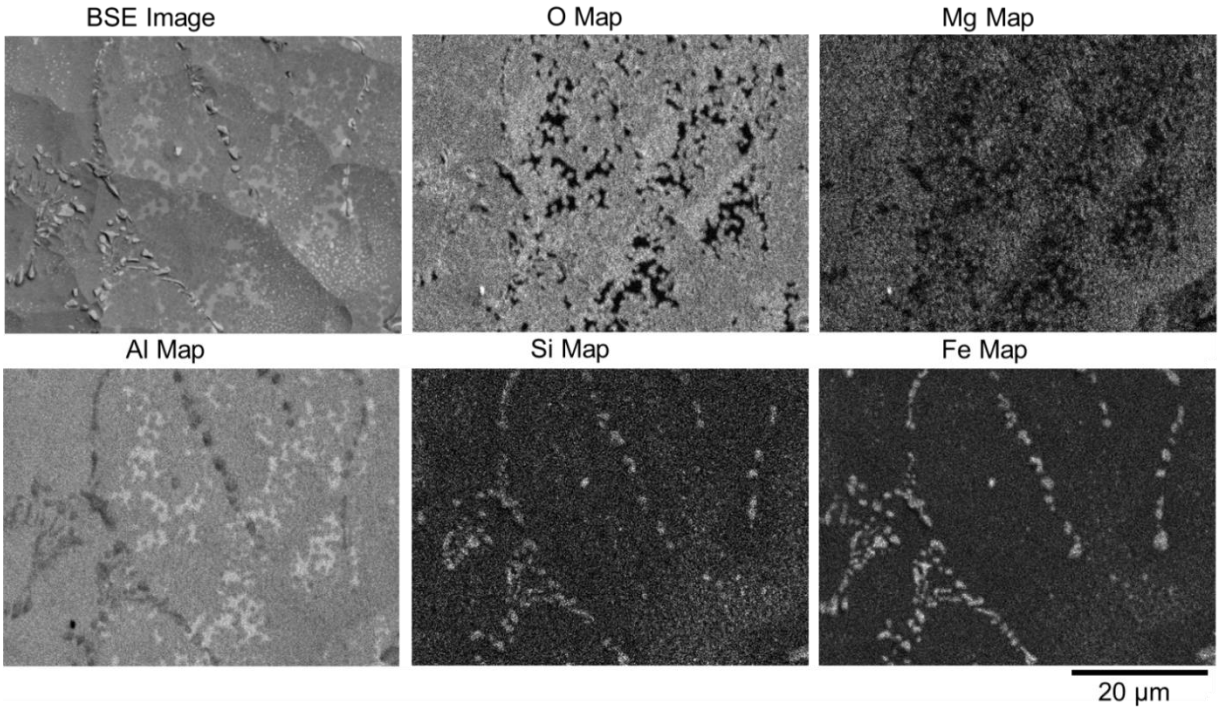

Figure 5-21 – Backscattered SEM (4 kV) image and EDS map showing surface distributions of O, Mg, Al, Si, and Fe. Calculated oxide thickness 95 nm.

AA3003 samples were also examined using EDS. The EDS intensity peaks of Al, O, and Mg signals as a function of calculated oxide thickness, are shown in Figure 5-22, using normalized intensity values. As shown, the O and Mg peak intensities increases with air exposure, while the Al peak intensity remains relatively constant. Furthermore, the normalized Mg peak intensity closely follows that of the normalized O peak signal intensity, indicating a link between Mg segregation and AA3003 surface oxidation.

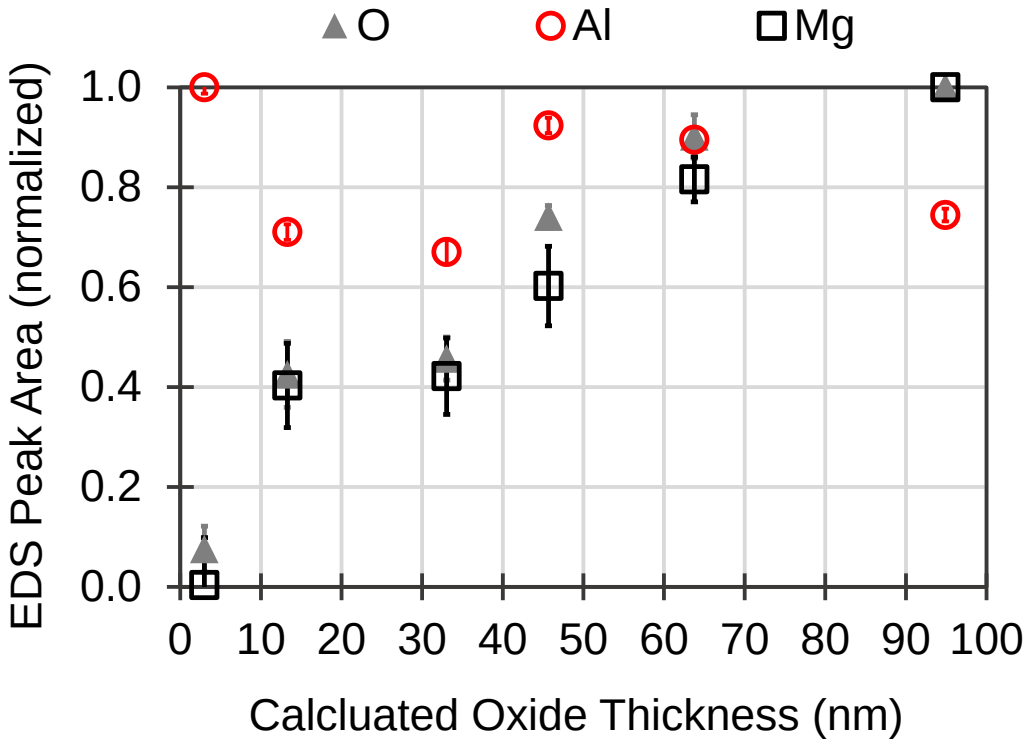

Figure 5-22 – Normalized EDS peak intensities for oxidized AA3003 samples, as a function of calculated oxide thickness. Results are graphed against the calculated oxide thickness. All EDS spectrums obtained using 1800 µm by 1800 µm field size.

As FE-SEM observations indicated a non-uniform surface morphology, possibly due to Mg segregation effects illustrated in Figures 5-19 through 5-21, further EDS studies were performed using: (i) large field sizes, 1800 µm by 1800 µm, selecting 5 random areas on each sample, (ii) small field sizes, 2 µm by 2 µm, selecting Mg rich areas (dark regions similar to the highlighted region a in Figure 5-17), selecting 5 areas per sample, and (iii) small field sizes, 2 µm by 2 µm,

selecting Mg lean areas (light regions similar to the highlighted region b in Figure 5-17) selecting 5 areas per sample. The measured O/Al EDS peak intensity ratios (an indicator of relative oxide thickness) were plotted against calculated oxide thickness (based on time, temperature and atmospheric condition), see Figure 5-23. The results indicate that the Mg rich areas appear to be increasing in thickness in addition to fractional area coverage, whereas the Mg lean areas remain relatively the same thickness while the fractional area coverage diminishes with time.

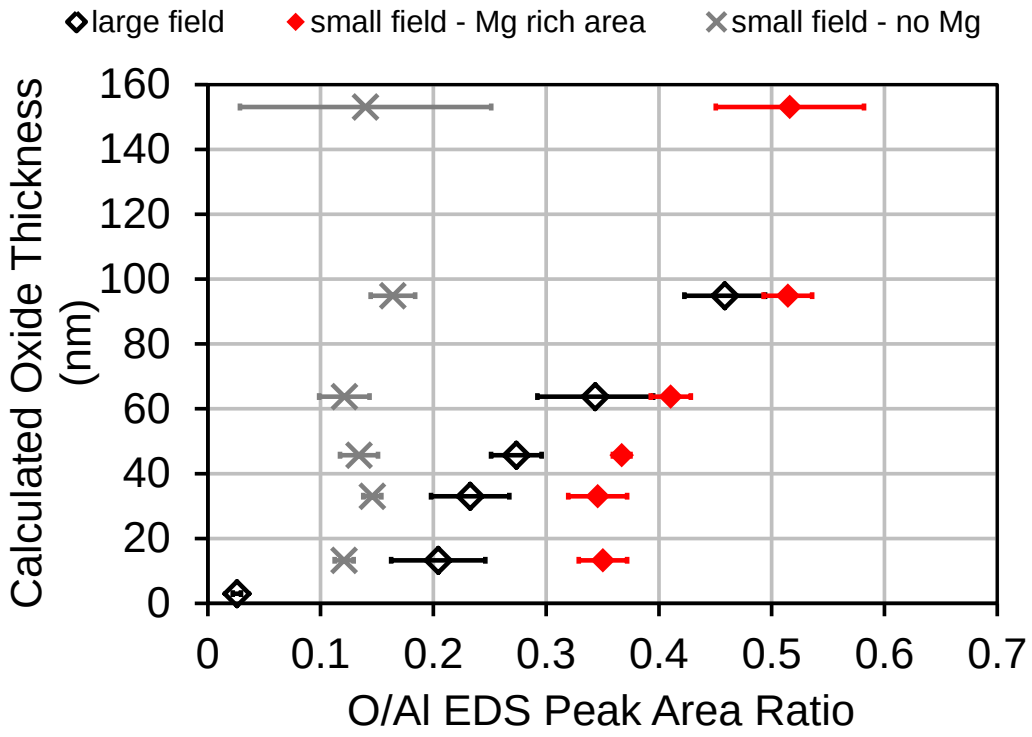

Figure 5-23 – Calculated oxide thickness vs. O/Al EDS peak ratios obtained from oxidized AA3003 samples. EDS spectrums obtained using 1800 µm by 1800 µm field size (black data points), data for samples heated in air and samples heated in inert environment, < 5 ppm O_2. EDS spectrums obtained on Mg rich (red data points) and Mg lean (gray data points) surface regions, using a 2 µm by µm field size.

5.6.1 Discussion

While the use of argon appeared to be beneficial in terms of promoting AA3003/AA4045 bond formation, the question still remains; what happens to the AA3003 oxide which makes it

amenable to wetting and bonding? The observation from the tests conducted with varying levels of AA3003 surface oxidation suggest that the oxide which grows on the AA3003 surface during heating can be sufficiently thick (~100 nm by estimate) and still be penetrated by the AA4045 liquid. Additionally, the trend was found that the bond quality, as evidenced by the: (i) lack of continuity at the contact line and (ii) increased frequency of dry areas on the sample decreased with increasing $t_{oxide,AA3003.}$ Considering this, in light of the observations on AA3003 oxidized surfaces examined by FE-SEM, suggest that Mg surface segregation may play a significant role.

It was observed that a Mg surface oxide (dark areas in Figure 5-17) both increases in surface area coverage (EDS Maps, Figures 5-19-5-21) and thickness (O/AL EDS peak intensity ratio, Figure 5-23) with increasing air exposure times. While the EDS could not be used to conclusively determine the structure of this Mg bearing oxide (as the interaction volume includes significant contribution from the underlying aluminum), it is likely to be MgO. Thermodynamic stability calculations of Al-Mg alloys in Silva [113], for the temperatures of 773 K and 998 K, show MgO to be the stable oxide when local Mg concentration is above 1.05 wt% Mg and 1.5 wt% Mg. Hence, fast diffusing Mg may segregate to the surface and be oxidized by the surrounding oxygen. The presence of MgO on the surface should inhibit wetting and bond formation, as studies on composite castings of Al alloys around solid Mg inserts have shown [114].

While the Mg rich areas may be detrimental to wetting and bond formation, the Mg lean areas (light regions shown in Figure 5-17) may be beneficial. While EDS spectrums of the light areas showed levels of Mg above the background level, one can assume that Mg was additionally segregating in the light regions. Observations, specifically the O/Al EDS ratio in the Mg-lean areas shown in the graph in Figure 5-23, suggest that the oxide thickness in these regions

remained relatively constant, but above that of the un-heated sample oxide thickness. This suggests that the Al_2O_3 oxide growth was either insensitive to air exposure time, or that at some point during heating, Al_2O_3 growth ceased in these regions. As Mg was found present in these areas, through EDS analysis, one could envision the following mechanism. As the sample temperature rises during heating, the kinetics of Mg surface segregation begins to be appreciable. Segregating Mg reacts with Al_2O_3 and local oxygen, according to the reaction:

$$\frac{3}{4}\mathrm{Mg} + \mathrm{Al_2O_3} \rightleftharpoons \frac{3}{4}\mathrm{MgAl_2O_4} + \frac{1}{2}\mathrm{Al} \qquad (5\text{-}1)$$

This reaction would liberate Al metal and potentially make the AA3003 surface amenable to wetting and bonding with AA4045 liquid. Similar behaviour has been observed in past studies on Mg segregation in Al [64], and [115-116]. Additionally, this idea of Mg-enhanced bonding has been used in the past (albeit with higher levels of Mg) for improving bonding of aluminum in powder metallurgy applications [67] and [117].

5.6.2 Comparison of AA3003 surface oxides

The results from Chapter 4 and 5 suggest that the AA3003 surface oxide is penetrable by liquid AA4045. Remelting does not appear to be a requirement for wetting and bond formation; however, there is still ambiguity with respect to how the AA3003 oxide is penetrated. At this juncture, the surfaces of the as-prepared test samples should be compared with the AA3003 chill bar cast surfaces from Section 4.4. Characteristics of both surfaces are summarized in Table 5-2.

Both oxides appear to be non-uniform in thickness: for the chill-cast surface there is evidence that the oxide growing on top of surface intermetallics is thinner than oxides grown above primary α-Al, for the AA3003 test samples, non-uniformity appeared to be a result of Mg segregation effects. Additionally, on the chill-cast surface, local remelting took place and

manifested itself as "spot exudates". It is safe to assume that any prior surface oxide would have been mechanically damaged as a result of this spot exudation process. In contrast, while no mechanically induced defects were present on the surface of the test samples, the sample preparation process, specifically the NaOH etching step, may have promoted defective oxide film growth as follows. The as-etched surface of the test samples left the sample surface with protruding intermetallics as well as some pitting, see Figure 5-14a and b. The surface roughness in these regions is highly irregular. Oxides growing over these areas of high surface roughness would be subject to high growth stresses, and be potential sites for oxide cracking, or defective oxide growth, similar to that observed on grooved iron substrates in [118]. Both surfaces showed evidence of Mg surface segregation, and hence the possible reduction of surface oxides by Mg cannot be ruled out as an oxide penetration mechanism. Finally, dispersoids were observed on the surface of the test sample. It is not known exactly how this might have affected oxide growth.

Table 5-2 – Comparison of AA3003 surface oxides: Fusion™ cast surfaces and test sample surfaces.

AA3003 test sample: surface structure and oxide	***AA3003 chill-cast: surface structure and oxide***
1. calculated oxide thickness of 12 – 104 nm. 2. oxide is non-uniform in thickness due to Mg surface segregation and oxidation. 3. etched surface morphology: -protruding intermetallic particles on surface, -etch pits present, and -scalloped surface texture. 4. dispersoid formation observed on surface as a result of sample heating to 640°C. 5. Mg segregation on surface.	1. observed oxide thickness of ~25 nm. 2. oxide film may not be uniform or continuous over surface intermetallics. 3. exudation spots observed on chill cast surface. 4. no observable Mg segregation on chill-cast surface, with exception of the region just above the last point of contact between AA4045 and AA3003 in the "interrupted" Fusion™ casting trial.

5.7 Summary

The key observations and results from Chapter 5 were:

i. For tests conducted in an argon atmosphere, remelting of the AA3003 sample was not a requirement for AA3003/AA4045 wetting and bond formation.

ii. Negligible AA3003 sample and AA4045 melt interaction occurred when tests were conducted in air, unless the sample temperature was above the onset of α-aluminum remelting. When sample remelting was used as a means to promote AA3003/AA4045 interaction, the resulting sample cross sections did not resemble the AA3003/AA4045 Fusion™ cast interfaces.

iii. Increasing the extent of sample oxidation prior to test sample immersion into the melt resulted in a reduced tendency for AA3003 sample dissolution into the melt.

iv. Mg segregation was found on oxidized AA3003 surfaces. The area covered by Mg increased as oxidation time increased. The oxide layer thickness in areas covered with Mg based oxides was relatively thicker than adjacent areas which were lean in Mg surface segregation.

From the Chapter 5 results, it was clear that AA3003 remelting was not a requirement for AA3003/AA4045 wetting and bond formation, as long as intimate contact between AA4045 liquid and the AA3003 surface could be achieved. In the experiments conducted in Chapter 4, this was achieved by use of argon purge gas during sample immersion into the melt. Again, the results from Chapter 5 were not adequate to determine the AA3003 surface oxide penetration mechanism.

In the following chapter, attempts were made to isolate the oxide penetration mechanism using additional interface formation tests (the subject of Chapter 6), as well as the following:

i. Use of iron and silicon free test samples. Use of Al-1Mn reduces the intermetallic content in the as-cast alloy and lowers the dispersoid formation kinetics [119].

ii. Use of varying Mg content in the sample alloy and well as the melt alloy, to determine the effect of Mg on the interface formation process.

iii. Use of a less severe etching procedure, see Section 3.3.1.2. This procedure was similar to that used in studies by Beck *et al.* [38] and Brock and Pryor [39], and said to reduce the risk of pitting on the sample surface.

Additionally, since the observations in Section 5.5 suggested that the thermal oxide films grown on AA3003 surfaces may not have been uniform on a micro-scale due to Mg segregation effects, attempts were made to observe oxide film uniformity using FIB-SEM techniques (mentioned previously in Section 3.3.2).

Chapter 6

Effect of Mg Impurity on Wetting and Interface Formation

6.1 Introduction

Thus far, results have shown that the AA3003 surface oxide is permeable to molten AA4045 liquid. Furthermore, examination of oxidized AA3003 surfaces in Chapter 5 revealed the presence of Mg oxides at the surface resulting from segregation of Mg to the surface during exposure of the AA3003 to high temperatures. Previous studies by Terril *et al.* [62] show that the presence of Mg (or other active metals) aids in the vacuum brazing of aluminum components, by means of reducing Al_2O_3 surface oxides and gettering of residual oxygen in the furnace atmosphere. Considering all of the above, the natural question was: do low levels of Mg in the AA3003 alloy affect the surface oxide in such a way that it is a critical requirement for making the oxide penetrable by molten AA4045. To answer this question, a second series of immersion tests were conducted. The alloys used in these tests were chosen to have varying levels of Mg. The alloys used for these tests are listed in Table 3-9 and the tests conducted are described in Section 3.3.1.2.

In Sections 6.2 and 6.3, the initial results of immersion tests are presented. Following that, microscopy of the immersion tests samples is presented in Section 6.4. The remaining section in this chapter is devoted to observations of the surface oxides, specifically the morphology and defects within the oxides and the implications with respect to oxide penetrability by a liquid AA4045 melt.

6.2 Effects of Mg in the Al-1Mn core sample on wetting and interface formation

A series of immersion tests were conducted using samples with composition of Al-1Mn-0.0008Mg (alloy Id # 1a in Table 3-9) and a melt composition of Al-10Si-0.0008Mg (alloy Id # 2a in Table 3-9). Alloys 1a and 2a in Table 3-9 represent the highest purity achievable using the raw material available at Novelis; due to impurities present in the grade of Al (alloy Id # 3 in Table 3-9) used to make up the alloy melts. These results would act as a baseline to results from alloys with other increased Mg contents. Aluminum oxidation studies conducted by Nylund *et al.* [64], with Al-0.0001Mg and Al-0.001Mg alloys and at a temperature of 620 °C, showed no Mg surface segregation on samples (Auger electron spectroscopy) after oxidation for 1 hour duration in air. Thus, it was assumed that the Al-1Mn-0.0008Mg sample would behave similarly to pure aluminum, in that minimal surface segregation would occur during sample heating. The immersion tests using smaller OD solid rods of cast Al-1Mn-0.0008Mg were immersed to a depth of 32 mm at three different temperatures, and four different sample oxide thicknesses, tests ***t1*** through ***t10*** in Table 3-10. Photomicrographs of these ten immersion tests are shown in Figure 6-1. In this image, the first row corresponds to tests performed at the 878 K (605 °C), the second row are tests performed at 893 K (620 °C), and the third row at 913 K (640 °C). Each column were tests done with progressively more oxidation on the samples prior to immersion into the melt. The calculated oxide thicknesses are between 10-14 nm for the first column, 20-30 nm for the second column, 125-160 nm for the third column, and 250-275 nm higher for the final column.

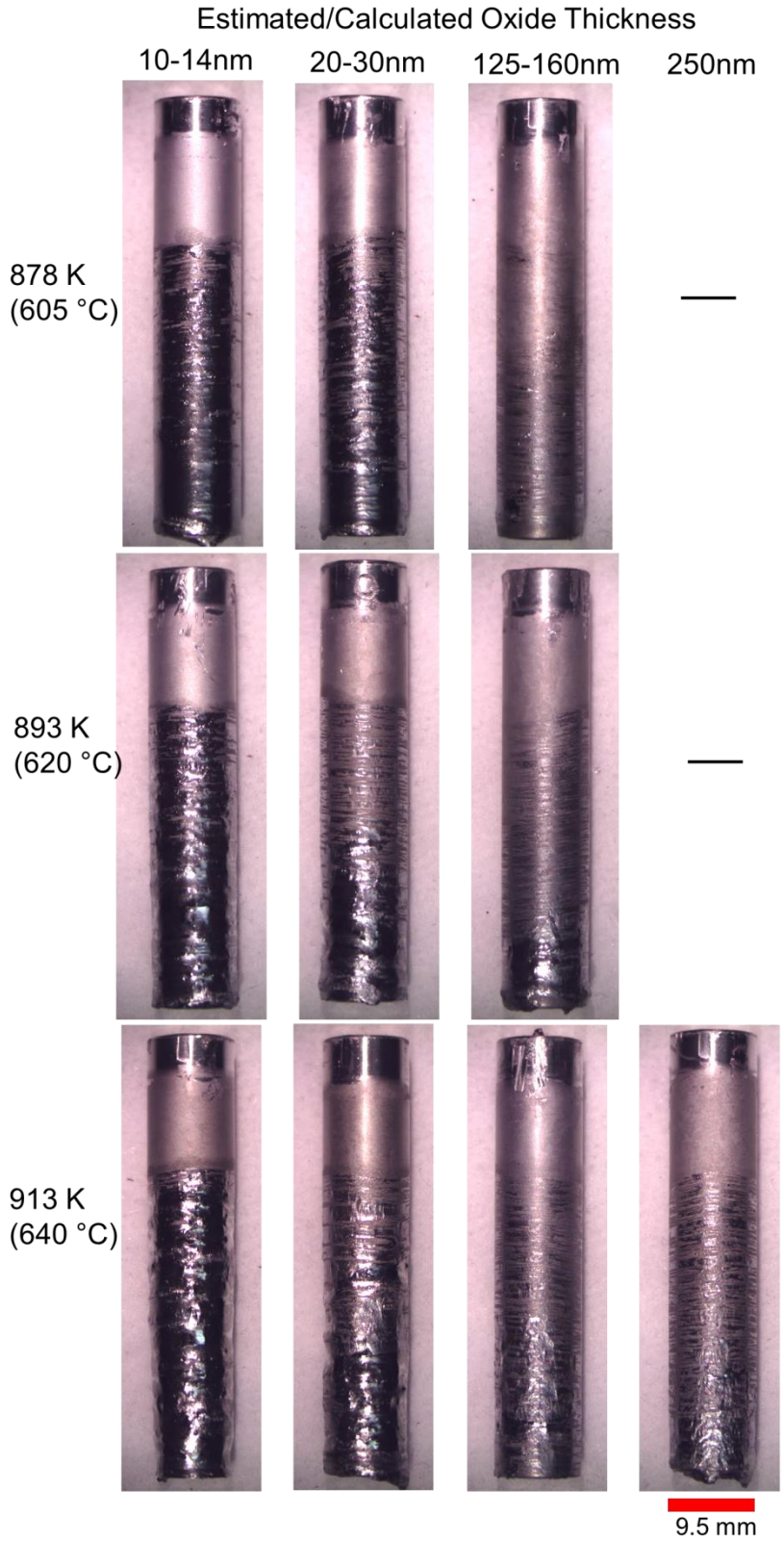

Figure 6-1 – Macro photos of Al-1Mn-0.0008Mg samples for various immersion temperatures (rows) and surface oxides (columns). Melt: Al-10Si-0.0008Mg for all tests.

In comparing the low and high temperature tests, there is a clear difference in overall sample interaction with the melt. For the thinnest oxide, 10-14 nm, the high temperature sample has a reduced sample diameter below the final contact line, and virtually no areas below the contact exists which show the original surface of the sample. For the low temperature test, the 10-14 nm test sample shows signs where the original sample surface remains unaltered. This is most evident directly below the final contact line. Additionally, unlike the higher temperature sample, it was not obvious whether the sample diameter had been reduced by solutal dissolution from the Al-10Si-0.0008Mg melt, as expected from the lower rate of dissolution at this temperature. Going to higher oxide thicknesses, 125-160 nm for instance, this difference becomes more evident between high and low temperature tests. In the low temperature test there is virtually no change in the sample appearance near the final contact line. Near the bottom edge of the sample there are horizontal markings (long and thin, with the long axis parallel to the sample circumference) which suggest that the melt altered the surface condition of the sample. It suggests that the sample, if left in the melt for a longer period of time, would have had the majority of its surface penetrated similar to the 10-14 nm sample. For the high temperature samples at 125-160 nm oxide thickness, there is a noticeable difference in the quality of the final sample. Near the final contact line, there are horizontal patches (again long and thin) where the sample surface remains unchanged, between these are similarly shaped areas which are shiny, suggested that the melt had begun to dissolve underlying material. Moving from the point of final contact towards the bottom of the sample, this pattern of alternating thin areas of unaltered sample surface and shinier sample surface continues, but becomes less noticeable. Also, regions near the bottom of some sample with higher oxide thicknesses did show clear sample dissolution, i.e., reduced sample diameter and a surface similar to that of the 10-14 nm oxide sample surface.

The intermediate temperature sample with an oxide thickness of 20-30 nm is a good example of this behaviour. Here the bottom portion of the sample has clearly undergone dissolution, while the pattern of alternating horizontal markings is also visible near the final contact line. There was no consistent distance along the length of the sample at which this would occur for these tests, suggesting an element of randomness with the mechanism leading to the complete dissolution of the sample.

Another feature which was observed on many of the samples was a distinct darkening of the sample surface at the final contact line. This is most easily observed in the high temperature sample for the 10-14 nm oxide thickness. At slightly higher magnifications this was observed on the majority of the samples, and will be explored in greater detail in Section 6.4.

The change in sample weight was also recorded for these tests. The weight change data is presented in Figure 6-2. Here, the high temperature tests show the largest weight losses, and all tests recorded had weight loss; however, the amount is reduced with increases surface oxide thickness. The weight loss results show significant scatter at high temperature and all but the thinnest oxide thickness. This is consistent with the qualitative observations of the test samples. For the intermediate temperature tests, the sample weight loss is significantly lower, but still negative for the 10-14 nm oxides and the 20-30 nm oxides. For the one test done at 125-160 nm oxide the change in weight was just slightly positive. For the low temperature tests, none of the samples registered a loss in weight, all showed slightly positive weight gains. This does not suggest that the samples surface oxide was not penetrated by the melt. It does suggest that given similar surface oxidation and immersion times, that a higher temperature results in more complete penetration of the oxide and sample dissolution by the melt. If the mechanism of wetting and bond formation relies on penetration of the oxide at discrete locations, dissolution of

underlying Al-1Mn by Al-10Si, and bridging between the discrete points of penetration, then the mechanistic process should be sensitive to the dissolution rate of Al-1Mn by the melt. Dissolution is known to be a strong function of temperature, as evidenced in Craighead *et al.* [23], and these results echo the same trend with temperature.

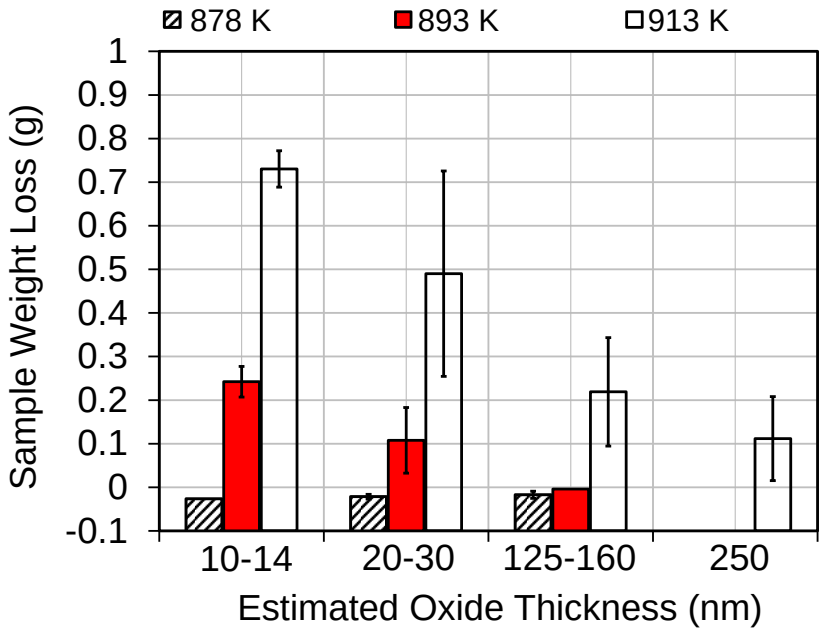

Figure 6-2 – Sample weight loss data for Al-1Mn-0.0008Mg immersed into Al-10Si-0.0008Mg for various immersion temperatures (colours) and sample oxide thicknesses (groupings).

After baseline tests with Al-1Mn-0.0008Mg samples and Al-10Si-0.0008Mg melts, the effect of Mg addition to the Al-1Mn-0.0008Mg sample was explored. In addition to the baseline, three different Mg amounts were used, Al-1Mn-0.01Mg (Id # 1b in Table 3-9), Al-1Mn-0.1Mg (Id # 1c in Table 3-9), and the third being the AA3003 from the previous chapter, i.e., Al-1Mn-Si-Fe-0.005Mg (Id # 1 in Table 3-9). A test temperature of 913 K (640 °C) was used, again with four different levels of surface oxides. These are tests ***s1*** through ***s12*** in Table 3-11.

Photographs of the immersion test results are presented in Figure 6-3 for the Al-1Mn-0.01Mg and Al-1Mn-0.1Mg samples. Qualitatively, there is no significant difference in results between the baseline and the Al-1Mn-0.01Mg tests, with the exception of the thickest

oxide, where the Al-1Mn-0.01Mg sample appears to exhibit more extensive sample dissolution. The other three oxide levels all appear very similar to the baseline; however, suggesting this particular test result was a potential outlier.

For the Al-1Mn-0.1Mg samples, presented in the third row in Figure 6-3, there is a dramatic difference in final sample appearance. For the 250-275 nm oxide, the test samples were unaltered by immersion into the melt. Of the four test samples tested at this condition, three of the samples were completely unaltered. One of the samples (not shown in Figure 6-3) showed some dissolution near the bottom edge of the test sample, similar in appearance to 125-160 nm oxide test sample shown in Figure 6-3 for the same sample composition.

For the other three oxide thickness test conditions at this sample composition, another qualitative difference was apparent. Firstly, the alternating pattern of horizontal bands which were seen in the baseline tests are not present on these samples. Although the immersion depth for all samples was similar, 32 mm in depth, there were less discernable signs of this intermediate stage between unaltered sample surface and noticeable sample dissolution. This is most noticeable on the 10-14 nm oxide sample and the 125-160 nm oxide sample.

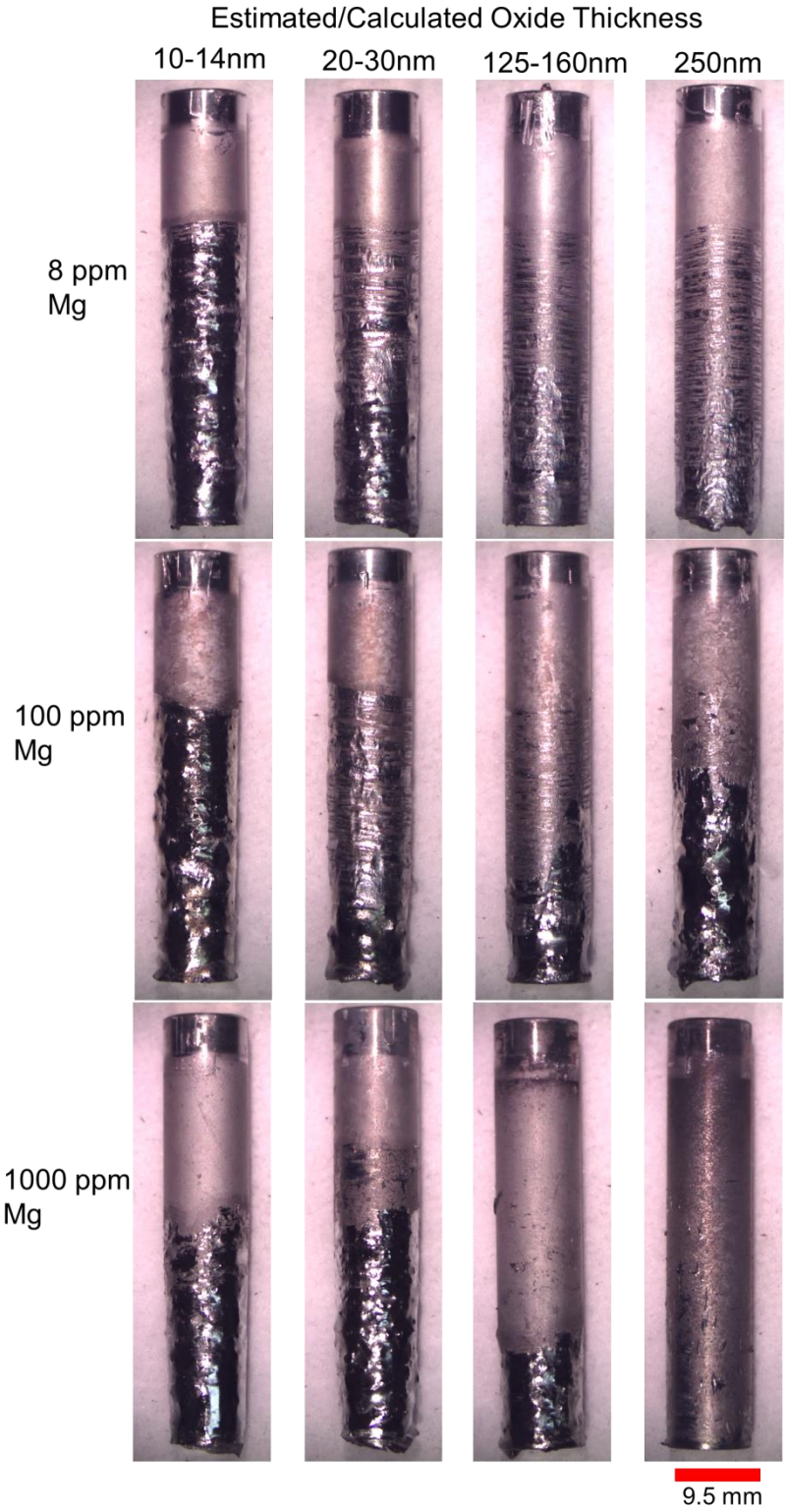

Figure 6-3 – Macro photos of various Al alloys (rows) and surface oxides (columns). Melt: Al-10Si-0.0008Mg for all tests.

The tests conducted with AA3003 (Id # 1 in Table 3-9), are presented in Figure 6-4. These samples showed little difference in final surface appearance with oxide thickness, which qualitatively disagrees with previous results with the same material tested in Chapter 5, see Figure 5-7. This discrepancy may be due to differences in sample preparation for tests in Chapters 5 and 6. Specifically, the etching time used for tests in Chapter 5 was longer than the etching times used on these test samples. When samples were etched for 2 minutes in NaOH, as in Chapter 5, the sample surface was prone to pitting on the surface. To avoid this, shorter etching times were employed; however, the short etch time may have not been sufficient to render the sample clean from debris embedded in the sample surface during the sample preparation, such as fine grinding. These results in Figure 6-4, compared to the baseline tests, suggest that for the high oxide thickness tests, 125-160 nm and 250-275 nm, the AA3003 oxide structure is more easily penetrated by the melt than the baseline Al-1Mn-0.0008Mg oxide.

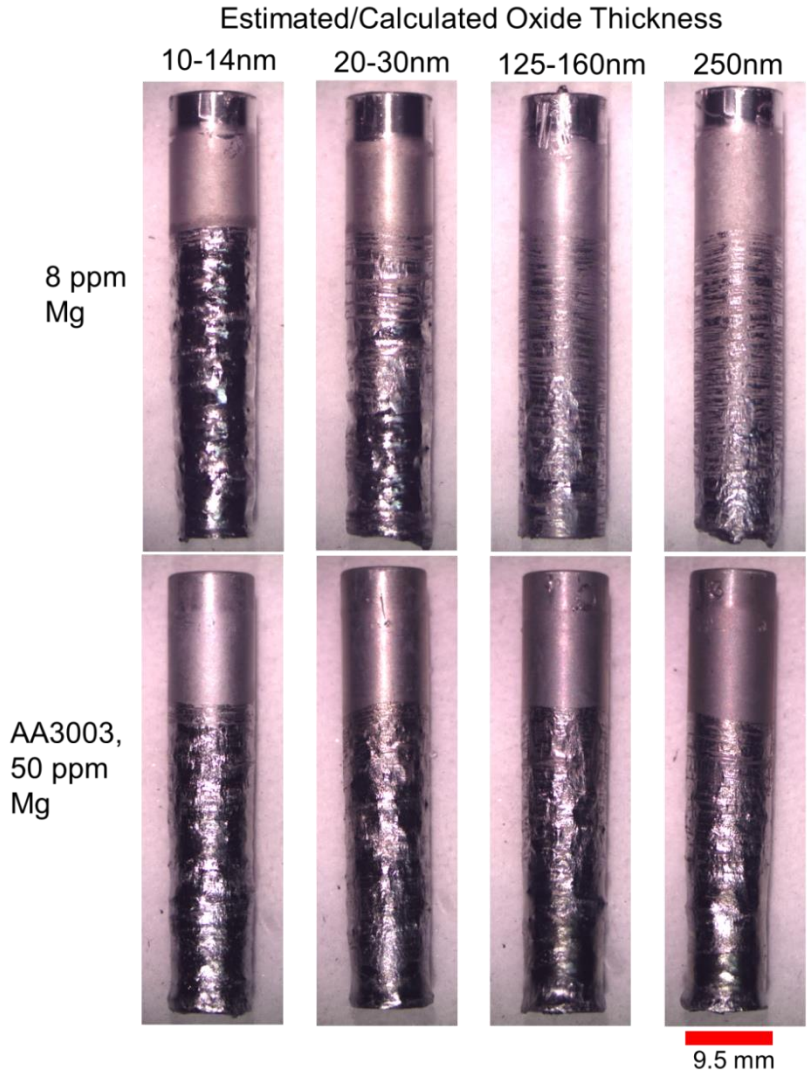

Figure 6-4 – Macro photos of AA3003 (bottom row) compared to the baseline alloy Al-1Mn-0.0008Mg (top row), for various surface oxides (columns). Melt: Al-10Si-0.0008Mg.

The weight change data for the tests conducted in Section 6.2 are presented in Figure 6-5. In comparison to the baseline values for 913 K (640 °C), there is a reduction for the Al-1Mn-0.1Mg samples, especially for the high oxide thickness of 250-275 nm. Out of the four samples tested in this condition, three had slight gains in weight, while one recorded a loss in weight (described previously). For the AA3003 sample, for the 125-160 nm oxide and 250-275 nm oxide thicknesses there appears to be a difference in sample weight loss from that of the baseline. The results for the Al-1Mn-0.01Mg alloy do not appear to be dissimilar to the

baseline values. The results from Figures 6-3 and 6-4, along with the weight loss values in Figure 6-5, suggest that the addition of Mg to the samples does not improve the wetting and bond formation process. Mg reduced the ability of the Al-10Si melt to penetrate the samples' surface oxide layer when added 0.1 wt% Mg was added to the Al-1Mn sample.

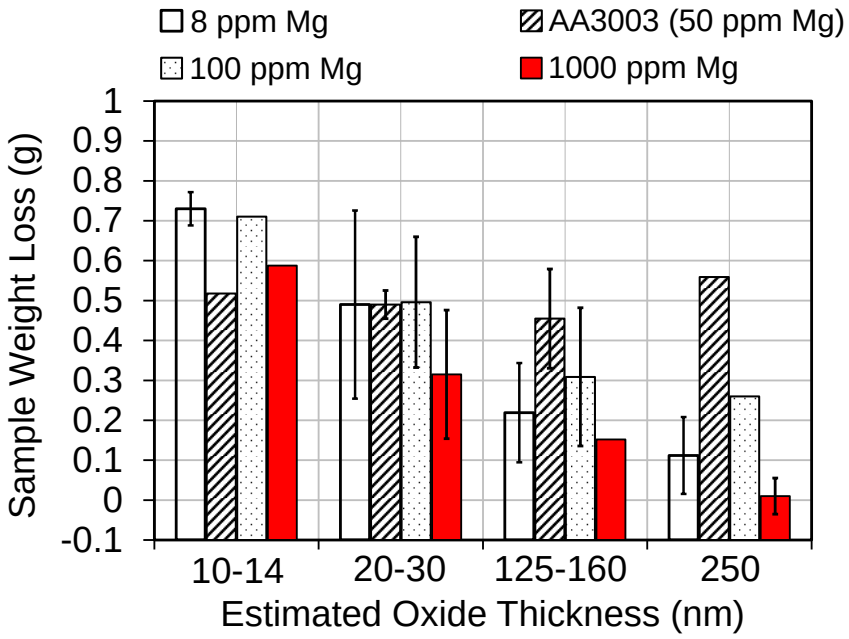

Figure 6-5 – Sample weight loss data for various Al alloys immersed into Al-10Si-0.0008Mg, for different sample oxide thicknesses. Alloys indicated by the different colours.

6.3 Effects of Mg in the Al-10Si clad alloy melt on wetting and interface formation

The effect of Mg addition to the Al-10Si clad alloy melt was explored. In addition to the baseline, two different Mg amounts were used in the melt, Al-10Si-0.01Mg (Id # 2b inTable 3-9) and Al-10Si-0.1Mg (Id # 2c in Table 3-9). A test temperature of 913 K (640 °C) was used, again with four different levels of surface oxides. These are tests ***m1*** through ***m6*** in Table 3-12. The results are presented in Figure 6-6.

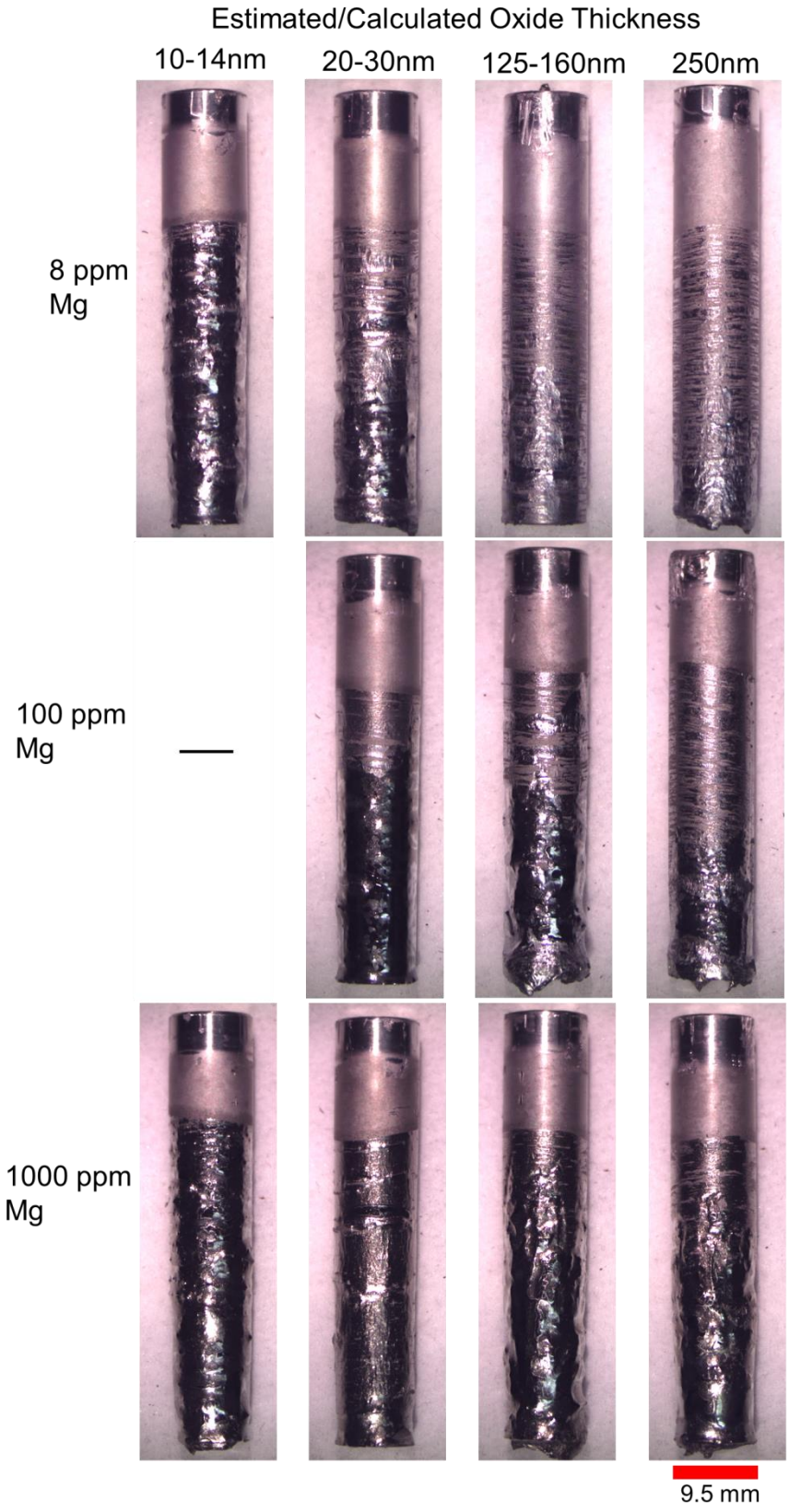

Figure 6-6 – Macro photos of for various Al alloy melts (rows) and surface oxides (columns). Samples: Al-1Mn-0.0008Mg for all tests.

For the Al-10Si-0.1Mg melt, bottom row in Figure 6-6, there is a clear improvement in the final sample appearance for the entire range of oxide thicknesses. Significant sample wetting and dissolution is seen on all of the samples, and only on the 250 nm oxide sample can the alternating horizontal striped pattern be seen near the final contact line. For the Al-10Si-0.01Mg tests, the results did not appear to differ significantly from the baseline tests with Al-10Si-0.0008Mg.

The weight change data for these tests are presented in Figure 6-7. The weight losses for the Al-10Si-0.1Mg tests show a clear increase in weight loss for the 125-160 nm and 250-275 nm oxide tests. At the lower oxide tests, the weight losses are not significantly different than the baseline. Similarly, the Al-10Si-0.01Mg tests did not show significant differences in weight loss from the baseline. It should be noted that the weight change for the 250-275 nm oxide test was not measured. In this test, the thermocouple became jammed into the sample and could not be removed post-test.

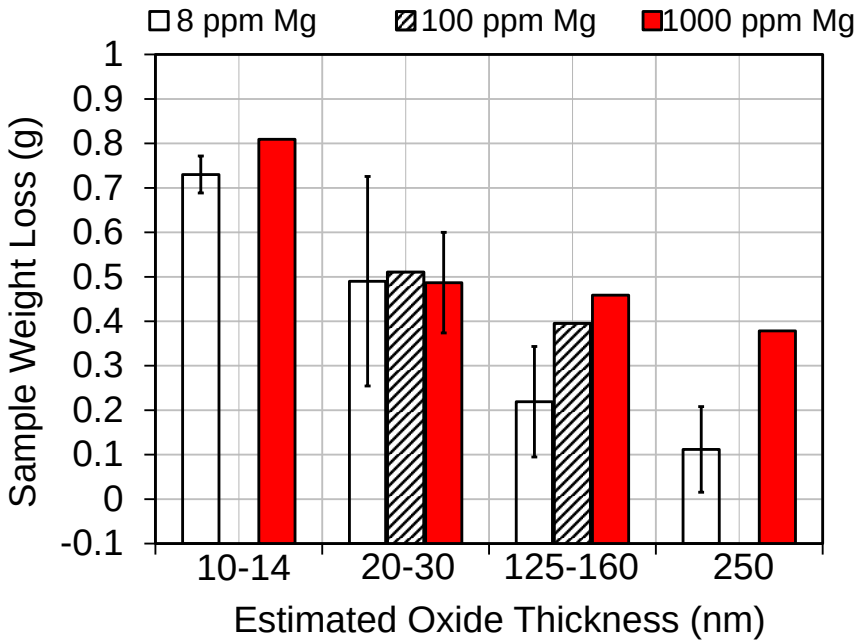

Figure 6-7 – Sample weight loss data for various Al-1Mn-0.0008Mg samples immersed into various Al-10Si alloy melts, for different sample oxide thicknesses. Melt alloys indicated by the different colours.

The results from Figures 6-6 and 6-7 show that more sample dissolution had taken place on samples which were immersed in the Al-10Si-0.1Mg melt Mg in comparison to the baseline. This suggested that the time to penetrate the sample surface oxide was less, and that more time was available for sample dissolution by the melt; i.e., Mg in the melt could potentially provide a benefit for bond formation in Fusion™ casting.

The results from these immersion tests are summarized below:

i. Mg additions to the Al-1Mn sample alloy composition did not appear to have a positive impact on sample/melt interaction. However, addition of 0.1 wt% Mg to the Al-10Si melt alloy did appear to have a beneficial effect on sample/melt interaction.

ii. Test temperature had the largest effect on sample/melt interaction, further supporting the penetration, dissolution and bridging mechanism of interface formation.

iii. Increasing the sample oxide layer thickness prior to test immersion had a similar effect to that in Chapter 5, i.e., increasing the extent of sample oxidation prior to test sample immersion into the melt resulted in a reduced tendency for AA3003 sample dissolution into the melt. Given all the tests performed, only one test condition resulted in minimal interaction with the melt: this was for the highest level of sample oxidation (estimated value 250-275 nm) and sample Mg content (Al-1Mn-0.1Mg). For this test condition, when the sample was immersed into the melt under an argon atmosphere, minimal sample and melt interaction occurred.

6.4 Microscopy of sample surface and final contact line regions

As discussed in the previous section, test samples displayed certain similarities. In this section, microscopy of a typical test result will be presented, looking at the sample surface morphology and how it changes as a function of length along the edge of the sample (from top to bottom).

Following this, the region at the final contact line, which looked visibly discolored on a macro scale, will be examined in an attempt to discern what was occurring in this region.

An Al-1Mn-0.0008Mg sample which was immersed at 913 K (640 °C) is shown in Figure 6-8. This sample underwent complete dissolution around the bottom of the sample, as evidenced by the reduction in sample diameter and clean/shiny final surface. Near the final contact line, the sample also exhibits the characteristic alternating horizontal "dry" markings described in the previous section. This sample was examined under SEM, specifically the five regions indicated by the labels (i) through (v) in Figure 6-8.

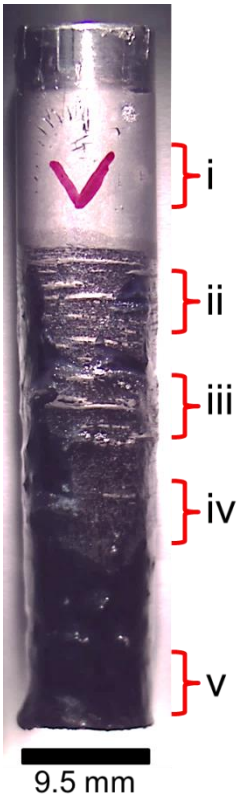

Figure 6-8 – Resulting sample surface after test immersion. Al-1Mn-0.0008Mg sample immersed in Al-10Si-0.0008Mg melt at 913 K (640 °C). Calculated oxide thickness on sample prior to immersion in the melt was 28 nm.

Surface morphology from regions (i) through (v) in this sample are shown in Figures 6-9-6-11. In Figure 6-9, taken above the final contact line and in the region where the

sample did not contact the liquid melt, the oxidized sample surface morphology is seen. The characteristic scalloping on the surface, from the NaOH etching step during sample preparation, is evident. Some SiC particles were occasionally embedded in the surface, and were identified using EDS. These were not seen in the tests samples used in Chapter 5. It is likely that the shorter etching time used for sample preparation might have resulted in a thinner etching depth and hence not all SiC from the SiC grinding paper was removed during etching.

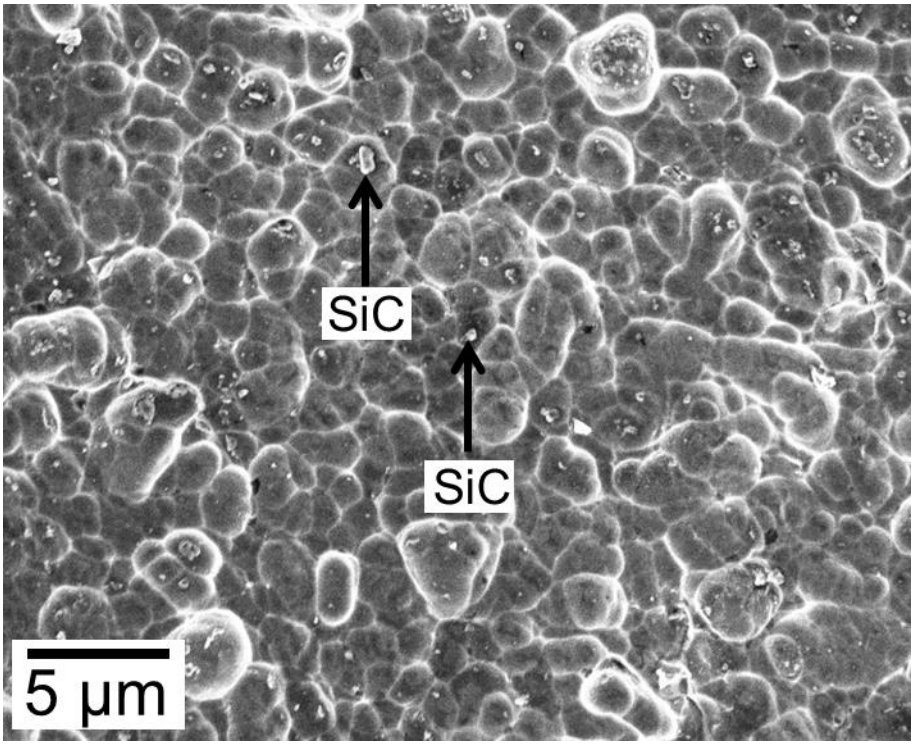

Figure 6-9 – SEM image from the sample surface of test sample shown in Figure 6-8. Image from region (i) identified in Figure 6-8.

Figure 6-10a shows the surface of the specimen just below the final contact line (region ii). Here, the bright areas are regions which are qualitatively similar to the unaltered sample surface in Figure 6-9. There are both large regions, which are long and thin with the long axis oriented parallel to the circumference of the sample. These correspond to the horizontal surface markings discussed in the previous section. It is also worth noting that between these horizontal patches, smaller and more circular bright areas are also present. While qualitatively there is little

observable difference between the unaltered sample surface and these horizontal patches, when examined with EDS, large Si peaks were observed in the spectra obtained from these horizontal patches, whereas the peaks were absent in spectra from unaltered sample surfaces. This suggests Si is present, sub-surface, in the regions where these horizontal patches exist.

Moving further down the sample, in the region labelled (iii), the associated surface morphology is shown in Figure 6-10b. Here, there is generally less of the horizontal markings present, as well as fewer and smaller circular patches. The boxed area in Figure 6-10b is shown in higher magnification in Figure 6-11 just to confirm that the circular areas have a similar surface morphology as that of the unaltered sample surface morphology in Figure 6-9. The bright white edges surrounding the area in Figure 6-11 are likely to be very thin oxides formed from non-adherent residual liquid upon removal of the sample from the melt. EDS spectra from these visually friable edges were high in Al, Si, and O.

The sample surface morphology of the region labelled (iv) is shown in Figure 6-10c. The majority of the sample surface appears to be smooth and noticeable different than the unaltered sample surface morphology. The presence of small circular patches still exists; however they are both smaller in size and less densely populated than the region labelled (ii) and (iii) in Figure 6-8. It is worth noting that a large horizontal patch, similar to those near the final contact line in Figure 6-10a is still present (in the middle of the field of view in Figure 6-10c), although in this case, it is noticeably thinner than the typical ones seen near the final contact line in Figure 6-10a.

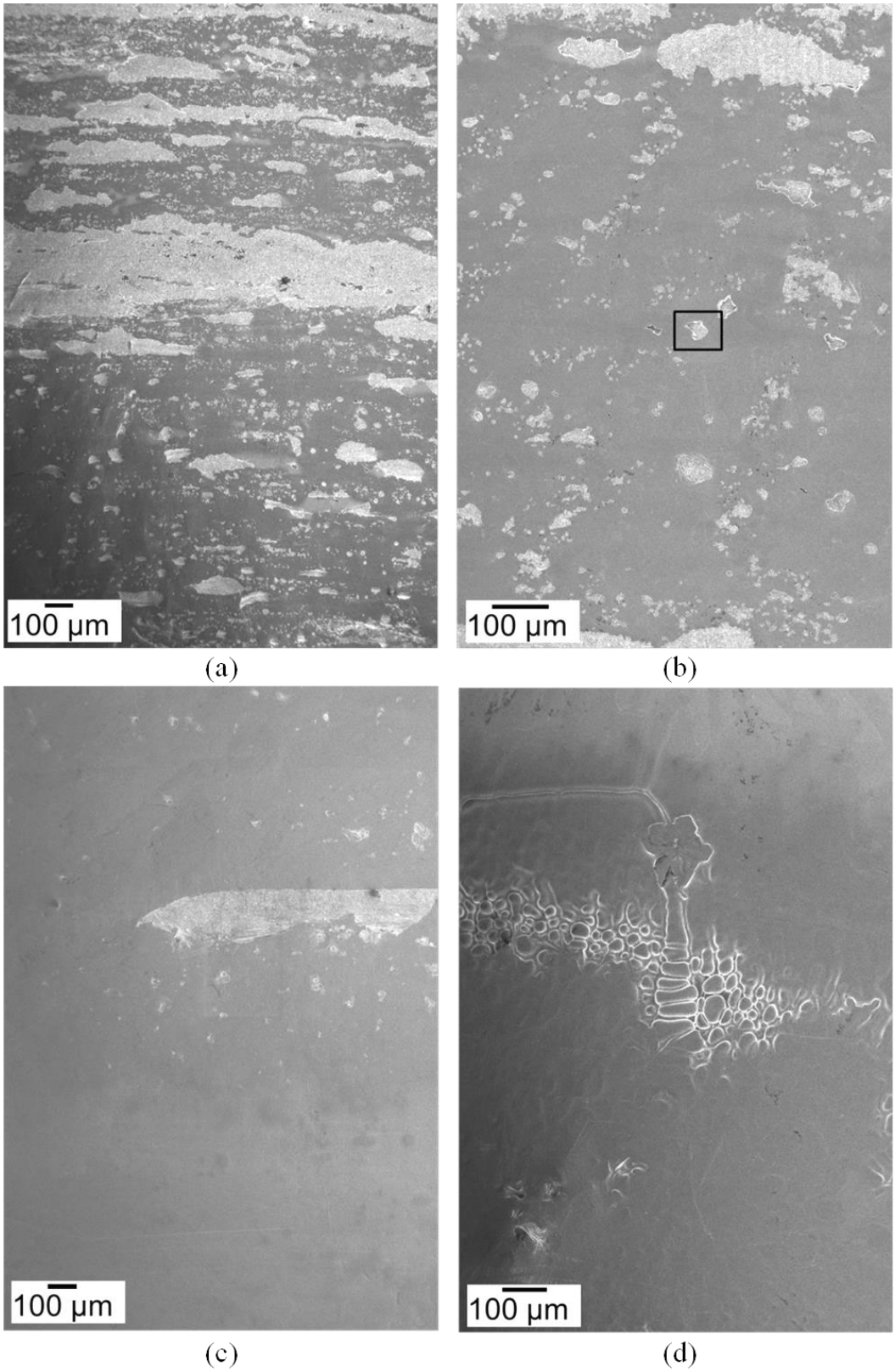

Figure 6-10 – SEM images from various regions taken from the sample surface of test sample shown in Figure 6-8. (a) region ii, (b) region iii, (c) region iv, and (d) region v.

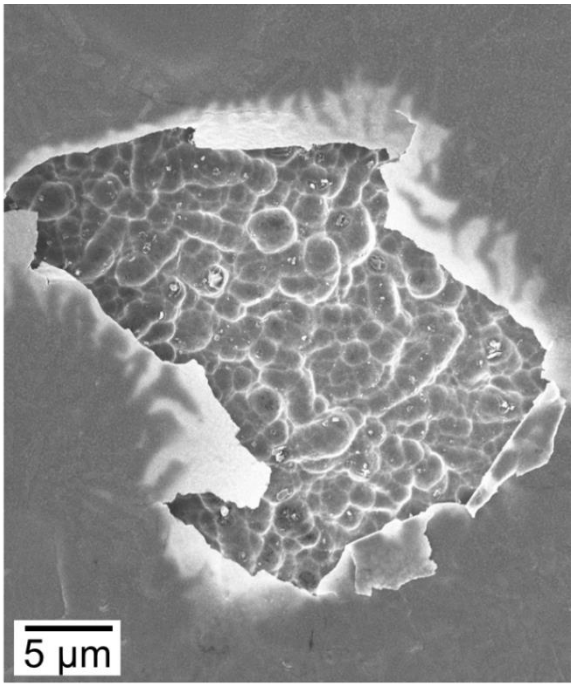

Figure 6-11 – Higher resolution SEM image of the boxed-region highlighted in Figure 6-10b.

Figure 6-10d shows the surface morphology near the bottom of the sample, region (v). Here, the surface is completely smooth. Additionally, the presence of what appears to be the early stages of interface growth is observed, as columnar shaped undulations on the surface of the sample. EDS spectrum of these regions are quantitatively very similar to the chemistry of the melt, Al-10Si. Additionally the patterns seen appear similar to those seen in cross section from tests in Chapter 5, see Figure 5-9b and c for example. The smooth portions in Figure 6-10d suggest a thicker amount of residual Al-10Si had adhered to the sample after it was removed from the melt, while the regions where these dendritic shaped surface undulations are present suggest less residual Al-10Si may have adhered to the surface in these areas.

A baseline test sample, Al-1Mn-0.0008Mg, which was immersed at 893 K (620 °C) is shown in Figure 6-12. There is a region between i and ii in Figure 6-8 which appears at the final contact line, above region ii in which noticeable dissolution of the surface has taken place that is slightly darkened with respect to the unaltered surface above it. This behaviour was consistently

seen in the immersion test samples. Higher resolution microscopy of this sample, in this region of interest, follows.

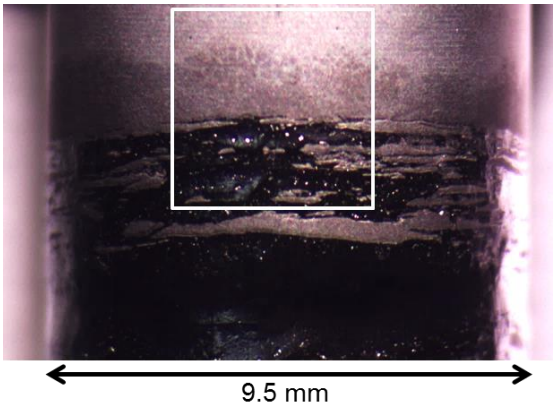

Figure 6-12 – Resulting sample surface after test immersion, highlighting the region at the final contact line, dark greyish in colour and discoloured from the un-immersed portion of the test sample. Al-1Mn-0.0008Mg sample immersed in Al-10Si-0.0008Mg melt at 893 K (620 °C). Calculated oxide thickness on sample prior to immersion in the melt was 11 nm.

Secondary and backscattered electron images of the boxed area in Figure 6-12 are shown in Figure 6-13a and b. From Figure 6-13a, the position where noticeable dissolution takes places is easily seen (indicated with arrow). Above this arrow, there is no visible difference in the surface morphology of the sample, hence the dark greyish area was indistinguishable from the unaltered sample surface slightly above it when viewed using secondary electrons. Looking at a backscattered electron image of the same area, Figure 6-13b, there are very faint signs that the dark greyish area in Figure 6-12 is different from the unaltered region above it. A band of small bright particles, only slightly visible in the low resolution image, Figure 6-13b, is apparent. Focusing on this band with higher magnification, in Figure 6-14a and b, a much clearer picture emerges. Whereas the secondary electron signal does not indicate any difference in surface morphology at this resolution, the backscattered image suggests the presence of intermetallics. EDS spectra of these intermetallics showed high concentration (~10 wt%) of both Si and Mn respectively. In the region surrounding these intermetallics, Si content was also in the range of

10 wt%. This suggests that Al-10Si was present in some capacity in this region. Given the secondary electron image shows no morphological difference between the unaltered sample surface morphology, it is very likely that the Si rich material is sub-surface in this region.

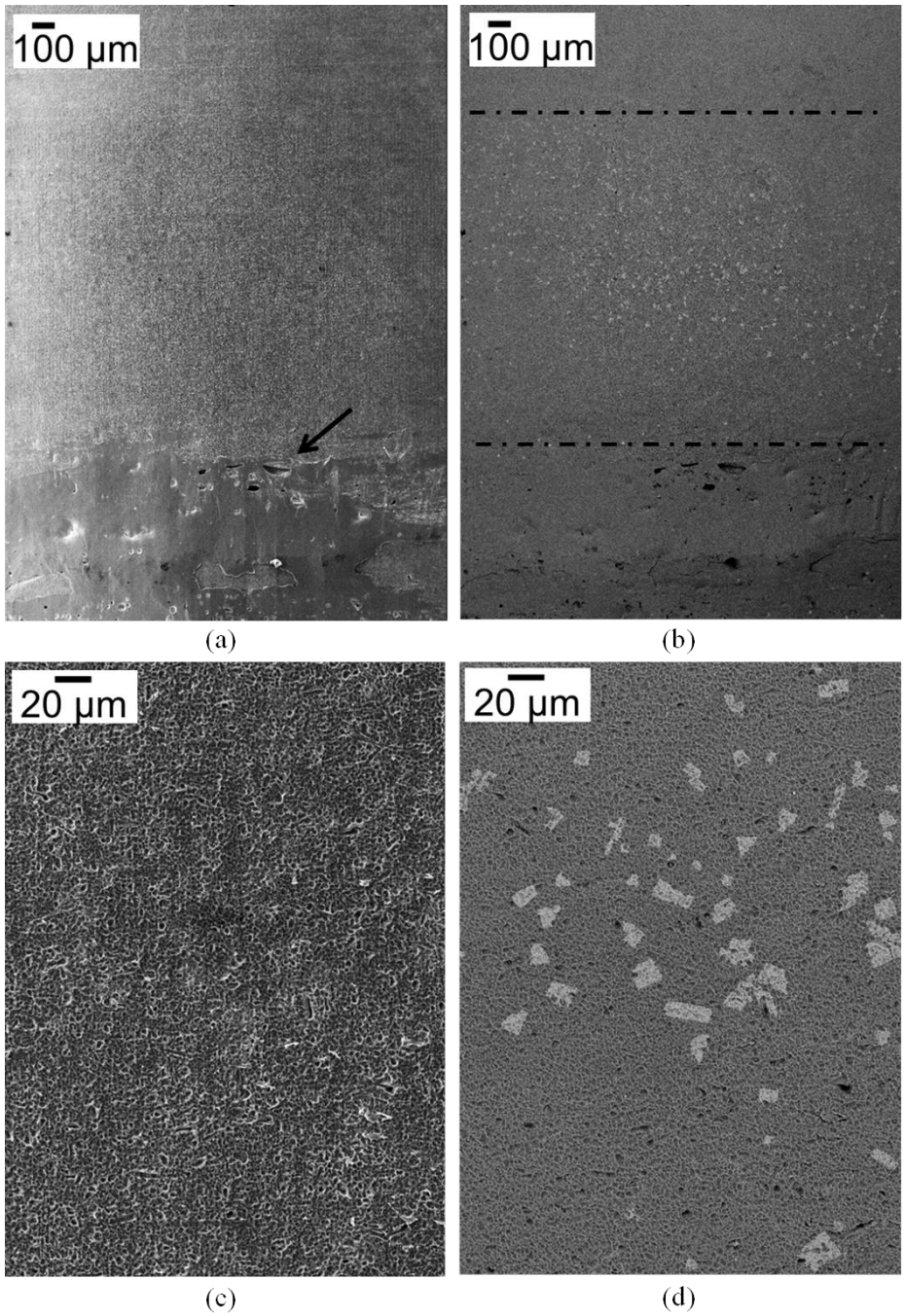

Figure 6-13 – SEM images of the sample surface taken from the boxed region of the sample shown in Figure 6-12. (a) Low resolution secondary electron image, (b) corresponding backscattered electron image, (c) secondary electron image of highlighted region in (b), and (d) corresponding backscattered electron image.

As further confirmation to the presence of Si rich material in this dark banded region, EDS spectra were acquired at points along the line shown in Figure 6-14. Starting at the point labelled A in Figure 6-14 which was above the dark greyish region, and moving down, EDS spectra were obtained, with special focus on Al, Si, and O contents.

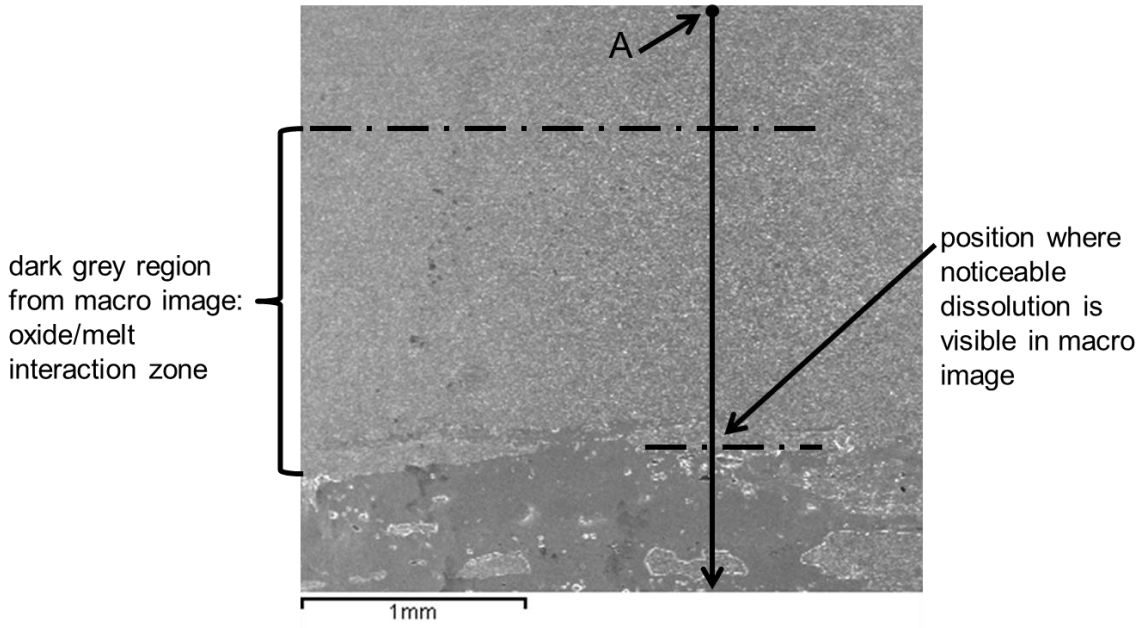

Figure 6-14 – Secondary electron image of the sample shown in Figure 6-12. The black line shown in the image indicates the position at which EDS profiles were performed.

The results from this EDS analysis are shown in Figure 6-15. Note the line plots shown in Figure 6-15 have been averaged with a 3 point averaging filter, thus the first data points are a distance not equal to point A in Figure 6-14. The results clearly indicate three chemically distinct regions along the line in Figure 6-14. Starting at point A and moving down, the first region is high in Al and has an O content of ~ 4 at%. There is zero Si in this region. This corresponds to the sample surface which was unaltered. Moving further down the line and into the region corresponding to the greyish region in Figure 6-12, the Si content begins to increase to a measurable value, increasing in content to a value close to ~ 12-15 at%. The O signal stays

more or less constant over this region. There is a slight decline in the measured O signal in the range 1.5-1.9 mm in Figure 6-15.

For the most part, the fact that the O content remains more or less constant is not unreasonable, and agrees with the secondary electron images showing no discernable change in the surface morphology in this region. The Al content decreases gradually from 95 at% to a value of ~ 80-85 at%. This decrease matches reasonably with the increase measured in the Si signal. The third region is indicated by a red vertical line in the plot in Figure 6-15. This corresponds to the visual final contact line, labelled in the secondary electron image in Figure 6-14. Moving into this region, the Al, Si, and O signals for the most part remain relatively constant at a level which is measurably than the 4 at% measured along the unaltered sample surface. Looking at the secondary electron image of this region, the smooth surface suggests that in this region Al-10Si liquid had bonded with the sample surface and that dissolution of the original sample had taken place. The O signal measured on this surface would then be from oxidation of the freshly dissolved sample surface which gets exposed to the furnace atmosphere as it gets removed from the melt. This surface, still hot after being removed from the melt, should itself oxidize; however, to a lesser extent than the original sample surface would have oxidized during sample heat up and prior to immersion. Thus, it is logical that the O signal is less in this region, ~ 1.5-2 at%, than the O signal on the unaltered sample surface of ~ 4 at%.

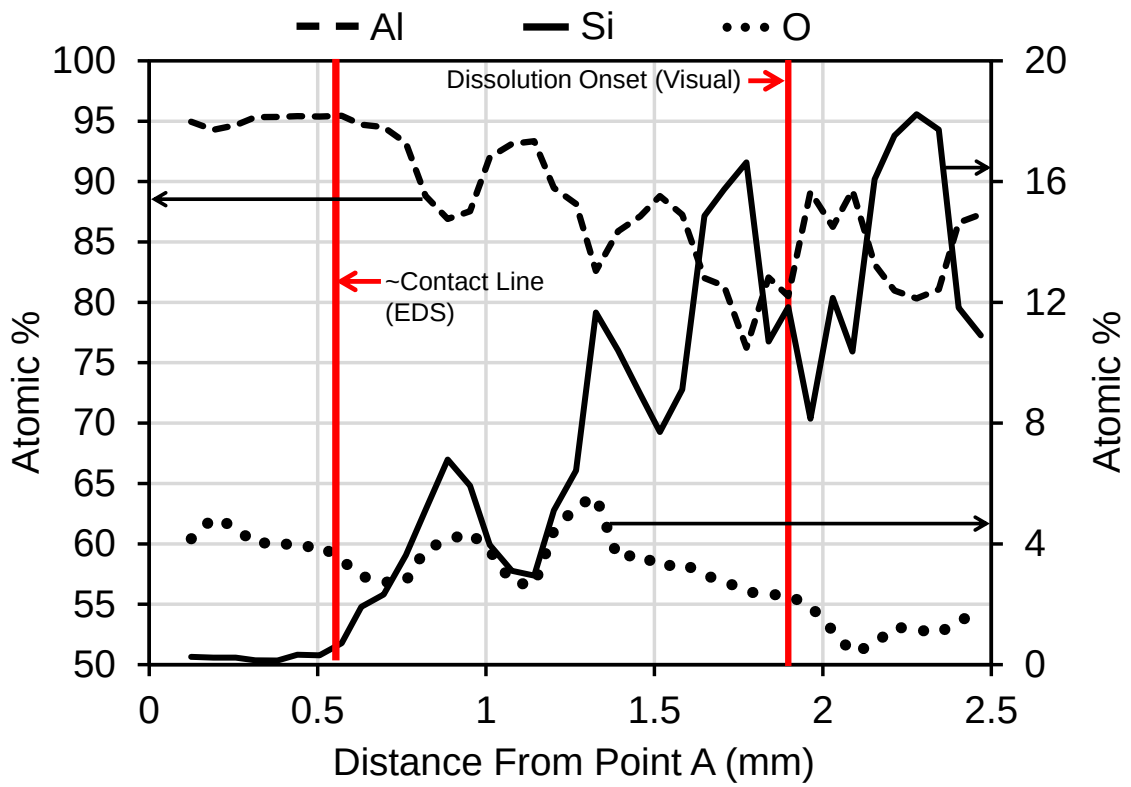

Figure 6-15 – Al, Si, and O profiles along line shown in Figure 6-14.

6.4.1 Fast immersion test

One additional test was conducted using a fast immersion speed, 9.0 mm/s, to determine its effect on the final sample wetting and appearance. The sample used was an Al-1Mn-0.0008Mg sample, and it was immersed into an Al-10Si-0.0008Mg melt. Sample preparation was similar to that mentioned in Section 3.2. The sample was heated to 913 K (640 °C), and left to grow an oxide of 250-275 nm. The sample was immersed as follows: 9 mm/s immersion speed to a depth of 13.5 mm. The motor was stopped for 2 seconds, then the sample was immersed an additional 9 mm, at a speed of 9.0 mm/s. The motor was stopped again briefly then raised out of the melt. The final appearance of the surface of this test sample was remarkably different than previously samples at 1.4 mm/s. A comparison of two tests samples, one immersed at 1.4 mm/s and the one at 9 mm/s is shown in Figure 6-16. There is a striking difference in the final surface of the test

samples. The 1.4 mm/s immersion speed sample (right) shows the characteristic horizontal marking on the sample surface, while they are not present on the 9.0 mm/s test sample. As a result of this, the bottom 13.5 mm of the 9.0 mm/s test sample displayed much cleaner sample dissolution than the 1.4 mm/s test sample. Despite the fact that the immersion time for the 9.0 mm/s test sample was less than the immersion time for the 1.4 mm/s test sample (all other conditions being equal), it is apparent that immersion speed does alter the wetting and bonding process. A replication was not conducted for this test; however, the sample was worthy of more detailed study as it displayed quite a different sample appearance to the slow immersion tests.

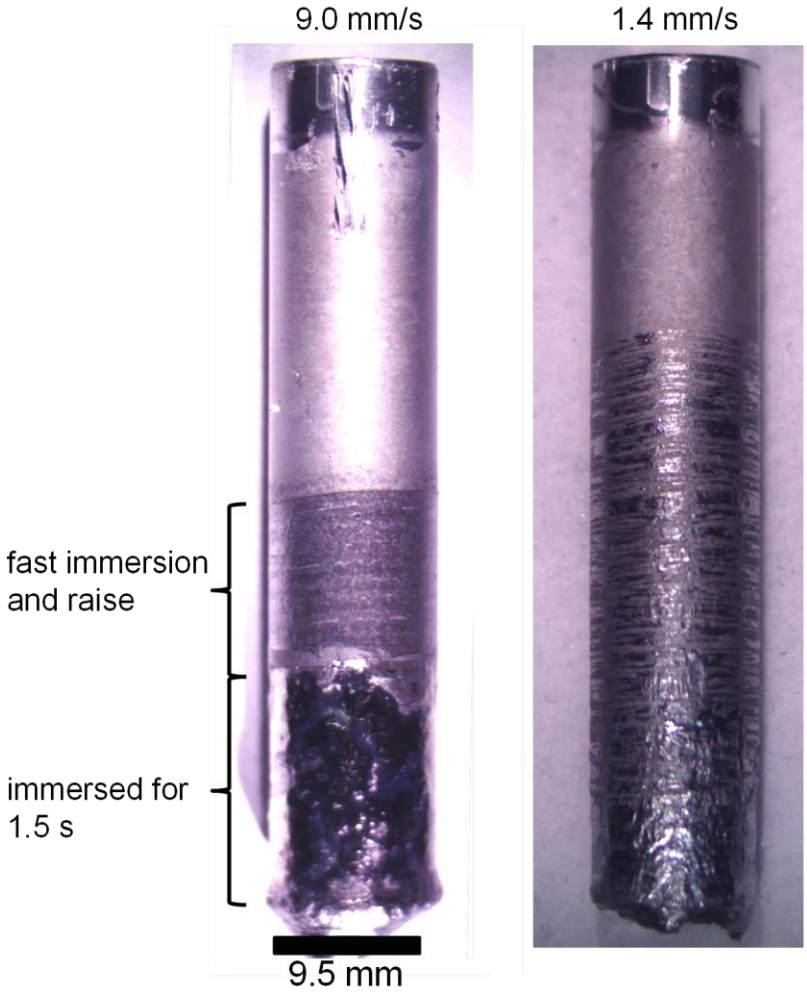

Figure 6-16 – Resulting sample surface from immersion tests performed at 9 mm/s (left) and 1.4 mm/s (right).

Looking at the macroscopic view of the fast immersed test sample, shown in Figure 6-16, the bottom portion of the sample which was immersed then left in the melt for 2 seconds has clearly been dissolved, as it displays the characteristic shiny surface and reduced diameter. The upper portion of the test sample that was quickly immersed then redrawn from the melt is discoloured and appears at first glance to be similar to the greyish colour region seen in many of the previous tests samples (see Figure 6-12). Upon closer examination, there appears to also be a faint greyish discoloration above the briefly immersed region, this is what more distinctly looks similar to what we see in Figure 6-12. None the less, the region which was briefly immersed, was clearly an intermediary between the final dissolution of the sample and initial contact with a liquid melt. As such, this sample was examined further using FIB and SEM imaging, to gain further insight as to the interface formation mechanism.

A low resolution SEM image of this intermediate region from the test sample immersed at 9.0 mm/s is shown in Figure 6-17. In this image we see circular shaped regions on the sample surface, varying from roughly 2-20 μm in diameter, as example of such an area is highlighted with a box in Figure 6-17. The sample surface in these regions appears as though the sample has not been modified from its original sample surface morphology. In between these circular shaped regions the sample surface is relatively smooth in comparison.

The boxed-in area in Figure 6-17 was examined using FIB cross sectioning. A low resolution image of the sectioned area is shown in Figure 6-18. The sacrificial W coating, about 1 μm in thickness appears as a bright white layer, and is indicated in the figure. The final section appears as dark grey in Figure 6-18, and is labelled as *α-Al* in the figure. The sectioned area traverses the region where the surface morphology reassembles that of the un-immersed sample surface to the region where the sample surface morphology was smooth.

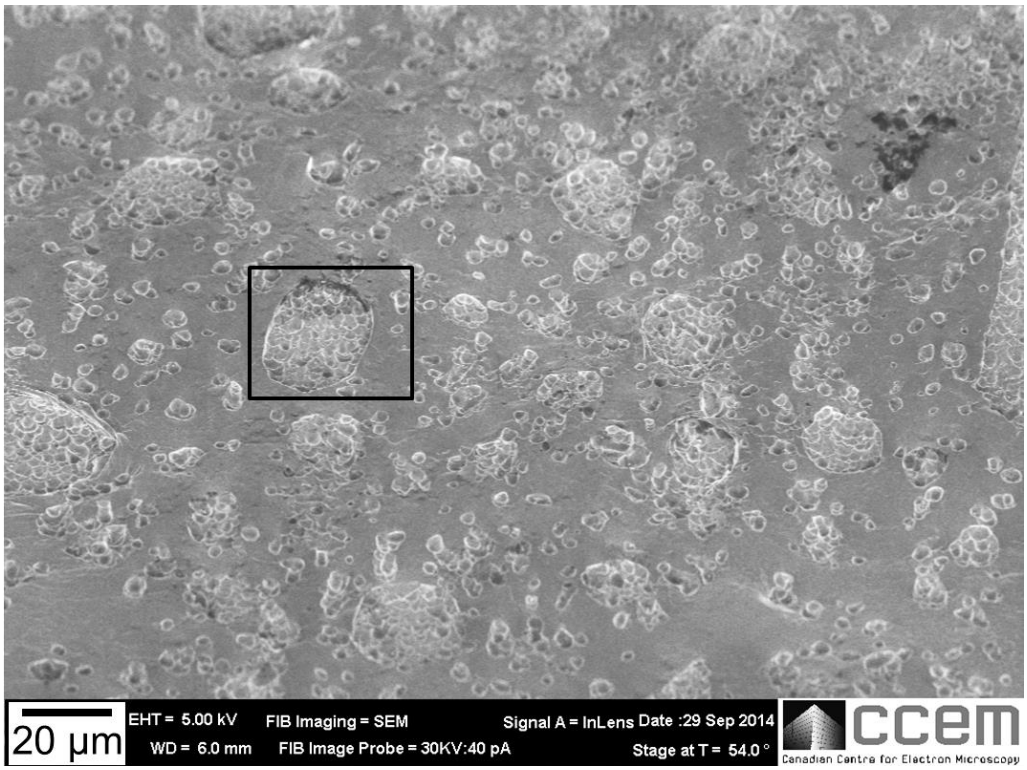

Figure 6-17 – Secondary electron image of the region below the final contact line, for the test performed at 9 mm/s.

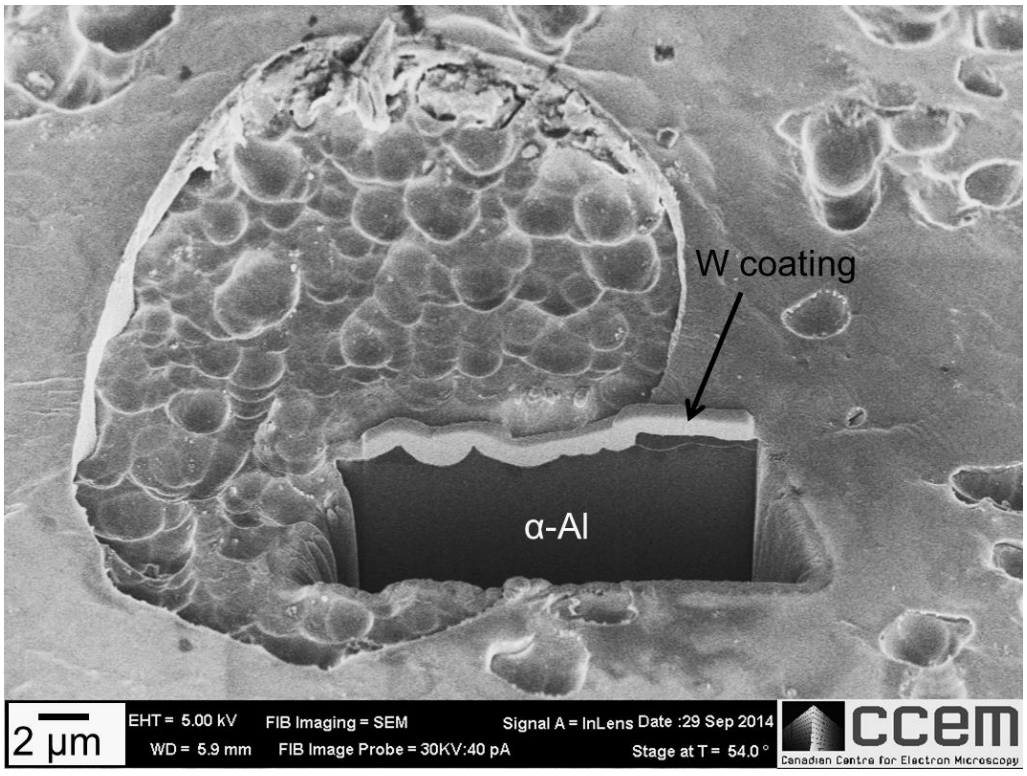

Figure 6-18 – Higher magnification of the boxed area in Figure 6-17, after FIB sectioning.

A high resolution image of the right hand side of the sectioned area in shown in Figure 6-19a. This corresponds to the region with the smooth sample morphology. Below the bright W coating, there is a very thin oxide, light grey. This oxide presumably formed on the surface of the residual liquid left on the sample after it was removed from the furnace. A Si-rich aluminum layer, about 0.5 μm in thickness appears as dark grey in the SEM image. This is likely the residual liquid left on the sample surface. Below this, a thicker oxide layer is present, the thickness consistent with the oxide layer thickness on un-immersed regions of the sample. Interestingly, below this oxide surface film discrete region of Si-rich aluminum was observed. This suggests that the Al-10Si has penetrated the oxide layer in discrete locations. That there is no discontinuity of the oxide overtop these discrete regions suggests that the Al-10Si liquid penetrated (or undermined) the oxide film at points not in the plane of section. As such, unless the section viewed in Figure 6-19a was coincident with such a point, the oxide would appear continuous.

A high resolution image of the right hand side of the sectioned area in shown in Figure 6-19b, corresponding to the region with the sample morphology that resembled that of the un-immersed sample surface morphology. Aside from the absence of any residual Si-rich aluminum above the ~50 nm surface oxide, the section appears very similar to that in Figure 6-19b. Si-rich aluminum was found in discrete regions beneath a continuous surface oxide layer. No visible defects in the surface oxide were found, and the thickness of the surface oxide was again similar to the oxide layer thickness found on un-immersed regions of the sample surface.

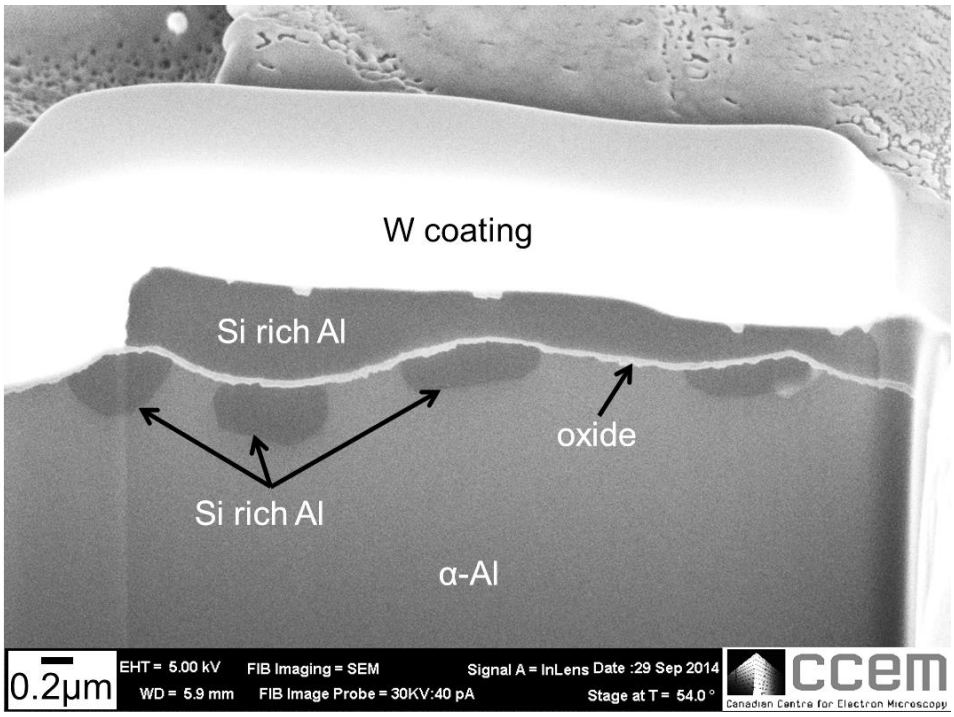

(a)

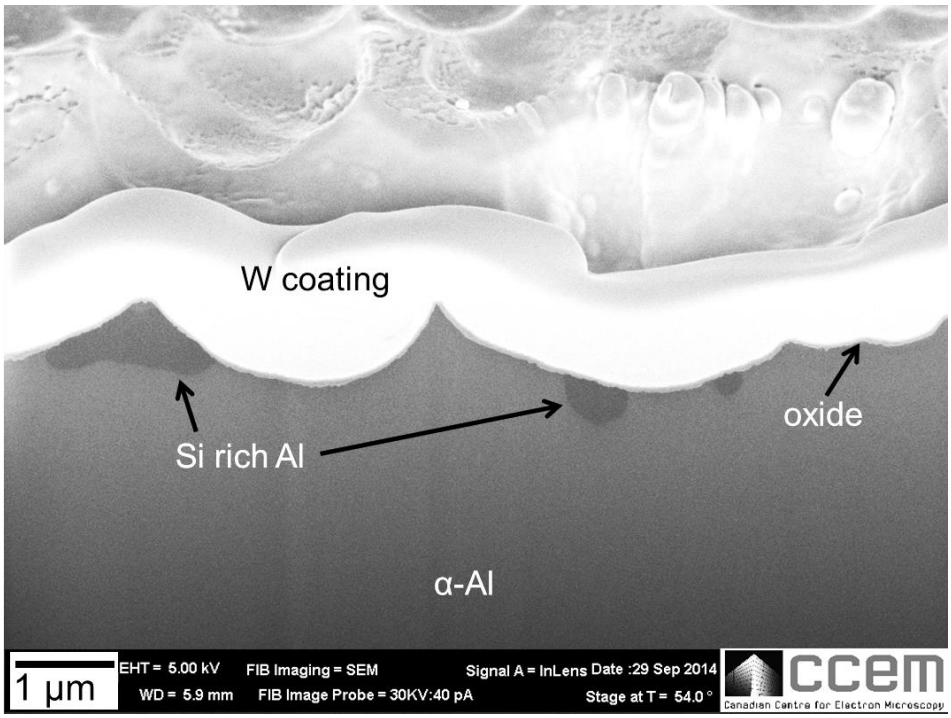

(b)

Figure 6-19 – High magnification secondary electron image of the (a) right side of the field showed in Figure 6-18, corresponding to the region with a smooth surface morphology, and (b) left side of the field showed in Figure 6-18, corresponding to the region where the surface morphology looks similar to that of the um-immersed surface.

6.5 Surface oxide uniformity, morphology, and defect observations

We have so far seen that the sample surface oxides are indeed undermined after immersion into an Al-10Si melt. Previous attempts at observing the oxide morphology, in Section 5.5, although useful for elucidating phenomenon of Mg surface segregation, were not helpful in determining the local oxide uniformity on a small scale, and whether the thermal oxide films grown during testing contained defects. To explore this further, thick oxide films were grown on various Al alloy samples, and the uniformity and morphology of these films were examined using FIB-SEM. Defects in the oxide film were also observed during FIB-SEM examination. Finally, surface defect densities were measured using a copper decoration technique. The cumulative results from this section are used to formulate a most probable mechanism for oxide film penetration by the Al-10Si melt.

6.5.1 Oxide Uniformity

Oxide uniformity was examined first. Five samples were examined (see Table 3-14 for alloy information), each sample being prepared as per Section 3.3.3, and oxidized in air at high temperature for 2 hrs. The temperature and expected oxide thickness are given in Table 3-14. A typical cross section of the oxides which were grown is shown in Figure 6-20a and b. In Figure 6-20a, the W coating shows up as bright white, and the aluminum sample is oriented horizontally and at the bottom of the image. In between the W coating and the aluminum is the oxide layer. Under low magnification, as in Figure 6-20a it is visible but hard to measure. Under higher magnification, shown in Figure 6-20b, although the SEM cannot pick up a high level of detail, the oxide layer thickness can be measured with some degree of accuracy.

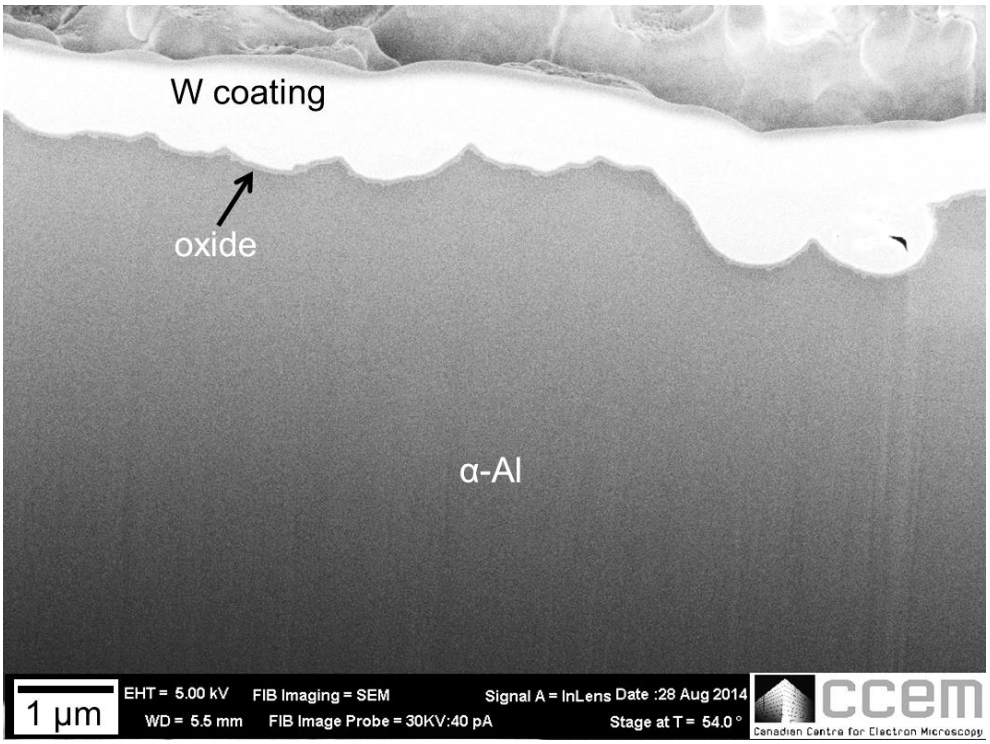

(a)

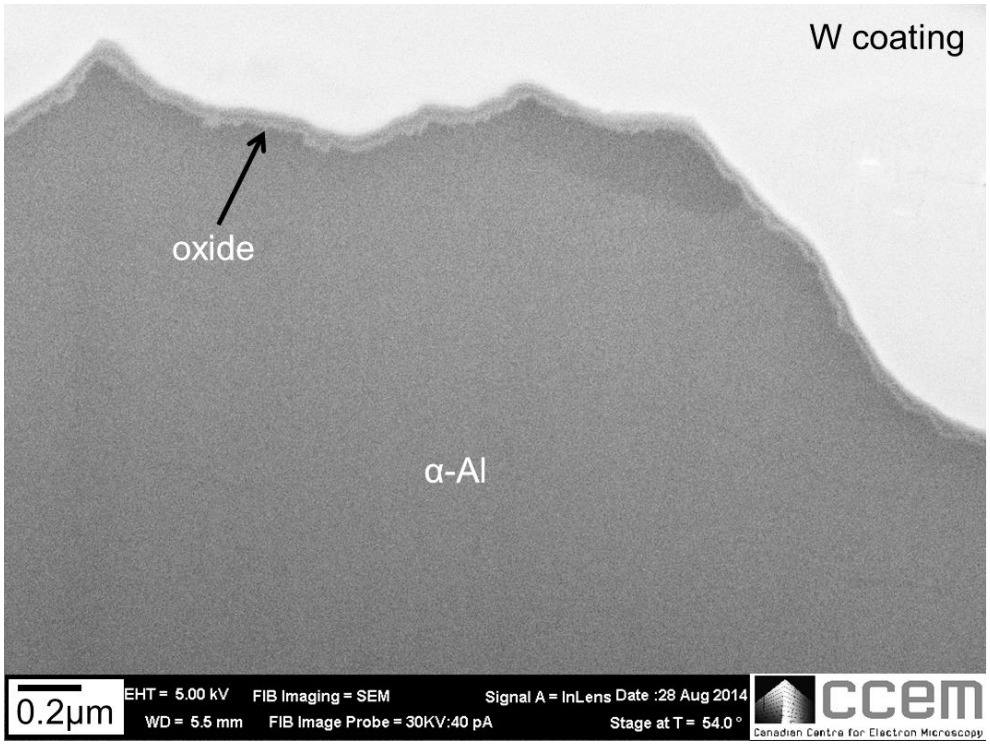

(b)

Figure 6-20 – Secondary electron image of FIB sectioned oxidized Al-1Mn samples. (a) Al-0.0008Mg sample oxidized at 913 K (640 °C) to a calculated oxide thickness of 250-275 nm and (b) higher magnification view of (a).

Measuring the oxide layer thickness from SEM images from multiple images of each FIB cross section, the average oxide thickness of each sample was computed, as is shown in Figure 6-21. The bar chart compares average values from each alloy sample, as well as the minimum observed oxide thickness noted from each sample. As shown, the averages as well as observed minimum are all very similar for each alloy. It is worth noting that the observed oxide thicknesses are quite different than the expected oxide thicknesses which were calculated using the parabolic oxidation kinetics in Appendix B. Additionally, for samples with greater than 0.005 Mg, although the average oxide thickness was similar to that of the other alloys, as shown by measurements in Figure 6-21, there were noticeable differences in its surface morphology, which will be elaborated on in Section 6.5.2.

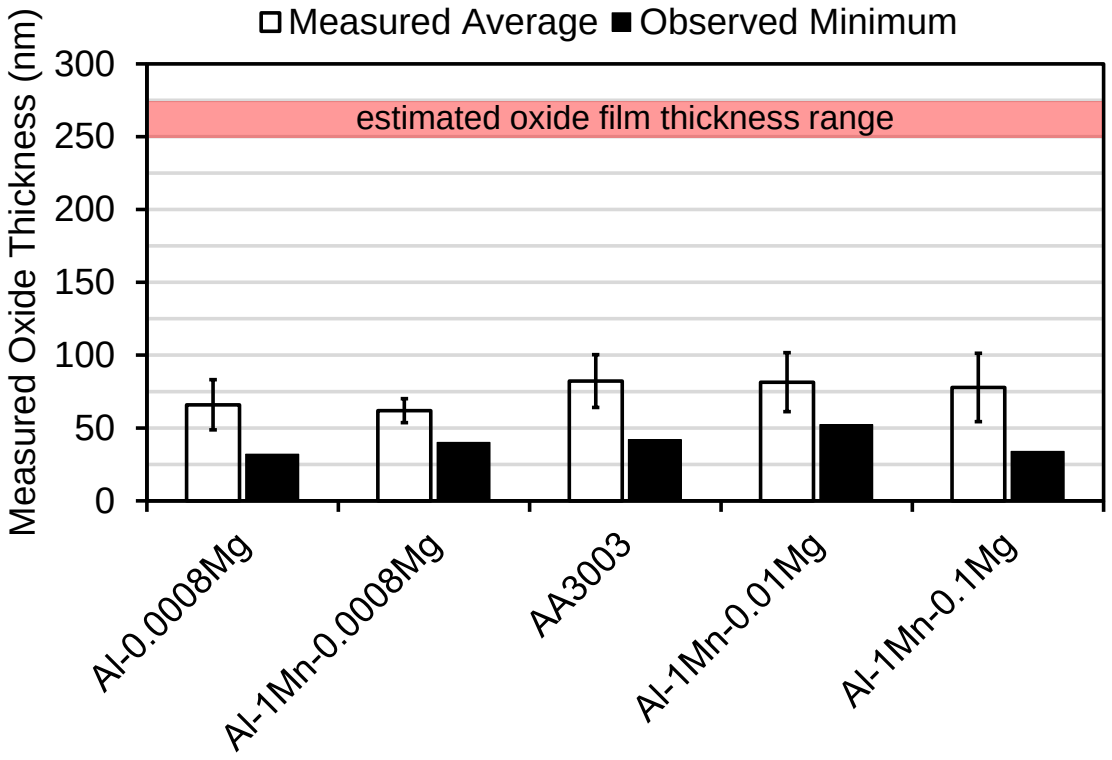

Figure 6-21 – Measured average and minimum observed oxide film thicknesses for samples examined with FIB sectioning and SEM imaging. Estimated oxide film thickness highlighted in red for comparison.

In addition to the oxide uniformity measured above, a FIB section was fabricated such that it bisected an intermetallic particle present on the AA3003 sample surface. The FIB section was then examined with SEM, to determine the extent of oxidation on top the intermetallic particle; specifically to compare it with oxidation of the surrounding α-aluminum on the FIB section. This was performed since the results from Section 4.4 suggested that the oxide growth on top of intermetallic particles which bisect the AA3003 surface may not have been uniform. As such, these areas of non-uniformity would potentially have been sites for AA4045 melt penetration.

The resulting FIB-section of a bisecting intermetallic particle is shown in Figure 6-22a. Here it can clearly be observed that an oxide layer does grow over top the intermetallic at the surface. The oxide appears to be more or less uniform in thickness over the entire top surface of the intermetallic particle. In the results from the chill-cast surface, this growth was not observed, see Figure 4-25. This may be due to the FE-SEM resolution limits, or possibly due to the nature of the intermetallics being different. The FIB-sectioned sample shown in Figure 6-22a was machined from a DC cast ingot, hence its microstructure was different then the surface structure of the chill cast surface, see Figure 4-19. Furthermore, the oxidation period for this FIB-sectioned sample was much longer than the oxidation period for the chill cast surface, allowing more time for oxide growth. In the chill cast surface, the oxidation time is shorter and the surface intermetallics are transforming, thus the oxide growth on top of these transforming intermetallics may not be uniform. The section shown in Figure 6-22b is the region immediately adjacent to the intermetallic particle region in Figure 6-22a. Comparing Figure 6-22a and b, both the oxide thickness and uniformity appear to be more or less equivalent.

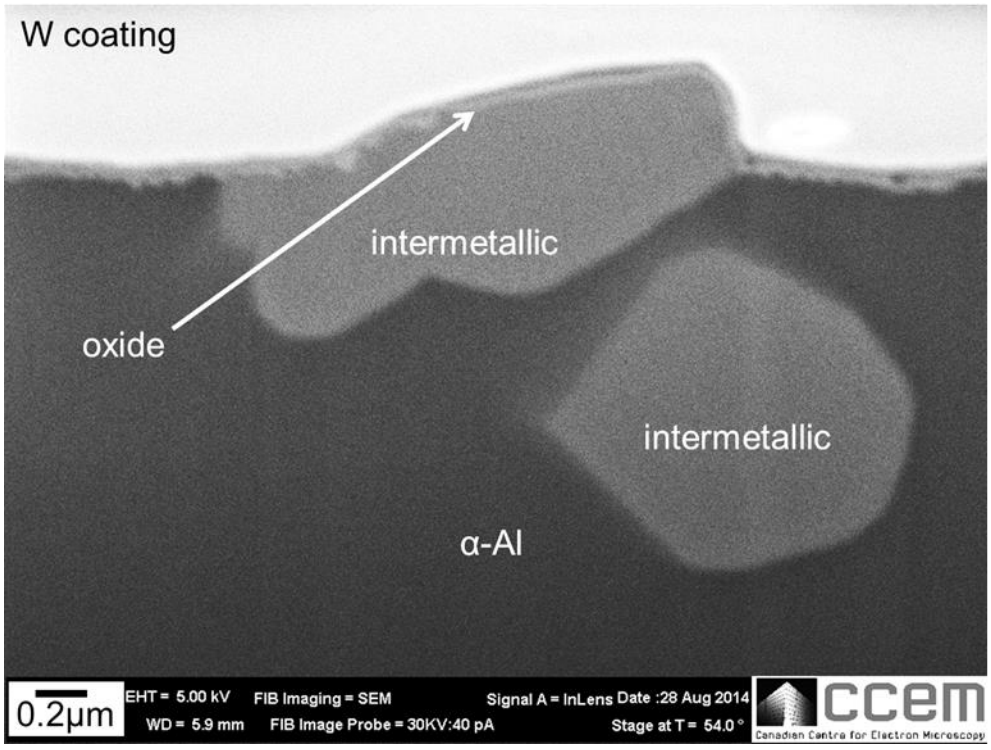

(a)

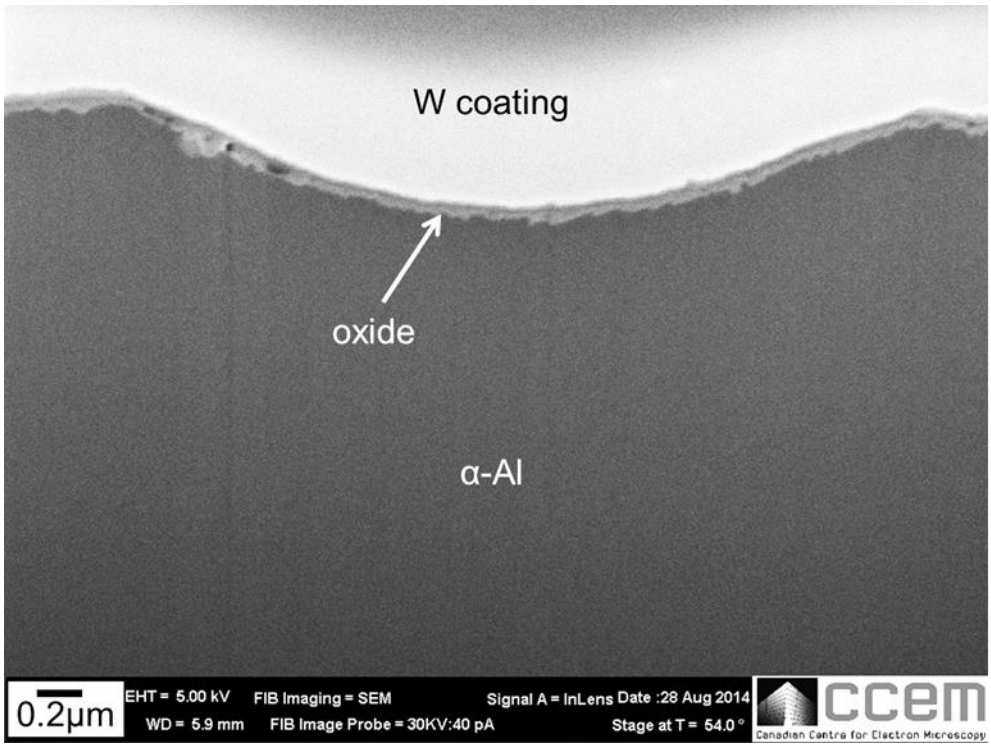

(b)

Figure 6-22 – Secondary electron image of FIB sectioned oxidized aluminum sample. AA3003 sample oxidized at 913 K (640 °C) to a calculated oxide thickness of 250-275 nm. (a) Oxide above an intermetallic particle at the surface of the sample. (b) Oxide above a primary α-Al region.

6.5.2 Oxide Morphology

From Section 5.5, there was expectation that Mg segregation would be present for all alloys containing at least 0.005 wt% Mg. It should be noted that the samples examined here were oxidized for longer times than the samples present in Section 5.5. An example of the resulting surface morphology for alloys with 0.005 wt% Mg (alloy Id # 1), 0.01 wt% Mg (alloy Id # 1b), and 0.1 wt% Mg (alloy Id # 1c) are shown in Figure 6-23. The oxidized surface morphology of the 0.005 wt% Mg alloy, in Figure 6-23a, shows the presence of small particles at the surface. These particles were randomly distributed along the surface. From the resolution at which these particles were observed, the morphology of the particles could not be adequately determined.

Looking at the 0.01 wt% Mg alloy, Figure 6-23b, the surface particles are larger and their growth slightly more advanced. The morphology of the particles that appear on the surface in Figure 6-23b are not spherical. The growth appears to show signs of needle-like growth, as indicated by the particles highlighted by arrows in Figure 6-23b. EDS spectrum of these needle-like particles were high in Al, O and Mg content. The peak height of the Al and O were about equal, while that of Mg was about half the height of the other two peaks.

Two images, a low and high resolution image, of the 0.1 wt% Mg alloy are presented in Figure 6-23c and Figure 6-24. Again, the particle growth on the 0.1 wt% Mg alloy surface is more advanced than the 0.01 wt% Mg and 0.005 wt% Mg sample surfaces. The particles, indicated with white arrows in Figure 6-23c and Figure 6-24 are larger in size than the two previous alloys, with a diameter close to 0.2 μm. The growth morphology of the particles, seen in Figure 6-24, is clearly needle-like in nature. EDS of these particles again show high levels of Al, O, and Mg. However, unlike the EDS spectra from the particles on the 0.01 wt% Mg alloy, the Al and Mg peaks were more or less equal, and the O peak slightly lower. In addition to these

particles, the surface of the 0.1 wt% Mg alloy appeared to have a rougher texture. This is particularly evident in comparing Figure 6-23b and c.

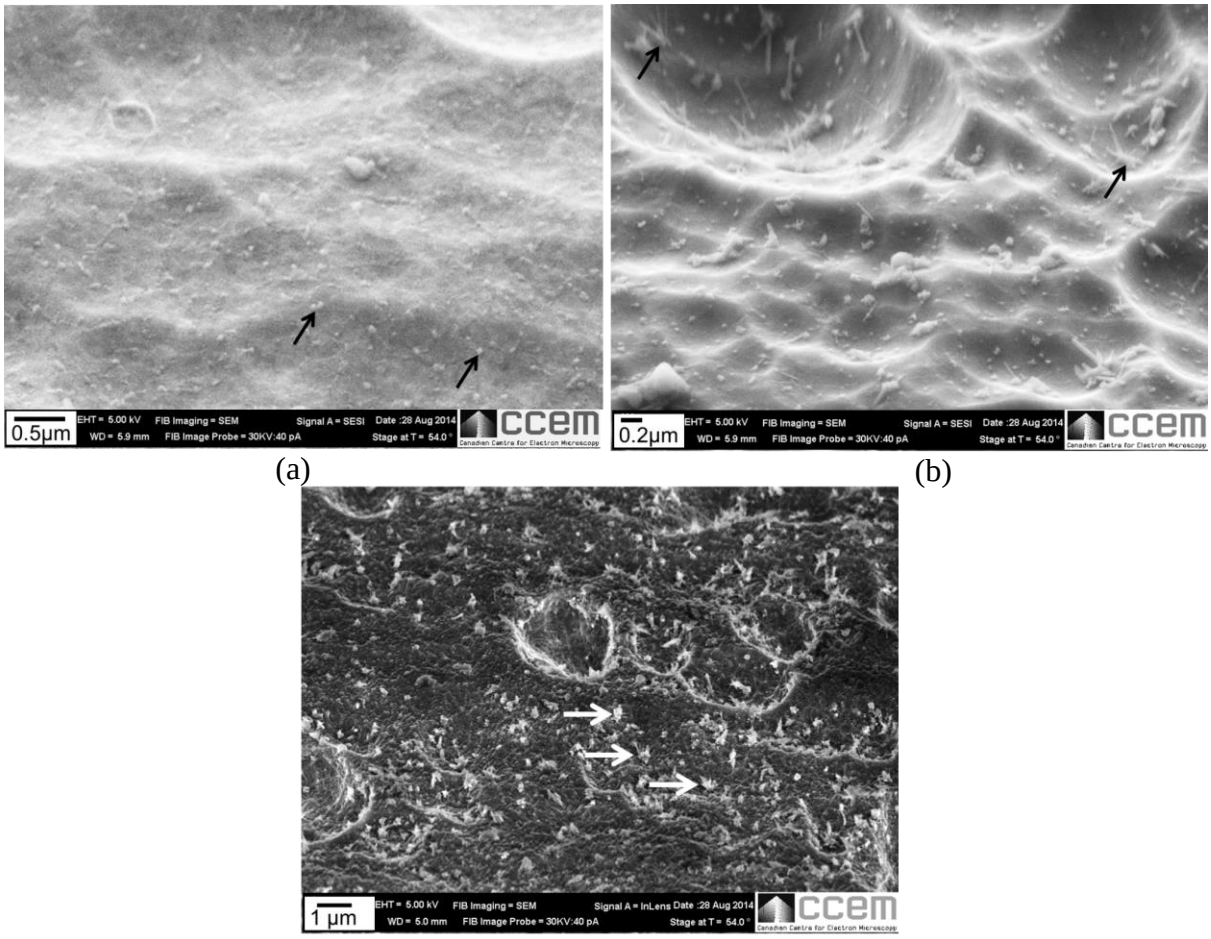

(a) (b)

(c)

Figure 6-23 – Surface morphology of samples oxidized to an estimated oxide film thickness of 250-275 nm. (a) Alloy Id # 1, Al-1.2Mn-0.7Fe-0.2Si-0.005Mg, (b) alloy Id # 1b, Al-1Mn-0.01Mg, (c) alloy Id # 1c, Al-1Mn-0.1Mg.

Figure 6-24 – Higher magnification SEM image of surface morphology shown in Figure 6-23c.

6.5.3 Oxide Defects

From the various FIB cross sections performed, what appeared to be defects in the oxide surface films were observed on more than one occasion. Two examples of what appears to be oxide defects are shown in Figure 6-25. The oxide in image Figure 6-25a came from an immersion test sample (from Section 6.2). The alloy was Al-1Mn-0.0008Mg sample and was oxidized at 913 K (640 °C) to an expected oxide thickness of 250-275 nm. The oxide layer is observed in the figure as the medium-level gray layer. Above the oxide is the protective W coating, which appears bright white in the figure. Below the oxide layer, are two instances where there appears to be a void below the surface, labelled a in the figure. Above this void, the oxide appears to be slightly thinned as well. Another example of this type of void is shown in Figure 6-25b, also labelled a in the figure. In this specific example, the sample was from those prepared specifically for oxide thickness/uniformity measurements (see Section 3.3.3). The alloy was

Al-1Mn-0.0008Mg sample and was oxidized at 913 K (640 °C) to an expected oxide thickness of 250-275 nm.

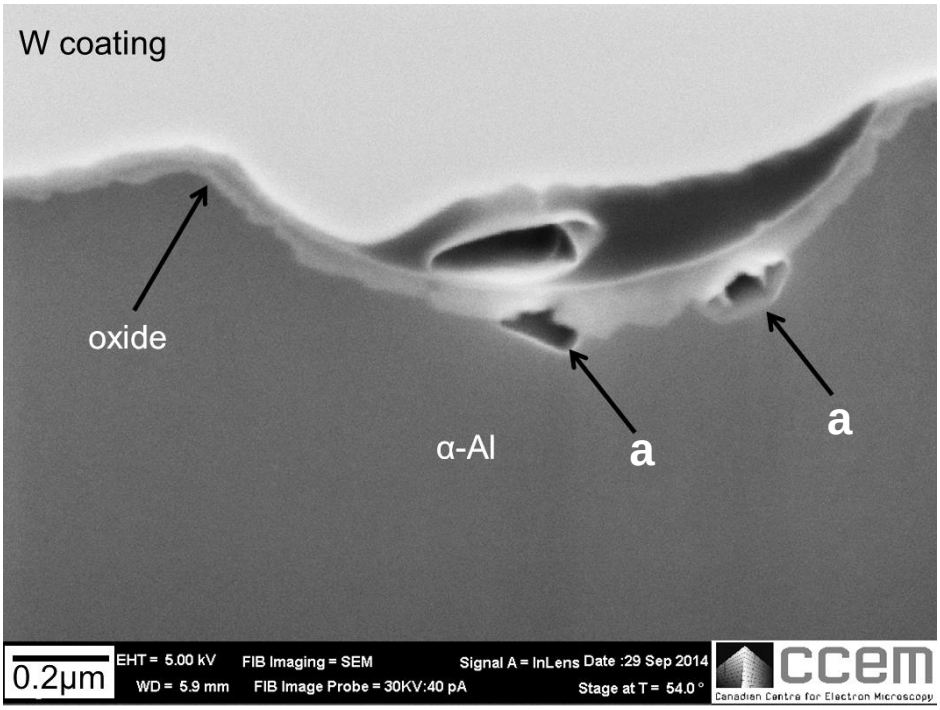

(a)

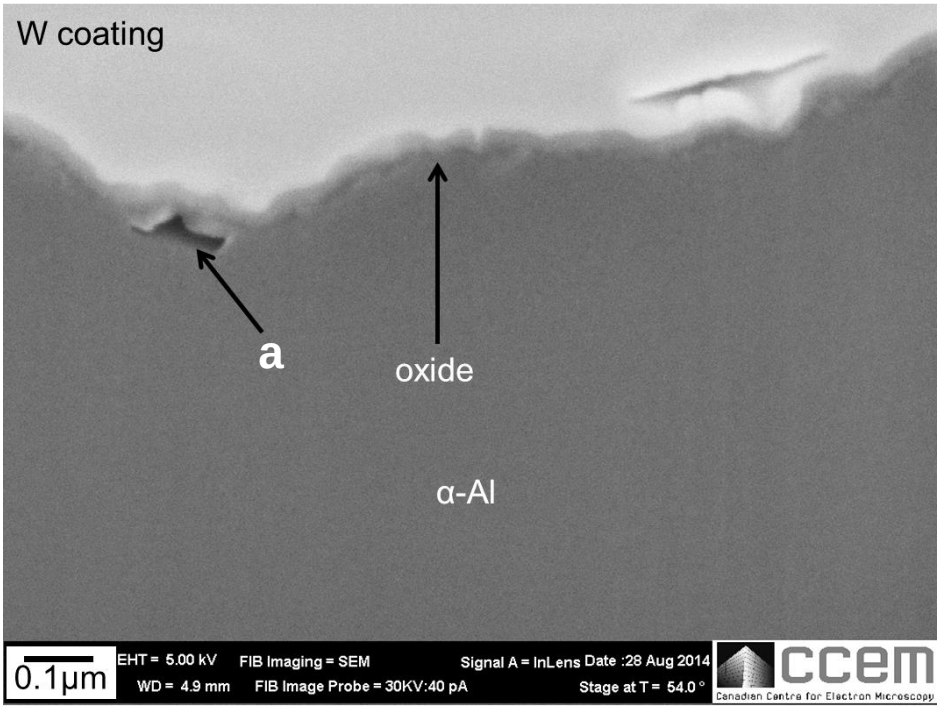

(b)

Figure 6-25 – Examples of oxide film defects observed in FIB sectioned samples. (a) Al-1Mn-0.0008Mg sample, and (b) Al-1Mn-0.1Mg sample.

To quantify the number of defects present in the surface oxide films, copper decoration was performed on a series of aluminum samples. The sample preparation procedure used is given in Section 3.3.4. Al-0.0008Mg samples were examined first. Three different oxidation conditions were prepared: (i) a room temperature formed oxide film, with an assumed oxide thickness of 2-4 nm, based on literature [26], (ii) a thermal oxide film with calculated film thickness of 10-14 nm, prepared by oxidizing in argon for 20 min at 907 K (634 °C), and (iii) thermal oxide film with calculated film thickness of 250-275 nm, prepared by oxidizing in air for 120 min at 907 K (634 °C). Copper decoration was performed, as per Section 3.3.4 and the resulting optical micrographs were analyzed by counting copper decoration sites on the sample surfaces.

A typical optical micrograph is shown in Figure 6-26. Here, the black spots are locations were copper has deposited onto the sample. SEM and EDS of these copper decorated surface confirmed that these deposits were in fact copper rich deposits. For all samples examined, the distribution of the copper deposits appeared to be randomly distributed over the sample surfaces.

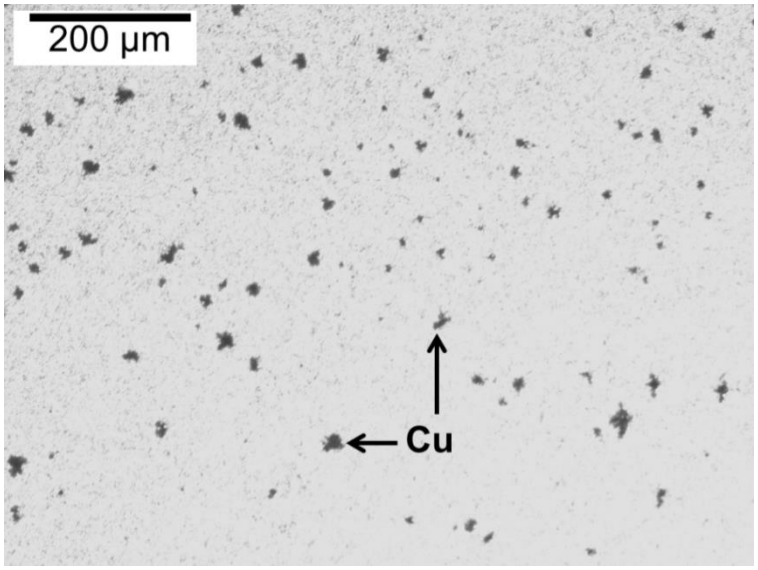

Figure 6-26 – Optical micrograph showing copper rich deposits on Al-0.0008Mg surface. Sample was prepared as per Section 3.3.4, allowed to oxidize at room temperature, then cathodically polarized using 0.5 V for a duration of 3 min.

The results from counting copper decoration sites for these initial three oxidation conditions are presented in Figure 6-27. The values shown in the figure are average values. In total, 3 samples were measured for each test condition in the figure, with a minimum of five fields, 0.7 mm by 0.9 mm in dimension, from each sample. For the first condition, i.e., the room temperature formed oxide film of 2-4 nm in thickness, the average defect density was 1.8×10^4 defects/cm^2, which was approximately 4 times greater than the other two conditions. The scatter is also large, of similar order of magnitude to the measurement itself. This suggests that the room temperature oxide film has numerous defects present. For the two other conditions, where the samples were oxidized at high temperature to a calculated oxide thickness of 10-14 nm and 250-275 nm, the overall number of defects is reduced. Additionally, standard deviation was also significantly reduced. Lastly, there appeared to be no noticeable difference between the number of defects measured for the two high temperature oxide conditions, 10-14 nm and 250-275 nm. This suggests that either: (i) the defects sites, highlighted by copper decoration, persist even after long periods of thermal oxidation, or (ii) the defects sites, highlighted by copper decoration, manifest themselves during sample cool down from high temperature and thus yield similar values, as both samples were cooled in a consistent manner.

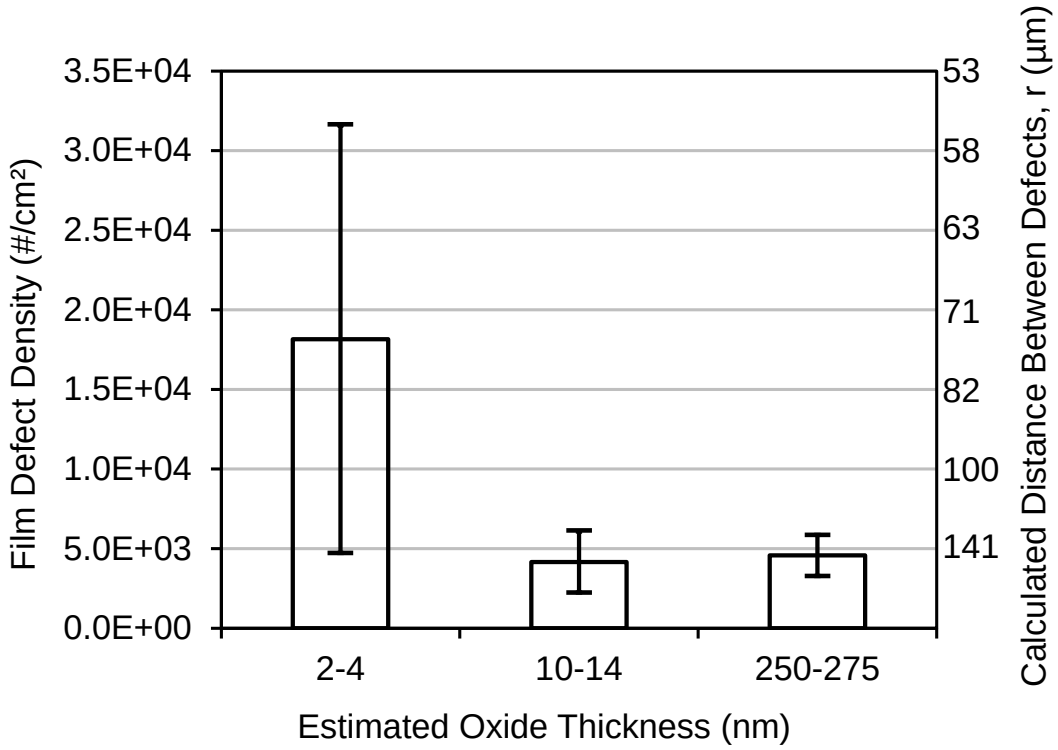

Figure 6-27 – Oxide film defect density for oxide films grown on Al-0.0008Mg samples. Three different oxidation conditions. Defects measured by counting copper deposit sites from optical metallographs.

6.6 Discussion

The test results from Section 6.2 suggest that sample and melt temperature is the most important parameter controlling final sample quality. This again agrees with the hypothesis that the interface formation process is a penetration, dissolution and bridging process. There was no observed benefit from having Mg present in the sample. However; the results in Figure 6-6 and 6-7 suggest a potential benefit of having 0.1 wt% Mg present in the melt. Possible reasons for this will be discussed in Section 6.6.2.

6.6.1 Meniscus effect on sample and melt contact condition

The observation of long and thin horizontal bare spots found on final samples, which were immersed at 1.4 mm/s, and the absence of them on the test sample immersed at 9.0 mm/s, was a

key result. The orientation of these bare spots was very specific, with the long axis parallel to the liquid metal level. Both the size and orientation of these dry spots suggest that they are not related to sample microstructure.

As observed and discussed in Section 5.5.1, the greatest overall impediment to bond formation appeared to be oxide-oxide contact, i.e., contact of an oxidized sample surface with an oxidized liquid meniscus. As such, a possible explanation for these horizontally oriented bare spots may be due to: (i) fluctuations of the liquid meniscus during immersion, or (ii) partial re-oxidation of the liquid meniscus during sample immersion.

A fluctuating meniscus can occur by: (i) rippling of the free surface of the liquid melt after initial breaking of the melt surface oxide film during immersion and (ii) the slowly rising free surface of the liquid which occurs due to displacing volume during sample immersion into the melt. As the meniscus fluctuates it can periodically release a small oxide fragment onto the surface of the sample and impede bonding over this area. This would qualitatively explain why the orientation of the patches are parallel to the metal level.

If the meniscus partially re-oxidizes at the liquid meniscus, it could also potentially explain the observed horizontal dry patches on test samples. A schematic explaining this process is shown in Figure 6-28. In Figure 6-28a, the sample and melt just prior to immersion into the melt are shown. Both the sample surface and melt top surface have oxides, which have formed during the sample heating phase. As the sample is immersed, it breaks through the surface oxide on the liquid, as shown in Figure 6-28b. This exposes fresh liquid to the ambient atmosphere. The freshly exposed liquid surface is then exposed to the atmosphere in the furnace, which will have an oxygen partial pressure, p_{o2}, above zero, even if the furnace is continuously purged with argon cover gas. The meniscus re-oxidizes as it is immersed. Depending on the oxygen partial

pressure, the time required to form a closed oxide on the meniscus will vary (sample calculation to follow). As the meniscus re-oxidizes while the sample is immersed, there is a potential for this newly formed oxide at the liquid meniscus to break-off and become entrained at the sample/melt interface, as depicted in Figure 6-28d. The breaking of the oxidized meniscus then exposes a fresh liquid aluminum surface again, and the process repeats itself. This manifests as periodic regions of poor and intimate contact, shown in Figure 6-28e. This leads to the markings which were commonly observed on final test samples. This further suggests that the intimate contact between the sample and the melt, for tests conducted in argon, is only periodic in nature.

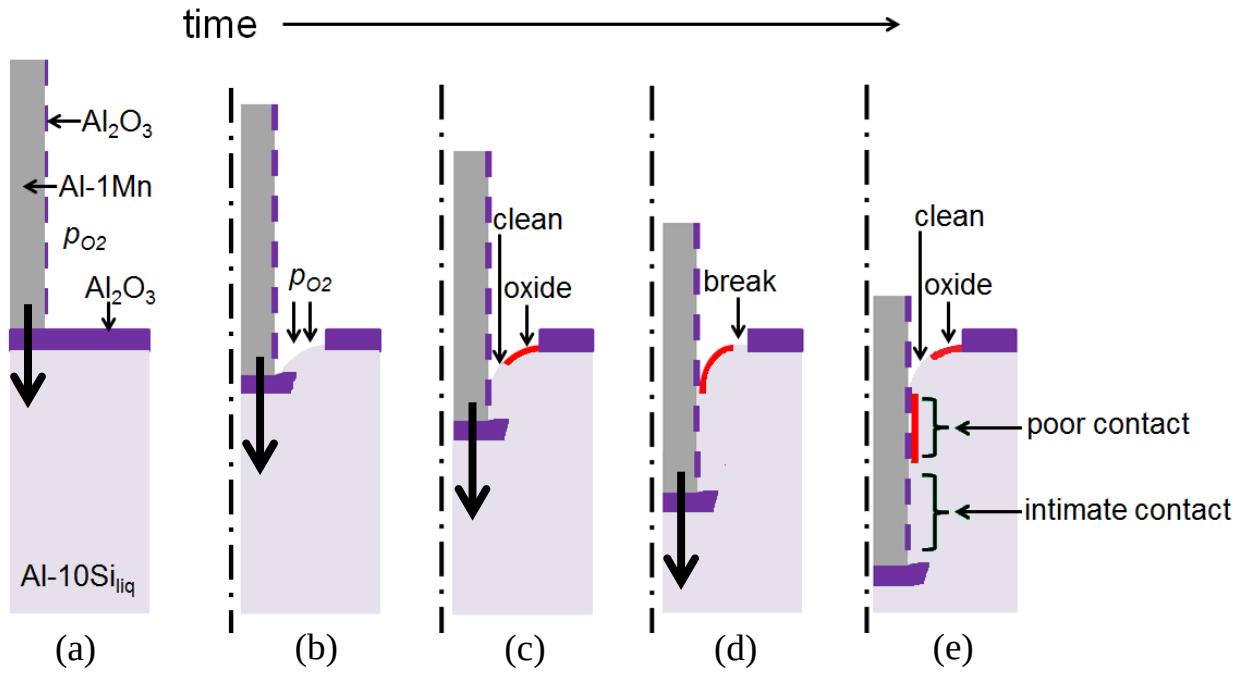

Figure 6-28 – Detailed schematic of the interface formation test, conducted in argon. (a) Sample and melt surface just prior to immersion into the melt. (b) Initial break of the Al-10Si$_{liquid}$ oxide film, exposing clean liquid Al-10Si$_{liquid}$ at the meniscus. (b) Re-oxidation of the meniscus. (c) Break-off of oxidized meniscus, exposing clean Al-10Si$_{liquid}$ at the meniscus again (d) Oxidized portion of the meniscus which has previously broken off gets entrapped at the AA3003/AA4045 interface. (e) Re-oxidation of the clean meniscus.

Considering the furnace completely purged with argon (99.998% Ar), the oxygen partial pressure can be calculated to be 1.52 x 10^{-3} Torr, i.e.,

$$p_{O_2} = 101325 \text{ Pa} \cdot \left(\frac{(100-99.998)}{100}\right) \cdot \left(\frac{133.32 \text{ Torr}}{1 \text{ Pa}}\right) = 1.52 \times 10^{-3} \text{ Torr} \quad (6\text{-}1)$$

Similarly, when the furnace atmosphere is air, as in tests from Section 5.2, the oxygen partial pressure is 158 Torr, i.e.,

$$p_{O_2} = 101325 \text{ Pa} \cdot (0.209) \cdot \left(\frac{133.32 \text{ Torr}}{1 \text{ Pa}}\right) = 158 \text{ Torr} \quad (6\text{-}2)$$

Using these two values, the oxygen exposure on a freshly broken Al-10Si liquid surface, as shown in Figure 6-28b for example, can be simply calculated by:

$$\text{oxygen exposure(L)} = \text{p}_{\text{o2}} \cdot \text{t} \quad (6\text{-}3)$$

The resulting curves for oxygen exposure versus time are shown in Figure 6-29. Considering the value measured in Stucki *et al.* [33] required to form a close oxide on a fresh aluminum surface, i.e., 3000 L, the resulting differences in exposure time between cases in air and argon are drastically different. In air, the fresh liquid surface is predicted to form a closed oxide in 1.9 x 10^{-5} s. As very little time is required to re-oxidize the surface, there is little expectation that contact between the sample surface and the melt will be intimate. The test mechanism described in Figure 5-13 is likely to occur. In argon, however, about 2 s is required to form a closed oxide on a fresh Al-10Si surface. Comparing this with the total time of immersion during testing (1.4 mm/s immersion speed and 32 mm immersion depth) of about 22.8 s, suggests that the fresh exposed surface will re-oxidized and form a closed surface oxide during immersion. Hence, the test mechanism in Figure 5-12, gives an incomplete picture of the interface formation test when conducted in argon. A more likely mechanism, which agrees qualitatively with test sample surfaces after immersion, is that described in Figure 6-28. This also suggests that a fast immersion speed, with all other conditions being equal, would result in

cleaner contact between the sample and the melt. This was indeed observed to be the case, as the sample surface shown in Figure 4-17a did not display any characteristic horizontal patches. This leads, to a final interface formation mechanism, which will be described in detail in following section.

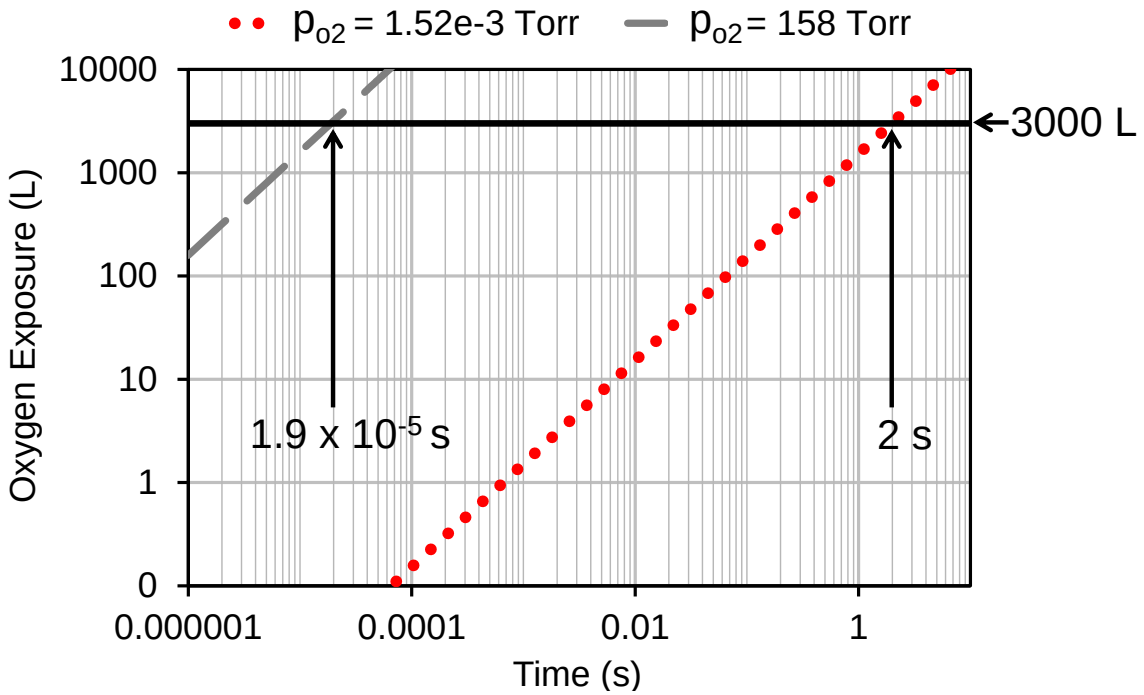

Figure 6-29 – Oxygen exposure, in Langmuir (L), for the two oxygen partial pressures used during testing. p_{O2} = 158 Torr corresponds to tests conducted in air, and p_{O2} = 1.52 x 10^{-3} Torr corresponds to tests conducted in argon. The time required to reach 3000 L, the exposure quoted by Stucki *et al.* [33] to form a closed surface oxide, is indicated in the figure.

6.6.2 A final interface formation mechanism

The cumulative results from Chapters 5 and 6 lead to the mechanistic model for interface formation between the Al-1Mn test samples and the Al-10Si melt shown in Figure 6-30. When the sample is immersed under an argon atmosphere, as mentioned in Section 6.6.1, intimate contact between the sample and the melt will be periodic, due to the re-oxidation of the meniscus and periodic entrainment of the meniscus oxide at the interface. Where oxide from the meniscus is entrained, no interaction between the sample and the melt occurs, as shown in Figure 6-30a.

In between these areas, intimate contact between the melt and the Al-1Mn surface occurs. The Al-1Mn surface oxide is penetrated at oxide defect sites and dissolution of the underlying Al-1Mn sample occurs. The specific oxide penetration mechanisms will be discussed in Section 6.6.3.

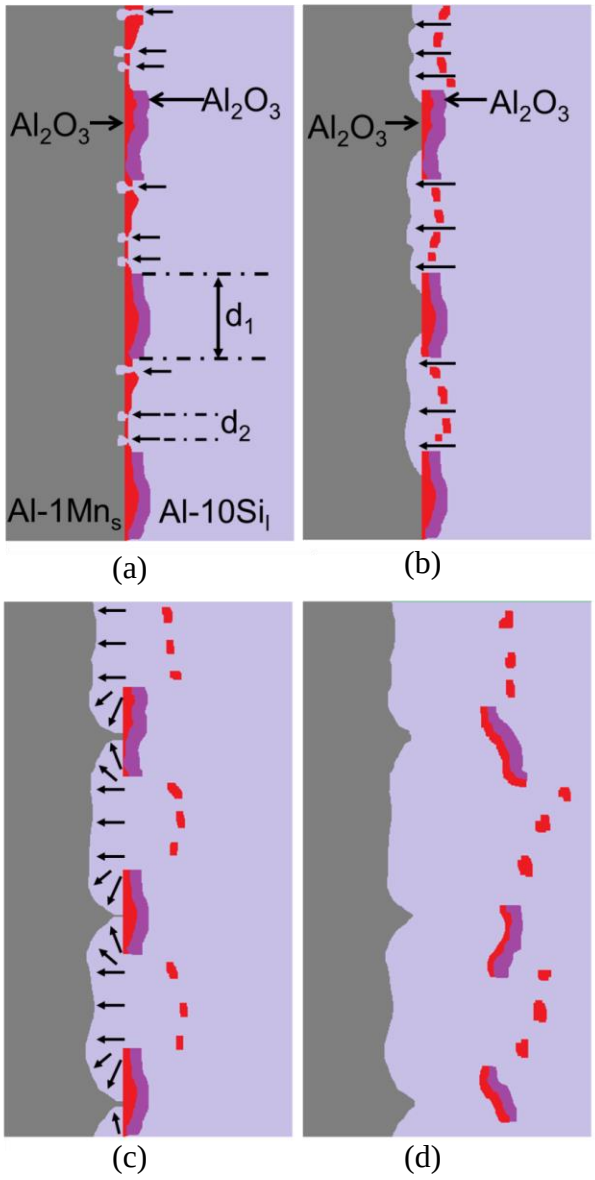

Figure 6-30 – Schematic of proposed interface formation process. (a) Penetration of oxide in discrete locations, and dissolution of underlying Al. (b) Bridging of oxide film (over spacing d_2). Oxide film breakup, and continued dissolution and undercutting of region above double oxide layer. (c) Bridging below double oxide film (over spacing d_1). (d) Break away of oxide film, and continued dissolution of Al, final interface is metallurgically sound.

The process then proceeds by bridging of oxide penetration points over the areas of intimate contact between Al-1Mn solid and the Al-10Si liquid, with a spacing labelled d_2 in Figure 6-30a as well as undercutting of the regions where oxide entrainment occurred, with spacing labelled d_1 in Figure 6-30a. This process continues, as shown in Figure 6-30b and c, until bridging is complete and the oxides are free to float away from the final interface, as in Figure 6-30d. It should be noted that the free floating oxides hypothesized and depicted schematicall in Figure 6-30d have not been observed in any of the Fusion™ cast interfaces examined in Chapter 4. To summarize, the first critical requirement for interface formation, as shown in Chapter 4, is that intimate contact between the Al-1Mn thermal oxide and the Al-10Si melt be formed. In the interface formation tests, this can be achieved by performing the tests with an argon cover gas. However; the meniscus does re-oxidize and periodically the contact between the Al-1Mn sample and the Al-10Si melt is hindered by entrainment of the meniscus oxide.

Examples can be found in the literature where bond formation between a low melting liquid Al-alloy melt and an oxidized metal substrate occurs, because steps were taken to break up the melt oxide and induce intimate contact between the liquid melt and the solid substrate [123-124]. Xu *et al.* [123] used ultrasonic vibration to join Zn-Al to an AA6061/Al_2O_3 composite material in an air atmosphere. The ultrasonic vibration provided a means to break up the Zn-Al surface oxide. Penetration of the surface oxide was suggested to occur naturally. Undermining and spreading of the Zn-Al beneath the AA6061/Al_2O_3 surface oxide was said to be aided by cavitation processes occurring on the surface, a result of ultrasonic vibration. Chen *et al.* [124] used ultrasonic vibration to join Al-Si liquid to a Ti-6Al-4V solid sample, also in air. Here, the authors suggested that ultrasonic assistance provided a means to get Al-Si into

intimate contact with the Ti-6Al-4V surface as well as produced surface defects on the oxidized Ti-6Al-4V. It should be noted that in the study of Chen *et al.* [124], the surface oxide is TiO_2 not Al_2O_3. Although disagreement regarding the role of surface cavitation persists, both Xu *et al.* [123] and Chen *et al.* [124] suggest that upon intimate contact of a liquid melt with a thermally oxidized surface, the oxide can be undermined and bonding can be achieved.

While the model for interface formation presented in Figure 6-30 appears to qualitatively agree with results from Chapters 5 and 6, it does not address the mechanism of oxide film penetration. Is the thermal oxide grown on Al-1Mn inherently permeable to Al-10Si? Or are other factors at play?

6.6.3 Al-1Mn oxide film penetration

Working from the basis that the Al-10Si melt penetrates the Al-1Mn sample surface oxide in discrete oxide defect locations, as evidenced in Figure 6-19, the mechanism regarding oxide penetration can be examined in detail by considering: the oxide observations in Section 6.5, and the immersion test results in Sections 6.2 and 6.3.

Observations of the oxide uniformity show that local minima exist in the oxide film thickness at random intervals over the oxide surface. Although FIB sections cannot reveal the full detail of the oxide uniformity (since this is only one slice through an area), the local minimum was about 30-50% that of the average thickness of the oxide films. Also, it is worth noting that the estimated oxide film thickness was far greater than the observed values. Possible reasons for the discrepancy are:

i. The assumption of parabolic kinetics from room temperature to 640 °C, which is an oversimplification of the actual observed kinetics.

ii. Experimentally derived aluminum oxidation kinetics has been predominately measured using isothermal oxidation tests; however, in these tests, samples were heated from room temperature to test temperature. The assumption that non-isothermal oxidation kinetics is similar to the isothermal kinetics may not have been a valid assumption.

iii. The assumed oxidation kinetics may have been an overestimation. Oxidation kinetics from Beck *et al.* [38] for instance, is lower than the assumed kinetics.

To summarize, the oxide films grown on the Al-1Mn samples prior to immersion into the Al-10Si melt were seen to be thinner than calculated estimates and contained local minimums which were 30% to 50% less than the measured average. Additionally, what appeared to be oxide defects were also observed on FIB sections, see Figure 6-25. Finally, defects sites were also seen by the copper decoration technique, and notably, the density of these copper decoration sites did not fall to zero, even after prolonged oxidation at high temperatures, see Figure 6-27.

The nature of the defect sites where copper decoration took place were not examined further in this thesis. FIB sectioning and SEM or TEM examination could be a potential future study to determine their nature. However, defects observed in Figure 6-25 reveal that defect sites are areas where the oxide thickness is locally a minimum, and below the thin oxide, a flaw (or void) is present. This matches the morphology proposed by Vermilyea [59] for anodic oxide growth over flaw regions of pre-existing Ta_2O_5 films. While the substrate and oxide type (Ta and anodic film) in Vermilyea [59] is different than the substrate and oxide type (Al-1Mn and thermal oxide film) in this thesis, the proposed reformation mechanism still applies. The oxide morphology above a pre-existing flaw, proposed by Vermilyea [59], is depicted in Figure 6-31.

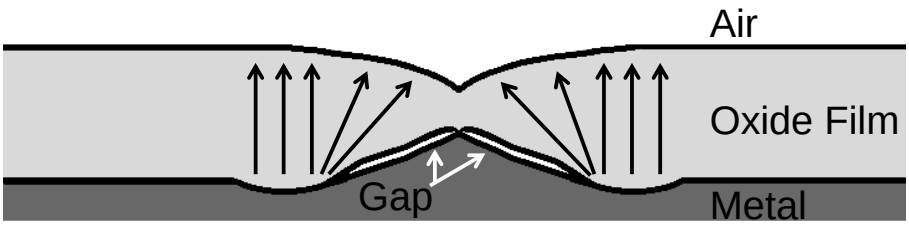

Figure 6-31 – Proposed model, by Vermilyea [59], of defect reformation on growing oxide films. Arrows indicate ionic diffusion pathways and subsequent oxide growth over top of the defect.

Here the oxide film is locally thin above the flaw. Necessary to this model, the oxide film must not be in contact with the underlying base metal at the site of the flaw, thus hindering oxide growth. The oxide overgrowth at the site of the flaw is due to ionic diffusion of metal ions from regions adjacent to the flaw, as indicated by the black arrows in the figure. As the diffusion path from the adjacent metal to the site above the flaw is longer than the diffusion path over non-flawed regions of the film, the resulting oxide growth rate over the flaw is less than the oxide growth rate in the surrounding material.

Furthermore, the effect that increasing average oxide thickness has on sample test results, see Figure 6-1 and 6-2, must also be considered. As observed in those results, as well as in Chapter 5 results, there is a noticeable effect of prolonged oxidation time on final sample appearance. The observed results suggested that an increase in oxidation time decreases the overall ability for the Al-10Si melt to penetrate the sample oxide. If the melt simply penetrates the oxide at defect sites, i.e., no additional step is required to penetrate the oxide, one would expect that the defect density of the surface oxide to decrease with oxidation time, to match the results observed from testing. However, the defect density as shown in Figure 6-28, appeared to be roughly constant for samples which were oxidized at high temperature. Furthermore, if the melt were to simply penetrate the oxide at defect sites, one would expect that little or no defects should be present in the Al-1Mn-0.1Mg samples oxidized to the longest oxidation time, since the samples immersed for this condition showed virtually no interaction with the melt, see

Figures 6-3 and 6-5. In actuality, copper decoration of Al-1Mn-0.1Mg samples oxidized for the longest oxidation period did reveal that defects did persist in these samples.

The results suggest that a secondary step is required to penetrate the oxide at the defect sites. If the defect model of Vermilyea [59] is accurate, a longer oxidation time not only increases the average oxide thickness, but should also increase the minimum oxide thickness above reforming defects, such as the one depicted in Figure 6-31. If the oxide must be dissolved by the melt in order to expose the underlying metal, then one would expect that the time required to dissolve the oxide should increase as the local oxide thickness above each defect increases. Further to this, the composition of the oxide would also be of importance, as an Mg rich oxide would be potentially stable and insoluble when exposed to a Al-10Si melt, whereas an Al_2O_3 oxide could in theory be dissolved by a melt which is unsaturated with respect to dissolve oxygen. This mechanism would match the observed test results.

The final and most plausible mechanism for penetration of melt material though the surface oxide is depicted in Figure 6-32. Here, when Al-10Si comes into intimate contact with the Al_2O_3 surface oxide, the Al_2O_3 is partially thinned by dissolution of the Al_2O_3 into the melt. This requires that the Al-10Si be unsaturated with respect to dissolved oxygen. At the thinnest regions, as shown in Figure 6-32b, oxide dissolution results in exposure of the bare underlying metal. At this point, the Al-10Si melt, being in direct contact with the underlying metal, begins to dissolve the metal and undercut the surface oxide, as in Figure 6-32d. The continued dissolution of the underlying metal leads to eventual bridging, as shown in Figure 6-30. The addition of an active species to the Al-10Si melt, such as Mg, could potentially accelerate the process of Al_2O_3 dissolution, by chemical reduction, as shown in Figure 6-32c. It should be noted that this also matches the results in Figure 6-6 and 6-7.

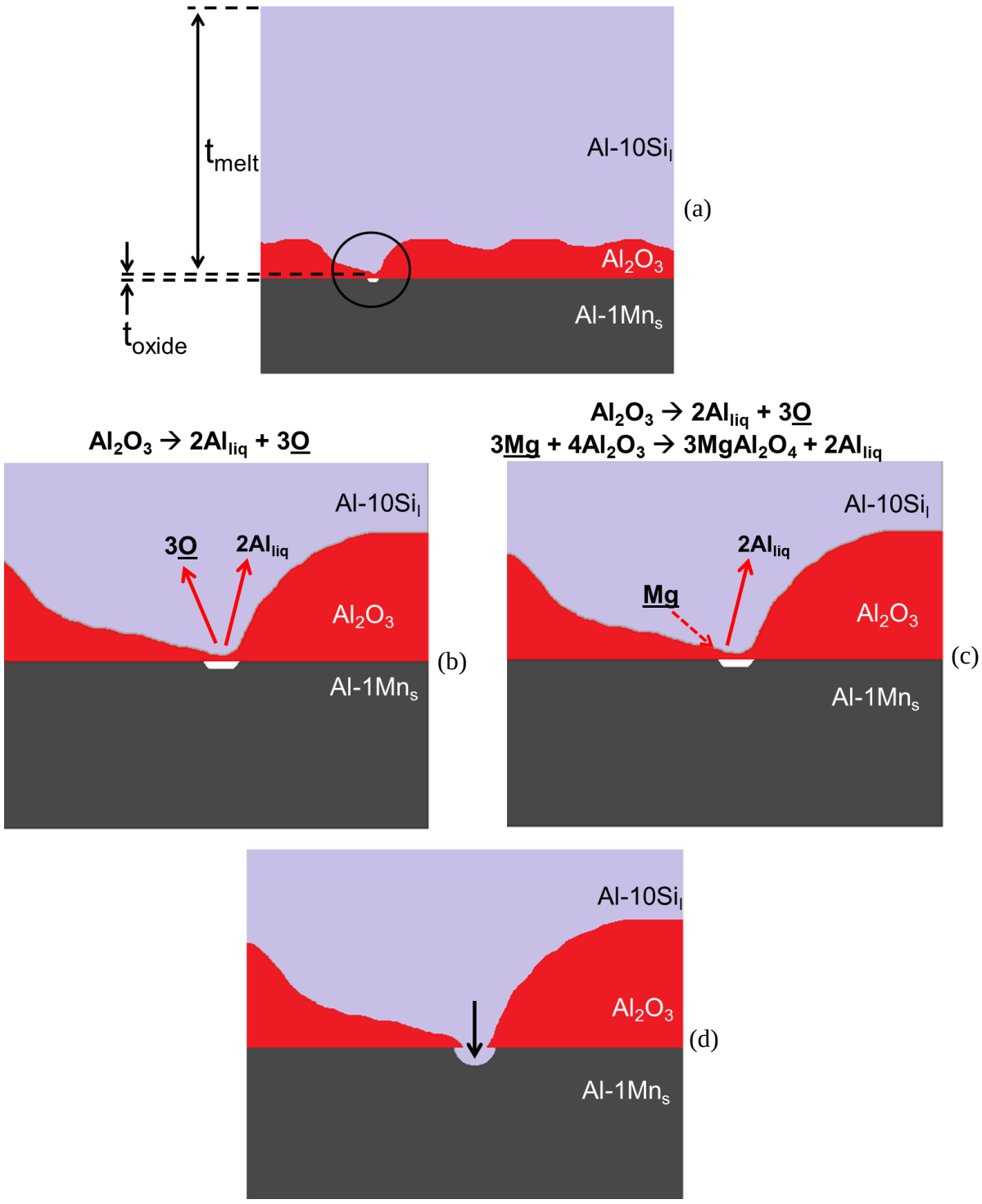

Figure 6-32 – Final proposed oxide penetration mechanism. (a) locally thin oxide, t_{oxide}, over top of a flaw, and in intimate contact with a melt layer of thickness t_{melt}. (b) Dissolution of the Al_2O_3 oxide in the Al-10Si melt (reaction written above figure). (c) Dissolution of the Al_2O_3 oxide in addition to reduction of the oxide by dissolved Mg in the Al-10Si melt (reactions written above figure). (d) Continued dissolution of the Al_2O_3 oxide results in exposure of the underlying Al-1Mn metal to the Al-10Si melt.

Given this mechanistic model for oxide penetration, the following question must be posed: given the limits of oxygen solubility in molten Al quoted in the literature [28-29], how thick an oxide can be dissolved by an unsaturated melt? One would expect a value similar in magnitude to the minimum oxide thickness observed in Figure 6-21 and 6-25, ~10-20 nm, if the mechanistic model proposed above were to be a valid model.

Consider a minimum Al_2O_3 oxide thickness, t_{Al2O3}, as shown in Figure 6-32a, exposed to an Al-10Si melt with thickness t_{melt} above it. For a given amount of melt, t_{melt}, above the oxide, if the following assumptions are made, one can calculate the maximum dissolvable oxide thickness which can be dissolved by the melt, t_{Al2O3}:

i. The sample surface oxide is Al_2O_3.
ii. The oxygen solubility of the Al-10Si melt is equivalent to the solubility of oxygen in pure aluminum at 933 K (660°C).
iii. The melt is assumed to have no oxygen dissolved in it prior to it being exposed to the Al_2O_3 sample surface oxide.
iv. The density of the Al-10Si melt at 933 K (660°C) is equal to the density of pure aluminum 2380 kg/m^3 [125].
v. The density of Al_2O_3 is 3790 kg/m^3 [129], and the wt% of oxygen in Al_2O_3 is 0.47.

For the solubility limit given by Ostuka and Kozuka [28], this can be expressed as follows:

$$t_{Al2O3} = (t_{melt}) \cdot (\rho_{Al-10Si}) \cdot \left(\frac{1}{mm_{Al}}\right) \cdot \left(\frac{2.90\times10^{-8}}{100}\right) \cdot \left(\frac{mm_O}{1}\right) \cdot \left(\frac{1}{0.47}\right) \cdot \left(\frac{1}{\rho_{Al2O3}}\right) \qquad (6\text{-}4)$$

For the solubility limit given by Taylor *et al*. [29], the following expression is used.

$$t_{Al2O3} = (t_{melt}) \cdot (\rho_{Al-10Si}) \cdot \left(\frac{1}{mm_{Al}}\right) \cdot \left(\frac{7.05\times10^{-5}}{100}\right) \cdot \left(\frac{mm_O}{1}\right) \cdot \left(\frac{1}{0.47}\right) \cdot \left(\frac{1}{\rho_{Al2O3}}\right) \qquad (6\text{-}5)$$

A plot comparing the maximum dissolvable oxide thickness which can be dissolved by the melt, t_{Al2O3}, using the two above expressions is given in Figure 6-33. For the solubility limits of

Otsuka and Kozuka [28], negligible amounts of Al_2O_3 would be dissolvable into the melt, as the value t_{Al2O3} is less than 1 nm. Using the Taylor *et al.* solubility limits [29] the result is quite different. For instance, given a melt thickness of 1 x 10^3 μm (or 1 mm), the resulting maximum dissolvable oxide thickness is close to 1 nm. For the tests conducted in Chapters 4 and 5, given the crucible and sample dimensions, the calculated values of t_{melt} are 2.7 x 10^4 μm and 2.3 x 10^4 μm, suggesting that the maximum dissolvable oxide, t_{Al2O3}, is greater than 10 nm. While this simple calculation fails to consider the kinetics of Al_2O_3 dissolution, it does provide a thermodynamic basis for the proposed interface formation mechanism in Figure 6-32. It is reasonable to assume that the Al_2O_3 dissolution into the melt will be limited by the transport of dissolved oxygen away from the Al_2O_3/Al_{liquid} interface, as a significant amount of melt, t_{melt}, must become saturated with oxygen in order to dissolve an appreciable amount of Al_2O_3.

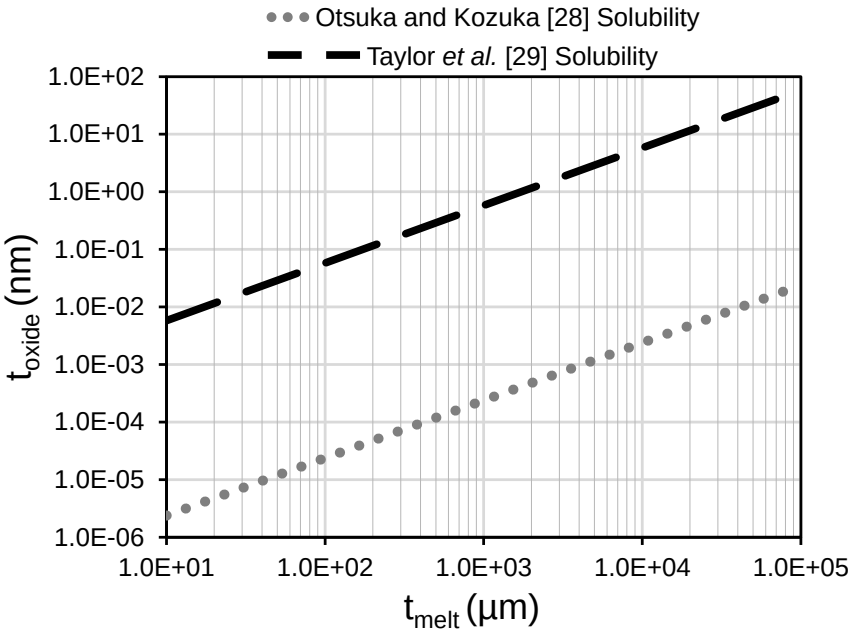

Figure 6-33 – Calculated thickness of Al_2O_3 (t_{oxide}) which can be dissolved by an unsaturated Al-10Si melt above it (t_{melt}) at 933 K (660°C). Oxygen solubility values in liquid Al from Taylor *et al.* [29] (dashed line) and Otsuka and Kozuka [28] (dotted line).

While the diffusivity of oxygen in liquid aluminum has not been reported in the literature, hydrogen diffusivity measurements in aluminum melts have been measured [126-127], due to the

relevance of hydrogen in porosity formation in aluminum castings. Zeng *et al.* [126] measured hydrogen diffusivity in aluminum melts from 973-1003 K (700-730 °C), and reported diffusivities in the range 9.4-10.2 x 10^{-3} cm^2/s. Eichenaueur and Markopoulos [127], give the following relation for hydrogen diffusivity in liquid aluminum, for the temperature range 1053-1274 K (780-1001 °C):

$$D_{H-Al}\left(\frac{cm^2}{s}\right) = (3.8 \times 10^{-2}) \cdot \exp\left(\frac{-4600(cal/mol)}{RT}\right)\left(\frac{cm^2}{s}\right) \quad (6\text{-}6)$$

Making the following assumptions with respect to the diffusivity of oxygen in aluminum:

i. The diffusivity of oxygen in aluminum is approximately equal to that of hydrogen in liquid aluminum (data for diffusivity of O in Al could not be found in the literature).
ii. The diffusivity relation of Eichenaueur and Markopoulos [127] can be extrapolated to temperatures lower than 1053 (780 °C).
iii. The diffusivity of oxygen in Al-10Si is equal to the diffusivity of oxygen in pure liquid aluminum.

The diffusivity of oxygen in Al-10Si at 913 K (640 °C) can then be approximated by using that of Eichenauer and Markopoulos [127] to be:

$$D_{O-Al10Si}\left(\frac{cm^2}{s}\right) = 3.01 \times 10^{-3}\left(\frac{cm^2}{s}\right) \quad (6\text{-}7)$$

Using this value as a first approximation for the oxygen diffusivity in liquid aluminum, it can be shown that typical diffusion distances will be of the order of mm after exposure to an oxygen source (i.e., Al_2O_3 dissolution at the sample/melt interface) for a matter of seconds, substantiating the oxide dissolution mechanism proposed in this thesis.

6.7 Summary

The key observations and results from Chapter 6 were:

i. Mg additions to the Al-1Mn sample alloy composition did not appear to have a positive impact on sample/melt interaction. However, addition of 0.1 wt% Mg to the Al-10Si melt alloy did appear to have a beneficial effect on sample/melt interaction, consistent with similar effects noted from fluxless brazing literature [62].

ii. Test temperature had the largest effect on sample/melt interaction, further supporting the penetration, dissolution and bridging mechanism of interface formation.

iii. Increasing the sample oxide layer thickness prior to test immersion had a similar effect to that in Chapter 5, i.e., increasing the extent of sample oxidation prior to test sample immersion into the melt resulted in a reduced tendency for AA3003 sample dissolution into the melt. Given all the tests performed, only one test condition resulted in minimal interaction with the melt: this was for the highest level of sample oxidation (estimated value 250-275 nm) and sample Mg content (Al-1Mn-0.1Mg). For this test condition, when the sample was immersed into the melt under an argon atmosphere, minimal sample and melt interaction occurred.

iv. Horizontally oriented dry patches were consistently observed on samples. The observed patches were postulated to be an effect of meniscus re-oxidation in the reduced oxygen atmosphere provided by argon cover gas during sample immersion into the melt.

v. In the region below the contact line (on an immersed sample) and above the point where visible dissolution of the sample was observable, Al-10Si liquid was observed to be present beneath the sample oxide layer. This was evidenced by SEM/EDS line scans as well as FIB-SEM sections. Additionally, from FIB-SEM sections, silicon rich aluminum was observed beneath the sample surface oxides, in discrete locations.

vi. The average oxide thickness on test samples, observed in FIB-SEM sections, was less than oxide thickness calculations by a factor of four. Local minimums in oxide thickness, as well as defects in the oxide layer were observed in FIB-SEM sections. Copper decoration experiments suggested that the defect concentration of thin oxide films (formed at room temperature), was greater than those of sample which underwent high temperature oxidation. From the copper decoration experiments, the observed defect density does not appear to go to zero, even after prolonged oxidation at high temperature.

The results from Chapter 6 appear to suggest that the AA3003 oxide penetration mechanism involves an interaction between the oxide and the melt. For thick oxides on Al-1Mn-0.1Mg samples, minimal interaction occurred between the melt and the sample upon immersion into the melt; whereas, the thick oxides grown for Al-1Mn-0.0008Mg samples were penetrable by the Al-10Si melt. Both samples were shown to have defects present after prolonged oxidation, as revealed by copper decoration experiments. Furthermore, the defects resolved during FIB-SEM imaging suggest a defect morphology similar to that proposed by Vermilyea [59], where the oxide is locally thinned at the defect site but not unbroken. It is thus proposed that penetration of the oxide involves a chemical interaction between the surface oxide and the Al-10Si melt. Calculations suggest that Al_2O_3 dissolution at locally thin regions of the oxide (i.e., at oxide defects) could be possible, if the solubility of oxygen in liquid aluminum is closer to the value postulated by Taylor *et al.* [29]. This mechanism for oxide film penetration further suggests that the process could be accelerated by the presence of an active metal in the Al-10Si melt, and is qualitatively consistent with test results from samples immersed in an Al-10Si-0.1Mg melt.

6.8 Practical Applications

Given the results presented in this thesis, see summary Sections 4.8, 5.7, and 6.7, three modifications to the practice of Fusion™ casting AA3003/AA4045 ingots can be made to improve the as-cast interface quality:

i. Use argon cover gas at the AA4045 meniscus with the AA3003 shell.

ii. Increase the heat input or decrease the cooling along the narrow edge of the Fusion™ casting mould.

iii. Use of Mg as a minor alloying element in AA4045 clad alloy to actively reduce the Al_2O_3 oxide on the AA3003 shell, similar to the use of active metal alloying additions in fluxless brazing literature [62].

The use of argon would reduce oxidation at the AA4045 clad alloy meniscus and potentially minimize the effects of entrainment which may occur due to AA4045 liquid metal level fluctuations. An example of how this could be implemented in an industrial Fusion™ casting process is schematically portrayed in Figure 6-34. The figure depicts a section of a Fusion™ casting process, where the core alloy is cast first (i.e., higher melt level), and the clad alloy cast second, similar to AA3003/AA4045 Fusion™ casting. Two "oxide restraints", as previously developed in a separate Novelis patent [18], are used to reduce the likelihood for oxide entrainment at the Fusion™ cast interface. The oxide restraints are typically a refractory material, which can withstand exposure to molten metal. The space between the oxide restraint and the chill bar, under regular Fusion™ casting conditions, is exposed to atmospheric conditions; therefore, oxidation of the core and clap sump surfaces is expected to occur. While the oxide restraints would reduce the likelihood of large/thick oxides becoming entrained at the interface, there still exists a potential for clad and core surface oxides to move/drift towards the

Fusion™ interface and obstruct bond formation when only the "oxide restraints" are utilized. Additionally, the clad meniscus would be prone to oxidation, which could affect wetting and bond formation, similar to what was observed when immersion tests were conducted in air and below the onset of AA3003 remelting, see Section 5.2. By flooding the space between the oxide restraint and the chill bar with argon gas, as shown in Figure 6-34, the rate of surface oxidation on the clad and core sumps could be reduced to a low level. This would also reduce the oxidation of the AA4045 clad meniscus (similar to the effect shown in Section 5.3), and would most likely improve the wetting and bond formation process during Fusion™ casting.

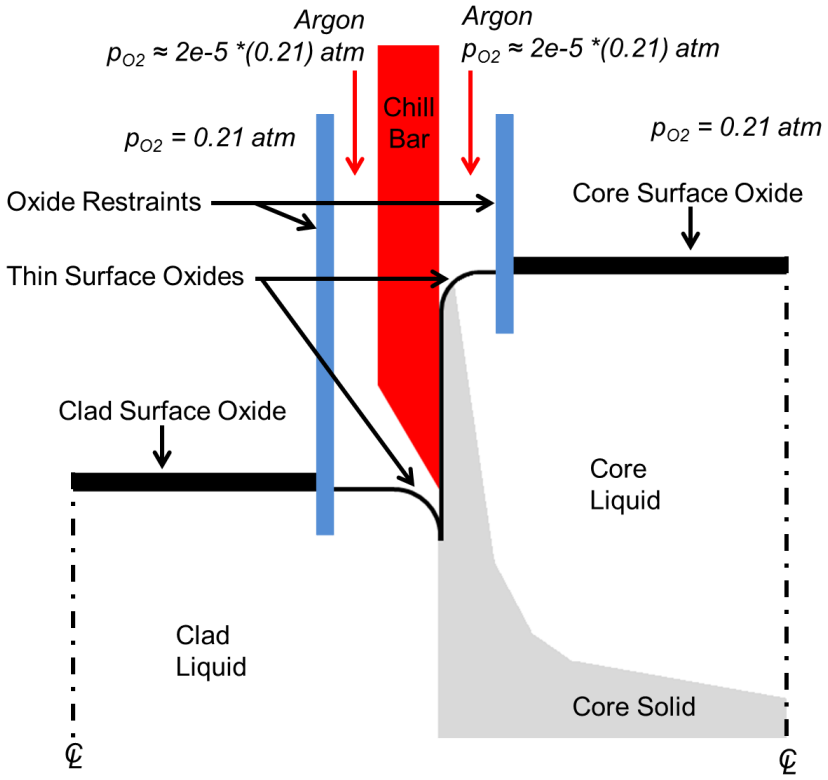

Figure 6-34 – Schematic depicting the implementation of Argon gas injection in conjunction with an oxide restraint [18], to improve the bonding of core and clad alloys during Fusion™ casting.

Increasing the heat input, or decreasing the cooling along the narrow edge of the Fusion™ casting mould, would increase the amount of time that AA4045 liquid remains in contact with the AA3003 shell prior to solidification of the interface should. Observations from Chapter 4

showed that the interface strength is poor at the edges. This correlates well with the reduced time available for bond formation in at the edge, and with the proposed interface formation mechanistic model, which requires dissolution and bridging. By reducing the cooling at the edge, a stronger interface at the edge of the ingot may be achieved. This could potentially be achieved by reducing DC water flow rates along the side edges of a Fusion™ casting mould in the vicinity of the core/clad interface, in order to reduce heat transfer along the narrow edge of a Fusion™ cast ingot. This could be achieved by two methods: (i) tailoring the liquid metal inlet streams to deliver more hot metal to the edges of the ingot as opposed to the centre of the ingot, and (ii) reducing the secondary cooling rates along the narrow edge of the ingot. This can be done by reducing the water spray along the narrow edge of the ingot; either by increasing the hole spacing along the narrow edge of the mould or reducing the hole size along the narrow edge of the mould.

The presence of dissolved Mg in the AA4045 melt should aid in disruption the AA3003 surface oxide and promote interface formation. The test results in Section 6.3 suggest that somewhere between 0.01 wt% Mg and 0.1 wt% Mg in the AA4045 could prove to be beneficial to bond formation during Fusion™ casting.

Chapter 7

Conclusions and Recommendations

7.1 Conclusions

During lab-scale Fusion™ casting trials, it was found that AA4045-clad melt could successfully wet and form a metallurgical and mechanically sound interface with the oxidized AA3003-core shell. The interface formation process was hypothesized to be a result of discrete penetration of AA4045 liquid through the AA3003 oxide at oxide defect sites followed by dissolution of the underlying solid AA3003 by the liquid AA4045 and subsequent bridging between discrete penetration sites. The primary conclusions from this thesis with respect to interface formation are as follows:

i. Wetting and interface formation was facilitated by the oxide motion on the AA4045 sump and the AA3003 sump, providing a means for clean contact between the AA4045 liquid sump and the AA3003 solid shell.

ii. Oxides are present on the AA3003-core alloy shell surface prior to it coming into contact with AA4045-clad alloy liquid; however, these oxides were not always a barrier to wetting and bonding at the AA3003/AA4045 interface.

iii. In the case of Fusion™ casting, spot exudation on the AA3003 chill cast surface improved the wetting and bonding process by providing macroscopic oxide defects along the chill cast surface that facilitated penetration of the AA4045 liquid through the oxide and into the AA3003.

iv. The mechanical integrity of the as-cast interface was strongly influenced by the liquid AA4045 contact time at the interface prior to interface solidification as well as the average interface temperature during this period of liquid contact.

Analog/immersion tests proved to be a straightforward and simple means to test wetting and bonding between dissimilar aluminum alloys. Providing an adequately inert atmosphere is maintained in the furnace during sample immersion into the melt, the sample surface oxide appears to be permeable to AA4045 melts. It was proposed that oxide penetration is the result of Al_2O_3 dissolution at locally thin regions of the oxide by the melt. The conclusions derived from these analog/immersion tests and subsequent sample analyses are:

i. Remelting of the AA3003 surface was not a necessary requirement for wetting and bonding to occur between the AA3003 core alloy and AA4045 clad alloy.

ii. The surface oxides on AA3003 and Al-1Mn test samples could be penetrated by AA4045 and Al-10Si melts, respectively.

iii. Mg additions in the range 0.01 to 0.1 wt% to Al-10Si melts accelerated the wetting and bonding process between Al-1Mn test samples and Al-10Si melts.

The results contained within this thesis were used to develop a set of practical changes which can be made to the Fusion™ casting process, as a means to improve the quality of as-cast AA3003-core/AA4045-clad ingot interfaces, specifically:

i. Use argon cover gas at the AA4045 meniscus with the AA3003 shell.

ii. Increase the heat input or decrease the cooling along the narrow edges of the Fusion™ casting mould.

iii. Addition of small amounts of Mg as a minor alloying element in the AA4045 clad alloy melt to actively reduce the Al_2O_3 oxide on the AA3003 shell, similar to the use of active metal alloying additions in fluxless brazing literature [62].

7.2 Recommendations for future work

The recommendations for future work are divided below into two categories: applied studies related specifically to the Fusion™ casting process and academic studies related to aluminum oxidation and joining of aluminum at high temperatures.

Recommendations for applied studies related specifically to the Fusion™ casting process:

i. Studies regarding the interface quality of commercial scaleFusion™ cast ingots. It should be noted that the results presented in Chapter 4 were done on a laboratory scale Fusion™ caster. In actuality, commercial cast Fusion™ ingots are larger in size, see Table 1-1. It would be of interest to study the as-cast interfaces of commercially cast ingots, to determine if ingot size effects interface quality. Additionally, the casting methods and techniques for Fusion™ casting commercial ingots do differ from the methods used in Chapter 4. Specifically, the degree of automation and control on casting parameters such as: clad and core alloy melt temperatures, sump level and flow control of liquid into the sump, casting speed, and cooling water temperature during commercial Fusion™ casting is significantly better in comparison to the laboratory scale Fusion™ caster. The ability to more tightly control the casting process parameters during commercial Fusion™ casting would be useful in determining the effect of casting process parameters on as-cast interface quality, something that could not be achieved with the laboratory scale Fusion™ casting machine in this thesis.

ii. Studies involving the homogenization, hot rolling, and cold rolling on Fusion™ cast ingots, with special focus on the evolution of the interfacial structure and overall microstructure of the Fusion™ product. Since all Fusion™ ingots must be processed to sheet form at some point, studying the evolution of the interfacial structure and overall microstructure of a Fusion™ cast ingot during homogenization, hot rolling, and cold rolling would be a topic worthy of further research.

Recommendations for studies related to aluminum oxidation and joining of aluminum at high temperatures:

i. Studies regarding defect characterization of thermal oxide films of aluminum alloys. The proposed mechanism of oxide penetration and bond formation discussed in Section 6.6, suggests that defects in thermal oxides play a major role in the process and that there is some reactivity which exists between Al_2O_3 and aluminum liquid. As the mechanism proposed in Section 6.6 was not definitely proven in this thesis, it would be of academic interest to further study and characterize defects in thermal oxide films of aluminum and to study the reactivity between Al_2O_3 and liquid aluminum.

ii. Studies regarding oxidation of aluminum alloys under non-isothermal conditions. As shown in the results presented in Section 6.5.1, there was significant discrepancy between the observed oxide thickness (using FIB-SEM measurements) and estimated oxide thickness (using oxidation calculations) for AA3003 test samples. The major contributing factor for this discrepancy may have been due to the fact that oxidation rate data (i.e., oxidation kinetic constants) in the literature are measured from tests which are typically performed using isothermal test conditions. This is achieved by heating test samples to their respective set-point temperatures in a high vacuum environment, then

admitting oxygen into the system once the sample temperature has been stabilized. Thus, all oxidation takes place at one temperature. In scenarios where aluminum is subject to oxidation during its heating cycle, the use of isothermal oxidation rate kinetics may not be appropriate; therefore, studies related to the non-isothermal oxidation of aluminum may be of future interest.

iii. Studies to explore the use of alloying additions, other than Mg, to the clad melt that might also be used for actively reducing the Al_2O_3 oxide on the core alloy shell during Fusion™ casting. The results in Section 6.3 suggested that that it was beneficial to add Mg as an alloying addition to the melt, as it promoted wetting and interface formation between the Al-10Si melt and the Al-1Mn test sample From the fluxless brazing research of Terrill *et al.* [62], other metals could potentially be used to achieve the same result, including: La, Ce, Pr, Nd, Sm, Li, Be, Ca, and Sr. Future research involving other alloying elements may be of interest.

References

[1] Dix, E.H. Jr., " 'Alclad': a new corrosion resistant aluminum product", National Advisory Committee for Aeronautics, Technical note no. 259, Washington, 1927.

[2] Dix, E.H. Jr., "Corrosion-resistant aluminum alloy articles and method of making them the same", US Patent Office, Patent Number 1,856,089, June 28, 1932.

[3] Nock, J.A. Jr., "Properties of Commercial Wrought Alloys", in Aluminum Processing and Physical Metallurgy, Hatch, J.E. (Ed.), ASM International, Materials Park, OH, 1984, p. 372.

[4] Papich, K., Bachowski, R., Baumann, S.F., Cargnel, R.A., Carkin, G.E., Clements, D.J., Gunkel, R.W., Hoffman, W.W., McKinney, L.G., Pajerski, A.V., Palko, J.P., Patrick, E.P. Jr., Rennekamp, S.J., Scheble, P.C., Sharkins, W.R., Swigon, F.P. and Truckner, W.G., "Clad Metallurgical Products and Methods of Manufacture", US Patent. US 1995-5,776,725, December 19, 1995.

[5] Kutsuna, M., "Roll Welding and Laser Welding", in ASM Handbook: Volume 6A: Welding Fundamentals and Processes, ASM International, Materials Park, OH, 2011, pp. 717-724.

[6] Liu, J., Li, M., Shen, S., Karabin, M.E. and Schultz, R.W., "Macro- and micro-surface engineering to improve hot roll bonding of aluminum plate and sheet", Materials Science and Engineering A, Vol. 479, 2008, pp. 45-57.

[7] Brown, R.H., "Aluminum Alloy Laminates: Alcald and Clad Aluminum Alloy Products", in Composite Engineering Laminates, Dietz, A.G.H. (Ed.), The MIT Press, Cambridge, MA, 1969.

[8] Sugiyama, Y., "Brazing of Aluminum Alloys", Welding International 1989, No. 8, pp. 700-710.

[9] Anderson, M.D., Kubo, K.T., Bischoff, T.F., Fenton, W.J, Reeves, E.W., Spendlove, B. and Wagstaff, R.B., "Method for Casting Composite Ingot", US Patent. US 2005-0011630 A1, January 20, 2005.

[10] Grandfield, J.F. and McGlade, P.T., "DC casting of Aluminium: Process Behaviour and Technology", Materials Forum (Australia), Vol. 20, 1996, pp. 29-51.

[11] Emley, E.F., "Continuous casting of aluminum", International Metals Reviews, Vol. 21, 1976, pp. 75-11.

[12] Rooy, E., "Aluminum Alloy Ingot Casting and Continuous Processes", in ASM Handbook Volume 15: Casting, ASM International, Materials Park, OH, 2008, pp. 1001–1008.

[13] Adenis, D.J.-P., Coats, K.H. and Ragone, D.V., "An Analysis of the Direct-Chill-Casting Process by Numerical Methods", Journal of the Institute of Metals, Vol. 91, 1963, pp. 395-403.

[14] Lloyd, D.J., Gallerneault, M. and Wagstaff, R.B., "The Deformation of Clad Aluminum Sheet Produced by Direct Chill Casting", Metallurgical and Materials Transactions A, Vol. 41A, August 2010, pp. 2093-2103.

[15] Gupta, A., Lee, S.T., Wagstaff, R.B., Gallerneault, M. and Fenton, W.J., "The Distribution of Magnesium and Silicon Across the As-Cast Interface of Aluminum Laminates Produced Via the Novelis Fusion Process", JOM, August 2007, pp. 62-65.

[16] Wagstaff, R.B., Lloyd, D.J. and Bischoff, T.F., "Direct Chill Casting of CLAD Ingot", Materials Science Forum, Vols. 519-521, 2006, pp. 1809-1814.

[17] Marshall, G.J., Bolingbroke, R.K. and Gray, A.; "Microstructural Control in an Aluminum Core Alloy for Brazing Sheet Applications", Metallurgical Transactions A, Vol. 24A, 1993, pp. 1935-1942.

[18] Bischoff, T.F., Womack, R., Fenton, W.J., Wagstaff, R.B. and Hudson, L.G.: U.S. Patent No. 8336603, U.S. Patent and Trademark Office, Washington, DC, 2009.

[19] Wagstaff, R.G., Bischoff, T.F. and Sinden, D., "Downstream Considerations of Fusion Casting Clad", Materials Science Forum, Vol. 630, October 2009, pp. 175-178.

[20] Hawksworth, D.K., "Fluxless brazing of aluminum", in Advances in brazing, Sekulic, D.P. (Ed.), Woodhead Publishing, Philadelphia, PA, 2013, pp. 566-586.

[21] Baserinia, A. R., Caron, E. J., Wells, M. A., Weckman, D. C., Barker, S. and Gallerneault, M., "A numerical study of the direct-chill co-casting of aluminum ingots via Fusion™ technology", Metallurgical and Materials Transactions B, Vol. 44B, No. 4, 2013, pp. 1017-1029.

[22] Caron, E. J., Pelayo, R. E. O., Baserinia, A. R., Wells, M. A., Weckman, D. C., Barker, S. and Gallerneault, M., "Direct-Chill Co-Casting of AA3003/AA4045 Aluminum Ingots via Fusion™ Technology", Metallurgical and Materials Transactions B, Vol. 45B, No. 3, 2014, pp. 975-987.

[23] Craighead, C.M., Cawthorne, E.W. and Jaffee, R.I., "Solution rate of solid aluminum in molten Al-Si alloy", Journal of Metals, Vol. 7, 1955, pp. 81-87.

[24] Wefers, K. and Misra, C., "Oxides and Hydroxides of Aluminum", Alcoa Technical Paper Number 19 Revised, Alcoa Laboratories, 1987.

[25] Wriedt, H.A., "The Al-O (Aluminum-Oxygen) System", Journal of Phase Equilibria, Vol. 6, No. 6, 1985, pp. 548-553.

[26] Wefers, K., "Properties and characterization of surface oxides on aluminum alloys", Aluminum, Vol. 57, 1981, pp. 722-726.

[27] Chase, M.W. Jr., "NIST-JANAF Themochemical Tables", Fourth Edition, Journal of Physical and Chemical Reference Data, Monograph 9, 1998.

[28] Otsuka, S. and Kozuka, Z., "Thermodynamic study of oxygen in liquid elements of Group Ib to VIb", Transactions of the Japan Institute of Metals, Vol. 22, No. 8, 1981, pp. 558-566.

[29] Taylor, J.R., Dinsdale, A.T., Hillert, M. and Selleby, M., "A Critical Assessment of Thermodynamic and Phase Diagram Data for the Al-O System", Calphad, Vol. 16, No. 2, 1992, pp. 173-179.

[30] Fitzner, K., "Prediction of thermodynamic properties of oxygen in liquid transition metals", Thermochimica Acta, Vol. 52, No. 1, 1982, pp. 103-111.

[31] San-Martin, A. and Manchester, F.D., "The Al-H (aluminum-hydrogen) system", Journal of Phase Equilibria, Vol. 13, No. 1, 1992, pp. 17-21.

[32] Krueger, Wm. H. and Pollack, S.R., "The Initial Oxidation of Aluminum Thin Films at Room Temperature", Surface Science, Vol. 30, 1972, pp. 263-279.

[33] Stucki, F., Erbudak, M. and Kostorz, G., "The initial oxidation of solid and liquid aluminium", Applied surface science, Vol. 27, No. 4, 1987, pp. 393-400.

[34] Jeurgens, L. P. H., Sloof, W. G., Tichelaar, F. D. and Mittemeijer, E. J., "Structure and morphology of aluminium-oxide films formed by thermal oxidation of aluminium", Thin solid films, Vol. 418, No. 2 2002, pp. 89-101.

[35] Jeurgens, L.P.H., Sloof, W.G., Tichelaar, F.D. and Mittemeijer, E.J., "Growth Kinetics and Mechanisms of Aluminum-Oxide Films Formed by Thermal Oxidation of Aluminum", Journal of Applied Physics, Vol. 92, No. 3, 2002, pp. 1649-1656.

[36] Gulbransen, E.A. and Wysong, W.S., "Thin oxide films on aluminum", The Journal of Physical Chemistry, Vol. 51, No. 5, 1947, pp. 1087-1103.

[37] Smeltzer, W.W., "Oxidation of Aluminum in the Temperature Range 400°C-600°C", Journal of the Electrochemical Society, Vol. 103, No. 4, 1956, pp. 209-214.

[38] Beck, A.F., Heine, M.A., Caule, E.J. and Pryor, M.J., "The Kinetics of the Oxidation of Al in Oxygen at High Temperatures", Corrosion Science, Vol. 7, 1967, pp. 1-22.

[39] Brock, A. J. and Pryor, M.J., "The kinetics of the oxidation of aluminum—copper alloys in oxygen at high temperature", Corrosion Science, Vol. 13, No. 3, 1973, pp. 199-227.

[40] Tenório, J.A.S. and Espinosa, D.C.R., "High-Temperature Oxidation of Al-Mg Alloys", Oxidation of Metals, Vol. 53, No. 3-4, 2000, pp. 361-372.

[41] Drouzy, M. and Mascré, C., "The oxidation of liquid non-ferrous metals in air or oxygen", Metallurgical Reviews, Vol. 14, 1969, pp. 25-46

[42] Thiele, W., "The Oxidation of Melts of Aluminum and Aluminum Alloys", Aluminum, Vol. 38, No. 12, 1962, pp. 707-715.

[43] Impey, S.A., Stephenson, D.J. and Nicholls, J.R., "Mechanism of Scale Growth on Liquid Aluminum", Materials Science and Technology, Vol. 4, 1988, pp. 1126-1132.

[44] Impey, S., Stephenson, D.J. and Nicholls, J.R., "A Study of the Effect of Magnesium Additions on the Oxide Growth Morphologies on Liquid Aluminum Alloys", 1st International Conference on the Microscopy of Oxidation, Bennett M.J. and Lorimer G.W. (Eds.), The Institute of Materials, Minerals and Mining, Cambridge, UK, March 1990, pp. 238-244.

[45] Impey, S., Stephenson, D.J. and Nicholls, J.R., "The Influence of Surface Preparation and Pretreatments on the Oxidation of Liquid Aluminum and Aluminum-Magnesium Alloys", 2nd International Conference on the Microscopy of Oxidation, Newcomb S.B. and Bennett M.J. (Eds.), The Institute of Materials, Minerals and Mining, Cambridge, UK, March 1993, pp. 323-337.

[46] Silva, M.P. and Talbot, D.E.J., "Oxidation of liquid aluminum-magnesium alloys", Light Metals 1989, Campbell P.G. (Ed.), The Minerals, Metals & Materials Society, Las Vegas, Nevada, 1988, pp. 1035-1040.

[47] Kofstad, P., High Temperature Corrosion, Elsevier Applied Science Publishers, Crown House, Essex, UK, 1988.

[48] Gourmiri, L. and Joud, J.C., "Auger Electron Spectroscopy Study of Aluminum-Tin Liquid System", Acta Metallurgica, Vol. 30, 1982, pp. 1397-1405.

[49] Molina, J.M., Voyotovych, R., Louis, E. and Eusthathopoulos, N., "The surface tension of liquid aluminum in high vacuum: The role of surface condition", International Journal of Adhesion & Adhesives, Vol. 27, 2007, pp. 394-401.

[50] Laurent, V., Chatain, D., Chatillon, C. and Eustathopoulos, N., "Wettability of monocrystalline alumina by aluminium between its melting point and 1273 K", Acta Metallurgica, Vol. 36, No. 7, 1988, pp. 1797-1803.

[51] Wang, D.-J. and Wu, S.-T., "The influence of oxidation on the wettability of aluminum on sapphire", Acta Metallurgica et Materialia, Vol. 42, No. 12, 1994, pp. 4029-4034.

[52] Bao, S., Tang, K., Kvithyld, A., Tangstad, M. and Engh, T.A., "Wettability of Aluminum on Alumina", Metallurgical and Materials Transactions B, Vol 42B, No. 6, 2011, pp. 1358-1366.

[53] Wall, A.J. and Milner, D.R., "Wetting and Spreading Phenomena in a Vacuum", Journal of the Institute of Metals, Vol. 90, 1961-62, pp. 394-402.

[54] Zähr, J., Ullrich, H.J., Oswald, S., Türpe, M. and Füssel, U., "Analyses about the influence of the natural oxide layer of aluminium on the brazeability in a shielding gas furnace", Welding in the World, Vol. 57, No. 4, 2013, pp. 449-455.

[55] Shimizu, K., Brown, G. M., Kobayashi, K., Skeldon, P., Thompson, G. E. and Wood, G. C., "Ultramicrotomy—a route towards the enhanced understanding of the corrosion and filming behaviour of aluminium and its alloys", Corrosion science, Vol. 40, No. 7, 1998, pp. 1049-1072.

[56] Shimizu, K., Brown, G. M., Kobayashi, K., Skeldon, P., Thompson, G.E. and Wood, G.C., "The early stages of high temperature oxidation of an Al-0.5 wt% Mg alloy", Corrosion science, Vol. 40, No. 4, 1998, pp. 557-575.

[57] Hart, R.K. and Maurin, J.K., "The Nucleation and Growth of Oxide Islands on Aluminum", Surface Science, Vol. 20, No. 2, 1970, pp. 285-303.

[58] Richardson, J.A., Wood, G.C. and Sutton, W.H., "The Interpretation of Impedance Measurements on Oxide-Coated Aluminum Part 2: The Effect of Flaws in as Formed Films", Thin Film Solids, Vol. 16, No. 1, 1973, pp. 99-116.

[59] Vermilyea, D. A., "Flaws in Anodic Ta_2O_5 Films", Journal of the Electrochemical Society, Vol. 110, No. 4, 1963, pp. 250-262.

[60] Eubanks, A. G., Moore, D. G. and Pennington, W. A., "Effect of Surface Roughness on the Oxidation Rate of Iron", Journal of The Electrochemical Society, Vol. 109, No. 5, 1962, pp. 382-389.

[61] Shimizu, K., Brown, G. M., Habazaki, H., Kobayashi, K., Skeldon, P., Thompson, G.E. and Wood, G.C., "Impurity distributions in barrier anodic films on aluminium: a GDOES depth profiling study", Electrochimica Acta, Vol. 44, No. 13, 1999, pp. 2297-2306.

[62] Terrill, J. R., Cochran, C. N. and Stokes, J.J., "Understanding the mechanisms of aluminum brazing", Welding Journal, Vol. 50, No. 12, 1971, pp 833-839.

[63] Holub, K. J. and Matienzo, L.J., "Magnesium diffusion in several aluminum alloys", Applications of Surface Science, Vol. 9, No. 1, 1981, pp. 22-38.

[64] Nylund, A., Mizuno, K. and Olefjord, I., "Influence of Mg and Si on the Oxidation of Aluminum", Oxidation of Metals, Vol. 50, No. 3-4, 1998, pp. 309-325.

[65] Creber, D. K., Ball, J. and Field, D.J., "A mechanistic study of aluminum vacuum brazing", No. 870185, SAE Technical Paper, 1987.

[66] Ohashi, O. and Sasabe, K., "Effect of alloying elements on the behaviour of oxide films at diffusion-welded interfaces of aluminium alloys-Study of surface films at diffusion-welded interfaces (Report 4)", Welding International, Vol. 4, No. 10, 1990, pp. 775-780.

[67] Lumley, R. N., Sercombe, T. B. and Schaffer, G.M., "Surface oxide and the role of magnesium during the sintering of aluminum", Metallurgical and Materials Transactions A, Vol. 30, No. 2, 1999, pp. 457-463.

[68] McLeod, A. D. and Gabryel, C. M., "Kinetics of the growth of spinel, $MgAl_2O_4$, on alumina particulate in aluminum alloys containing magnesium", Metallurgical Transactions A, Vol. 23, No. 4, 1992, pp. 1279-1283.

[69] ASM Specialty Handbook Aluminum and Aluminum Alloys. ASM International, Materials Park, OH, USA, 1993.

[70] McAlister, A.J. and Murray, J.L., "The (Al-Mn) Aluminum-Manganese System", Journal of Phase Equilibria, Vol. 8, No. 5, 1987, pp. 438-447.

[71] Bäckerud, L., Krol, E. and Tamminen, J., Solidification Characteristics of Aluminium Alloys, Vol. 1: Wrought Alloys, SkanAluminium, Olso, Sweden,1986.

[72] FactSage™, Version 6.1, Thermfact and GTT-Technologies. (1976–2007)

[73] Baserinia, A., personal communication, University of Waterloo, Waterloo, Ontario, 2011.

[74] Chen, S.-W. and Jeng, S.-C., "Determination of the Solidification Curves of Commercial Aluminum Alloys", Metallurgical and Materials Transactions A, Vol. 27A, 1996, pp. 2722-2726.

[75] McAlister, A.J. and Murray, J.L., "The (Al-Si) Aluminum-Silicon System", Journal of Phase Equilibria, Vol. 5, No. 1, 1984, pp. 74-84.

[76] Bäckerud, L., Chai, G. and Tamminen, J., Solidification Characteristics of Aluminium Alloys, Vol. 2: Foundry Alloys, AFS/SkanAluminium, Des Plaines, Illinois, 1990.

[77] Elliot, R., Eutectic Solidification Processing: Crystalline and Glassy Alloys, Butterworths & Co. Ltd., London, UK, 1983.

[78] Dantzig, J.A. and Rappaz, M., Solidification, EPFL Press, Lausanne, Switzerland, 2009.

[79] Benum, S., Håkonsen, A., Hafsås, J.E. and Sivertsen, J., "Mechanisms of surface formation during direct chill (DC) casting of extrusion ingots", Light Metals 1999, Eckert C.E. (Ed.), The Minerals, Metals & Materials Society, 1999, pp. 737-742.

[80] Collins, D.L.W., "A New Explanation of the Surface Structures of DC Ingots", Metallurgia, October 1967, pp. 137-144.

[81] Morishita, M., Nakayama, K., Tokuda, K. and Yoshikawa, K., "Laboratory Study of Cast Surface Structure Evolution II. Macro Air Gap Stage", Light Metals 2000, Peterson R.D. (Ed.), The Minerals, Metals & Materials Society, Nashville, Tennessee, 2000, pp. 657-662.

[82] McGurran, B. and Nicholas, M.G., "A Study of Aluminum Brazes Using Hot-Stage Scanning Electron Microscopy", Journal of Materials Science, Vol. 19, 1984, pp. 2713-2718.

[83] Ng, H., MASc thesis, University of Waterloo, Waterloo, ON, Canada, 2010.

[84] Barker, S., personal communication, February 15, 2012.

[85] Ortega Pelayo, R.E., MASc thesis, University of Waterloo, Waterloo, ON, Canada, 2012.

[86] Aliravci, C.A. and Pekgüleryüz, M.Ö., "Calculation of phase diagrams for the metastable Al-Fe phases forming in direct-chill (DC)-cast aluminum alloy ingots", Calphad, Vol. 22, No. 2, 1998, pp. 147-155.

[87] ASTM Standard B557-10, "Standard Test Methods for Tension Testing Wrought and Cast Aluminum- and Magnesium-alloy Products", ASTM International, 2010.

[88] ASTM Standard E8/E8M-11, "Standard Test Methods for Tension Testing of Metallic Materials", ASTM International, 2011.

[89] Bennon, W. D. and Incropera F. P., "A continuum model for momentum, heat and species transport in binary solid-liquid phase change systems—I. Model formulation," International Journal of Heat and Mass Transfer, Vol. 30, No. 10, 1987, pp. 2161-2170.

[90] Weckman, D. C. and Niessen, P., "A numerical simulation of the DC continuous casting process including nucleate boiling heat transfer," Metallurgical transactions B, Vol. 13, No. 4, 1982, pp. 593-602.

[91] LabVIEW 2012 (v12.0f3). Austin Texas: National Instruments Corporation, 2012.

[92] Hebert, K.R., Wu, H., Gessmann, T. and Lynn, K., "Positron Annihilation Spectroscopy Study of Interfacial Defects Formed by Dissolution of Aluminum in Aqueous Sodium Hydroxide", Journal of the Electrochemical Society, Vol. 148, No. 2, 2001, pp. B92-B100.

[93] Adhikari, S., Lee, J. and Hebert, K.R., "Formation of Aluminum Hydride during Alkaline Dissolution of Aluminum", Journal of the Electrochemical Society, Vol. 155, No. 1, 2008, pp. C16-C21.

[94] Waldo, R.A., Militello, M.C. and Gaarenstroom, S.W., "Quantitative thin-film analysis with an energy-dispersive x-ray detector", Surface and Interface Analysis, Vol. 20, No. 2. 1993, pp. 111–114.

[95] Wirth, R., "Focused Ion Beam (FIB) combined with SEM and TEM: Advanced analytical tools for studies of chemical composition, microstructure and crystal structure in geomaterials on a nanometre scale," Chemical Geology, Vol. 261, No. 3, 2009, pp. 217-229.

[96] Baserinia, A.R., Ng, H., Weckman, D.C. and Wells, M.A., "A simple model of the mold boundary condition in direct-chill (DC) casting of aluminum alloys," Metallurgical and Materials Transactions B, Vol 43, No. 4, 2012, pp. 887-901.

[97] Brody, H.D. and Flemings, M.C., "Solute Redistribution in Dendritic Solidification", Transactions of the Metallurgical Society of AIME, Vol. 236, May 1966, pp. 615-624.

[98] Combeau, H., Drezet, J.-M., Mo, A. and Rappaz, M., "Modeling of microsegregation in macrosegregation computations," Metallurgical and Materials Transactions A, Vol. 27, No. 8, 1996, pp. 2314-2327.

[99] Rappaz, M. and Voller, V., "Modeling of micro-macrosegregation in solidification processes," Metallurgical and Materials Transactions A, Vol. 21, No. 2, 1990, pp. 749-753.

[100] ASTM Standard D3418-12, "Standard Test Method for Transition Temperatures and Enthalpies of Fusion and Crystallization of Polymers by Differential Scanning Calorimetry", ASTM International, 2012.

[101] ASTM Standard E967-08 (Re-approved 2014), "Standard Test Method for Temperature Calibration of Differential Scanning Calorimeters and Differential Thermal Analyzers", ASTM International, 2014.

[102] Gali, O. A., Riahi, A. R. and Alpas, A. T., "The tribological behaviour of AA5083 alloy plastically deformed at warm forming temperatures", Wear, Vol. 302, No. 1, 2013, pp. 1257-1267.

[103] Davis, J.L. and Mendez, P.F., "Wrinkling Phenomena to Explain Vertical Fold Defects in DC-Cast Al-Mg4.5", Light Metals 2008, DeYoung, D.H. (Ed.), The Minerals, Metals & Materials Society, New Orleans, Louisiana, 2008, pp. 733-748.

[104] Niederberger, Ch., Michler, J. and Jacot, A., "Origin of intragranular crystallographic misorientations in hot-dip Al–Zn–Si coatings", Acta Materialia, Vol. 56, No. 15, 2008, pp. 4002-4011.

[105] Cohen, J. M., Castle J. E. and Waldron, M. B., "High-temperature observations of braze alloy spreading by oxide penetration," Metal Science, Vol. 15, No.10, 1981, pp. 455-462.

[106] Dutta, B. and Rettenmayr, M., "An Experimental Investigation on the Kinetics of Solute Driven Remelting", Metallurgical and Materials Transactions A, Vol. 31A, 2000, pp. 2713-2720.

[107] Craighead, C.M., Cawthorne, E.W. and Jaffee, R.I., "Solution Rate of Solid Aluminum in Molten Al-Si Alloy", Journal of Metals, Vol. 7, 1955, pp. 81-87.

[108] Yin, L., Murray, B.T. and Singler, T.J., "Dissolutive Wetting in the Bi-Sn System", Acta Materialia, Vol. 54, 2006, pp. 3561-3574.

[109] Sekulic, D. P., Galenko, P.K., Krivilyov, M.D., Walker, L. and Gao, F., "Dendritic growth in Al–Si alloys during brazing. Part 1: Experimental evidence and kinetics", International journal of heat and mass transfer, Vol. 48, No. 12, 2005, pp. 2372-2384.

[110] DeVore, J.L., Probability and Statistics for Engineering and the Sciences, 5th Edition, Duxbury Press, Pacific Grove, CA, 2000.

[111] Hertzberg, R.W., Deformation and Fracture Mechanics of Engineering Materials, 4th Edition, John Wiley and Sons, New York City, NY, 1996.

[112] Bay, N., "Cold Welding", in ASM Handbook: Volume 6A: Welding Fundamentals and Processes, ASM International, Materials Park, OH, 2011, pp. 711-716.

[113] Silva, M. P. "Oxidation of Aluminium-Magnesium alloys at elevated temperature in the solid, semi-liquid and liquid states," Brunel University School of Engineering and Design PhD Thesis, Uxbridge, UK,1987.

[114] Hajjari, E., Divandari, M., Razavi, S. H., Emami, S. M., Homma, T. and Kamado, S., "Dissimilar joining of Al/Mg light metals by compound casting process," Journal of materials science, Vol. 46, No. 20, 2011, pp. 6491-6499.

[115] Ritchie, I.M., Sanders, J.V. and Weickhardt, P.L., "Oxidation of a Dilute Aluminum Magnesium Alloy", Oxidation of Metals, Vol. 3, No. 1, 1971, pp. 91-101.

[116] Goldstein, B. and Dressner, J., "Growth of MgO Films with High Secondary Emission on Al-Mg Alloys," Surface Science, Vol. 71, 1978, pp.15-26.

[117] Kimura, A., Shibata, M., Kondoh, K., Takeda, Y., Katayama, M., Kanie, T. and Takada, H., "Reduction mechanism of surface oxide in aluminum alloy powders containing magnesium studied by x-ray photoelectron spectroscopy using synchrotron radiation," Applied physics letters, Vol. 70, No. 26, 1997, pp. 3615-3617.

[118] Eubanks, A.G. and Moore, D.G., "Effect of Surface Roughness on the Oxidation Rate of Iron", Journal of the Electrochemical Society, Vol, 109, No. 5, 1962, pp. 382-389.

[119] de Haan, P.C.M., van Rijkom, J. and Söntgerath, J.A.H., "The Precipitation Behaviour of High-Purity Al-Mn Alloys", Materials Science Forum, Vols. 217-222, 1996, pp. 765-770.

[120] Mondolfo, L.F., "Aluminum-Managese Alloys", in Aluminum Alloys: Structure and Properties: Volume 5. Butterworths Publishing, London, UK, 1976, pp. 834-841.

[121] Sanders, R. E., Baumann, S. F. and Stumpf, H. C., "Wrought non-heat treatable aluminum alloys," Treatise in Materials Science & Technology, Vol. 31, 2012, pp. 65-105.

[122] Li, Y. J. and Arnberg L., "Quantitative study on the precipitation behavior of dispersoids in DC-cast AA3003 alloy during heating and homogenization," Acta Materialia, Vol. 51, No. 12, 2003, pp. 3415-3428.

[123] Xu, Z., Yan, J., Zhang, B., Kong, X. and Yang, S., "Behaviors of oxide film at the ultrasonic aided interaction interface of Zn-Al alloy and Al_2O_3/6061Al composites in air", Materials Science and Engineering A, Vol. 415, 2006, pp. 80-86.

[124] Chen, X., Yan, J., Gao, F., Wei, J., Xu, Z. and Fan, G., "Interaction behaviors at the interface between liquid Al-Si and solid Ti-6Al-4V in ultrasonic-assisted brazing in air", Ultrasonics Sonochemistry, Vol. 20, 2000, pp. 144-154.

[125] Mills, K.C., Recommended Values of Thermophysical Properties for Selected Commercial Alloys. Woodhead Publishing Limited, Abington Hall, Cambridge, UK, 2002.

[126] Zeng, J.M., Tang, L.W. and Lin, S.Y., "Experimental Study on Hydrogen Diffusion in Molten Aluminum", Reviews on Advanced Materials Science, Vol. 33, 2013, pp. 257-260.

[127] Eichenaueur, W. and Markopoulos, J., "Measurement of the Diffusion Coefficients of Hydrogen in Liquid Aluminum", Zeitschrift für Metallkunde, Vol. 65, 1974, pp. 649-652.

[128] MATLAB R2014a. Natick, Massachusetts: The Mathworks Incorporated, 2014.

[129] Samsonov, G.V., The Oxide Handbook, Plenum, New York, 1973.

[130] Murray, J.L., "The Al− Mg (Aluminum− Magnesium) system", Bulletin of Alloy Phase Diagrams, Vol. 3, No.1, 1982, pp. 60-74.

[131] Brown, J. A. and Pratt, J. N., "The thermodynamic properties of solid Al− Mg alloys", Metallurgical Transactions, Vol. 1, No.10, 1970, pp. 2743-2750.

Appendix A

Tests performed prior to use of interface formation test apparatus

Verification of furnace purging system

Prior to running interface formation tests, the adequacy of the purging system was verified. To determine the quality of the seal at the bottom of the furnace, and the purge rate required to adequately flush the furnace, the oxygen concentration of the furnace was measured during purging of the furnace at 488 K (215 °C). With a purge rate of 0.226 m^3h^{-1} (8 scfh), the oxygen content of the furnace was measured by insertion of a Honeywell O_2 sensor (Honeywell: Oxygen Sensor, GMS-10). The results of the test are shown in Figure A-1. It should be noted that the minimum oxygen pressure of the sensor is 200 Pa (2 mbar) is slightly higher than the expected oxygen partial pressure of the purge gas being used. However; by considering the results in Figure A-1, the assumption can be made that a purge rate of 0.226 m^3h^{-1} (8 scfh) can be used to successfully purge the furnace of residual air.

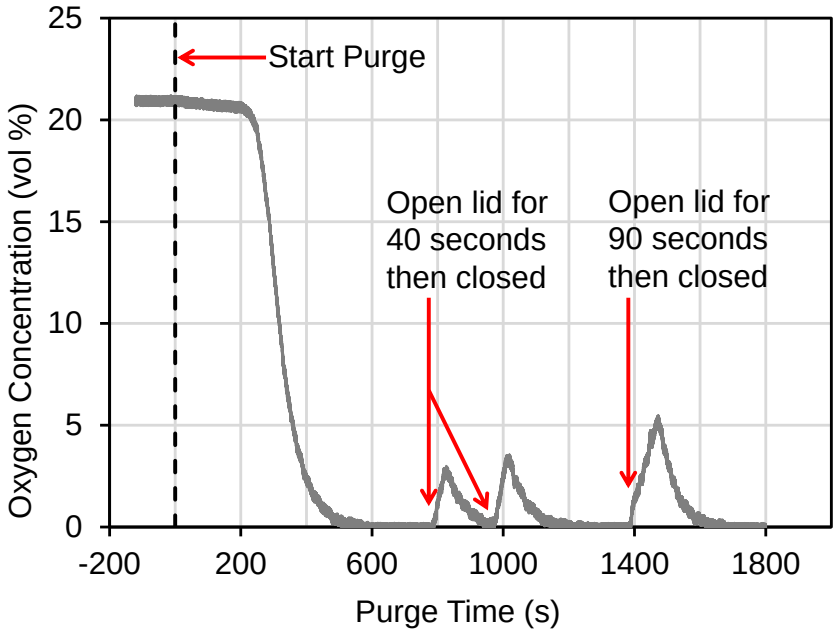

Figure A-1 – Oxygen concentration in furnace and response to argon purging at 488 K (215 °C).

Thermocouple calibration at high temperature

To check the accuracy of the thermocouples at temperatures above 600 °C, the following procedure was performed. This procedure was performed once prior to running interface formation tests in Table 3-7 and 3-8, and a second time prior to running interface formation tests in Table 3-10, 3-11, and 3-12.

Roughly 250 grams of super-pure aluminum was melted in a ceramic crucible and allowed to equilibrate at a temperature of 670 °C. The temperature in the furnace was slowly lowered to a value below 660 °C, to initiate solidification of the liquid aluminum. In this manner, the solidification of the aluminum liquid take place over a period of time of several minutes, over which the temperature of the liquid remained constant. During this time, thermocouples were immersed into the solidifying molten aluminum bath, to a depth of at least 25.4 mm. Thermocouples were left in the bath until the temperature readout from the thermocouple signal reached a steady reading. A minimum of five thermocouples were measured in this fashion. As some molten aluminum adhered to the thermocouples upon removal of the thermocouples from the solidifying aluminum bath, the thermocouples were not reusable. However; subsequent thermocouples used for measuring sample temperatures during interface formation tests of the same make, model, and batch number.

From the first tests, the measured solidification temperature was 657.7 °C with a standard deviation of 0.2 °C. From the second series of tests, the measured solidification temperature was 657.9 °C with a slightly higher standard deviation of 0.4 °C. Thus, the thermocouples measurement system was biased at high temperature, as the published value for the solidification point of liquid aluminum is 660.3 °C. Subsequent temperature measured using the same data acquisition setup and thermocouples were adjusted to account for this bias at high temperature.

Linear transducer calibration

To check the accuracy of the linear displacement transducer, the following procedure was performed. This procedure was performed once prior to running interface formation tests in Table 3-7 and 3-8, and a second time prior to running interface formation tests in Table 3-10, 3-11, and 3-12.

Using gauge blocks of 25.4 mm (1"), 50.8 mm (2"), and 76.2 mm (3") in length, blocks were held beside the transducer as shown in Figure A-2. Steady state voltages were read 3 times per each distance measurement. This process was repeated by stacking gauge blocks, to also get distances in 25.4 mm (1") increments for up to 228.6 mm (9"). The voltage values for each distance were then averaged, and a calibration curve was generated relating measured transducer voltage, in V, to actual displacement in mm.

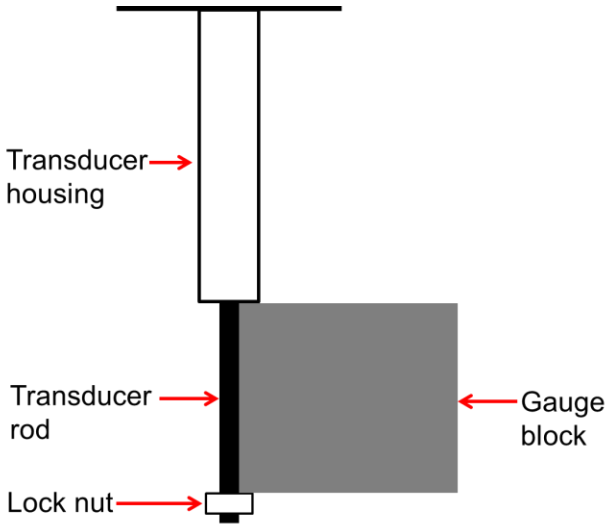

Figure A-2 – Schematic showing gauge block positioning with respect to linear transducer for calibration of displacement transducer.

Appendix B

Sample oxidation calculations

Using the temperature and time history obtained during sample heating, the oxide growth on the samples, prior to immersion in the liquid, was estimated by assuming parabolic oxidation kinetics. The kinetic values which were adopted are based on the values reported by Tenório and Espinosa [40]. The calculations were done using a MATLAB [128] script.

Tenório and Espinosa [40] measured the weight gain, due to sample oxidation, for AA3004 and AA5182 under different atmospheric conditions, from 723-1073K (450-800 °C). For AA3004, which is similar to AA3003 but with 0.8-1.3 wt% Mg added, they observed parabolic weight gain for samples oxidized in air over that temperature range. The parabolic weight gain constant, k_p, was fitted to the following logarithm equation by Tenório and Espinosa [40]:

$$\log_{10} k_{p,AA3004} = -4.23 \cdot \left(\frac{1000}{T(K)}\right) - 1.42 \tag{B-1}$$

For AA5182 (4.0-5.0 wt% Mg) the parabolic weight gain constant, k_p, was fitted to the following logarithm equation, over the temperature range 873-1073K (600-800 °C):

$$\log_{10} k_{p,AA5182} = -1.1839 \cdot \left(\frac{1000}{T(K)}\right) - 3.6135 \tag{B-2}$$

As Mg is commonly observed to increase the oxidation kinetics of an aluminum alloy, the following was done to scale the kinetics measured by Tenório and Espinosa [40]:

$$\mathrm{k_{p,AA5182}} = \mathrm{k_{p,Al}} \cdot (wt\%\, Mg)^2 = \mathrm{k_{p,Al}} \cdot (5.0)^2 = \mathrm{k_{p,Al}} \cdot 25.0 \tag{B-3}$$

$$\mathrm{k_{p,Al}} = \mathrm{k_{p,AA5182}} \cdot 0.04 \tag{B-4}$$

$$\mathrm{k_{p,AA3004}} = \mathrm{k_{p,Al}} \cdot (wt\%\, Mg)^2 = \mathrm{k_{p,Al}} \cdot (1.3)^2 = \mathrm{k_{p,Al}} \cdot 1.7 \tag{B-5}$$

$$\mathrm{k_{p,Al}} = \mathrm{k_{p,AA3004}} \cdot 0.6 \tag{B-6}$$

The resulting oxidation rates, $k_{p,\ Al,}$ estimated using equations B-4 and B-6 are shown in Figure B-1. As shown the scaled kinetics match up reasonably well over the temperature range 823-973 K (550-700 °C).

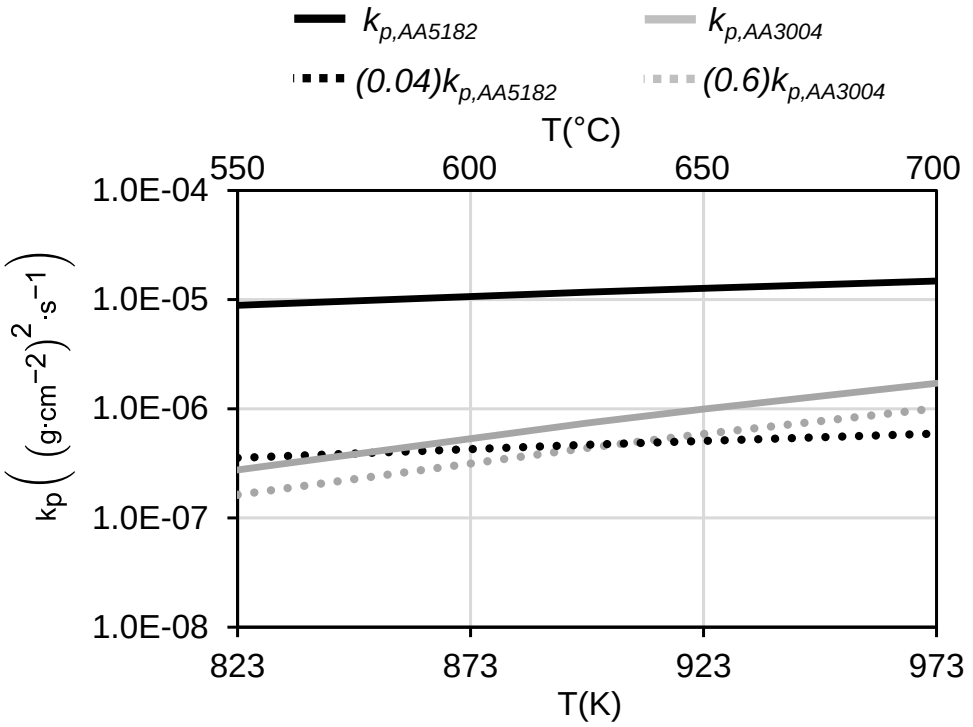

Figure B-1– Comparison of resulting values for $k_{p,Al}$ using the scaling from equations B-5 and B-6.

The final equation for the AA3003 oxidation kinetics which was used for subsequent calculations was:

$$\log_{10}(k_{p,AA3004} \cdot 0.6) = -4.23 \cdot \left(\frac{1000}{T(K)}\right) - 1.42 \qquad \text{(B-7)}$$

The assumed kinetics which were used for subsequent oxidation calculations are shown in Figure B-2. As shown, the assumed kinetics lay between the values from Tenório and Espinosa [40] and the values from Smeltzer [37]. For samples exposed to argon, the rate constant was scaled by a factor of 16, this gave weight gain values 4 times less than the corresponding weight gain in air, consistent with observations by Tenório and Espinosa [40].

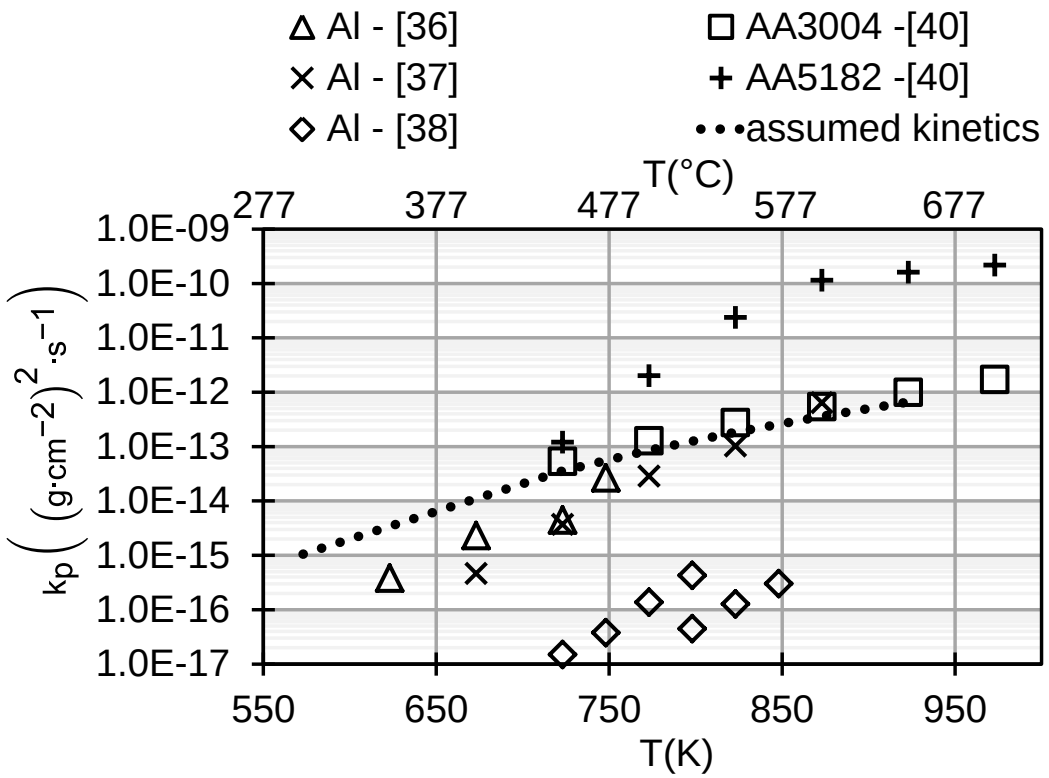

Figure B-2– High temperature oxidation kinetic value (dotted line), compared with other parabolic rate constants in the open literature.

For the assumed parabolic rate constant given in equation B-7, the weight gain per unit area, *w*, can be written as follows:

$$w = \sqrt{k_p t} + const \tag{B-8}$$

Where k_p is the parabolic rate constant, and follows an Arrhenius relation with sample temperature. The constant in this equation was set to zero.

Since the sample temperature may not be constant with time, the weight gain is solved for as a function of time using a numerical integration spreadsheet. Taking the derivative of *w* as a function of time gives:

$$\frac{dw}{dt} = \frac{1}{2}\frac{\sqrt{t}}{\sqrt{k_p}} \tag{B-9}$$

Using piecewise integration, the weight gain over a small period of time is approximately:

$$\Delta w = \frac{1}{2}\frac{\sqrt{t}}{\sqrt{k_p}}\Delta t \qquad \text{(B-10)}$$

For the integration, the started time for oxidation, i.e. *t=0*, was set to be the time at which the sample was placed in the furnace. Althogh test samples were were intentionally stored overnight in a dry box, to grow a repetable intial oxide layer of 2-4 nm, this was not accounted for. To convert weight gain to oxide thickness, recognize that the weight gain due to oxidation is solely from oxygen atoms. Thus, an approximate depth of oxide can be established by equating the following relation and solving for *x*:

$$w\left(SA_{sample}\right) = \left(\rho_{Al_2O_3}\right)\left(SA_{sample}\right)(x)\left(wt\%\ O_{Al_2O_3}\right) \qquad \text{(B-11)}$$

The density of Al_2O_3 used for calculations was given as 3790 kg/m^3 [129], and the calculated weight fraction of oxygen in Al_2O_3 is 0.47.

Appendix C

FIB section low resolution images

In Figure C-1, the chill-bar cast surface which was examined in cross section, using FIB-milling and SEM (see Section 4.4) is shown during various stages of the FIB sectioning process. In Figure C-1a, the chill-bar cast surface is viewed from an angle of zero degrees, in low resolution. The areas encircled in white shows the region where a tungsten sacrificial layer was deposited using e-beam deposition (for details see Section 3.3.2). This image was taken prior to ion beam milling of a trench (cross section). The tungsten (W) layer is oriented in such a way that it bisects one of the surface intermetallics. An enlarged view of this area is shown in Figure C-1b, again prior to trench milling. Here the angle is tiled with respect to the SEM detector, and the thickness of the W layer coating can be shows up as bright white in the SEM image. In Figure C-1c, a trench has been milled away, and again the sample is tilted with respect to the SEM detector in order to view the resulting section. Here, the W coating, cross section, and trench are clearly labelled. Higher resolution imaging of the section allow for the visual measurement of surface oxide thickness, which is barely visible in Figure C-1c given the low resolution and thin surface oxide on this sample.

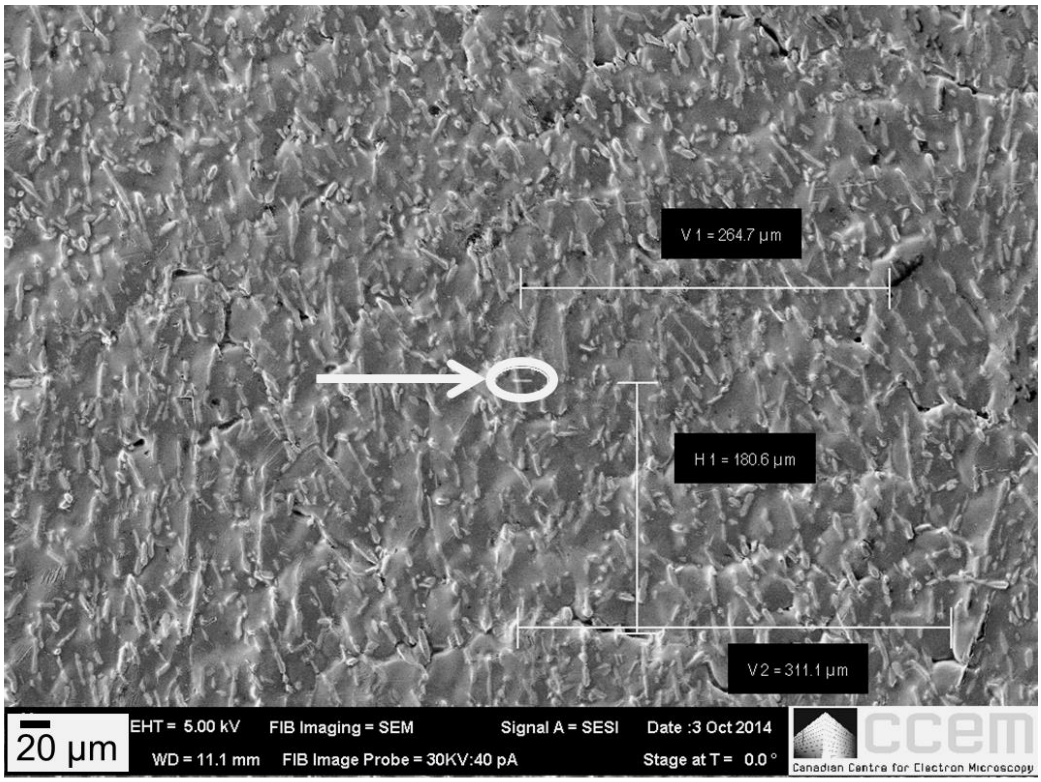

(a)

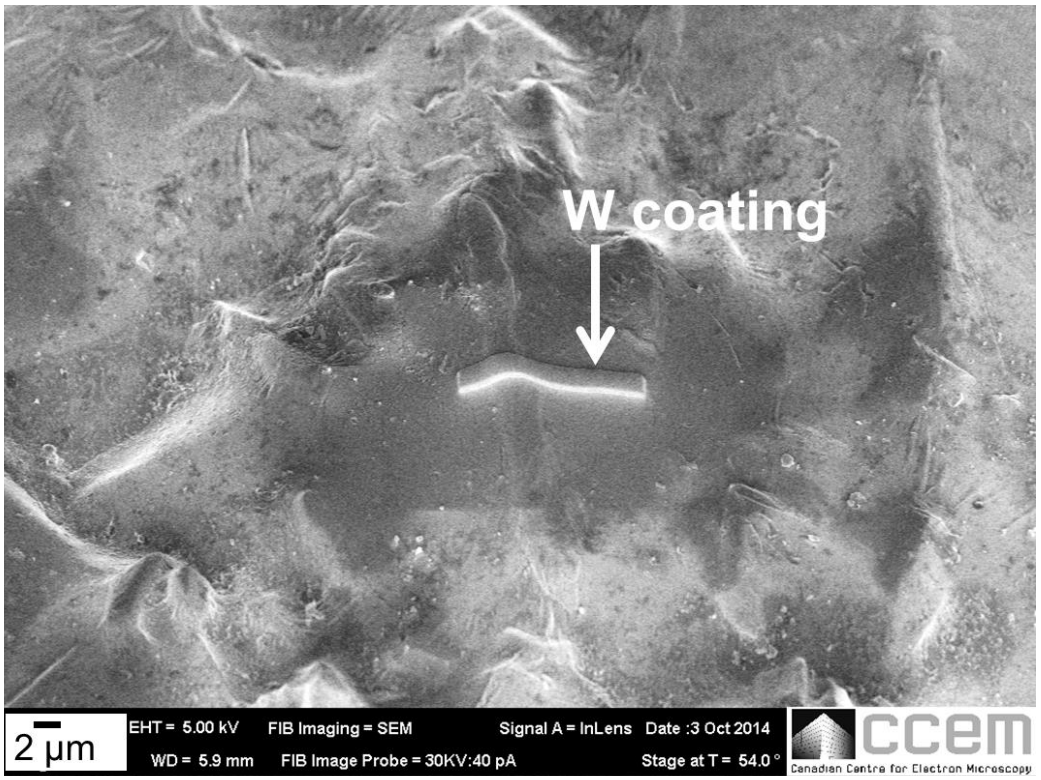

(b)

Figure C-1– (a) low resolution SEM image showing chill-bar cast surface and region where sacrificial tungsten layer was deposited on surface prior to ion beam milling. (b) high resolution image of circled region in image (a).

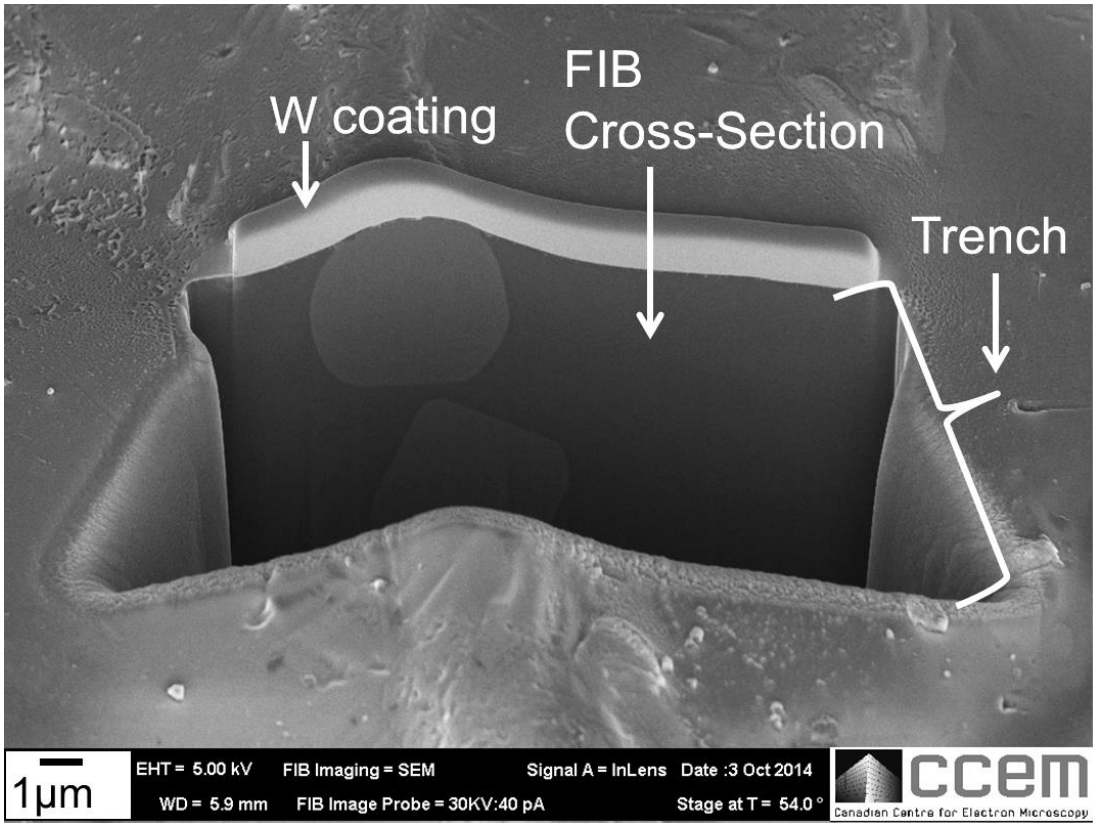

Figure C-2– Section after ion beam milling.

Appendix D

Reduction of Al_2O_3 by Mg

Neglecting the effects of Mn and Si on thermodynamic stability of Al_2O_3, the following calculations were performed to determine the stability of Al_2O_3 in the presence of Mg. In order for Mg to reduce surface oxides, the following reactions must be thermodynamically assessed:

$$3Mg + Al_2O_{3,gamma} = 3MgO + 2Al \quad \text{(D-1)}$$

$$3\mathrm{Mg} + 4\mathrm{Al_2O_{3,gamma}} = 3\mathrm{MgAl_2O_4} + 2\mathrm{Al} \quad \text{(D-2)}$$

$$\mathrm{MgAl_2O_4} + 3\mathrm{Mg} = 4\mathrm{MgO} + 2\mathrm{Al} \quad \text{(D-3)}$$

JANAF tables [27] can be used obtain values for the standard Gibbs free energy from each component species, thus the standard Gibbs free energy of reaction for (D-1)-(D-3) may be computed by:

$$\Delta G^o_{reaction} = \sum_{i=1}^{\#\ products} n\Delta G^o_{f,j} - \sum_{j=1}^{\#\ reactants} n\Delta G^o_{f,j} \quad \text{(D-4)}$$

For each of reactions (D-1)-(D-3), note that each equilibrium reaction has one oxide on either side of the reaction. The stability of one oxide relative to the other can be assessed by the setting the standard Gibbs free energy to zero, to give:

$$\Delta G_{reaction} = 0 \rightarrow \Delta G^0_{reaction} = -\mathrm{RT} \cdot \ln K \quad \text{(D-5)}$$

For a given temperature, *T*, the stability of the oxides then relies on the equilibrium constant, *K*, which for a general reaction:

$$\mathrm{aA} + \mathrm{bB} = \mathrm{cC} + +\mathrm{dD} \quad \text{(D-6)}$$

Is defined as:

$$K = \frac{a_C^c \cdot a_D^d}{a_A^a \cdot a_B^b} \quad \text{(D-7)}$$

The oxides were assumed to be pure, and hence there activities were set equal to a value of one. With respect to this thesis, Mg is present as an alloying element (or impurity) with Al, either in the sample or melt. The Al-Mg phase equilibrium [130] was consulted to determine the activity of Mg in solution with Al. Within this reference, the author refers to the work of Brown and Pratt [131]. Here, Mg in solution with Al is said to behave as a regular solution, where the activity of Mg can be defined by the mol fraction, x_{Mg}, multiplied by a regular solution parameter, γ_{Mg}:

$$a_{Mg} = \gamma_{Mg} x_{Mg} \quad \text{(D-8)}$$

The value of the regular solution parameter, γ_{Mg}, is defined over the temperature range 523-723 K (250-450 °C) in [131]:

$$RT \cdot \gamma_{Mg} = 1370\left(\frac{cal}{K \cdot mol}\right) \cdot x_{Al}^2 \quad \text{(D-9)}$$

Note, it was assumed that the above definition above was valid for higher temperatures.

Aluminum was assumed to behave ideally; hence its activity was set to be equivalent to its molar fraction.

$$a_{Al} = x_{Al} \quad \text{(D-10)}$$

With the proceeding information, a spreadsheet was made to solve for the molar values, x_{Mg} and x_{Al}, required to satisfy the equilibrium of equation (D-5). Performing this equation over a range of temperatures allows for the plotting of the relative stability of the oxides as a function of temperature, *T*, and Mg content, x_{Mg}.

This was performed for each of equation (D-1)-(D-3), hence the relative stability of the oxides γ-Al_2O_3, $MgAl_2O_4$, and MgO. The results are plotted in Figure D-1. As shown, only small amounts of Mg are required to be present in the system to make $MgAl_2O_4$ more stable than γ-Al_2O_3. It should be noted that for thermodynamic data given for γ-Al_2O_3, for the temperature range 873-923 K (600-650 °C), less than 8 ppm is required to make the $MgAl_2O_4$ phase stable. This is slightly different than the calculations given by other authors, for instance [68], which is due to the differences in thermodynamic data for γ-Al_2O_3 and α-Al_2O_3. For comparison purposes, the γ-Al_2O_3:$MgAl_2O_4$ and α-Al_2O_3:$MgAl_2O_4$ stabilty curves were both calculated using JANAF data [27], and are shown in Figure D-2. Here the α-Al_2O_3:$MgAl_2O_4$ stability curve is above the γ-Al_2O_3:$MgAl_2O_4$ curve by an order of magnitude.

While the thermodynamics suggest that γ-Al_2O_3 is not stable with respect to $MgAl_2O_4$ even in the presence of such small quantities of Mg, this does not forego that $MgAl_2O_4$ will form in any appreciable amount in real scenarios. In fact, Nylund *et al.* [64] studied the process of Mg surface segregation during high temperature oxidation of aluminum alloys, and found that for an alloy with a bulk content of 10 ppm Mg, that surface segregation did not take place during high temperature oxidation. Samples were oxidized in a dry air environment, for 1 hour at 893 K (620 °C). In samples with 190 ppm Mg, oxidized under the same test conditions, Mg surface segregation was observed. Additionaly, XRD of the 190 ppm Mg oxidized samples displayed peaks (GA-XRD was not used to enhance the surface signal) corresponding to the $Mg_2Al_2O_4$ phase. The results of Nylund *et al.* [64], for the samples with a bulk content of 190 ppm Mg, agree with the thermodynamics presented in Figure D-1.

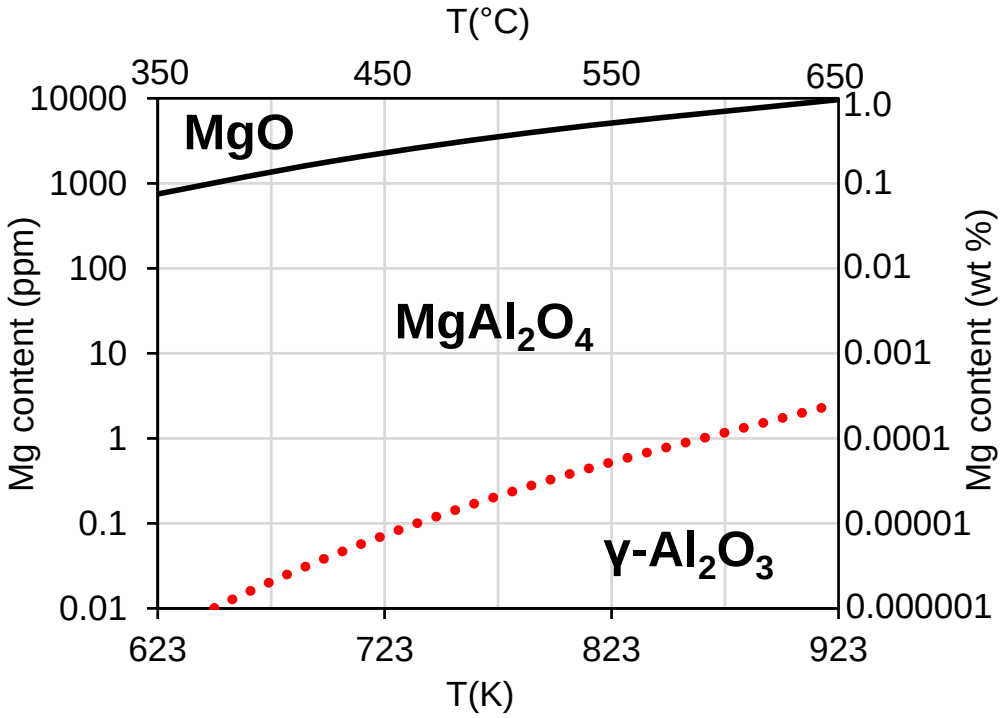

Figure D-1– Thermodynamic stability regions of γ-Al_2O_3, $MgAl_2O_4$, and MgO, as a function of temperature and Mg content.

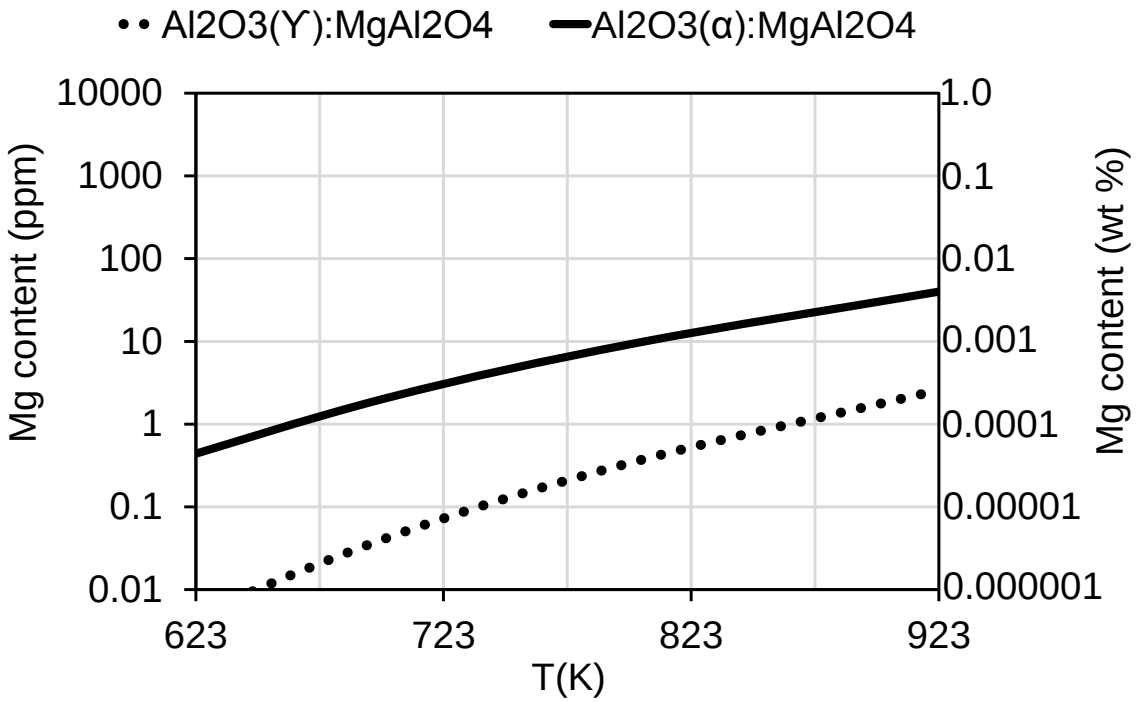

Figure D-2– Comparison of γ-Al_2O_3:$MgAl_2O_4$ and α-Al_2O_3:$MgAl_2O_4$ stabilty curves from thermodynamic data from JANAF tables [27].